

DISSERTATION

LOW-LATITUDE IONOSPHERIC SCINTILLATION SIGNAL SIMULATION,
CHARACTERIZATION, AND DETECTION ON GPS SIGNALS

Submitted by

Yu Jiao

Department of Electrical and Computer Engineering

In partial fulfillment of the requirements

For the Degree of Doctor of Philosophy

Colorado State University

Fort Collins, Colorado

Fall 2017

Doctoral Committee:

Advisor: Yu Morton

Charles Rino

J. Rockey Luo

Clayton Shonkwiler

Copyright by Yu Jiao 2017
All Rights Reserved

ABSTRACT

LOW-LATITUDE IONOSPHERIC SCINTILLATION SIGNAL SIMULATION, CHARACTERIZATION, AND DETECTION ON GPS SIGNALS

Severe signal fluctuations during ionospheric scintillation poses a threat to GNSS signal tracking and degrades position, navigation, and timing solution accuracy, especially in low-latitude regions. To understand the behavior of ionospheric scintillation better, this dissertation research presents several methods regarding scintillation signal simulation, signal characterization and signal detection. The signal simulation is based on the two-dimensional two-component power-law phase screen theory, which is capable of simulating multi-frequency GPS scintillation signals for both stationary and dynamic platforms. The signal characterization is conducted in both time and spatial frequency domains, which lays a foundation for the scintillation signal simulation and detection, and verifies the simulation effectiveness. The scintillation signal detection system is implemented via the support vector machine framework, which can capture amplitude and phase scintillation events, enable future scintillation signal classification and processing, and further validate the effectiveness of the simulation process. The results of this research will provide a thorough investigation of how to characterize, simulate, and detect low-latitude scintillation signals, and will be helpful for the scientific research of space weather and the development of robust GNSS receivers.

ACKNOWLEDGEMENTS

I wish to thank the following people for their assistance and support during my PhD study:

My advisor, Dr. Jade Morton, for her patient mentoring and guidance during my master's and PhD research, and for her generous help in my life in America. It would not have been a wonderful time as an international student here without her.

One of my committee members, Dr. Charles Rino, for his great patience and help during my PhD research. Without his generosity in sharing his knowledge and code, part of this dissertation would not have been accomplished.

All my other current and past committee members, Dr. Rockey Luo, Dr. Clayton Shonkwiler, Dr. Branislav Notaros, and Dr. Richard Aster, for their help and constructive advice in my PhD exams.

My current and past colleagues and friends in the CSU GPS Lab, Dongyang Xu, Jun Wang, Steve Taylor, Harrison Bourne, Brian Breitsch, Greg Myer, Ian Collett, Rong Yang, Zhe Yang, and Bo Han, for learning and growing together as an intimate group.

My parents for their long-term encouragement and selfless support during my stay in America.

My boyfriend, Jack Hall, for his assistance in my research and for making my everyday life even more wonderful.

My other relatives in China and other friends from different parts of the world, for their encouragement and support in my study, and for helping me grow and build a colorful life in America.

I would also like to thank Dr. Don Hampton at the University Alaska Fairbanks, Mr. Marty Karjala at HAARP, Dr. T. Pedersen from Air Force Research laboratory at Kirkland AFB, Mr. Kevin Abnett at Poker Flat Research Range, Dr. Ding Yu Heh at the Nanyang Technological University, Dr. Marco Milla at the Jicamarca Radio Observatory, and Dr. Zhizhao Liu at the Hong Kong Polytechnic University for their support and hosting of the GNSS data collection systems. Jicamarca Radio Observatory is a facility of the Instituto Geofisico del Peru operated with support from NSF grant AGS-0905448 through Cornell University. My PhD research is funded through a startup grant from Colorado State University and a grant from AFOSR (FA9550-14-1-0265). The data collection systems were deployed with funding support from AFRL (FA8650-08-D-1451), AFOSR (FA9550-10-1-0346), the Consortium of Ohio Universities on Navigation and Timekeeping (COUNT), and NSF (AGS-1428042).

TABLE OF CONTENTS

ABSTRACT.....	ii
ACKNOWLEDGEMENTS.....	iii
LIST OF TABLES.....	viii
LIST OF FIGURES.....	x
LIST OF SYMBOLS.....	xvii
1. CHAPTER 1 – BACKGROUND AND INTRODUCTION.....	1
1.1. Ionospheric Scintillation Phenomenon.....	1
1.2. Effects of Ionospheric Scintillation on GNSS Receiver Operations.....	5
1.3. Ionospheric Scintillation Indices.....	7
1.4. Global GNSS Data Collection Systems Established by CSU GPS Lab.....	9
1.5. Literature Research.....	13
1.5.1. Previous Research on Scintillation Signal Simulation.....	13
1.5.2. Previous Research on Scintillation Signal Characterization.....	16
1.5.3. Previous Research on Scintillation Signal Detection.....	17
1.6. Motivations and Contributions of Dissertation Research.....	19
1.7. Dissertation Outline.....	21
2. CHAPTER 2 – GPS CIVIL SIGNAL STRUCTURES.....	22
2.1. GPS L1 C/A Signal.....	22
2.2. GPS L2C Signal.....	26
2.3. GPS L5 Signal.....	29
3. CHAPTER 3 – PROPAGATION GEOMETRY.....	34
3.1. Coordinate Systems.....	34
3.1.1. Earth-Centered Earth-Fixed (ECEF) Coordinate.....	35
3.1.2. Geodetic Coordinate.....	35
3.1.3. World Geodetic System 1984 (WGS-84).....	37
3.1.4. Topocentric Horizon Coordinate.....	38
3.1.5. Horizontal Coordinate System.....	39
3.2. Global Geomagnetic Field Model.....	39
3.2.1. Components of Geomagnetic Field.....	40
3.2.2. International Geomagnetic Reference Field.....	41
3.3. Satellite Position and Velocity Calculation with GPS Ephemeris.....	42
4. CHAPTER 4 – PROPAGATION THEORY AND STRUCTURE REALIZATION.....	46
4.1. Forward Propagation Theory.....	46
4.1.1. Maxwell's Equations.....	46
4.1.2. Freely Propagation of Waves in Homogeneous Media.....	48
4.1.3. Forward Propagation Theory.....	50
4.1.4. Split-step Algorithm.....	52
4.1.5. Oblique Propagation.....	53
4.2. Structure Realization.....	55
4.2.1. Structure Sources.....	55
4.2.2. Spectral Representation.....	56
4.2.3. One-component Power-law Spectral Model.....	57

4.2.4.	Power-law Spectral Model in Anisotropic Media.....	58
4.2.5.	Two-component Power-law Spectral Model.....	59
4.2.6.	Sample Translation between Time and Space.....	59
4.2.7.	Total Electron Content (TEC).....	60
4.3.	Time-domain Data Surrogate Methodology.....	63
5.	CHAPTER 5 – DETECTION METHODOLOGY FOR SCINTILLATION DETECTION.....	67
5.1.	Fundamental Detection Theory.....	67
5.2.	Mathematics of Support Vector Machines (SVMs).....	69
5.2.1.	Optimal Hyperplane via Margin of Separation.....	70
5.2.2.	Optimal Hyperplane with Soft Margin SVM.....	74
5.2.3.	SVM Kernel Extension.....	75
6.	CHAPTER 6 – RESULTS ON SCINTILLATION SIGNAL CHARACTERIZATION.....	79
6.1.	Data Set for Scintillation Signal Characterization.....	79
6.2.	Spatial Spectrum Density Function.....	84
6.3.	Auto-correlation Function.....	87
6.4.	Probability Distribution Function on Detrended Signal Intensity.....	89
6.5.	Multi-band Fading Characteristics on Signal Intensity.....	91
6.5.1.	Fading Duration.....	92
6.5.2.	Fading Time Separation.....	94
6.5.3.	Fading Characteristics vs. Scintillation Level.....	96
6.5.4.	Fading Overlap.....	98
6.6.	Concluding Remarks on Scintillation Signal Characterization.....	99
7.	CHAPTER 7 – RESULTS ON SCINTILLATION SIGNAL SIMULATION.....	101
7.1.	Scintillation Simulation Scheme.....	101
7.2.	Scintillation Simulation Initialization Data.....	103
7.3.	Scintillation Simulation for Stationary Receivers Using Wave Propagation Method..	104
7.3.1.	Parameter Extraction and Data Interpretation.....	104
7.3.2.	Comparison of Signal Characteristics of Simulated Data and Real Data.....	111
7.4.	Scintillation Simulation for Dynamic Receivers Using Data Surrogate Method.....	124
7.4.1.	Propagation Geometry for Dynamic Platforms.....	125
7.4.2.	Receiver Dynamics, Geomagnetic Field, and Irregularity Drift.....	126
7.4.3.	Scintillation Simulation Parameters for Dynamic Receiver Platforms.....	131
7.4.4.	Evaluation of Dynamic Scintillation Signal Simulation.....	133
7.5.	Concluding Remarks on Scintillation Signal Simulation.....	136
8.	CHAPTER 8 – RESULTS ON SCINTILLATION SIGNAL DETECTION.....	140
8.1.	Amplitude Scintillation Signal Detection.....	140
8.1.1.	Training Data and Observation Matrix.....	140
8.1.2.	Validation Performance.....	145
8.1.3.	Test on Novel Data.....	150
8.2.	Phase Scintillation Signal Detection.....	157
8.2.1.	Training and Validation Performance.....	157
8.2.2.	Test Performance on Novel Data.....	164
8.3.	Concurrent Amplitude and Phase Scintillation Signal Detection.....	167
8.4.	Scintillation Detection on Simulated Scintillation Signals.....	174
8.5.	Concluding Remarks on Scintillation Signal Detection Using SVM.....	174
9.	CHAPTER 9 – CONCLUSIONS AND FUTURE WORK.....	177

REFERENCES	179
APPENDIX.....	194
A. Fading Characteristics of Scintillation Data from Singapore and Hong Kong	194
LIST OF ABBREVIATIONS	201

LIST OF TABLES

Table 1-1. Locations and operational durations of the current GNSS data collection sites established by CSU GPS Lab. The locations are divided into high-latitude, mid-latitude, and low-latitude regions, the definitions of which are denoted in the table	10
Table 2-1. Summary of the signal structures of current GPS civil signals (L1 C/A, L2C, and L5)	33
Table 3-1. Fundamental parameters defined in WGS-84.....	38
Table 3-2. Ephemeris parameter definitions [IS-GPS-200H, 2013]	43
Table 3-3. User algorithm for satellite position and velocity calculation [Remodi, 2004; IS-GPS-200H, 2013]	43
Table 5-1. Illustration of the components of a confusion matrix	69
Table 6-1. Data segment length (hours) used in this chapter from visible satellites that broadcast L2C signals. The elevation mask is 10°	80
Table 6-2. The ranges of satellite elevation angles for the data segments used in this chapter with the elevation mask of 10°	80
Table 6-3. Total number of observed deep signal intensity fades on GPS L1, L2C, and L5 under different thresholds	92
Table 6-4. The percentage of detrended signal intensity fading overlaps on GPS L1 and L2C observed on PRN 29 and PRN 31 on March 7-10, 2013 on Ascension Island.....	99
Table 6-5. The percentage of detrended signal intensity fading overlaps on GPS L1, L2C, and L5 observed on PRN 24 and PRN 25 on March 7-10, 2013 on Ascension Island.....	99
Table 7-1. Values of the spectral parameters obtained using the IPE technique for the two-component power-law structure model for scintillation signal simulation using the traditional wave propagation method	108
Table 7-2. Number of fades below the -10 dB threshold on the three GPS frequencies in the three segments of real data, 20 segments of simulation data, and their corresponding processed data.....	116
Table 7-3. Velocities for a receiver platform with respect to the geomagnetic field direction. The magnitude of the velocities is 100 m/s except for Velocity #0	127
Table 7-4. Values of the parameters used in the scintillation signal simulation for dynamic receiver platforms	132
Table 8-1. Data used for training and validation. The data are divided into strong scintillation data from Ascension Island and Hong Kong, and moderate scintillation data from Jicamarca, Peru. The elevation mask for all the data is 30°	142
Table 8-2. Content of a column training vector used in the SVM amplitude scintillation detector	144
Table 8-3. The TPR and FPR at the operating points in the validation for the 12 combinations shown in Figure 8-2, Figure 8-3, and Figure 8-4.....	150
Table 8-4. Training data set from Gakona, AK.....	158
Table 8-5 Content of a column training vector used in the SVM phase scintillation detector. Each training vector corresponds to a training data block of 3 minutes in length.....	159
Table A- 1. Strong scintillation events for the analysis of fading characteristics from Singapore and Hong Kong	194
Table A- 2. Numbers of signal intensity fading events extracted on the three GPS frequency	

bands from the data collected at Singapore and Hong Kong under the thresholds of -10 dB and -15 dB.....	195
Table A- 3. The percentage of multi-frequency signal intensity fading overlaps on GPS L1, L2C and L5 in Singapore (first lines) and Hong Kong (second lines), for satellites that broadcast all three GPS signals only.....	200

LIST OF FIGURES

Figure 1-1. Scintillation occurrence frequency on GPS L1C/A with respect to hours after local sunset at Gakona, Jicamarca, and Ascension Island. The data from these locations were collected from August 2010 to June 2014, November 2012 to July 2014, and March 1 st to 10 th 2013, respectively. The data sets also apply to Figure 1-2 and Figure 1-3.	4
Figure 1-2. Seasonal scintillation occurrence frequency on GPS L1C/A, determined by the mean event number (the histogram), compared with the seasonal sunspot number (the black dotted line) for Gakona and Jicamarca.	4
Figure 1-3. Daily scintillation event occurrence frequency on GPS L1C/A with respect to Ap index at (a) Gakona, Alaska, (b) Jicamarca, Peru, and (c) Ascension Island. A linear least-mean-square fit is imposed on subplot (a) based on the data points. Ap index is a global geomagnetic activity index, a higher value of which indicates a more intense geomagnetic activity world-wise.	5
Figure 1-4. Global map showing the geographic locations of the GNSS data collection sites established by CSU GPS Lab. The bands of the magnetic low-latitude area and the auroral ovals are estimations. Credit: plot courtesy of Brian Breitsch at CSU GPS Lab.	9
Figure 1-5. General architecture of the event-driven GNSS data collection systems deployed at several high-latitude and low-latitude sites. The GSV4004B and the PolaRxS receivers are the commercial ISM receivers which are used to collect full-time navigation data and trigger the data collection of the RF front ends [Jiao and Morton, 2015].	11
Figure 1-6. Relationships of the three major topics in this dissertation, involving two types of data: the real GPS scintillation data and the simulated GPS scintillation data.	20
Figure 2-1. Current GPS signal generation on L1 band [Morton, 2014-16].	23
Figure 2-2. Structure of the GPS L1 C/A signal [Morton, 2014-16].	24
Figure 2-3. L1 C/A code generation [Morton, 2014-16].	25
Figure 2-4. Structure of the LNAV data on L1 [Borre et al., 2007].	26
Figure 2-5. Current GPS signal generation on L2 band. The dotted line encircles the generation scheme of the L2C signal [Morton, 2014-16].	27
Figure 2-6. Generation scheme of L2 CM and CL codes [IS-GPS-200H, 2013].	28
Figure 2-7. Structure of L2-CNAV messages [IS-GPS-200H, 2013].	29
Figure 2-8. Current GPS signal generation on L5 band [Morton, 2014-16].	30
Figure 2-9. Generation of I5 and Q5 codes on L5 signal [IS-GPS-705D, 2013].	31
Figure 2-10. Structure of L5-CNAV messages [IS-GPS-705D, 2013].	32
Figure 3-1. Illustration of ECEF coordinate (x, y, z) and geodetic coordinate (ϕ, λ, h). The Earth surface is modeled as an ellipsoid.	35
Figure 3-2. Conversions between ECEF and geodetic coordinates. a and b are the semi-major and semi-minor axes.	36
Figure 3-3. Topocentric horizon coordinate ($xtcs, ytcs, ztcs$) and horizon coordinate system (θ, φ).	38
Figure 3-4. Components of geomagnetic field.	40
Figure 4-1. Reference coordinate system for oblique propagation. x_p is downward, y_p is geomagnetically eastward and z_p is geomagnetically southward. The boundaries of the disturbed layers are perpendicular to the x_p -axis [Rino, 2011].	54

Figure 4-2. Detrended signal intensity on L1, and relative STECs calculated from phase measurements on L1 and L2C, and L1 and L5. The data was collected on PRN 24 from 20:09:43 to 21:09:36 UTC on March 8, 2013 on Ascension Island. The first half of the data is quiet and the second half is scintillating.....	63
Figure 5-1. Illustration of TNR, FNR, FPR, and TPR.....	68
Figure 5-2. Illustration of optimal decision boundary in SVM.....	71
Figure 6-1. Sky view plots of all visible satellite (SV) tracks during local time 8 pm – 1 am on March 7-10 on Ascension Island. The tracks are color-coded by the values of the S ₄ index on L1. White points in the plots are tracks without reliable S ₄ observables below an elevation of 10°. The ends with PRN numbers represent the starting points of the tracks. The centers of the rings are elevation 90°, and the rings are equal-elevation contours with an increment of 10°. The tracks defined by the black lines are the approximate ranges of satellite elevation angles for the data segments used in this chapter listed in Table 6.1-1.....	81
Figure 6-2. Signal intensity (SI) measurements collected from PRN 24 from 20:09:43 to 21:09:36 UTC on March 8, 2013 on Ascension Island. Subplots in the top row are raw signal intensity on different GPS frequencies with the black lines showing the trend using wavelet detrending. Bottom row subplots are detrended signal intensity. The data is divided into 5-minute segments for analysis, with the last one slightly shorter than 5 minutes. The centers of the segments are shown as the black dots in the bottom row.....	82
Figure 6-3. Same as Figure 6-2 but for PRN 31 from 23:03:03 to 23:32:58 UTC on March 8, 2013.....	83
Figure 6-4. Same as Figure 6-2 but for PRN 24 from 20:01:00 to 21:55:55 UTC on March 10, 2013.....	83
Figure 6-5. Spatial SDFs for the six segments of 5-min data from PRN 31 on March 8, 2013. The x-axes are the log ₁₀ of the wavenumber. The vertical bars in the bottom center of each subplot are the Fresnel scales for L1 and L2 frequencies. The eastward drift velocity of the ionospheric irregularity is assumed to be 50 m/s.....	85
Figure 6-6. Spatial SDFs for segment 2 (quiet) and segment 5 (strong scintillation) in the data from PRN 31 on March 8, 2013. The eastward drift velocity of the ionospheric irregularity is altered to be 25 m/s, 50m/s or 75 m/s.....	86
Figure 6-7. ACFs for segment 1 (quiet) and segment 4 (strong scintillation) in the data from PRN 31 on March 8, 2013. The circles and the legends in the plot denote the 1/e de-correlation distances. The eastward drift velocity of the ionospheric irregularity is assumed to be 50 m/s...	87
Figure 6-8. The S ₄ index values and the 1/e de-correlation distances for all the data segments from PRN 24 on March 8, 2013. The eastward drift velocity of the irregularity is assumed to be 50 m/s. Any de-correlation value that is greater than 300 m is set as invalid.....	88
Figure 6-9. Same as Figure 6-8, but for PRN 31 on March 8, 2013.....	89
Figure 6-10. Same as Figure 6-8, but for PRN 24 on March 10, 2013.....	89
Figure 6-11. PDFs of the detrended signal intensity (SI) on L1, L2C, and L5 for all the data segments collected from PRN 24 on March 8, 2013 on Ascension Island.....	90
Figure 6-12. PDFs of the detrended signal intensity (SI) on L1 and L2C for all the data segments collected from PRN 31 on March 8, 2013 on Ascension Island.....	91
Figure 6-13. Detrended signal intensity (SI) fading example across three GPS bands on PRN 24 on March 10, 2013 on Ascension Island. During deep fading, the signals on different frequencies become less correlated both in time and in magnitude.....	92
Figure 6-14. Illustration of fading duration, time separation between fades and fading overlaps	

on normalized signal intensity using the threshold of -15 dB.	93
Figure 6-15. Distributions of GPS L1, L2C, and L5 fading duration on detrended signal intensity (SI) under the thresholds of (a) -10 dB, (b) -15 dB, (c) -20 dB, and (d) -25 dB. Mean durations are labeled in the legends.	94
Figure 6-16. Distributions of single-band fading time separation for GPS L1, L2C, and L5 under the thresholds of (a) -10 dB, (b) -15 dB, (c) -20 dB, and (d) -25 dB. Mean time separations are labeled in the legends. The mean separations are averaged among separations under 60 seconds.	95
Figure 6-17. Distributions of multi-band fading time separation for L2C from L1, L5 from L1, and L5 from L2C under the thresholds of (a) -10 dB, (b) -15 dB, (c) -20 dB, and (d) -25 dB. Mean time separations are labeled in the legends. The mean separations are averaged among separations under 60 seconds.	96
Figure 6-18. Mean fading numbers and fading durations as a function of S_4 index values on the three GPS bands under the thresholds of -10 dB, -15 dB, -20 dB, and -25 dB. The fading number in (a) is the number of fades observed with their mid-points within an S_4 calculation interval (60 s). It is reciprocally related to the mean time separation. The average duration of these fades is the mean fading duration shown in subplot (b).	97
Figure 7-1. Flow chart of the static GPS scintillation signal simulation using phase screen theories, and its relationship with signal post-processing. The GPS scintillation signal simulator consists of user input, scintillation generator, and GPS IF sample generator. The output of the simulator can be used to test receiver signal processing algorithms and to characterize signal statistics.	102
Figure 7-2. Detrended signal intensity measurements on GPS L1, L2, L5 on PRN 24 collected in Hong Kong from 12:00:00 to 12:59:59 UTC on October 5, 2013. The stars mark the centers of each 5-minute segment of data. The 6 th segment is picked as the simulator initializer.	103
Figure 7-3. Scintillation signal propagation geometry in the reference coordinate system for oblique propagation in the single layer phase screen simulation. The coordinate system was introduced in Figure 4-1 with the origin at the IPP. The irregularity layer is a slab of Δx thickness above the IPP and perpendicular to the x-direction. The irregularity is assumed to be invariant along the z -direction.	105
Figure 7-4. Propagation geometry of the one-hour Hong Kong data in Figure 7-2. The geometry for the selected initialization data (Segment 6) is shown between the vertical lines. The geometry parameters included in this figure are satellite range from the satellite to the receiver, IPP range from IPP to the receiver, propagation angles θ and φ , and effective velocity v_{eff}	106
Figure 7-5. Spectrum density functions of the L1, L2, and L5 detrended signal intensity measurements in the initialization data from Hong Kong. In this study, wavenumber $q = kyp$	108
Figure 7-6. The detrended signal intensity and phase of the initialization data (left), the example segment of simulation data (middle), and its processed data (right) on the three GPS bands. The S_4 values of the signals are labeled in the legends.	113
Figure 7-7. Comparison of the detrended signal intensity and phase of the simulation, and its processed data in Figure 7-6 on the three GPS bands. The S_4 values of the signals are labeled in the legends.	114
Figure 7-8. The spatial SDFs and the PDFs of the detrended signal intensity of the initializer (blue), the example segment of simulation data (green), and its processed data (red) on the three GPS bands. A raised noise floor at high frequencies can be observed on SDFs of the initializer	

and the processed data.	115
Figure 7-9. Illustration of the parameters characterized in the statistics in Subsection 7.3.2.2, which include fading duration and depth, peak-to-peak phase change, and max phase rate during fading.	117
Figure 7-10. Histograms of the fading depth for fades below the -10 dB threshold on the three GPS frequencies in (a) the real data, (b) the simulation data, and (c) the processed data.	118
Figure 7-11. Histograms of the fading duration for fades below the -10 dB threshold on the three GPS frequencies in (a) the real data, (b) the simulation data, and (c) the processed data. The legends indicate the average fading duration.	118
Figure 7-12. Relationships between fading duration and fading depth for fades below the -10 dB threshold on the three GPS frequencies in (a) the real data, (b) the simulation data, and (c) the processed data.	119
Figure 7-13. Histograms of the single-band fading separation for fades below the -10 dB threshold on the three GPS frequencies in (a) the real data, (b) the simulation data, and (c) the processed data. The legends indicate the average fading separation for the separations below 60 seconds.	120
Figure 7-14. Histograms of the multi-band fading separation for fades below the -10 dB threshold on the three GPS frequencies in (a) the real data, (b) the simulation data, and (c) the processed data. The legends indicate the average fading separation for the separations below 60 seconds.	120
Figure 7-15. Histograms of the peak-to-peak phase change during fading below the -10 dB threshold on the three GPS frequencies in (a) the real data, (b) the simulation data, and (c) the processed data.	122
Figure 7-16. Histograms of the max phase rate during fading below the -10 dB threshold on the three GPS frequencies in (a) the real data, (b) the simulation data, and (c) the processed data.	122
Figure 7-17. Relationships between the absolute value of the peak-to-peak phase change and the fading depth for fades below the -10 dB threshold on the three GPS frequencies in (a) the real data, (b) the simulation data, and (c) the processed data.	123
Figure 7-18. Relationships between the log10 of the absolute value of the max phase rate and the fading depth for fades below the -10 dB threshold on the three GPS frequencies in (a) the real data, (b) the simulation data, and (c) the processed data. The two show well-correlated linear relationships. The linear fits are given in black lines with corresponding equations shown below the lines together with the correlation coefficients. In subplot (a), red, green, and blue markers represent data collected on Sept. 24, Oct. 5, and Oct. 6 2013, respectively.	124
Figure 7-19. One-dimensional illustration of the IPP velocity v_{IPP} at the phase screen which includes contributions from the satellite velocity v_{sat} and the receiver velocity v_{rx} . The ionospheric irregularity drift velocity v_{drift} and v_{IPP} together determine the value of v_{eff} . The illustration is not to scale.	126
Figure 7-20. Illustration of the different velocity configurations of the receiver platform listed in Table 7.4-1 with respect to the geomagnetic field direction.	128
Figure 7-21. The values of the time scale factor $\rho F/v_{eff}$ for different velocity designs of the receiver platform with respect to the local geomagnetic field direction. The geometry used is extracted from the initializer shown in Figure 7-2.	129
Figure 7-22. Same as Figure 7-21 but for the geometry in the data collected on PRN 24 from 14:30:00 to 14:34:59 UTC on September 24, 2013 at Hong Kong. The velocity configurations are designed the similar way to those listed in Table 7.4-1 according to the geomagnetic direction	

at the IPP.	130
Figure 7-23. Same as Figure 7-21 but an eastward irregularity drift velocity of 100 m/s is added.	131
Figure 7-24. Comparison of the signal intensity and phase in the initialization data and the simulation data for Velocity #0.	133
Figure 7-25. Simulation signal intensity and phase on GPS L1 band for Velocities #0, 3, and 4. Velocities #3 and 4 are the slowest and the fastest scenarios in Figure 7-23. The S_4 index values are denoted in the legend in the upper subplot. The random number sequence ηn used in the three scenarios is the same.	134
Figure 7-26. A zoom-in plot of Figure 7-25 between the 1 st and 2 nd minute. The difference in the decorrelation time of the signal intensity and phase for different velocity designs is obvious. .	135
Figure 7-27. Same as Figure 7-25 but for GPS L2 band.	135
Figure 7-28. Same as Figure 7-25 but for GPS L5 band.	136
Figure 8-1. Examples of S_4 index values on GPS L1C/A in the training data from (a) Ascension Island, (b) Hong Kong, and (c) Jicamarca, Peru. Scintillation observed in Ascension Island and Hong Kong is generally stronger than that observed in Jicamarca, Peru. The stair lines in the plot are class labels, assigned manually.	143
Figure 8-2. Validation performance on (a)(c) linear SVM and (b)(d) medium Gaussian SVM. Only strong scintillation data from Ascension Island and Hong Kong are used here for training and validation. S_4 features (2 nd and 3 rd entries in training vectors) are included in training in (a) and (b), but excluded in (c) and (d). The circle markers on the ROC curves on the left are the operating points for the confusion matrices on the right. The total accuracies of the classifiers are denoted in the labels on the left.	147
Figure 8-3. Same as Figure 8-2, but only moderate scintillation data from Jicamarca, Peru is used here for training and validation.	148
Figure 8-4. Same as Figure 8-2, but all the data listed in Table 8.1-1 is used here for training and validation.	149
Figure 8-5. Test results on the novel data from Singapore. The data was collected on GPS L1C/A PRN01 from 13:19:55 to 17:12:39 UTC on March 26, 2012. Subplots (a) through (l) correspond to the test results using the 12 SVM variations. Last subplot (m) shows the trigger result.	153
Figure 8-6. Incorrect classification results on a segment of novel data containing strong scintillation signals. The data was collected on GPS L1C/A PRN31 from 23:14:00 to 23:59:59 UTC on March 9, 2013 on Ascension Island.	154
Figure 8-7. Test results on the novel data from Ascension Island. The data was collected on PRN 31 from 23:14:00 to 23:55:39 UTC on March 9, 2013. Subplots (a) through (d) correspond to the results using the four training combinations. Subplot (e) shows the result using the trigger criteria.	155
Figure 8-8. Same as Figure 8-7, but for test data from Hong Kong which was collected on PRN 24 from 12:18:27 to 15:38:26 UTC on September 29, 2013.	156
Figure 8-9. Same as Figure 8-7, but for test data from Jicamarca, Peru which was collected on PRN 23 from 00:22:06 to 04:32:05 UTC on March 11, 2013.	156
Figure 8-10. An example of training data from Gakona, AK. The data was collected on PRN 16 from 12:49:54 to 13:44:46 UTC on March 17, 2013. Subplot (a) shows σ_ϕ index values and class labels assigned manually. Subplot (b) shows the spectrogram on the detrended phase measurements with 3-minute non-overlapping windows.	160
Figure 8-11. Validation performance on (a)(c) linear SVM and (b)(d) medium Gaussian SVM. σ_ϕ	

features (2nd and 3rd entries in training vectors) are included in (a) and (b) in the training, but excluded in (c) and (d). The red dots on the ROC curves on the left are the operating points for the confusion matrices on the right, with the corresponding TPR and FPR denoted. The total accuracies of the classifiers are given in the subplot titles. 163

Figure 8-12. Classification prediction results on novel data collected on GPS L1C/A PRN01 from 01:43:18 to 04:23:18 UTC on November 14, 2012 at Gakona, AK. Subplots (a) through (d) are test results using different SVM algorithms with (w/) and without (w/o) σ_ϕ features. Last subplot (e) shows the trigger result using the four trigger criteria..... 165

Figure 8-13. Classification prediction results on novel data from Poker Flat, AK. The data was collected on GPS L1C/A PRN25 from 11:27:33 to 13:47:33 UTC on December 20, 2015. 166

Figure 8-14. Concurrent phase and amplitude scintillation detection on novel data from Jicamarca, Peru. The data was collected on GPS L1C/A PRN13 from 01:40:00 to 03:40:00 UTC on March 11, 2013. Subplots (a) and (c) are detection results using linear SVM without σ_ϕ/S_4 features. Subplots (b) and (d) are detection results using the hard threshold-based trigger systems. The detector used in subplot (c) is trained only by strong scintillation data listed in Table 1 in [14]..... 169

Figure 8-15. Concurrent phase and amplitude scintillation detection on novel data from Singapore. The data was collected on GPS L1C/A PRN01 from 12:22:28 to 14:22:28 UTC on April 09, 2012. 170

Figure 8-16. Concurrent phase and amplitude scintillation detection on novel data from Hong Kong. The data was collected on GPS L1C/A PRN24 from 12:41:36 to 14:41:36 UTC on September 10, 2014. 171

Figure 8-17. Relationship between σ_ϕ and S_4 index values with detected amplitude scintillation in the 15 segments of test data from Jicamarca, Singapore, and Hong Kong. The detectors are linear SVM detectors trained without σ_ϕ/S_4 features. The linear fit shown as the black line in the plot is zero-intercept using data points satisfying $\sigma_\phi < 1$ and $S_4 < 1$ 172

Figure 8-18. (a) The percentage of phase scintillation detection when amplitude scintillation is detected within a block, and (b) the percentage of amplitude scintillation detection when phase scintillation is detected within a block. The percentage is evaluated with respect to the scintillation level (mean S_4/σ_ϕ) within that block. The detectors are linear SVM detectors trained without σ_ϕ/S_4 features. 173

Figure 8-19. Detection results on simulated scintillation signals using SVM techniques for (a) amplitude scintillation and (b) phase scintillation. The detector outputs shown as the red lines in the lower panels demonstrate that the detectors can work correctly on simulated signals. 174

Figure A- 1. Distributions of GPS L1, L2C and L5 signal intensity fading duration in (a) Singapore and (b) Hong Kong under the thresholds of -10 dB and -15 dB. Mean durations are labeled in the legends. 196

Figure A- 2. Distributions of single-band time separation for (a) L1, (b) L2C, and (c) L5 at Singapore and Hong Kong under the thresholds of -10 dB and -15 dB. The mean separations in the legends are averaged among separations under 60 seconds. 197

Figure A- 3. Distributions of multi-band time separation for (a) L2 from L1, (b) L5 from L1, and (c) L5 from L2 at Singapore and Hong Kong under the thresholds of -10 dB and -15 dB. The mean separations in the legends are averaged among separations under 60 seconds. 198

Figure A- 4. Mean fading numbers and fading durations for certain levels of S_4 index values on the three GPS bands under the thresholds of -10 dB and -15 dB in (a) Singapore and (b) Hong Kong. The fading number is the number of fades observed with their middle points within an S_4

calculation interval (60 s). It is reciprocally related to the mean time separation. The average duration of these fades is the mean fading duration shown in the right panel..... 199

LIST OF SYMBOLS

The symbols listed here only apply for Chapter 4.

Symbol	Definition
E	Electric field (Volts/m)
H	Magnetic field (Amps/m)
r	Position vector (m)
J	Current density (Amps/m ²)
k	Wave number (/m)
κ	Transverse components of wave number vector (/m)
ς	Transverse vectors perpendicular to the reference axis (<i>x</i> axis)
a_{kT}	Unit vector along the transverse component
ζ	Transverse coordinate in the displaced system
v_k	Apparent velocity in the measurement plane (m/s)
$\widehat{\cdot}$	The complex amplitude of a vector
$\widetilde{\cdot}$	Spatial Fourier decomposition of a field
ψ	Complex scalar wave field for FPE solution
ψ_k	Complex scalar wave field for FPE solution in CDCS
Φ	Spatial spectral density function
φ	The phase of a field (rad)
η	White noise field
R	Autocorrelation function
t	Time (s)
ρ	Volume charge density (Coulombs/m ³)
ε	Electric permittivity (Farads/m)
μ	Magnetic permeability (Henries/m)
ω	Angular frequency (radians/s)
ω_p	Plasma frequency (radians/s)
f, f_D	Frequency, Doppler frequency (Hz)
q, q₀	One-dimensional wave number, break wave number (/m)
μ, μ₀	Normalized wave number and break wave number
v_p	Propagation phase velocity (m/s)
n; n_d, n_t, δn	Refractive index; deterministic, slow-varying, and random components
θ	Propagation angle from downward axis
φ	Propagation azimuth angle from eastward axis
c	The speed of light in vacuum (m/s)
N_e	Electron density (/m ³)
r_e	Classical electron radius (m)
v	Scale-free spectral index

C_S, C_p	Turbulence strength, phase turbulence strength
l_p	Layer thickness (m)
p_1, p_2	Two-component power-law indices
ρ_F	Fresnel scale (m)
U_1, U_2, U	Normalized scattering strength and universal scattering strength in two-component power-law spectral form
v_{eff}	Effective velocity scaling time displacement (m/s)
M, N	Size of DFT, number of samples
Δt	Time interval between samples
TEC	Total electron content (electrons/m ²)
P	Pseudorange measurements (m)
R_E	Earth radius (m)
el	Satellite elevation angle in horizon coordinate system (rad)
h_I	Height of the ionospheric layer (m)
r_p, r_s	Range from IPP to receiver, range from satellite to receiver (m)
$\delta(\cdot)$	Dirac delta function
$\Gamma(\cdot)$	Gamma function
∇	Gradient of a scalar function
$\nabla \cdot$	Divergence of a vector
$\nabla \times$	Curl of a vector
∇^2	Vector Laplacian
∇_{\perp}^2	Transverse Laplacian
Θ	Propagation operator
$\langle \cdot \rangle$	Ensemble average

1. CHAPTER 1 – BACKGROUND AND INTRODUCTION

The main focus of this PhD dissertation is ionospheric scintillation on Global Navigation Satellite System (GNSS) signals. This chapter provides an introduction to the phenomenon of ionospheric scintillation, and its impact on conventional GNSS receivers. In pursuit of the three goals in this dissertation, to effectively simulate, characterize, and detect scintillation in GNSS signals, a large amount of data collected by CSU GPS Lab has been utilized, the details of which are provided in this chapter. In addition, previous related research on scintillation simulation, characterization, and detection is presented, and the motivations and contributions of this PhD dissertation are emphasized.

1.1. Ionospheric Scintillation Phenomenon

Ionospheric scintillation refers to the random amplitude and phase fluctuations observed in radio signals propagating through electron density irregularities in the ionospheric plasma, which most commonly occurs in low-latitude, auroral, and polar regions [*Yeh and Liu, 1982; Aarons, 1982; Aarons and Basu, 1994; Jiao et al., 2013c; Jiao and Morton, 2015*]. Occurrence of scintillation is difficult to predict and model due to the variability of its numerous influencing factors, which include solar activities, inter-planetary magnetic field activities, local electric field and conductivity, convection processes, wave interactions, etc. [*Aarons, 1982; Tsunoda, 1988; Pi et al., 1997; Basu et al., 2002; Kintner et al., 2004; Smith et al., 2008; Redmon et al., 2010; Liu et al., 2013*]. Trans-ionospheric radio waves, such as the GNSS signals, are vulnerable to scintillation. Strong scintillation can severely impact the acquisition and tracking process in GNSS receivers, causing a degradation in navigation solution accuracy, integrity, and continuity [*Skone, 2001*;

Skone et al., 2001; Kintner et al., 2007; Seo et al., 2007; Xu et al., 2012; Carroll et al., 2014; Fortes et al., 2014; Morton et al., 2014; Jiao et al., 2014b, 2015; Xu and Morton, 2015].

The occurrence of ionospheric scintillation is most prominent in two contrasting regions in the world: the low-latitude region (within $\pm 20^\circ$ around the magnetic equator), and high-latitude regions including auroral and polar zones [*Aarons, 1982; Basu et al., 2002; Jiao et al., 2014a*]. Low-latitude region is known to be plagued with frequent and strong scintillation, especially deep amplitude fading after local sunset, caused by the up-rising and disintegration of the Rayleigh-Taylor instability (bubbles) in the *F*-region equatorial ionosphere [*Kelley et al., 1981; Hysell et al., 1990; Hysell and Kudeki, 2004*]. Research also shows that low-latitude scintillation is more frequent and intense around equinoxes, and subsides in the summer [*Aarons, 1982; Tsunoda, 1985; Kintner et al., 2007; Beniguel et al., 2009; Akala et al., 2015*].

In high-latitude regions, where irregularity patches are presumed to be caused by gradient drift instability and accelerated energetic electron precipitation along geomagnetic field lines, the observed ionospheric scintillation is greatly associated with solar transients and thus may become severe during disturbances in the Earth geomagnetic field [*Basu et al., 2002; Jin et al., 2014, 2015; Cherniak and Zakharenkova, 2016; van der Meer et al., 2016*]. Positive correlation between high-latitude scintillation and global geomagnetic field activities has been observed using the global geomagnetic field activity indices *K/Kp, Ap* and *Dst* [*Dagg, 1957; Das Gupta et al., 1985; Basu et al., 2002; Rodrigues et al., 2004; Reggiani et al., 2005; Hasbi et al., 2007; Li et al., 2008; Shang et al., 2008*]. Studies have also revealed scintillation's close relationship with variations in local geomagnetic field components [*Prikryl et al., 2010, 2011; Jiao et al., 2013b; Ghoddousi-*

Fard et al., 2015; Jiao and Morton, 2015]. In addition, high-latitude scintillation usually features strong phase fluctuations with small amplitude fading at the L-band frequencies used by GNSS signals [*Buchau et al., 1984; Valladares et al., 2002; Kintner et al., 2007; Skone et al., 2008; Azeem et al., 2013; Jiao, 2013; Jiao et al., 2013a; Jin et al., 2016*], which may be caused by large-scale structures that do not generally cascade into smaller-scale structures at high latitudes [*Forte et al., 2016*]. Several previous research findings showed that auroral scintillation is usually a nighttime phenomenon, while polar cap scintillation exists at all local times [*Kintner et al., 2007; Li et al., 2010; Jiao et al., 2013c*]. Previous literature also showed that high-latitude scintillation has a location-dependent seasonal pattern of occurrence with more events reported during the winter and equinoxes [*Rino et al., 1983; Kersley et al., 1988, 1995; Aquino et al., 2005; Kintner et al., 2007; De Franceschi et al., 2008; Li et al., 2010; Alfonsi et al., 2011; Prikryl et al., 2011; Jiao et al., 2013c*].

Figure 1-1 through Figure 1-3 summarize the major findings in [*Jiao and Morton, 2015*], which utilized a large amount of real Global Positioning System (GPS) data collected by CSU GPS Lab in the auroral (Gakona) and low-latitude (Jicamarca and Ascension Island) regions. These results show the dependency of scintillation occurrence on local time, seasons, solar activity, and geomagnetic activity, which are consistent with the previous research discussed in the above text.

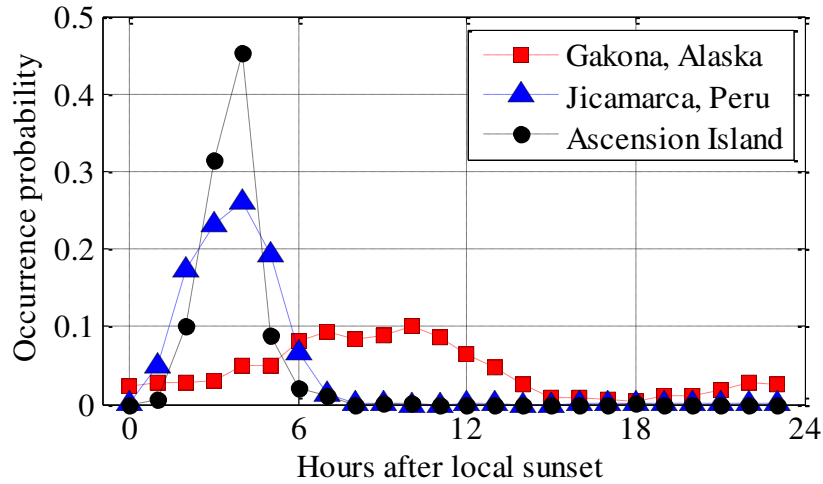


Figure 1-1. Scintillation occurrence frequency on GPS L1C/A with respect to hours after local sunset at Gakona, Jicamarca, and Ascension Island. The data from these locations were collected from August 2010 to June 2014, November 2012 to July 2014, and March 1st to 10th 2013, respectively. The data sets also apply to Figure 1-2 and Figure 1-3.

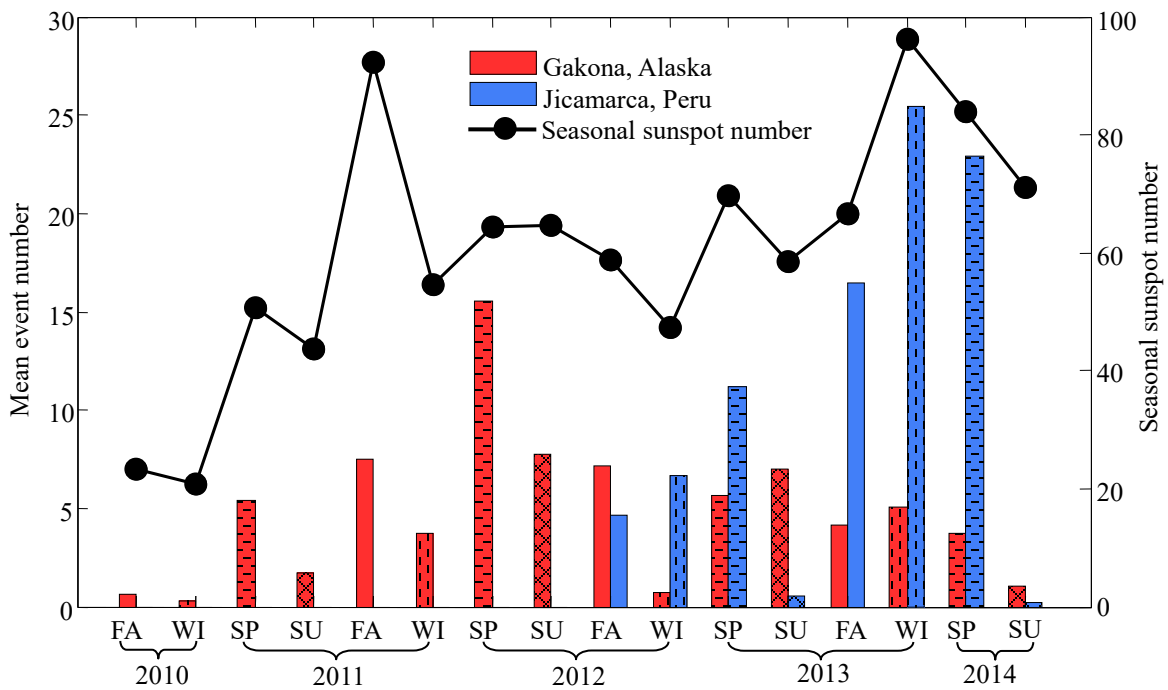


Figure 1-2. Seasonal scintillation occurrence frequency on GPS L1C/A, determined by the mean event number (the histogram), compared with the seasonal sunspot number (the black dotted line) for Gakona and Jicamarca.

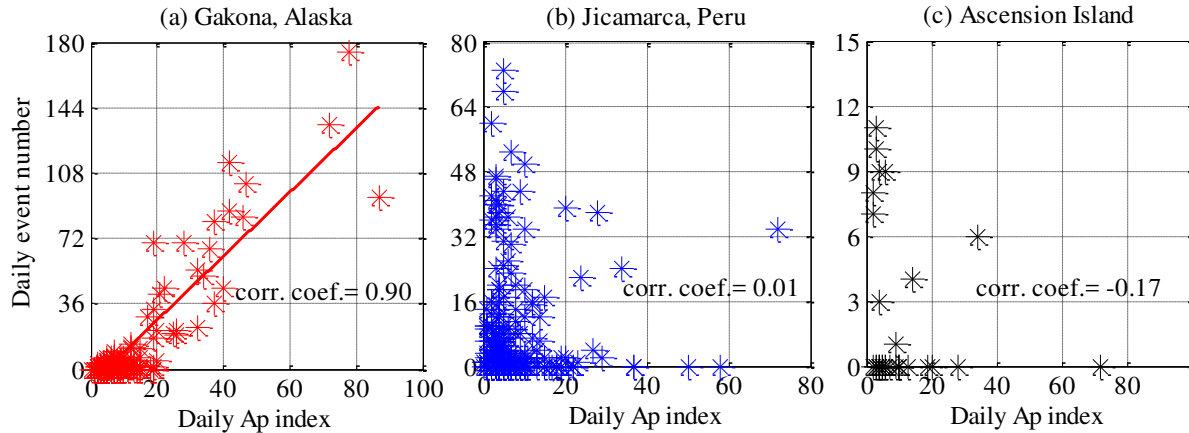


Figure 1-3. Daily scintillation event occurrence frequency on GPS L1C/A with respect to A_p index at (a) Gakona, Alaska, (b) Jicamarca, Peru, and (c) Ascension Island. A linear least-mean-square fit is imposed on subplot (a) based on the data points. A_p index is a global geomagnetic activity index, a higher value of which indicates a more intense geomagnetic activity world-wide.

Other than low-latitude and high-latitude regions, scintillation on GNSS signals is also occasionally observed in mid-latitude areas. These mid-latitude scintillation events are typically associated with poleward moving equatorial irregularities during magnetic storms near solar maxima [Ledvina et al., 2002; Kelley et al., 2002; Sojka et al., 2004; Kintner et al., 2007; Wautelet and Warnant, 2014; Vadakke Veetil et al., 2017]. Overall, mid-latitude scintillation is much less often and intense than scintillation at high latitudes and low latitudes, thus is seldom studied in the literature.

1.2. Effects of Ionospheric Scintillation on GNSS Receiver Operations

Ionospheric scintillation can affect the operation of GNSS receivers in various ways. Carrier tracking of GNSS signals is a fragile component of GNSS receiver signal processing and is more seriously impacted by scintillation than code tracking because of the much shorter wavelength of the sinusoidal carrier [Sreeja, 2016; Myer, 2017]. In addition, the narrower bandwidth of the code tracking loop improves its immunity to amplitude scintillation [Knight et al., 1997]. However, as

carrier aiding of the code tracking loop is performed in GNSS receivers, it can be assumed that loss of carrier lock is shortly followed by loss of code lock [Knight and Finn, 1998]. In our experimental data analysis, for low-latitude scintillation, cycle slips and loss of lock are frequently observed in commercial receivers [Jiao *et al.*, 2014b, 2016ab]. Some loss of lock can last more than two hours due to persistent strong scintillation in both amplitude and phase. For our high-latitude data, cycle slips and loss of lock due to severe amplitude scintillation are relatively scarce, whereas phase scintillation or a combination of phase and amplitude scintillation poses a real threat. Cycle slips and loss of lock are frequently detected even when the σ_ϕ index is only about 10 degrees (0.17 radians) [Jiao, 2013].

The legacy L2 P(Y) signal of GPS is more susceptible to loss of lock (L1 frequency: 1575.42 MHz; L2 frequency: 1227.6 MHz) [Jiao, 2013; Jiao *et al.*, 2013c]. This is because the L2 P(Y) tracking is based on the semi-codeless tracking due to the unknown protected code. Semi-codeless tracking results in higher noise levels and hence lower signal-to-noise ratio (SNR), which impacts signal tracking during scintillation. Additionally, both L2 signal amplitude and phase are affected more adversely by scintillation due to the inverse frequency scaling relationship of scintillation [Rino, 1979a, 1979b]. For this last reason, L5 signal with even lower frequency is supposed to be more severely influenced by ionospheric scintillation (L5 frequency: 1176.45 MHz). It should be noted here that the new GPS civilian L2C and L5 signals both carry a data-less channel which can be tracked using four-quadrant discriminators with twice of that of the traditional data-bearing channel's carrier phase pull-in range, as well as a 6-dB increase in processing gain [IS-GPS-200H, 2013]. This leads to a larger phase error tolerance range and more robust performance during scintillation.

When an L2 or L5 signal loses lock, dual frequency ionosphere delay correction is unavailable and the receiver will have degraded position solution accuracy. When the number of satellites that remain locked is less than four, a GNSS receiver will not be able to generate position solutions. Ionospheric scintillation also has a big influence on differential GPS (DGPS) which relies on the spatial correlation between reference and user stations. The error induced by the ionosphere at the reference is assumed to be the same as that at the user. However, in the presence of ionospheric irregularities, spatial decorrelation may occur, which consequently leads to errors in DGPS positioning [Moore *et al.*, 2002]. Satellite Based Augmentation System (SBAS) can also be affected by ionospheric scintillation in a similar way [Skone and Knudsen, 2000; Klobuchar, 2002].

1.3. Ionospheric Scintillation Indices

The widely-used indices to measure ionospheric scintillation activity are the S_4 index and σ_ϕ index, for amplitude and phase scintillation respectively. S_4 is the standard deviation of the received signal power normalized to the average signal power [Briggs and Parkin, 1963]. σ_ϕ is defined as the standard deviation of the signal phase [Yeh and Liu, 1982]:

$$S_4 = \sqrt{\frac{\langle I^2 \rangle - \langle I \rangle^2}{\langle I \rangle^2}} \quad (1-1)$$

$$\sigma_\phi = \sqrt{\langle \phi^2 \rangle - \langle \phi \rangle^2} \quad (1-2)$$

In the two equations, I is the detrended signal intensity and ϕ is the detrended carrier phase [Van Dierendonck *et al.*, 1993]. $\langle \cdot \rangle$ represents ensemble average which, under the assumption of ergodicity, is practically the expected value over the interval of interest. In our study, the interval of interest is usually set to 10 seconds in order to most effectively highlight scintillation features

based on evaluations of several different time intervals between 10 and 60 seconds [Pelgrum *et al.*, 2011]. Also a sliding window is often used, so that the rate of the indices is 1 Hz. It should be noted that although some commercial receivers output S_4 and σ_ϕ measurements (e.g. GSV4004B receivers), the values of the two indices used in this research are calculated from the high rate raw signal intensity and phase data in order to maintain consistency among different receivers (e.g. PolaRxS receivers do not output these index values). Calculation of the indices using high-rate raw data also enables the customization of parameters, such as time interval, sliding window size, and low-pass delay correction.

As a normalized indicator, S_4 typically falls into the range of 0 to 1, with larger values representing stronger scintillation. However, as focusing effects become prominent in the saturation regime, the value of S_4 can slightly exceed unity [Singleton, 1970]. Empirically, for background signals without obvious scintillation, the S_4 index is usually below 0.2; for moderate scintillation, S_4 is normally between 0.2 and 0.5; when S_4 is above 0.5, it is often considered as strong amplitude scintillation [Jiao, 2013]. The range of σ_ϕ is defined by the receiver's carrier tracking pull-in range. For scintillation that results in phase fluctuations beyond such a range, the receiver has a high probability of losing lock of the signal. At that point, the value of σ_ϕ carries no significance.

To calculate the values of these two indices, the measurements acquired from the receiver must be detrended to remove the low-frequency contributions from satellite-receiver range variations, antenna patterns, background ionosphere, troposphere delays, and receiver and satellite oscillator drifts etc. The conventional method is to apply a 6th order Butterworth filter with a 0.1 Hz cut-off

frequency [Van Dierendonck et al., 1993]. However, the effectiveness of this method has long been questioned by previous studies without a confirmed better replacement [Forte and Radicella, 2002; Beach, 2006; Mushini et al., 2011; Niu, 2012]. In this research, different detrending methods are applied to achieve balance between conventions and physical effectiveness. The specific method used will be emphasized in the result chapters (Chapters 6 through 8).

1.4. Global GNSS Data Collection Systems Established by CSU GPS Lab

Since 2008, CSU GPS Lab has been deploying GNSS data collection systems worldwide, especially in the auroral and the low-latitude regions. Figure 1-4 is a global map showing the geographic locations of the established GNSS data collection sites [Jiao and Morton, 2015; Morton et al, 2015a]. Table 1-1 summarizes the operational duration for each data collection site. As can be seen the antenna sites cover high, mid, and low latitude regions, which provide a vast variety of GNSS and scintillation signals for different research topics.

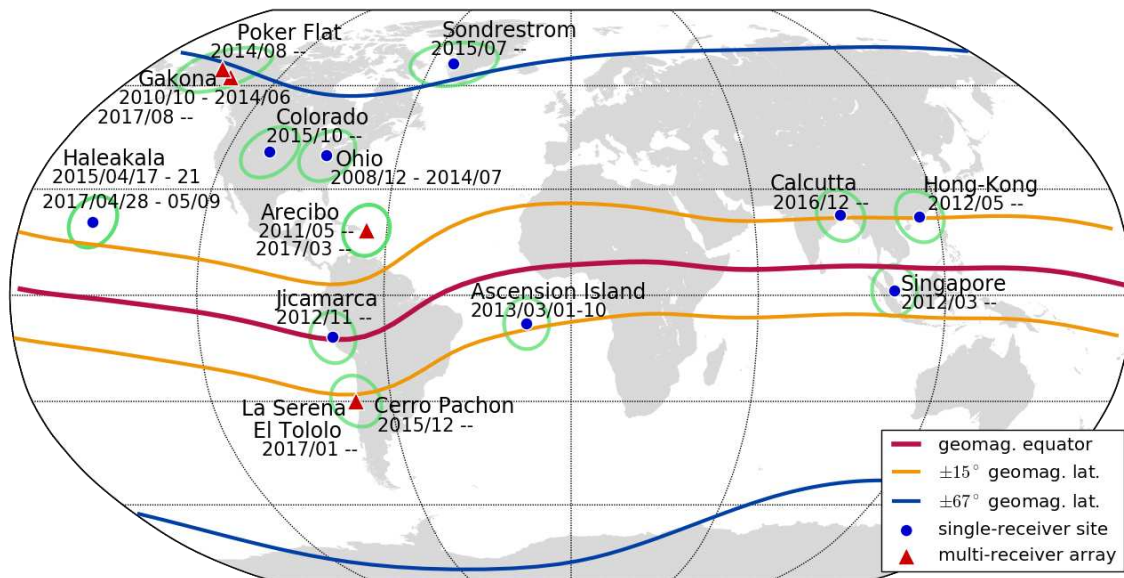


Figure 1-4. Global map showing the geographic locations of the GNSS data collection sites established by CSU GPS Lab. The bands of the magnetic low-latitude area and the auroral ovals are estimations. Credit: plot courtesy of Brian Breitsch at CSU GPS Lab.

Table 1-1. Locations and operational durations of the current GNSS data collection sites established by CSU GPS Lab. The locations are divided into high-latitude, mid-latitude, and low-latitude regions, the definitions of which are denoted in the table

	Location	Operational Duration
High latitude (within 50% auroral oval)	Sondrestrum, Greenland	07/2015 – Present
	Poker Flat, AK	08/2014 – Present
	Gakona, AK	10/2010 – 06/2014*
Mid latitude	Fort Collins, CO	10/2015 – Present
	Haleakala, HI	04/17/2015 – 04/21/2015
	Arecibo, Puerto Rico	05/2011 – Present
	Oxford, OH	12/2008 – 07/2014
Low latitude (within $\pm 20^\circ$ magnetic latitude)	La Serena, Chile	01/2017 – Present
	El Tololo, Chile	01/2017 – Present
	Calcutta, India	12/2016 – Present
	Cerro Pachon, Chile	12/2015 – Present
	Ascension Island	03/01/2013 – 03/10/2013
	Jicamarca, Peru	11/2012 – Present
	Hong Kong, China	05/2012 – Present
Singapore	03/2012 – Present	

*: A single GSV4004B receiver is left in operation near the original site after June 2014.

The data used in the author’s dissertation research is mainly from six antenna sites: Gakona, Alaska (geographic: 62.4°N, 145.2°W; geomagnetic: 63.5°N, 92.2°W); Poker Flat, Alaska (geographic: 65.1°N, 147.5°W; geomagnetic: 65.4°N, 96.8°W); Ascension Island (geographic: 7.9°S, 14.4°W; geomagnetic: 12.3°S, 55.8°N); Jicamarca, Peru (geographic: 11.9°S, 76.9°W; geomagnetic: 0.8°N, 5.6°W); Hong Kong, China (geographic: 22.3°N, 114.2°E; geomagnetic: 15.3°N, 179.3°W); Singapore (geographic: 1.3°N, 103.8°E; geomagnetic: 7.6°S, 175.2°E). The following is a detailed description of the arrangement of each of these six antenna sites.

The Gakona data collection system was established in 2009 near the facility of the High Frequency Active Auroral Research Program (HAARP) and developed into an array of four antennas in the following years. Each antenna was connected to a commercial ionospheric scintillation monitoring

(ISM) receiver (NovAtel GSV4004B receiver or Septentrio PolaRxS receiver) to monitor ionospheric scintillation activities, and to initiate and terminate the intermediate-frequency (IF) data collection process (Figure 1-5) [Jiao and Morton, 2015]. The ISM receivers continuously collect measurement data including I and Q channel correlator outputs and carrier phase, from which scintillation indices and scintillation event indicators are computed. The indicators are continuously compared with preset threshold values to trigger the data server to record raw IF samples generated by the software-defined radio-frequency (RF) front-ends [Taylor et al., 2013]. These event-driven front-end recorded IF data are used for advanced scintillation receiver algorithm development in software-defined receivers (SDR), and for postprocessing and analysis of strong scintillation signals. A detailed description of the configuration of the data collection system at Gakona, AK can be found in [Jiao et al., 2013c].

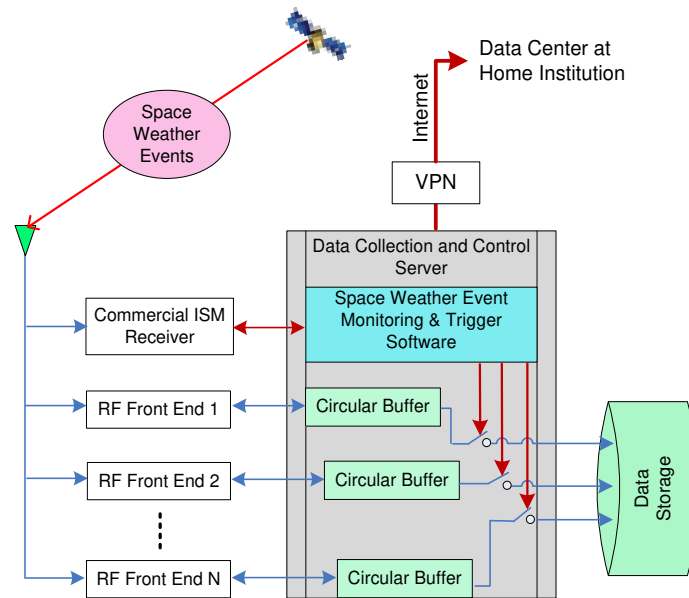


Figure 1-5. General architecture of the event-driven GNSS data collection systems deployed at several high-latitude and low-latitude sites. The GSV4004B and the PolaRxS receivers are the commercial ISM receivers which are used to collect full-time navigation data and trigger the data collection of the RF front ends [Jiao and Morton, 2015].

In the summer of 2014, a multi-constellation GNSS receiver array system was established at Poker Flat, Alaska. This new data collection system consists of three antennas, each of which also connects to an ISM receiver. These ISM receivers operate continuously and generate high quality 100 Hz GPS/GLONASS/Galileo/BeiDou carrier phase measurements during scintillations. In addition, the signal from one of the antennas is also split to input to a bank of software-defined multi-GNSS RF front-ends. The front-ends collect wideband IF samples which are post-processed using custom-designed SDR algorithms [*Wang and Morton, 2017*].

On Ascension Island, a portable event-driven GNSS data collection system was deployed during a campaign in March 2013. The system architecture was the same as illustrated in Figure 1-5, which configured a Septentrio PolaRxS receiver as an ISM receiver and several software RF front-ends to collect data on GPS L1, L2C, L5, GLONASS L1 and L2, BeiDou B1, and Galileo E1 [*Jiao and Morton, 2015; Jiao et al., 2016a*].

The scintillation events collected on Ascension Island are especially strong [*Jiao and Morton, 2015*]. In order to preserve the true behavior of the ionosphere and its impact on signal processing, the post-processed data from the IF samples using SDR algorithms are mainly used in this dissertation. A new tracking algorithm, called the Fixed Position Feedback (FPF) tracking algorithm, has been implemented to post-process the IF data from Ascension Island to ensure that the receiver maintained lock of signals and to minimize signal parameter estimation errors [*Xu and Morton, 2015; Xu et al., 2015*]. The FPF is based on the fact that for scintillation monitoring applications, the receiver position is fixed and can be surveyed beforehand. The receiver position information, and satellite position and velocity computed using real time ephemeris can be used to

accurately estimate scintillation signal code phase and carrier Doppler during deep fading, while signals from satellites with nominal signal intensity are used to estimate time. FPF is effectively a semi-open loop (SOL) architecture for the brief period when deep fading occurs. This algorithm incorporates a moving window correlator that spans a relatively long integration period with small time-steps to harness more signal power while preserving the fine temporal structures of the measurements during deep fading. In this research, to maintain consistency of the measurements with those from the ISM receiver, the integration time of the signal tracking is fixed to 10 ms, which leads to a 100 Hz sampling rate of the I/Q correlator outputs, and a 50 Hz sampling rate of the signal intensity measurements.

In Jicamarca Peru, a similar event-driven multi-GNSS data collection system has been collecting data since November 2012. In Singapore and Hong Kong, Septentrio PolaRxS receivers were put into operation in March and May 2012 respectively. Each receiver was configured to generate scintillation measurements on GPS L1, L2C, L5, GLONASS L1 and L2 bands. Additional capabilities to capture raw IF samples at these sites are currently underway [*Jiao and Morton, 2015; Morton et al., 2015b*].

1.5. Literature Research

1.5.1. Previous Research on Scintillation Signal Simulation

There have been two types of approaches in developing GPS scintillation simulators. The first type is based on the physics of signal wave propagation through the ionospheric irregularities. Reviews of the scintillation theories are provided in [*Yeh and Liu, 1982; Bhattacharyya et al., 1982*], including phase screen approximation, Rytov solution for weak scintillation, and parabolic

equations in the multiple scattering regime. The most commonly used theory for scintillation signal simulation is the phase screen theory, which has been developed since 1950s [*Booker et al.*, 1950; *Hewish*, 1951; *Tatarskii*, 1967]. In the following two decades, a statistical scintillation theory was developed based on the phase screen theory that the phase and signal intensity spectral density function (SDF) can be analytically represented by an inverse power law form under weak scatter conditions [*Rufenach*, 1974; *Rino*, 1979a]. The one-component power-law spectral model has since been widely used for describing weak scintillation signal spectra, in which the spectral index and the turbulent strength determine the shape of the spectra [*Shkarofsky*, 1968]. As scintillation becomes more intense, the strong scattering and focusing effects add complexity to theoretical treatment, as was evident by its inadequacy in interpreting observed measurements from in situ rockets and satellite beacons [*Rino*, 1979b]. A two-component power-law spectrum model has been developed to capture the effects of strong scintillations [*Shishov*, 1974; *Rino and Carrano*, 2013]. A recent paper [*Carrano and Rino*, 2016] provides a thorough asymptotic and numerical analysis of the two-component power-law model, which are partially verified by real scintillation data in the strong scatter regime [*Rino et al.*, 2014, 2016].

Based on the phase screen theory, scintillation simulation models have been developed based on wave propagation equations and power-law spectrum models. *Priyadarshi* [2015] provided a summary of analytical and climatological scintillation models developed in the past. Most of the models listed in this article only estimate the statistics of scintillation, such as S_4 and σ_ϕ indices, for a given geographic location. Driven by the need to have scintillation signal model to test GPS receiver performance, *Psiaki et al.* [2007] developed a simple physics-based simulation model which generates phase fluctuations with a given total electron content (TEC) profile, and

propagates the phase perturbation to the receiver using Huygens-Fresnel formulation [Veselov, 1995]. The biggest problem with this model is the assumption of normal propagation with respect to the phase screen, which is unrealistic and underestimates the effects of scintillation. A later work in [Deshpande et al., 2014, 2016; Chartier et al., 2016] introduced a three-dimensional GPS scintillation signal simulation model at high latitudes, analyzed its sensitivity to model parameters, and utilized it to deduce high-latitude irregularity physical parameters. Another work by Ghafouri and Skone [2015] described an equatorial GPS scintillation signal simulator based on the one-component power-law phase screen theory, and investigated the receiver performance using real and synthetic scintillation signals. The most current development of phase-screen based scintillation simulation model was provided in [Rino et al., 2017; Jiao et al., 2017d], which introduced a data surrogate method for low-latitude scintillation simulation. This model is described by a compact set of parameters and can directly simulate scintillation signals in the time domain on both stationary and dynamic receiver platforms.

The second type of scintillation simulator is solely based on the statistics of the scintillation signals. The representative work can be found in the work of Humphreys et al. [2009, 2010a, 2010b], in which the scintillation simulator models the probability distribution function (PDF) of the scintillation signal amplitude as well as its decorrelation time τ_0 . There are only two inputs of the simulator, S_4 index and τ_0 , which makes the simulator easy to use. The downside of this model is that it does not provide any information regarding the irregularity that generates scintillation effects, so that it is not able to generate correlated scintillation signals on different GNSS frequencies. Also, the pre-set characteristics (e.g. Rician distribution) of the scintillation signal amplitude may not reflect the characteristics of the real scintillation signals which may vary with

scintillation strength and may be distorted by the receiver processing. This effect of receiver processing on scintillation signal characteristics motivates the author to develop a physics-based scintillation model to characterize scintillation signals before and after signal processing.

1.5.2. Previous Research on Scintillation Signal Characterization

While the phase screen theory provides the foundation of scintillation physics, the availability of ground-measured and in-situ scintillation data has led to data-driven methods that are focused on the statistical characterization of the scintillation signal amplitude and phase. In the early development of scintillation signal statistics, a few models gained popularity in the field. One of the models postulates that logarithmic amplitude and the phase are jointly Gaussian assuming the phase undergoes a random walk process in a phase-changing screen [*Strohbehn and Wang, 1972; Wang and Strohbehn, 1974*]. The second model supports Rician statistics and Rayleigh statistics, assuming the in-phase and quadrature components are jointly Gaussian [*Chytil, 1967; Fremouw et al., 1980*]. Another empirical model for amplitude PDF is the Nakagami- m distribution that is related to the scintillation index S_4 [*Nakagami, 1960*]. The Nakagami- m distributions have been found to represent a good fit for the variability of the amplitude of scintillating signals [*Whitney et al., 1972; Fremouw et al., 1980; Rino, 1980*]. A recent model on scintillation amplitude is called α - μ distribution, which is proposed by *Yacoub* [2002, 2007]. This model is a generalization of Rayleigh, Weibull, and Nakagami- m distributions, depending on the values of the parameters α and μ which are also related to S_4 index. The α - μ PDF is found to outperform the Nakagami- m and Rician PDFs in the statistical characterization of amplitude scintillation in some recent works [*Moraes et al., 2013, 2014; Oliveira et al., 2014*].

In addition to the PDFs of the scintillation signals, some researchers have studied the fading characteristics on carrier-to-noise ratio (C/N_0) measurements and their effects on receiver performance for aviation applications [Seo *et al.*, 2009, 2011; Akala *et al.*, 2012]. However, as pointed out in [Jiao *et al.*, 2014b], C/N_0 under-estimates the scintillation signal fading level and drastically over-estimates fading duration, mainly due to the averaging operation over an extended time period in its calculation. To overcome these drawbacks, Jiao *et al.* [2016a] characterized the fading statistics on signal intensity measurements across the three GPS frequencies, and further showed that inter-frequency aiding during scintillation is possible to maintain lock of deep fading signals [Yin *et al.*, 2015].

1.5.3. Previous Research on Scintillation Signal Detection

There has been little descriptive literature on scintillation detection techniques. In most past techniques, the lower moments of the scintillation amplitude and phase statistics, e.g. the mean and the variation of the signal amplitude and phase as well as the S_4 and σ_ϕ indices, are used. In earlier approaches by CSU GPS Lab, a hard threshold-based scintillation event trigger system is implemented based on evaluation of the scintillation index values: if the S_4 or σ_ϕ index computed from a continuously operating commercial GNSS receiver passes a preset threshold value, then scintillation event monitoring software will trigger a data collection system to store raw IF samples from an array of RF front ends [Vikram, 2011; Taylor *et al.*, 2012; Jiao and Morton, 2015]. This event trigger method is simple to implement, but it overlooks the higher-moment features of the signals, so that scintillation can be confused with multipath and interference. Another issue with the S_4 and σ_ϕ indices is that to calculate the two indices, the received signal power or raw carrier phase measurements need to be detrended as described in Section 1.3.

Approaches to detrending the measurements including using a 6th order Butterworth filter and wavelet transformations, as well as the specific filter parameter selections, have been topics of debate in the past decade, as the selection of detrending method actually affects the values of an S_4 or σ_ϕ index [Forte and Radicella, 2002; Mushini et al., 2011; Niu, 2012].

Several other scintillation detection methods were proposed mostly based on the Neyman-Pearson (NP) detection theory. The work of Fu et al. [1999] defined several scintillation observables which are similar to the S_4 index and decomposed them using a wavelet technique by assuming that the wavelet coefficients are Gaussian for both non-scintillation and scintillation hypotheses with different means, but the same variance. The work of Miriyala et al. [2015] applied complementary ensemble empirical mode decomposition in combination with multifractal detrended fluctuation analysis on C/N_0 measurements to detect and mitigate noise components due to ionospheric scintillations in GNSS signals. However, it is well known that C/N_0 is not an accurate estimator especially when the signal is experiencing deep fading, as is the case during ionospheric scintillation [Jiao et al., 2016a]. Moreover, how the detection decision was made is not explained clearly in the literature. A more detailed discussion on a NP scintillation detector was provided in the work of Ratnam et al. [2015]. In this proposed method, the S_4 index is decomposed using a wavelet technique and Hilbert-Huang transform. The components are also assumed to be Gaussian-distributed under non-scintillation and scintillation hypotheses with different means and identical variance. The decisions made on individual components are combined to make a final decision. However, none of these papers have provided a quantitative analysis on the detection performance such as the commonly used receiver operating characteristic (ROC) curve and confusion matrix (see Section 5.1 for definitions).

1.6. Motivations and Contributions of Dissertation Research

This PhD dissertation includes three major topics: scintillation signal simulation, scintillation signal characterization, and scintillation signal detection. The enabler of this PhD research is a large volume of real GPS scintillation data collected at different locations around the world. To extract scintillation data from an enormous quantity of raw measurements, the development of an effective and efficient scintillation detection technique is necessary. The extracted real scintillation data facilitate the study of ionospheric scintillation phenomenon in various ways. By characterizing the general statistics of scintillation signals, we can have a better understanding of the mechanisms of the scintillation phenomenon, deduce space weather parameters, and build robust GPS receiver techniques to reduce the effects of scintillation. In order to fully test the performance of the GPS signal processing algorithms during scintillation, simulated signals are needed other than real data to mimic all different scenarios, especially for circumstances where scintillation signals are difficult to collect, such as on a dynamic platform. By comparing the simulated signal with the receiver-processed signal, the receivers' effects on scintillation signal characteristics can also be revealed, which otherwise is impossible to investigate with real data.

The relationships of the three major topics are depicted in Figure 1-6. The three topics are closely related and one assists the development of the others. Regarding the three major topics, several contributions have been made in this dissertation:

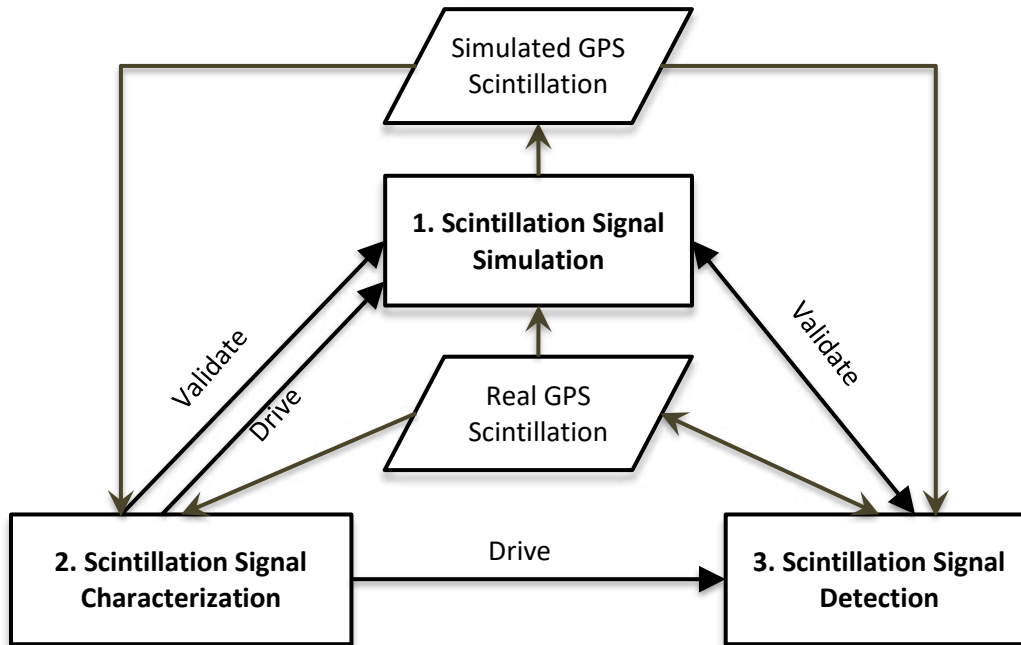


Figure 1-6. Relationships of the three major topics in this dissertation, involving two types of data: the real GPS scintillation data and the simulated GPS scintillation data.

- a) Two data-driven multi-frequency GPS scintillation signal simulators have been developed based on the two-dimensional two-component power-law phase screen theories. The first simulator is mainly for stationary scintillation signal simulation, which is based on the traditional wave propagation method. The second simulator is based on the time-domain data surrogate method which can be used for scintillation signal simulation for dynamic receiver platforms. The simulators can effectively generate simulation scintillation signals with similar characteristics to real scintillation signals. Also, the simulators are able to simulate scintillation modulated GPS IF samples on L1, L2, and L5 frequencies, which can be processed using conventional GPS receiver algorithms.
- b) A large amount of real scintillation data collected at the low-latitude GNSS receiver stations has been characterized in both the spatial frequency and time domains. The statistics have been used to develop models for scintillation signal simulation and detection.

- c) A large amount of simulation scintillation data and receiver-processed simulation data has been characterized and compared with the characteristics of real data. The similarities in the characteristics demonstrated the effectiveness of the simulators, and the differences revealed the effects of receiver processing on signal characteristics.
- d) A new automatic scintillation detection technique has been developed using a machine learning algorithm. The new detection method can effectively and efficiently detect amplitude and phase scintillation in the high-latitude and equatorial regions.
- e) The simulated scintillation signals have been applied to the new scintillation detector, which verified the effectiveness of both the simulator and the detector.

1.7. Dissertation Outline

This dissertation starts with an overview of background in Chapters 1 and 2, which introduce ionospheric scintillation phenomenon, the GNSS data collection systems, GPS civil signals and previous literature related to this dissertation. Chapters 3 and 4 elaborate on the wave propagation geometry and theories that are implemented in scintillation signal simulation. Chapter 5 explains the methodology for scintillation signal detection developed in this research. Chapter 6 presents results for scintillation signal characterization using real data. Chapter 7 presents results for scintillation signal simulation for stationary and dynamic platforms, and compares signal characteristics between simulated data and real data. Chapter 8 summarizes results for scintillation signal detection on amplitude and phase scintillation for both real and simulated data. Finally, Chapter 9 concludes the dissertation and provides guidelines for future work.

2. CHAPTER 2 – GPS CIVIL SIGNAL STRUCTURES

The knowledge of the signal structure of GPS signals is fundamental to the work covered in this dissertation, especially for the task of scintillation signal simulation. Generating simulated GPS scintillation signals requires the modulation of GPS signal samples using simulated scintillation amplitude and phase realizations, in order for regular GPS SDRs to be able to acquire and track the simulated signals. This chapter summarizes the major structures of the three GPS civil signals that are currently available: L1 C/A, L2C, and L5. Most details can be found in the interface control documents (ICDs) published at <http://www.gps.gov>.

There are mainly three components in transmitted GPS signals: pseudo-range noise (PRN) code sequence, which is unique to each satellite; navigation message, which carries information about ephemeris, clocks, satellite status etc.; and RF carrier wave, whose center frequencies for L1, L2, and L5 are 1575.42 MHz, 1227.60 MHz, and 1176.45 MHz respectively. While synchronized, the modulo-2 sum of the PRN code sequence and the navigation data bit modulates the RF carrier wave using the bi-phase shift keying (BPSK) method. For different civil signals on different bands, nevertheless, the frequencies and generation methods of the three components are different. The following sections will elaborate on how the signals are constructed for the three GPS civil signals.

2.1. GPS L1 C/A Signal

The legacy GPS signals on L1 frequency contain two ranging codes: the coarse/acquisition (CA) code, which is freely available to the public; and the restricted precision (P(Y)) code, which was designed for military use. In the time domain, each GPS satellite broadcasts the following signals

on L1 [Misra and Enge, 2011] with an illustration shown in Figure 2-1:

$$s_{L1}(t) = A_{C1}D(t)C_{C1}(t) \cos(2\pi f_{L1}t + \theta_{L1}) + A_{P1}D(t)C_{P1}(t) \sin(2\pi f_{L1}t + \theta_{L1}) \quad (2-1)$$

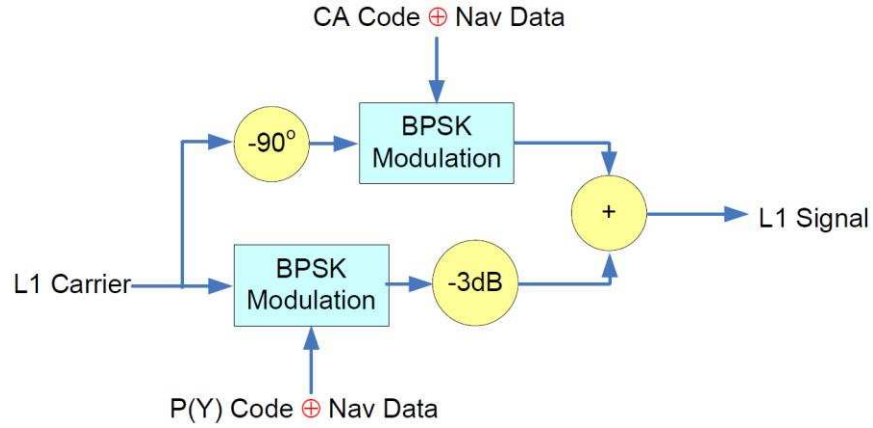


Figure 2-1. Current GPS signal generation on L1 band [Morton, 2014-16].

The first line in (2-1) is for the L1 C/A signal, while the second line is for the P(Y) code. A_{C1} and A_{P1} are the signal amplitudes, $D(t)$ is the navigation data, $C_{C1}(t)$ and $C_{P1}(t)$ are the ranging codes, and sinusoidal waves in the end are carrier waves with f_{L1} being the center frequency and θ_{L1} being the initial phase. The L1 C/A signal is of main interest in this dissertation, whose structure is illustrated in Figure 2-2. This section mainly focuses on the generation of the L1 C/A code, and the structure of the navigation data bit.

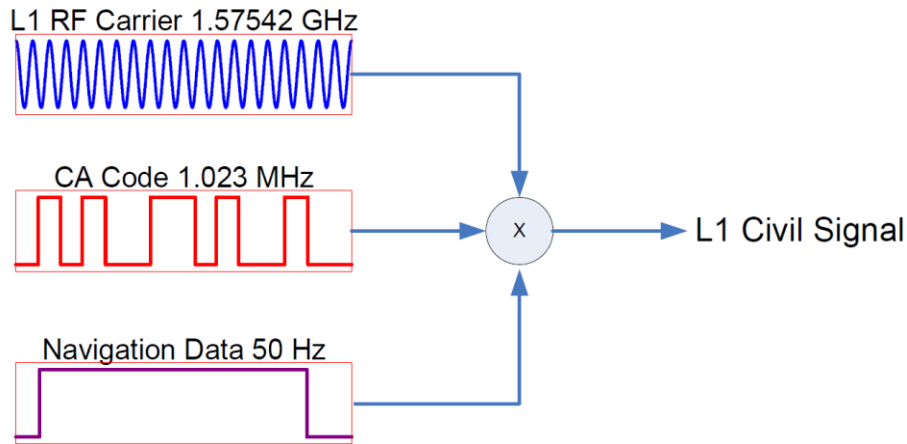


Figure 2-2. Structure of the GPS L1 C/A signal [Morton, 2014-16].

The code generation of all GPS signals is based on the code division multiple access (CDMA) technique. For a specific signal (e.g. L1 C/A and L1 P(Y)), each satellite is assigned a unique spread spectrum code, so that the cross-correlation between different codes are nearly zero. For GPS L1 C/A signal, each C/A code is a 1023-bit Gold-code which is itself the modulo-2 sum of two 1023-bit linear patterns, G1 and G2, as shown in Figure 2-3. The G1 and G2 sequences are generated by two 10-state registers, which have the following polynomials [IS-GPS-200H Section 3.3.2.3, 2013]:

$$\begin{aligned}
 G1 &= x^{10} + x^3 + 1 \\
 G2 &= x^{10} + x^9 + x^8 + x^6 + x^3 + x^2 + 1
 \end{aligned}
 \tag{2-2}$$

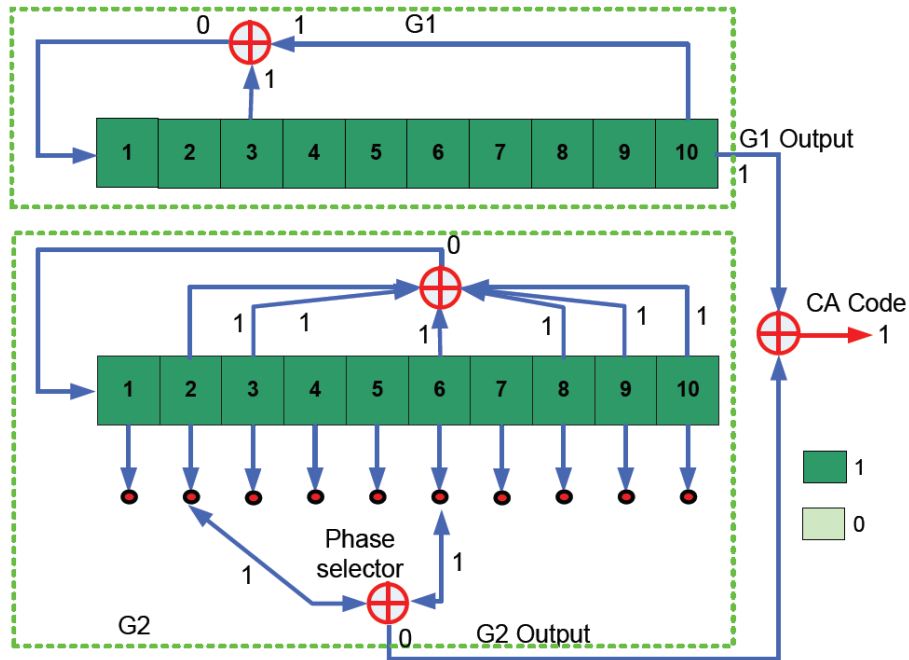


Figure 2-3. L1 C/A code generation [Morton, 2014-16].

Both G1 and G2 registers are clocked at 1.023 MHz, so that one period of a C/A code is 1 ms. With initial states for both registers being 1111111111, the phase selector in G2 selects different taps for different satellites (PRNs). Details on the code phase selection in G2 for each PRN satellite can be found in Table 3-1a in [IS-GPS-200H, 2013].

The navigation data, also known as the legacy navigation (LNAV) data, on GPS L1 and L2 P(Y) is transmitted at the rate of 50 Hz. An entire message takes 12.5 minutes to transmit, which contains 25 frames of 30 seconds each. Each frame is divided into 5 subframes. The first three subframes are repeated in each frame, with subframe 1 providing information about satellite clock status and satellite health condition, and subframes 2 and 3 providing information about satellite ephemeris. Subframes 4 and 5 contain 25 different pages each, which provide information about ionospheric model parameters, Coordinated Universal Time (UTC) information, almanac, anti-spoofing indications etc. In addition, each subframe starts with the telemetry (TLM) and the handover word

(HOW), which provide synchronization and time information, respectively. An illustration of the structure of the LNAV data is shown in Figure 2-4 [Borre et al., 2007]. Again, detailed information can be found in [IS-GPS-200H Appendix II, 2013].

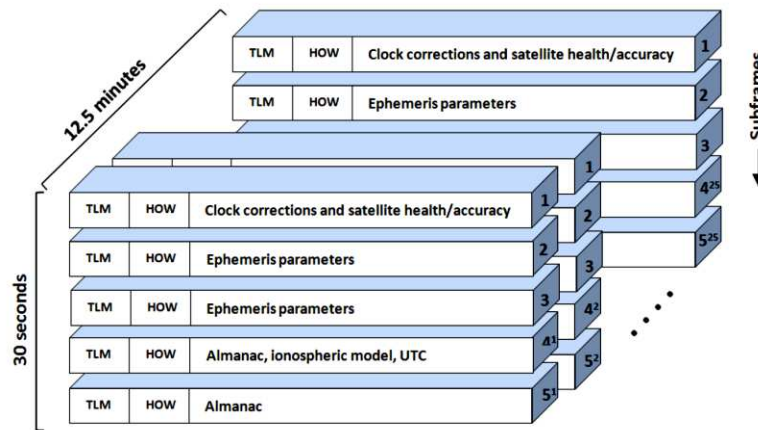


Figure 2-4. Structure of the LNAV data on L1 [Borre et al., 2007].

It is noteworthy that another civil signal on L1, called L1C, is also planned on L1 band, which will be launched with GPS III satellites. This new civil signal features Multiplexed Binary Offset Carrier (MBOC) modulation scheme to enable interoperability between GPS and international satellite navigation systems (e.g. Galileo) [IS-GPS-800D, 2013]. The navigation data on L1C will also adopt a new format called CNAV-2. This dissertation will not cover this new civil signal, as it is unavailable as of the date of the writing.

2.2. GPS L2C Signal

The L2C signal is the second GPS civil signal, that was designed specifically to meet commercial needs. In 2005, with the launch of the first GPS IIR(M) satellite, the L2C signal started to be available for civilian use. With a dual-frequency receiver, this new civil signal enhances system reliability, and boosts navigation accuracy by enabling ionospheric correction. Currently, the time

domain representation of the GPS signal on L2 band is as follows:

$$s_{L2}(t) = A_{C2}D_{C2}(t)C_{C2}(t) \cos(2\pi f_{L2}t + \theta_{L2}) + A_{P2}D(t)C_{P2}(t) \sin(2\pi f_{L2}t + \theta_{L2}) \quad (2-3)$$

where the first line is the L2C signal, while the second line is the legacy L2P(Y) code that is for military use.

An illustration of the generation of signals on L2 is shown in Figure 2-5. The L2C code consists of two codes, the CM code (for medium-length code) and the CL code (for long code) with the same code rate at 511.5 KHz. The CM code has a length of 10,230 chips with a period of 20 ms, while the CL code has a much longer length of 767,250 chips with a period of 1.5 s. As shown in Figure 2-5, the CM code is modulated by the navigation data, and is then time multiplexed with the CL code, which are combined to BPSK-modulate the carrier wave. Due to the time multiplex scheme, the actual code chipping rate for L2C signal is 1.023 MHz. It should be noted that the L2 CL code is not modulated by navigation data, which is very helpful for receiver operation (e.g. acquisition and tracking), especially in low SNR environments [Misra and Enge, 2011].

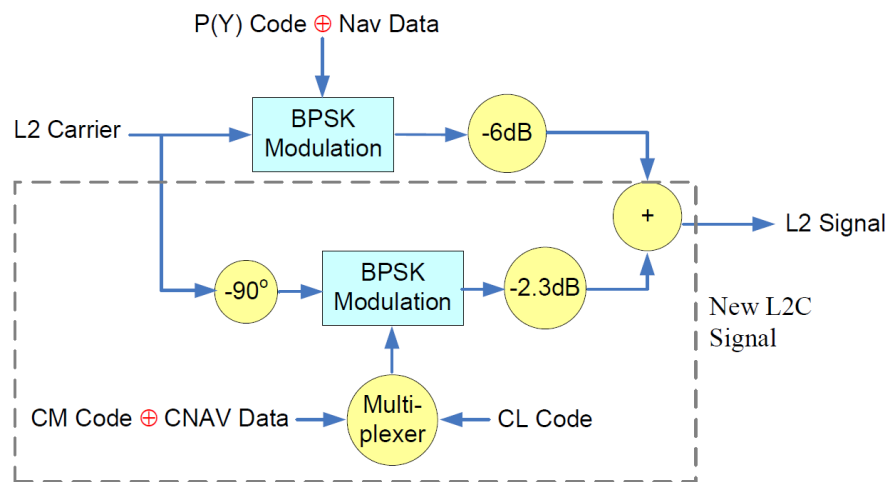


Figure 2-5. Current GPS signal generation on L2 band. The dotted line encircles the generation scheme of the L2C signal [Morton, 2014-16].

The CM and CL codes are generated using the same code generator polynomial (Figure 2-6):

$$C2 = x^{27} + x^{24} + x^{21} + x^{19} + x^{16} + x^{13} + x^{11} + x^9 + x^6 + x^5 + x^4 + x^3 + 1 \quad (2-4)$$

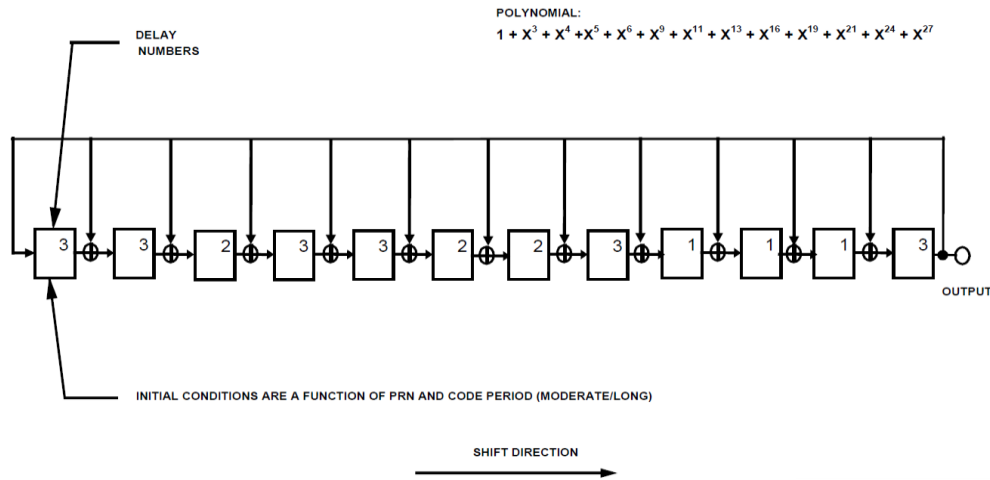


Figure 2-6. Generation scheme of L2 CM and CL codes [IS-GPS-200H, 2013].

For different satellites, the initial states for CM and CL generators are different (see [IS-GPS-200H, 2013] for details). After 10,230 and 767,250 chips respectively, the two code generators are reset to their initial values.

As noted in equation (2-3), the navigation data on the L2C signal is different from that on L1 and L2 P(Y). A new navigation data format is deployed on L2C and L5 signals, which is called civil navigation (CNAV) data to be distinguished from the LNAV data. In April 2014, the CNAV messages started to be broadcasted on L2C and L5, although only considered preoperational and restricted to test. Prior to that, the L2C and L5 provided a default message (Message Type 0) containing no data.

The CNAV data still contains the same type of information including time, status, ephemeris, and almanac etc. However, it replaces the use of frames and subframes with a pseudo-packetized format made of 12-second 300-bit messages analogous to LNAV frames. Compared to

LNAV, this message format allows a flexible order with variable repeat cycles for individual broadcast messages. In addition, forward error correction (FEC) and advanced error detection techniques, such as a cyclic redundancy check (CRC), are used to achieve better error rates and reduced data collection times. An illustration of the structure of CNAV messages is shown in Figure 2-7, with details elaborated in [IS-GPS-200H, Appendix III, 2013]. For a detailed comparison and performance analysis of LNAV and CNAV, the readers are referred to the work in [Yin *et al.*, 2015].

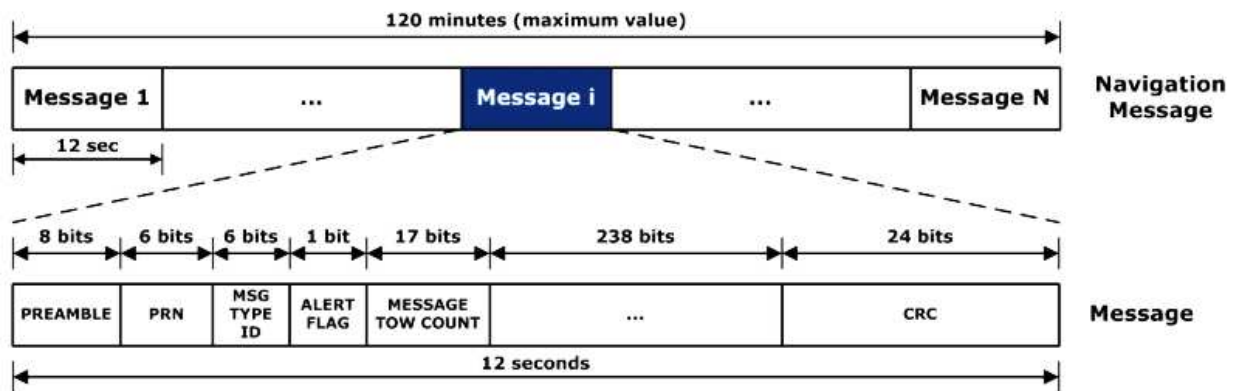


Figure 2-7. Structure of L2-CNAV messages [IS-GPS-200H, 2013].

2.3. GPS L5 Signal

The third civilian GPS signal is the L5 signal, that is assigned in a radio band reserved exclusively for aviation safety services. This new civil signal was originally designed to meet demanding requirements for safety-of-life transportation and other high-performance applications [Spilker and Van Dierendonck, 2001]. With GPS receivers that work with the civil signals on all three bands (L1 C/A, L2C, and L5), the users can enjoy highly robust service with sub-meter accuracy. The L5 signal has been officially broadcasted since May 2010 with the launch of the GPS IIF satellites.

The time domain representation of the signals on L5 is

$$s_{L5}(t) = A_{I5}D_{I5}(t)C_{I5}(t)h_{I5}(t) \cos(2\pi f_{L5}t + \theta_{L5}) + A_{Q5}C_{Q5}(t)h_{Q5}(t) \sin(2\pi f_{L5}t + \theta_{L5}) \quad (2-5)$$

where the first line is called in-phase (I5) channel, the second line is called quadrature-phase (Q5) channel, and both channels are for civilian use. An illustration of the signal structure on L5 is provided in Figure 2-8.

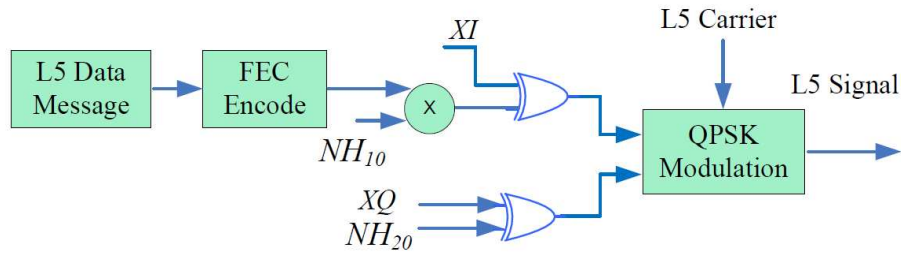


Figure 2-8. Current GPS signal generation on L5 band [Morton, 2014-16].

The spreading codes $C_{I5}(t)h_{I5}(t)$ and $C_{Q5}(t)h_{Q5}(t)$ on I and Q channels are both transmitted at 10.23 MHz. From the representation, it can be seen that the two spreading codes each consist of two parts. The first components $C_{I5}(t)$ and $C_{Q5}(t)$, called I5 code and Q5 code respectively, are both 10,230 chips in length (1 ms repetition period). For a specific satellite i , both the I5 and Q5 code patterns are generated by the modulo-2 summation of two PRN codes, $XA(t)$ and $XBI(nI_i, t)$ or $XBQi(nQi, t)$, where nI_i and nQi are initial states of XBI_i and $XBQi$. An illustration of the generation of I5 and Q5 codes is shown in Figure 2-9 [IS-GPS-705D, 2013].

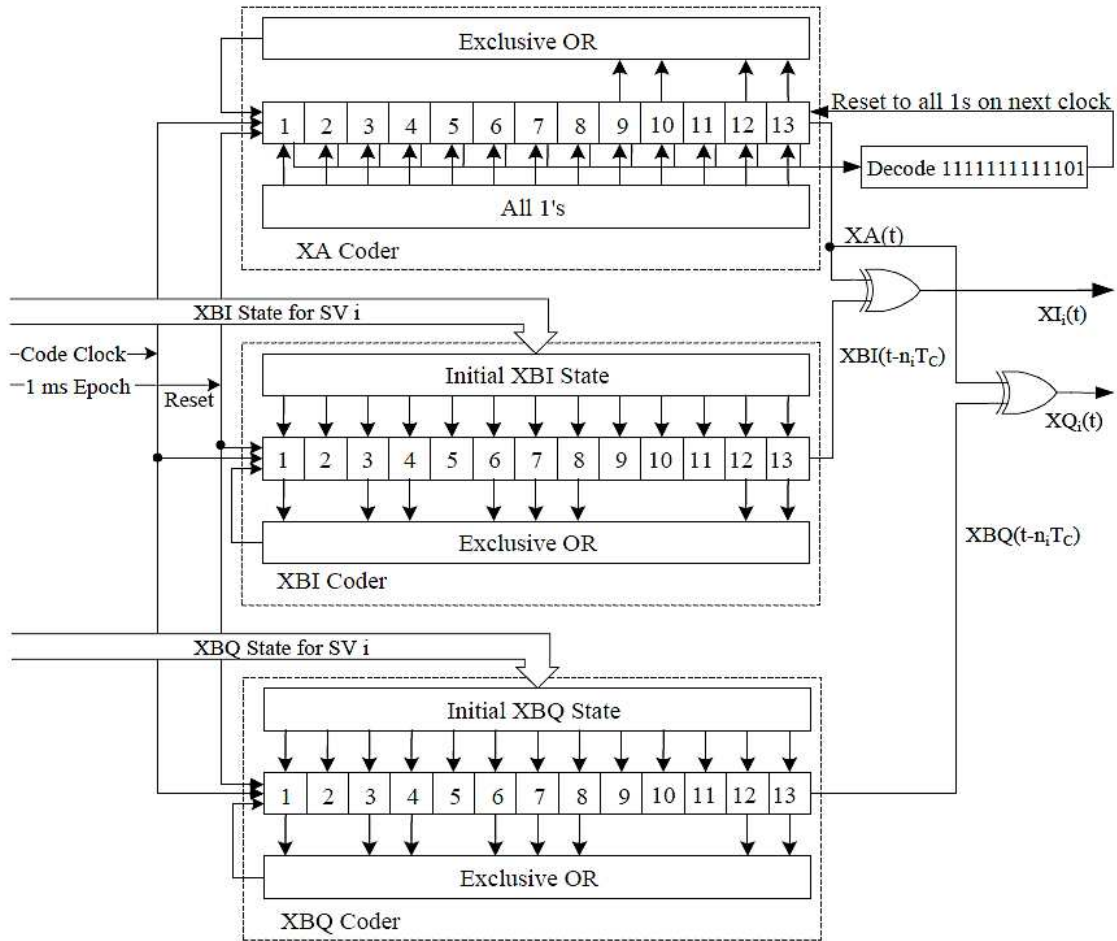


Figure 2-9. Generation of I5 and Q5 codes on L5 signal [IS-GPS-705D, 2013].

The XA code has a length of 8190 chips, with an initial state of all 1's. It is short cycled 1 chip before its natural conclusion and restarted to run over a period of 1 ms. For different satellites, the initial states of XBI and XBQ coders are different (details in [IS-GPS-705D, 2013]). Both XBI and XBQ codes are 8191 chips in length, that are not short cycled and restarted at their natural completion, and run over a period of 1 ms. The polynomials of the coders in Figure 2-9 are as follows:

$$\begin{aligned}
 XA &= x^{13} + x^{12} + x^{10} + x^9 + 1 \\
 XBI \text{ or } XBQ &= x^{13} + x^{12} + x^8 + x^7 + x^6 + x^4 + x^3 + x^1 + 1
 \end{aligned}
 \tag{2-6}$$

The second components of the spreading codes are Neuman-Hofman (NH) codes, which are mainly chosen for their auto-correlation properties [Spilker and Van Dierendonck, 2002]. For the I channel, the NH code is ten chips long (NH10) with the duration of each chip being 1 ms. For the Q channel, the NH code has a length of 20 chips (NH20) which also clocks at a rate of 1 KHz. The two NH sequences are given as follows, with the first chip shown on the leftmost:

$$\begin{aligned}
 NH10 &= [0,0,0,0,1,1,0,1,0,1] \\
 NH20 &= [0,0,0,0,0,1,0,0,1,1,0,1,0,1,0,1,0,0,1,1,1,0]
 \end{aligned}
 \tag{2-7}$$

The Q channel of L5 signal is free of navigation data, which usually serves as a pilot channel for receiver signal acquisition and tracking. The I channel, on the other hand, is modulated by navigation data, which is very similar to the CNAV data on L2C signal. Compared to the CNAV on L2C, the CNAV data on L5 has exactly the same structure, yet two times the data rate. Also, the content may vary slightly. Figure 2-10 illustrates the structure of the CNAV messages on L5.

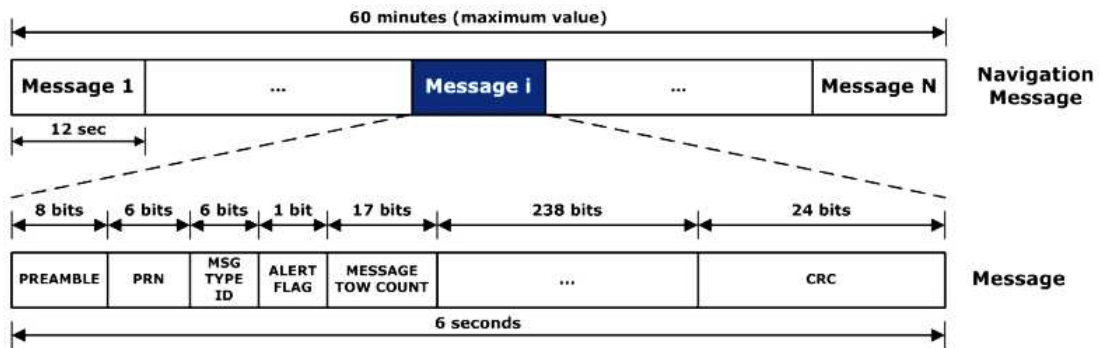


Figure 2-10. Structure of L5-CNAV messages [IS-GPS-705D, 2013].

In summary of this chapter, Table 2-1 lists the most important features regarding the signal structures of GPS L1 C/A, L2C, and L5 signals, which have been discussed in the previous text. More information is provided in [IS-GPS-200H, 2013; IS-GPS-705D, 2013; IS-GPS-800D, 2013].

Table 2-1. Summary of the signal structures of current GPS civil signals (L1 C/A, L2C, and L5)

GPS Civil Signal	L1 C/A	L2C		L5	
		L2 CM	L2 CL	L5 I	L5 Q
Carrier Frequency (MHz)	1575.42	1227.60		1176.45	
Code Frequency (MHz)	1.023	0.5115	0.5115	10.23	10.23
Code Length (Chips)	1023	10,230	767,250	10,230	10,230
Navigation Data Type	LNAV	L2-CNAV	None	L5-CNAV	None
Navigation Data Rate (Hz)	50	50	N/A	100	N/A
Secondary Code	None	None	None	NH10	NH20
Satellite Blocks	All	From IIR-M		From IIF	

3. CHAPTER 3 – PROPAGATION GEOMETRY

This chapter introduces the basic knowledge in the geometry calculation which is used for wave propagation in scintillation signal simulation. Different coordinate systems are first introduced as the foundation for the propagation geometry calculation. A global geomagnetic model used in this dissertation is then presented, as the knowledge of the geomagnetic field is necessary for wave propagation calculation and scintillation signal simulation for dynamic receiver platforms. This chapter also covers the procedure to calculate satellite position and velocity from satellite-broadcasted ephemeris, which is essential in generating scintillation modulated GPS IF samples in the scintillation simulators.

3.1. Coordinate Systems

In real-world applications, different coordinate systems are required in order to properly represent and manipulate stationary and dynamic position data. This section gives a brief introduction to the most commonly used coordinate systems in the study of GPS technologies and ionospheric scintillation.

3.1.1. Earth-Centered Earth-Fixed (ECEF) Coordinate

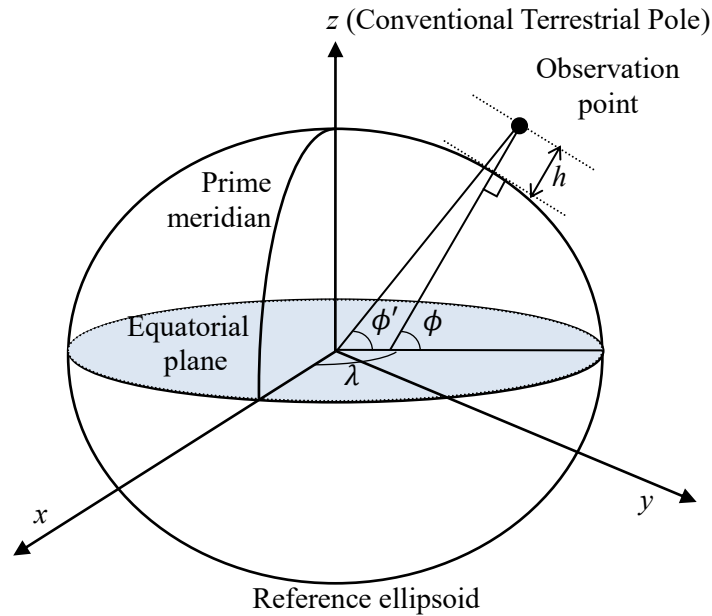


Figure 3-1. Illustration of ECEF coordinate (x, y, z) and geodetic coordinate (ϕ, λ, h) . The Earth surface is modeled as an ellipsoid.

ECEF is a Cartesian coordinate system with the origin defined as the center of the mass of the Earth, and positions represented as x , y , and z coordinates. As illustrated in Figure 3-1, the x -axis of ECEF is in the equatorial plane and intersects the prime meridian (Greenwich meridian). The z -axis is aligned with the Conventional Terrestrial Pole pointing northward, which does not coincide exactly with the instantaneous Earth rotational axis. In this system, the coordinates of a point fixed with respect to the surface of the Earth do not change. Nevertheless, ECEF is not an inertial system due to the rotation of the Earth and polar motion [Leick *et al.*, 2015].

3.1.2. Geodetic Coordinate

The geodetic coordinate is one of the most commonly used coordinate systems, in which the Earth's surface is approximated by an ellipsoid and locations near the surface are described in terms

of latitude (ϕ), longitude (λ), and height (h) (Figure 3-1). The latitude of a point is the angle from the equatorial plane to the vertical direction of a line normal to the reference ellipsoid. It is essentially different from the geocentric latitude represented as ϕ' in Figure 3-1. The longitude of a point is the angle between the prime meridian plane and a plane passing through the point, both planes being perpendicular to the equatorial plane. The geodetic height at a point is the distance from the reference ellipsoid to the point in a direction normal to the ellipsoid [Dana, 2015].

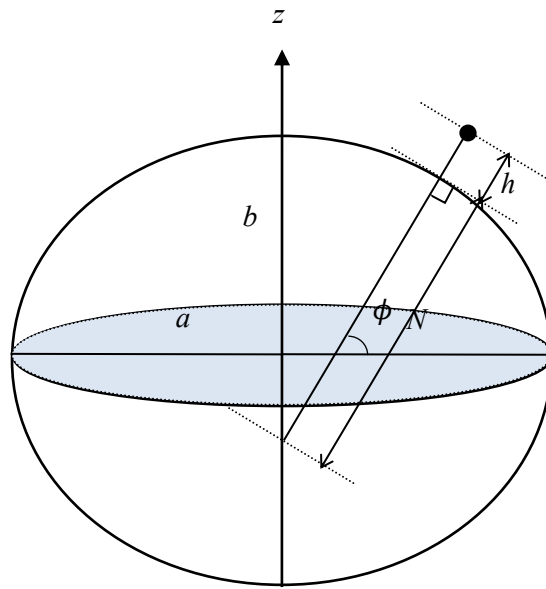


Figure 3-2. Conversions between ECEF and geodetic coordinates. a and b are the semi-major and semi-minor axes.

Conversions between ECEF coordinates (x, y, z) and geodetic coordinates (ϕ, λ, h) are straightforward using Figure 3-1 and Figure 3-2. From geodetic to ECEF coordinates, the following equations can be used [Misra and Enge, 2011]:

$$x = (N + h) \cos \phi \cos \lambda \quad (3-1)$$

$$y = (N + h) \cos \phi \sin \lambda \quad (3-2)$$

$$z = \left(N \left(\frac{b}{a} \right)^2 + h \right) \sin \phi \quad (3-3)$$

where $N = \frac{a^2}{\sqrt{a^2 \cos^2 \phi + b^2 \sin^2 \phi}}$ is illustrated in Figure 3-2, and a and b are the semi-major and semi-minor axes of the reference ellipsoid.

The conversion from geodetic coordinates to ECEF coordinates is written as follows:

$$\lambda = \arctan \left(\frac{y}{x} \right) \quad (3-4)$$

$$\phi = \arcsin \left(\frac{z}{(b/a)^2 N + h} \right) \quad (3-5)$$

$$h = \frac{\sqrt{x^2 + y^2}}{\cos \phi} - N \quad (3-6)$$

Equations (3-5) and (3-6) need to be calculated iteratively until convergence in order to solve for ϕ and h .

3.1.3. World Geodetic System 1984 (WGS-84)

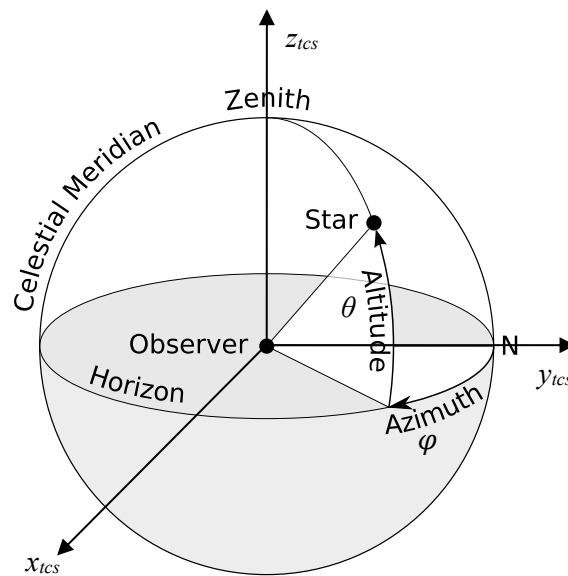
WGS-84 is the reference system for GPS, which is also the standard U.S. Department of Defense definition of a global reference system for geospatial information [Snay and Soler, 2000]. It is an ECEF system and geodetic datum that defines the Cartesian coordinate frame and the Earth ellipsoid, and models the Earth gravity field. WGS-84 is based on a consistent set of constants and model parameters that describe the Earth's size, shape, gravity, and geomagnetic fields. The four main parameters identified in WGS-84 are listed in Table 3-1:

Table 3-1. Fundamental parameters defined in WGS-84

Parameter	Notation	Value
Semi-major axis	a	6378137.0 m
Ellipsoid reciprocal flattening factor	$1/f$	298.257223563
Nominal mean Earth angular velocity	ω_E	7292115×10^{-11} rad/s
Geocentric Gravitational Constant	GM	3986004.418×10^8 m ³ /s ²

3.1.4. Topocentric Horizon Coordinate

Topocentric horizon coordinate system is also known as local tangential coordinate. It is a local Cartesian system with the location of the observer near the surface of the Earth as the origin. There are different ways to define the axes. In this study, the x -axis positive is defined to be along the eastward direction; the y -axis positive is along the northward direction; and the z -axis positive is vertical up normal to the surface of the Earth. To distinguish from the ECEF coordinates, the three coordinates in a topocentric system are denoted x_{tcs} , y_{tcs} , and z_{tcs} here as illustrated in Figure 3-3.



Background is from https://en.wikipedia.org/wiki/Horizontal_coordinate_system

Figure 3-3. Topocentric horizon coordinate ($x_{tcs}, y_{tcs}, z_{tcs}$) and horizon coordinate system (θ, φ).

In GNSS applications, topocentric horizon coordinate is often used to identify the relative locations of satellites with respect to the receiver. Let the ECEF coordinate of a satellite be $\mathbf{r}_s = [x_s, y_s, z_s]$, and the ECEF coordinate of the observer/receiver be $\mathbf{r}_0 = [x_0, y_0, z_0]$. The conversion to the topocentric coordinates of the satellite involving frame rotation is

$$\begin{bmatrix} x_{tcs} \\ y_{tcs} \\ z_{tcs} \end{bmatrix} = \begin{bmatrix} -\sin \lambda & \cos \lambda & 0 \\ -\sin \phi \cos \lambda & -\sin \phi \sin \lambda & \cos \phi \\ \cos \phi \cos \lambda & \cos \phi \sin \lambda & \sin \phi \end{bmatrix} \begin{bmatrix} x_s - x_0 \\ y_s - y_0 \\ z_s - z_0 \end{bmatrix} \quad (3-7)$$

where ϕ and λ are the latitude and longitude of the observer/receiver.

3.1.5. Horizontal Coordinate System

Another commonly used coordinate for representing relative locations with respect to the observer is called horizontal coordinate system, in which elevation angle (also called altitude) and azimuth angle are described as illustrated in Figure 3-3. It is easy to write that

$$\tan \varphi = \frac{x_{tcs}}{y_{tcs}} \quad (3-8)$$

$$\sin \theta = \frac{z_{tcs}}{\sqrt{x_{tcs}^2 + y_{tcs}^2 + z_{tcs}^2}} \quad (3-9)$$

Generally speaking, for a visible satellite, the elevation angle is between 0° and 90° . When the elevation is -90° - 0° , the satellite is below the horizon. The azimuth angle is 0° - 180° for the satellite on the eastside of the observer, and 180° - 360° for the satellite on the westside.

3.2. Global Geomagnetic Field Model

The knowledge of the geomagnetic field is important in this dissertation, especially for scintillation signal characterization and signal simulation. In the big picture, the occurrence and strength of

ionospheric scintillation are correlated with geomagnetic activities [Rodrigues *et al.*, 2004; Aquino *et al.* 2005; Jiao *et al.*, 2013c, 2015]. On the local scale, the existence of the geomagnetic field determines the anisotropy of the low-latitude ionosphere medium, as ionospheric irregularities are usually aligned with local geomagnetic field lines [Kintner *et al.*, 2014]. This section provides an overview of the components of the geomagnetic field and how to calculate them using the International Geomagnetic Reference Field (IGRF) model described in this dissertation.

3.2.1. Components of Geomagnetic Field

Geomagnetic field is the Earth’s main magnetic field whose form is largely subject to the Earth’s inner core and solar activity. The field can be represented in XYZ coordinates, which are three orthogonal directions with positive values for geographic northward (X), eastward (Y), and vertical into the Earth (Z). Another popular set of coordinates for geomagnetic field consists of the horizontal magnitude (H), the eastward angular direction of the horizontal component from geographic northward (D), and the downward component (Z). Figure 3-4 illustrates the components of the geomagnetic field, and the conversion equations are shown in equation (3-10):

$$X = E \cos D^\circ, \quad Y = H \sin D^\circ \quad (3-10)$$

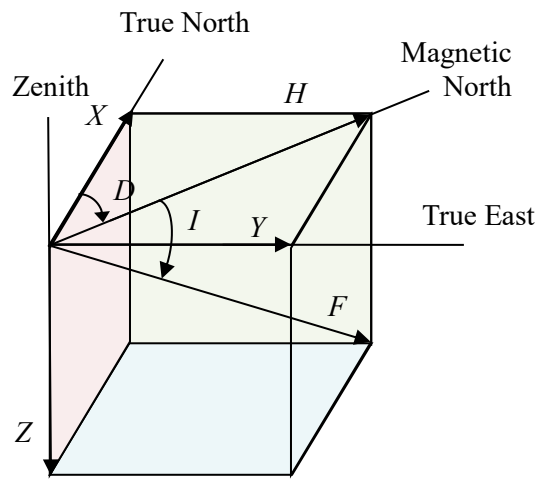


Figure 3-4. Components of geomagnetic field.

On occasion, the declination angle D° in degrees is expressed in magnetic eastward directed field strength $D(nT)$, which can be obtained from the relationship [Campbell, 2003]:

$$D(nT) = H \tan D^\circ \quad (3-11)$$

Another two useful variables for describing the geomagnetic field are I : inclination or dip, the angle the field vector makes with the horizontal, taking positive values below the horizontal; F : the total intensity of the field (as illustrated in Figure 3-4).

3.2.2. International Geomagnetic Reference Field

There are several popular global geomagnetic models, including International Geomagnetic Reference Field (IGRF), World Magnetic Model (WMM), and other high-resolution models. The IGRF model is chosen in this study, as it is a retrospective model which provides more accurate “definitive” field values for past epochs [Thébault *et al.*, 2015].

IGRF is a historic global geomagnetic field model that is updated every five years by the International Association of Geomagnetism and Aeronomy (IAGA). It models the spherical harmonic expansion of the geomagnetic scalar potential by defining a certain degree and order of Gauss coefficients as well as the annual change rate (secular variation) of the field:

$$V(r, \phi', \lambda, t) = R \sum_{n=1}^N \sum_{m=0}^n \left(\frac{R}{r}\right)^{n+1} [g_n^m(t) \cos m\lambda + h_n^m(t) \sin m\lambda] P_n^m(\sin \phi') \quad (3-12)$$

where R is the Earth radius, r is the radial distance from the Earth's center, N is the maximum degree of the expansion, ϕ' and λ are the geocentric latitude and longitude of the point of interest, g_n^m and h_n^m are Gauss coefficients defined for every five years since 1900, and $P_n^m(\sin \phi')$ are Schmidt semi-normalized associated Legendre functions of degree n and order m .

In a source-free region on the surface of the Earth and above, the main geomagnetic field is the negative gradient of the potential V . For most IGRF calculation tools, the inputs are the geodetic or geocentric coordinates and date, and the outputs are the field components, namely X, Y, Z, H, D, I, F as mentioned before. An analysis of the accuracy of the model compared with satellite measurements can be found in [Matteo and Morton, 2011].

The latest IGRF model, as of the writing of this dissertation, is the 12th generation adopted in December 2014 by IAGA. It consists of secular variation and Gauss coefficients of degree and order 13. It provides a new Definitive Geomagnetic Reference Field model for epoch (year) 2010.0, and also proposes a provisional reference field model for epoch 2015.0 and a predictive part for epochs ranging from 2015.0 to 2020.0 [Thébault et al., 2015; Hamilton et al., 2015].

3.3. Satellite Position and Velocity Calculation with GPS Ephemeris

The knowledge of the satellite position and velocity is essential for determining some important propagation parameters, including signal propagation angles, location of ionosphere penetration point (IPP), satellite scan velocity, etc. The relatively precise satellite position and velocity can be calculated using the ephemeris data broadcasted by the satellite. The GPS Interface Specification (IS) describes the detailed information of the broadcasted satellite ephemeris data, as well as the user algorithm for ephemeris determination [IS-GPS-200H Section 20.3.3.4, 2013]. The following is a summary of the ephemeris parameters and the calculation algorithm.

Table 3-2. Ephemeris parameter definitions [IS-GPS-200H, 2013]

Parameter	Definition	Unit
M_0	Mean anomaly at reference time	semi-circles
Δn	Mean motion difference from computed value	semi-circles/secs
e	Eccentricity	dimensionless
\sqrt{A}	Square root of the semi-major axis	$\sqrt{\text{meters}}$
Ω_0	Longitude of ascending node of orbit plane at weekly epoch	semi-circles
i_0	Inclination angle at reference time	semi-circles
ω	Argument of perigee	semi-circles
$\dot{\Omega}$	Rate of right ascension	semi-circles/secs
$IDOT$	Rate of inclination	semi-circles/secs
C_{uc}	Amplitude of the cosine harmonic correction term to the argument of latitude	radians
C_{us}	Amplitude of the sine harmonic correction term to the argument of latitude	radians
C_{rc}	Amplitude of the cosine harmonic correction term to the orbit radius	meters
C_{rs}	Amplitude of the sine harmonic correction term to the orbit radius	meters
C_{ic}	Amplitude of the cosine harmonic correction term to the angle of inclination	radians
C_{is}	Amplitude of the sine harmonic correction term to the angle of inclination	radians
t_{oe}	Ephemeris reference time	seconds
$IODE$	Issue of data of the ephemeris	(See IS-GPS-200H)

Table 3-3. User algorithm for satellite position and velocity calculation [Remodi, 2004; IS-GPS-200H, 2013]

Step	Description
$\mu = 3.986005 \times 10^4 \text{ meter}^3/\text{sec}^2$ $\dot{\Omega}_e = 7.2921151467 \times 10^{-5} \text{ rad/sec}$	WGS-84 value of the earth's gravitational constant and rotation rate (Table 3-1)
$A = (\sqrt{A})^2$	Semi-major axis of the satellite orbit
$n_0 = \sqrt{\frac{\mu}{A^3}}$	Computed mean motion (rad/sec)
$t_k = t - t_{oe}$	Time from ephemeris reference epoch

	$(t_k \leq 302,400)$
$n = n_0 + \Delta n$	Corrected mean motion
$M_k = M_0 + nt_k$ $\dot{M}_k = n$	Mean anomaly and its rate
$E_k = M_k + e \sin E_k$ $\dot{E}_k = \frac{\dot{M}_k}{1 - e \cos E_k}$	Kepler's equation for eccentric anomaly (solved by iteration) (rad) Eccentric anomaly rate
$v_k = \tan^{-1} \left\{ \frac{\sqrt{1 - e^2} \sin E_k / (1 - e \cos E_k)}{(\cos E_k - e) / (1 - e \cos E_k)} \right\}$ $\dot{v}_k = \frac{\dot{E}_k (1 + e \cos v_k) \sin E_k}{(1 - e \cos E_k) \sin v_k}$	True anomaly and its rate
$\Phi_k = v_k + \omega$	Argument of latitude
$\delta u_k = C_{us} \sin 2\Phi_k + C_{uc} \cos 2\Phi_k$ $\delta r_k = C_{rs} \sin 2\Phi_k + C_{rc} \cos 2\Phi_k$ $\delta i_k = C_{is} \sin 2\Phi_k + C_{ic} \cos 2\Phi_k$	Argument of latitude correction Radius correction Inclination correction
$u_k = \Phi_k + \delta u_k$ $r_k = A(1 - e \cos E_k) + \delta r_k$ $i_k = i_0 + (IDOT)t_k + \delta i_k$	Corrected argument of latitude Corrected radius Corrected inclination
$\dot{u}_k = \dot{v}_k + 2(C_{us} \cos 2u_k - 2C_{uc} \sin 2u_k)$ $\dot{r}_k = \frac{Aen \sin E_k}{1 - e \cos E_k} + 2\dot{v}_k(C_{rs} \cos 2u_k - C_{rc} \sin 2u_k)$ $IDOT = IDOT + 2\dot{v}_k(C_{is} \cos 2u_k - C_{ic} \sin 2u_k)$	Corrected rate of argument of latitude Corrected rate of radius Corrected rate of inclination rate
$x'_k = r_k \cos u_k$ $y'_k = r_k \sin u_k$	Positions in orbital plane
$\dot{x}'_k = \dot{r}_k \cos u_k - y'_k \dot{u}_k$ $\dot{y}'_k = \dot{r}_k \sin u_k + x'_k \dot{u}_k$	Velocities in orbital plane
$\Omega_k = \Omega_0 + (\dot{\Omega} - \dot{\Omega}_e)t_k - \dot{\Omega}_e t_{oe}$ $\dot{\Omega}_k = \dot{\Omega} - \dot{\Omega}_e$	Corrected longitude of ascending node and its rate
$x_k = x'_k \cos \Omega_k - y'_k \cos i_k \sin \Omega_k$ $y_k = x'_k \sin \Omega_k + y'_k \cos i_k \cos \Omega_k$ $z_k = y'_k \sin i_k$	Positions in ECEF coordinate
$\dot{x}_k = (\dot{x}'_k - y'_k \dot{\Omega}_k \cos i_k) \cos \Omega_k$ $\quad - (x'_k \dot{\Omega}_k + \dot{y}'_k \cos i_k - y'_k (IDOT) \sin i_k) \sin \Omega_k$ $\dot{y}_k = (\dot{x}'_k - y'_k \dot{\Omega}_k \cos i_k) \sin \Omega_k$ $\quad + (x'_k \dot{\Omega}_k + \dot{y}'_k \cos i_k - y'_k (IDOT) \sin i_k) \cos \Omega_k$ $\dot{z}_k = \dot{y}'_k \sin i_k + y'_k (IDOT) \cos i_k$	Velocities in ECEF coordinate

The satellite position and velocity calculated using the procedures in Table 3-3 are in the ECEF coordinates. Usually for propagation study, the position and velocity are needed in topocentric or horizontal coordinate systems. The translation is simple with the methods discussed in Section 3.1.

4. CHAPTER 4 – PROPAGATION THEORY AND STRUCTURE REALIZATION

The foundation for GPS scintillation signal simulation is the propagation theory which is discussed in detail in this chapter. The derivation of the forward propagation equation explains the physical process of how the complex wave field propagates from the GPS satellite to the receiver through the ionosphere medium, and forms the scintillation signals at the observation plane. The subsequent section on structure realization describes how to abstract the ionosphere medium to a statistical model that can be implemented in the scintillation simulators. This chapter also discusses the newly-developed data surrogate method which is extracted from the traditional wave propagation theory and can be used to directly simulate time-domain scintillation signals. All the symbols used in this chapter and their meanings are provided in LIST OF SYMBOLS.

4.1. Forward Propagation Theory

4.1.1. Maxwell's Equations

The conventional vector field formulation of Maxwell's equations is known as:

$$\text{Gauss's Law} \quad \nabla \cdot \mathbf{E}(\mathbf{r}, t) = \frac{\rho(\mathbf{r}, t)}{\varepsilon} \quad (4-1)$$

$$\text{Gauss's Law for Magnetism} \quad \nabla \cdot \mathbf{H}(\mathbf{r}, t) = 0 \quad (4-2)$$

$$\text{Faraday's Law} \quad \nabla \times \mathbf{E}(\mathbf{r}, t) = -\mu \frac{\partial \mathbf{H}(\mathbf{r}, t)}{\partial t} \quad (4-3)$$

$$\text{Ampère's Law} \quad \nabla \times \mathbf{H}(\mathbf{r}, t) = \varepsilon \frac{\partial \mathbf{E}(\mathbf{r}, t)}{\partial t} + \mathbf{J}(\mathbf{r}, t) \quad (4-4)$$

where \mathbf{E} and \mathbf{H} are complex electric and magnetic fields. The volume charge density ρ and the electric current density \mathbf{J} form the sources of the fields. Note that the above Maxwell's equations are not in symmetric form, as the existence of magnetic monopoles is not confirmed so far.

Let the time-harmonic electric and magnetic fields be given as:

$$\mathbf{E}(\mathbf{r}, t) = \text{Re}(\mathbf{E}(\mathbf{r})e^{i\omega t}) \quad (4-5)$$

$$\mathbf{H}(\mathbf{r}, t) = \text{Re}(\mathbf{H}(\mathbf{r})e^{i\omega t}) \quad (4-6)$$

$$\rho(\mathbf{r}, t) = \text{Re}(\rho(\mathbf{r})e^{i\omega t}) \quad (4-7)$$

$$\mathbf{J}(\mathbf{r}, t) = \text{Re}(\mathbf{J}(\mathbf{r})e^{i\omega t}) \quad (4-8)$$

Omitting the position vector, the time-harmonic form (phasor form) of Maxwell's equations is:

$$\text{Gauss's Law} \quad \nabla \cdot \mathbf{E} = \frac{\rho}{\varepsilon} \quad (4-9)$$

$$\text{Gauss's Law for Magnetism} \quad \nabla \cdot \mathbf{H} = 0 \quad (4-10)$$

$$\text{Faraday's Law} \quad \nabla \times \mathbf{E} = -i\omega\mu\mathbf{H} \quad (4-11)$$

$$\text{Ampère's Law} \quad \nabla \times \mathbf{H} = i\omega\varepsilon\mathbf{E} + \mathbf{J} \quad (4-12)$$

where $\omega = 2\pi f$ is the angular frequency of the field in radians/s and f is the wave frequency in Hz. Note that in the phasor form, the constitutive parameters μ and ε are complex scalars.

In a source-free region, $\rho = \mathbf{J} = 0$. Thus, from equations (4-11) and (4-12) we get

$$\nabla \times \nabla \times \mathbf{E} = \omega^2 \mu \varepsilon \mathbf{E} \quad (4-13)$$

Applying one of the vector calculus identities

$$\nabla \times \nabla \times \mathbf{E} = \nabla(\nabla \cdot \mathbf{E}) - \nabla^2 \mathbf{E} \quad (4-14)$$

to equation (4-13), the wave equation is obtained as follows:

$$\nabla^2 \mathbf{E} + \omega^2 \mu \varepsilon \mathbf{E} = \nabla(\nabla \cdot \mathbf{E}) = 0 \quad (4-15)$$

For waves propagating through the ionosphere, the volume charge density ρ is not strictly 0.

Therefore, a more general way to treat equation (4-15) is to apply divergence operator to (4-12):

$$\nabla \cdot (\nabla \times \mathbf{H}) = \nabla(i\omega\varepsilon\mathbf{E}) = 0 \quad (4-16)$$

which yields

$$\varepsilon\nabla \cdot \mathbf{E} + \mathbf{E} \cdot \nabla\varepsilon = 0 \quad (4-17)$$

Thus

$$\begin{aligned} \nabla^2\mathbf{E} + \omega^2\mu\varepsilon\mathbf{E} &= \nabla(\nabla \cdot \mathbf{E}) \\ &= -\nabla\left(\mathbf{E} \cdot \frac{\nabla\varepsilon}{\varepsilon}\right) \end{aligned} \quad (4-18)$$

Nevertheless, the theory of scintillation starts with the assumption that the gradients in the propagation media of interest are small enough. As a result, the gradient term $\nabla\varepsilon$ in equation (4-18) can be neglected, and the equation degrades to (4-15) [Rino, 2011].

4.1.2. *Freely Propagation of Waves in Homogeneous Media*

The form of freely propagating waves in strictly homogeneous media can be obtained by solving equation (4-15). It is easy to show that the family of plane waves of form

$$\mathbf{E}(\mathbf{r}) = \hat{\mathbf{E}}(\mathbf{k})e^{-i\mathbf{k}\cdot\mathbf{r}} \quad (4-19)$$

satisfy equation (4-15) when the amplitude of the wave number \mathbf{k} is confined to the constant value

$$k = |\mathbf{k}| = \omega\sqrt{\mu\varepsilon} = \omega/v_p \quad (4-20)$$

where v_p is the phase velocity of the propagating wave.

It should be noted that plane waves approximate the local fields measured at large distances from the field sources. This approximation, sometimes called the far field effect, is a good approximation for most GNSS studies where the GNSS receivers are close to the ground and the

GNSS satellites orbit the Earth at medium earth orbit (MEO) (e.g. about 20,000 km for GPS satellites).

Considering the constraint in equation (4-20), the components of the wave number vector are not independent. If we take the x axis as a reference direction, a wave number of vector \mathbf{k} of constant amplitude k has the form

$$\mathbf{k} = [k_x(\kappa), \boldsymbol{\kappa}] \quad (4-21)$$

where $\boldsymbol{\kappa}$ is the transverse component so that

$$k_x(\kappa) = k \sqrt{1 - \left(\frac{\kappa}{k}\right)^2} = kg(\kappa) \quad (4-22)$$

At a reference plane $x = x_0$, which is perpendicular to the x axis, the spatial two-dimensional Fourier decomposition of an electric field is defined as

$$\tilde{\mathbf{E}}(x_0; \boldsymbol{\kappa}) = \iint \mathbf{E}(x_0, \boldsymbol{\varsigma}) \exp\{-i\boldsymbol{\kappa}\boldsymbol{\varsigma}\} d\boldsymbol{\varsigma} \quad (4-23)$$

The field at a point in space beyond the reference plane can be written using inverse Fourier transform:

$$\mathbf{E}(x, \boldsymbol{\varsigma}) = \iint \tilde{\mathbf{E}}(x_0; \boldsymbol{\kappa}) \exp\{ik_x(\kappa)|x - x_0|\} \exp\{i\boldsymbol{\kappa}\boldsymbol{\varsigma}\} \frac{d\boldsymbol{\kappa}}{(2\pi)^2} \quad (4-24)$$

It can be verified that equation (4-24) satisfies equation (4-15).

4.1.3. Forward Propagation Theory

Rewriting equation (4-18) in terms of refractive index n yields

$$\nabla^2 \mathbf{E} + k_0^2 n^2 \mathbf{E} = -\nabla \left(\mathbf{E} \cdot \frac{\nabla \varepsilon}{\varepsilon} \right) \quad (4-25)$$

as $n = c/v_p$, and $k_0 = \omega/c$ which is an invariant wave number representing a vacuum background reference.

As mentioned before, in a weakly inhomogeneous medium, the gradient of the structure is considered very small so that the right-hand side of (4-25) can be approximated to zero. The perturbation of the local refractive index is defined as δn , so that the total local refractive index can be written as

$$n = 1 + \delta n \quad (4-26)$$

Thus, equation (4-25) becomes

$$\begin{aligned} \nabla^2 \mathbf{E} + k_0^2 \mathbf{E} &= -k_0^2 (2\delta n + \delta n^2) \mathbf{E} \\ &\approx -2k_0^2 \delta n \mathbf{E} \end{aligned} \quad (4-27)$$

To solve the wave equation represented in (4-27), an equivalent integral form based on Green functions is used. A detailed derivation is given in the work of *Rino and Fremouw* [1977], *Rino and Kruger* [2001], and *Rino* [2011]. Under the weak-scatter approximation, the following first-order differential equation defines the forward propagation equation (FPE) with the subscript of k_0 omitted:

$$\frac{\partial \mathbf{E}^+(x, \boldsymbol{\varsigma})}{\partial x} = ik\Theta \mathbf{E}^+(x, \boldsymbol{\varsigma}) + ik\delta n(x, \boldsymbol{\varsigma}) \mathbf{E}^+(x, \boldsymbol{\varsigma}) \quad (4-28)$$

The first term on the right-hand side is the propagation term, while the second term is the media-interaction term. Θ is the propagation operator defined as

$$\Theta = \sqrt{1 + \nabla_{\perp}^2/k^2} \quad (4-29)$$

where ∇_{\perp}^2 represents the transverse Laplacian ($\nabla_{\perp}^2 = \partial^2/\partial y^2 + \partial^2/\partial z^2$).

Under the parabolic approximation, the propagation operator is approximated by truncating its Taylor series expansion at the leading term:

$$\Theta \approx I + \frac{1}{2k^2} \nabla_{\perp}^2 \quad (4-30)$$

where I is an identity matrix.

Applying this approximation to equation (4-28) and multiplying both sides of the equation by $\exp\{-ikx\}$ lead to the following parabolic wave equation (PWE):

$$\begin{aligned} 2k \frac{\partial[\mathbf{E}^+(x, \boldsymbol{\varsigma})\exp\{-ikx\}]}{\partial x} \\ = i\nabla_{\perp}^2[\mathbf{E}^+(x, \boldsymbol{\varsigma})\exp\{-ikx\}] + 2ik^2\delta n(x, \boldsymbol{\varsigma})[\mathbf{E}^+(x, \boldsymbol{\varsigma})\exp\{-ikx\}] \end{aligned} \quad (4-31)$$

In weakly inhomogeneous scalar media, no polarization change is induced by field interaction, thus we can use a complex scalar wave field $\psi(x, \boldsymbol{\varsigma})$ to represent any component of $\mathbf{E}^+(x, \boldsymbol{\varsigma})\exp\{-ikx\}$ without losing generality. As a result, equations (4-28) and (4-31) can be rewritten as

$$\frac{\partial\psi(x, \boldsymbol{\varsigma})}{\partial x} = ik[\Theta - I]\psi(x, \boldsymbol{\varsigma}) + ik\delta n(x, \boldsymbol{\varsigma})\psi(x, \boldsymbol{\varsigma}) \quad (4-32)$$

4.1.4. Split-step Algorithm

A numerical way to simulate propagation theory represented in equation (4-32) is introduced in Section 2.2 in the work of *Rino* [2011]. This section gives a brief summary of the method. In the simple case of two-dimensional propagation media, with x being the propagation direction and y being the transverse direction, the FPE in equation (4-32) can be simplified as

$$\frac{\partial \psi(x, y)}{\partial x} = ik[\Theta - I]\psi(x, y) + ik\delta n(x, y)\psi(x, y) \quad (4-33)$$

The general formal solution to equation (4-33) with $\delta n(x, y) \approx 0$ is already given in equation (4-24), which can be rewritten as

$$\psi(x, y) = \int \tilde{\psi}(x_0; \kappa_y) \exp\{ik_x(\kappa_y)(x - x_0)\} \exp\{i\kappa_y y\} \frac{d\kappa_y}{2\pi} \quad (4-34)$$

$$\tilde{\psi}(x_0; \kappa_y) = \int \psi(x_0, y) \exp\{-i\kappa_y y\} dy \quad (4-35)$$

In numerical simulations, quantization must be applied to x , y , and κ_y , which leads to the division of these parameters into layers of thickness Δx , Δy , and $\Delta \kappa_y$, with each layer numbered as j , m , and l respectively. Thus, the split-step algorithm can be implemented using the following equations:

$$\psi(x_j, m\Delta y) = \psi(x_{j-1}, m\Delta y) \exp\{ik\delta n(x_j, m\Delta y)\Delta x\} \quad (4-36)$$

$$\tilde{\psi}(x_j; l\Delta \kappa_y) = \sum_{m=0}^{M-1} \psi(x_j, m\Delta y) \exp\{-2\pi i l m / M\} \quad (4-37)$$

$$\psi(x_{j+1}, m\Delta y) = \frac{1}{M} \sum_{l=0}^{M-1} \tilde{\psi}(x_j; l\Delta \kappa_y) (P_l)^{\Delta x} \exp\{2\pi i l m / M\} \quad (4-38)$$

where

$$P_l = \exp\{ikg(\kappa_y(l\Delta\kappa_y))\} \quad (4-39)$$

and

$$\kappa_y(l\Delta\kappa_y) = \left[-\frac{M}{2}, -\frac{M}{2} + 1, \dots, -1, 0, 1, \dots, \frac{M}{2} - 1\right]\Delta\kappa_y \quad (4-40)$$

Equation (4-36) is constructed under the assumption that the amplitude change over a layer is small. Thus the exponential term is applied as the phase perturbation at the beginning of each layer. Equations (4-37) and (4-38) are the corresponding discrete Fourier transform (DFT) and inverse DFT of (4-35) and (4-34), with the DFT size M to be further defined in the simulation. Other parameters that need to be defined in the simulation are the initial field, layer thicknesses, numbers of layers, and the profile of δn (see Section 7.3.1 for parameter value selections).

4.1.5. Oblique Propagation

In most real-world applications, signals from GNSS satellites are propagated obliquely to the receivers with respect to the media layers (e.g. ionosphere layers). To accommodate this reality, *Rino* [2011] has introduced a propagation coordinate system with a continuously displaced measurement plane centered on the main propagation direction, CDCS (continuously displaced coordinate system) in short.

The geometry representation of CDCS is shown in Figure 4-1, where the propagating wave intersects the phase screen with orientation x_p downward, y_p geomagnetically eastward, and z_p geomagnetically southward. Propagation angle from downward axis is denoted by θ , and propagation azimuth angle from eastward axis is denoted by φ .

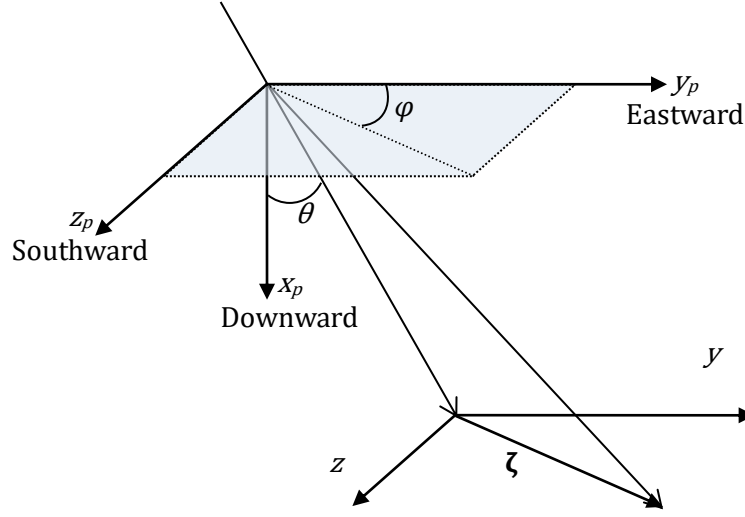


Figure 4-1. Reference coordinate system for oblique propagation. x_p is downward, y_p is geomagnetically eastward and z_p is geomagnetically southward. The boundaries of the disturbed layers are perpendicular to the x_p -axis [Rino, 2011].

In this system, the fixed propagation vector is \mathbf{k} as

$$\mathbf{k} = k[\cos \theta, \sin \theta \cos \varphi, \sin \theta \sin \varphi] = [kg(\mathbf{k}), \mathbf{k}_T] \quad (4-41)$$

The sliding origin of the CDCS is located at $[x - x_0, \tan \theta \mathbf{a}_{k_T}(x - x_0)]$, where \mathbf{a}_{k_T} is the unit vector along the transverse component:

$$\mathbf{a}_{k_T} = \frac{\mathbf{k}_T}{k_T} = [\cos \varphi, \sin \varphi] \quad (4-42)$$

Let $\psi_{\mathbf{k}}(x, \zeta)$ represent the observable field in the CDCS with ζ being the transverse coordinate in the displaced system. After moving the field in the transverse direction and compensating for the lateral displacement of the origin, it can be shown that [Rino, 2011]

$$\psi_{\mathbf{k}}(x, \zeta) = \iint \tilde{\psi}_{\mathbf{k}}(x_0; \boldsymbol{\kappa}) \exp\{i(kg(\boldsymbol{\kappa} + \mathbf{k}_T) - \tan \theta \mathbf{a}_{k_T} \cdot \boldsymbol{\kappa})(x - x_0)\} \cdot \exp\{i\boldsymbol{\zeta} \cdot \boldsymbol{\kappa}\} \frac{d\boldsymbol{\kappa}}{(2\pi)^2} \quad (4-43)$$

4.2. Structure Realization

In order to be able to carry out the FPE integration discussed in the previous section, a realization of the perturbation to the local refractive index $\delta n(x, \zeta)$ needs to be generated. This section summarizes the realization of the random medium structure using the statistical theory of scintillation developed in the work of *Rino* [2011].

4.2.1. Structure Sources

A more general form of equation (4-26) considers the local refractive index to be composed of three spatial and temporal variations:

$$n(\mathbf{r}; t) = 1 + n_d(\mathbf{r}(t)) + n_t(\mathbf{r}(t); t) + \delta n(\mathbf{r}(t); t) \quad (4-44)$$

where $n_d(\mathbf{r}(t))$ is the deterministic component containing variations caused by known average structure whose temporal variation is negligible over the typical observation duration. $n_t(\mathbf{r}(t); t)$ describes the slow-varying variations driven by processes that are not statistically homogeneous. $\delta n(\mathbf{r}(t); t)$ is a pure random process, that is of interest in this section.

When the frequency of the propagating signal is higher than 30 MHz, which is true for GNSS signals, we can use the scalar cold-plasma approximation in a dielectric medium to estimate the refractive index as [*Goldston and Rutherford, 1995*]:

$$n = \sqrt{\frac{1}{\epsilon}} = \sqrt{1 - \frac{\omega_p^2}{\omega^2}} \quad (4-45)$$

where ω_p is the plasma frequency that is defined as

$$\omega_p^2 = 4\pi r_e N_e c^2 \quad (4-46)$$

where N_e is the electron density, and r_e is the classical electron radius ($2.8197402894 \times 10^{-15}$ m).

For signal frequency well above the plasma frequency, the Taylor series expansion of equation (4-45) yields

$$\begin{aligned}\delta n &\approx -2\pi r_e \delta N_e c^2 / \omega^2 \\ &= -2\pi r_e \delta N_e / k^2\end{aligned}\quad (4-47)$$

4.2.2. Spectral Representation

The stochastic component of the refractive index $\delta n(x, \boldsymbol{\varsigma})$ is a realization of homogeneous random process with a specified SDF. The most common method of generating such a stochastic realization is by imposing the desired SDF on a white-noise field, written as

$$\delta n(x, \boldsymbol{\varsigma}) = \iiint \sqrt{\Phi_{\delta n}(k_x, \boldsymbol{\kappa})} \eta(k_x, \boldsymbol{\kappa}) \exp\{i(k_x x + \boldsymbol{\kappa} \cdot \boldsymbol{\varsigma})\} \frac{dk_x}{2\pi} \frac{d\boldsymbol{\kappa}}{(2\pi)^2} \quad (4-48)$$

where $\eta(k_x, \boldsymbol{\kappa})$ has the formal white-noise property:

$$\langle \eta(k_x, \boldsymbol{\kappa}) \eta(k'_x, \boldsymbol{\kappa}') \rangle = (2\pi)^3 \delta(k_x - k'_x) \delta(\boldsymbol{\kappa} - \boldsymbol{\kappa}') \quad (4-49)$$

in which $\langle \cdot \rangle$ represents ensemble average, and $\delta(\cdot)$ is the Dirac delta function.

It follows that the autocorrelation function of $\delta n(x, \boldsymbol{\varsigma})$ is

$$\begin{aligned}R_{\delta n}(\Delta x, \Delta \boldsymbol{\varsigma}) &= \langle \delta n(x, \boldsymbol{\varsigma}) \delta n(x - \Delta x, \boldsymbol{\varsigma} - \Delta \boldsymbol{\varsigma}) \rangle \\ &= \iiint \Phi_{\delta n}(k_x, \boldsymbol{\kappa}) \exp\{i(k_x \Delta x + \boldsymbol{\kappa} \cdot \Delta \boldsymbol{\varsigma})\} \frac{dk_x}{2\pi} \frac{d\boldsymbol{\kappa}}{(2\pi)^2}\end{aligned}\quad (4-50)$$

It is obvious that the autocorrelation function of this random process and its SDF are Fourier-transform pairs, which is usually referred to as the Wiener-Khinchin theorem [Wiener, 1964].

4.2.3. One-component Power-law Spectral Model

The spatial spectrum of δn for normal propagation in homogeneous media is constructed based on turbulence theory which states that the three-dimensional SDF of a passive scalar in the turbulent flow field can be characterized by the power-law form q^{-p} over the spatial wave number range $q_L \ll q \ll q_S$. The lower bound q_L is called the outer scale, which represents the largest structure. The upper bound q_S is called the inner scale, which corresponds to the smallest structure. Using the method proposed by *Shkarofsky* [1968], this power-law characterization can be represented by an analytic form as

$$\begin{aligned}\Phi_{\delta n}(q) &\approx C_S(q_L^2 + q^2)^{-(\nu + \frac{1}{2})} \\ &\approx C_S q^{-(2\nu + 1)}\end{aligned}\quad (4-51)$$

where ν is the scale-free spectral index, and C_S is the turbulent strength defined as

$$C_S = \frac{\langle \delta n^2 \rangle (4\pi)^{3/2} \Gamma(\nu + 1/2)}{\Gamma(\nu - 1) q_L^{-2\nu + 2}} \quad (4-52)$$

where $\Gamma(\cdot)$ is Gamma function.

According to the work of *Rino* [2011], the phase spectrum is related to the refractive index spectrum by scaling and projection:

$$\Phi_{\delta\phi}(q) = k^2 l_p \Phi_{\delta n}(q) \approx C_p q^{-(2\nu + 1)} \quad (4-53)$$

where l_p is the thickness of the medium layer.

The phase turbulent strength C_p in equation (4-53) is effectively a measured parameter, which is dependent on the wave frequency:

$$C_p(f) = C_p(f_r) \left(\frac{f_r}{f} \right)^2 \quad (4-54)$$

where f_r is the reference wave frequency.

In CDCS, the two-dimensional phase SDF is computed to be

$$\begin{aligned} \Phi_{\delta\phi_k}(\mathbf{\kappa}) &= \iint R_{\delta\phi_k}(\Delta\boldsymbol{\zeta}) \exp\{-i\mathbf{\kappa} \cdot \Delta\boldsymbol{\zeta}\} d\Delta\boldsymbol{\zeta} \\ &= k^2 l_p \sec^2 \theta \Phi_{\delta n}(\tan \theta \mathbf{a}_{k_T} \cdot \mathbf{\kappa}, \mathbf{\kappa}) \end{aligned} \quad (4-55)$$

4.2.4. Power-law Spectral Model in Anisotropic Media

In the ionosphere, charged particles tend to move along the magnetic field lines, which results in the formation of field-aligned rod-shaped anisotropic irregularities. The impact of this anisotropy on the trans-ionosphere wave propagation is discussed in the work of *Singleton* [1970]. This theory generates the anisotropic correlation function by rotating and scaling the displacement coordinates for the isotropic correlation function. In order to do this, irregularity elongation factors and the local geomagnetic field within the propagation medium are required.

According to the work of *Singleton* [1970] and *Rino* [2011], the SDF of the integrated phase in the CDCS anisotropic system is

$$\begin{aligned} \Phi_{\delta\phi_k}(\mathbf{\kappa}) &= k^2 l_p \sec^2 \theta \Phi_{\delta n}(\mathbf{\kappa}) \\ &\approx \frac{k^2 l_p C_s a b \sec^2 \theta}{q^{2\nu+1}} \\ &= \frac{k^2 l_p C_s a b \sec^2 \theta}{(A\kappa_y^2 + B\kappa_y \kappa_z + C\kappa_z^2)^{\nu+1/2}} \end{aligned} \quad (4-56)$$

where a and b are the principal and secondary elongation factors which represent the

irregularity dimensions along and across the magnetic field respectively. The two-dimensional quadratic form of q is

$$q^2 = A\kappa_y^2 + B\kappa_y\kappa_z + C\kappa_z^2 \quad (4-57)$$

where A , B , and C are anisotropy factors that are related to the propagation angle and azimuth angle defined in Section 4.1.5. Their calculation is elaborated in Appendix A.3 in the work of *Rino* [2011].

4.2.5. Two-component Power-law Spectral Model

In situ measurements of low-latitude structure also show evidence of two-component power-law spectra, which have been used to explain observed low-latitude scintillation from Very High Frequency (VHF) to S-Band. In GPS observation, two-component power-law spectra are statistically prominent, but usually confined to highly structured pre-midnight data [*Rino et al.*, 2016].

The two-component power-law spectra are defined as

$$\Phi_{\delta\phi}(q) = \begin{cases} C_p q^{-p_1}, & q \leq q_0 \\ C_p q_0^{p_2-p_1} q^{-p_2}, & q > q_0 \end{cases} \quad (4-58)$$

where q_0 is the break wave number, and p_1 and p_2 are the power-law indices. If $p_1 = 0$, q_0 becomes an outer scale. If $p_2 = 0$, the phase SDF is noise limited. If $p = p_1 = p_2$, (4-58) becomes the unbounded power law in (4-53).

4.2.6. Sample Translation between Time and Space

Typically, GNSS signals received at the measurement plane are sampled uniformly in the time domain. To acquire the spatial spectrum parameters in (4-53) or (4-58), the measurements are

required to be translated into the spatial domain. The measured samples in the time domain can be assigned in the spatial domain to the following grid:

$$s_{space}[j] = s_{space}[j - 1] + v_{eff}[j - 1]\Delta t \quad (4-59)$$

where s_{space} is the spatial grid in the receiver observation plane on y axis, j is the grid index, Δt is the uniform time interval between samples in time. v_{eff} is the effective velocity scaling, with the time displacement defined as [equation 4.48 in *Rino, 2011*]:

$$v_{eff} = \sqrt{\frac{Cv_{ky}^2 - Bv_{ky}v_{kz} + Av_{kz}^2}{AC - B^2/4}} \quad (4-60)$$

in which v_{ky} and v_{kz} are the transverse components of the apparent velocity \mathbf{v}_k in the measurement plane, and A , B , and C are the anisotropy factors mentioned in (4-56).

The spatial samples obtained from (4-59) are not uniform in space as v_{eff} changes over time. A one-dimensional data interpolation can be performed to generate uniform samples in space. To convert back from spatial to time domain, uniform spatial samples are first translated to non-uniform time samples, and then interpolated to uniform samples in the time domain.

4.2.7. Total Electron Content (TEC)

Based on equation (4-44), the measured signal phase can be modeled as

$$\phi(t) = -\frac{2\pi fr(t)}{c} - \frac{r_e c}{2\pi} TEC/f + \phi_{scin}(t) + \phi_{noise}(t) \quad (4-61)$$

where $r(t)$ is the propagation range. TEC can be defined by a path integral based on the conversion from refractive index to electron density shown in equation (4-47):

$$TEC = \int \delta N_e(\mathbf{r}) dr \quad (4-62)$$

With dual-frequency measurements, TEC can be estimated using the approximation of equation (4-61) by neglecting the last two terms on the right-hand side, given that the propagation range $r(t)$ for the two frequencies is the same. For GPS signals, both pseudorange and phase measurements can be utilized. The TEC calculated from pseudorange measurements is absolute TEC, while that calculated from phase measurements is relative TEC (ΔTEC) considering that the integer ambiguities for the two frequencies are different [*Misra and Enge, 2011*]:

$$TEC = \frac{f_1^2 f_2^2}{40.3(f_1^2 - f_2^2)} (P_2 - P_1) \quad (4-63)$$

$$\Delta TEC = \frac{c f_1^2 f_2^2}{2\pi \times 40.3(f_1^2 - f_2^2)} \left(\frac{\phi_1}{f_1} - \frac{\phi_2}{f_2} \right) \quad (4-64)$$

where P_1 and P_2 represent pseudorange measurements in meters on the two frequencies, and ϕ_1 and ϕ_2 are phase measurements in radians.

The relative TEC calculated from dual-frequency phases is much smoother than that calculated from pseudoranges, due to the significantly less noise in the phase measurements. In practice, the integer ambiguity is estimated by averaging the difference between TEC and ΔTEC . After adding the difference back onto ΔTEC , a smoothed estimation of the absolute TEC can be obtained.

The TEC obtained from equations (4-63) and (4-64) is essentially slant TEC (STEC) along the oblique propagation path. To translate the STEC into vertical TEC (VTEC) along the zenith propagation path, a mapping function can be used to account for the longer path length with oblique propagation [*Misra and Enge, 2011*]:

$$VTEC = STEC \sqrt{1 - \left(\frac{R_E \cos el}{R_E + h_I}\right)^2} \quad (4-65)$$

where R_E is the radius of the Earth which is 6,368 km, h_I is the height of the ionospheric layer which is usually set to 350 km, and el is the satellite elevation angle in the topocentric system.

In the GPS system, there are three different signal frequencies that are currently available for civilian use: L1C/A, L2C, and L5 (Chapter 2). In theory, TEC can be obtained from measurements of any pair of frequencies. During a quiet period, $TEC_{L1,L2}$, $TEC_{L1,L5}$, and $TEC_{L2,L5}$ are supposed to be similar theoretically. However, during scintillation, these three TECs deviate from each other due to the significant difference in the $\phi_{scin}(t)$ term in equation (4-61). In practice, $TEC_{L2,L5}$ is often not used, due to the vicinity of the two frequencies which amplifies noise when applying equations (4-63) and (4-64).

Figure 4-2 shows an example of different relative STECs calculated from phase measurements on L1 and L2C pair, and L1 and L5 pair. Also plotted in the figure is the detrended signal intensity measurements on L1, which shows that the first half of the data is quiet while the second half is plagued with strong scintillation. It can be seen that during the quiet time, the two STECs have similar trends. During strong scintillation, on the other hand, the trends in the two STECs become obviously different with varied fluctuations.

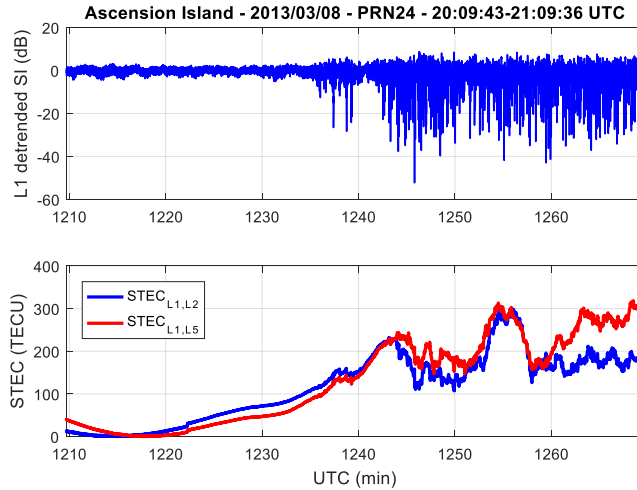


Figure 4-2. Detrended signal intensity on L1, and relative STECs calculated from phase measurements on L1 and L2C, and L1 and L5. The data was collected on PRN 24 from 20:09:43 to 21:09:36 UTC on March 8, 2013 on Ascension Island. The first half of the data is quiet and the second half is scintillating.

4.3. Time-domain Data Surrogate Methodology

The time-domain data surrogate method has been developed from the traditional phase-screen wave propagation theories and newly improved by *Carrano et al.* [2016] and *Rino et al.* [2017]. This method extracts spectral and geometrical parameters from real scintillation signals, which can be used to directly simulate the time sequence of scintillation signals. The simulator built on this method is relatively easy to implement and contains more flexibility compared with the simulator based on the traditional wave propagation method. This section summarizes the mathematics for the data surrogate method using two-dimensional two-component power-law single phase screen realization. Readers are referred to [*Rino et al.*, 2017] for more details.

When only considering a single phase screen during two-dimensional signal propagation for scintillation simulation. The complex field ψ at a distance x from the phase screen can be generated by iterating equations (4-36) through (4-38) once:

$$\tilde{\psi}(0; l\Delta q) = \sum_{m=0}^{M-1} \exp\{i\phi(m\Delta y)\} \exp\{-2\pi i l m / M\} \quad (4-66)$$

$$\psi(x, m\Delta y) = \frac{1}{M} \sum_{l=0}^{M-1} \tilde{\psi}(0; l\Delta q) \exp\{-ik(l\Delta q/k)^2 x/2\} \exp\{2\pi i l m / M\} \quad (4-67)$$

where ϕ represents the path-integrated phase, and $q = |\kappa_y|$.

The Fresnel scale is defined as

$$\rho_F = \sqrt{x/k} \quad (4-68)$$

where x is the corrected propagation distance from the effective ionosphere penetration point (IPP) of the phase screen to the receiver by taking into consideration the wavefront curvature:

$$x = r_p(r_s - r_p)/r_s \quad (4-69)$$

where r_p is the actual physical range from the IPP to the receiver, and r_s is the range from the satellite to the receiver.

Substituting x with the Fresnel scale, equation (4-67) becomes

$$\psi(\rho_F; m\Delta y) = \frac{1}{M} \sum_{l=0}^{M-1} \hat{\psi}(0; l\Delta q) \exp\{-i(l\Delta q\rho_F)^2/2\} \exp\{2\pi i l m / M\} \quad (4-70)$$

Considering that the path-integrated phase structure can be characterized by a two-component power-law SDF as described in equation (4-58), normalizing the wave number with the Fresnel scale yields the normalized SDF of the phase screen:

$$P(\mu) = \Phi_{\delta\phi}(q)/\rho_F = \begin{cases} U_1\mu^{-p_1}, & \mu \leq \mu_0 \\ U_2\mu^{-p_2}, & \mu > \mu_0 \end{cases} \quad (4-71)$$

where $\mu = q\rho_F$ is the normalized wave number, $\mu_0 = q_0\rho_F$ is the normalized break wave

number, $U_1 = C_p \rho_F^{p_1-1}$, and $U_2 = C_p \rho_F^{p_1-1} \mu_0^{p_2-p_1}$. Thus, the universal scattering strength U can be defined as [Carrano et al., 2016]:

$$U = \begin{cases} U_1, & \mu_0 \geq 1 \\ U_2, & \mu_0 < 1 \end{cases} \quad (4-72)$$

U is essentially the normalized phase spectral power at the Fresnel scale. When $U \ll 1$ the scatter is weak, and when $U \gg 1$ the scatter is strong.

The values of ρ_F , μ_0 , and U can also be scaled from one frequency to another frequency using the following relationships:

$$\rho_F(f) = \rho_F(f_r) \sqrt{\frac{f_r}{f}} \quad (4-73)$$

$$\mu_0(f) = \mu_0(f_r) \sqrt{\frac{f_r}{f}} \quad (4-74)$$

$$U(f) = \begin{cases} U(f_r) \left(\frac{f_r}{f}\right)^{\frac{1}{2}p_1 + \frac{3}{2}}, & \mu_0(f_r) \geq 1, \mu_0(f) \geq 1 \\ U(f_r) \frac{1}{\mu_0(f_r)^{p_2-p_1}} \left(\frac{f_r}{f}\right)^{\frac{1}{2}p_1 + \frac{3}{2}}, & \mu_0(f_r) < 1, \mu_0(f) \geq 1 \\ U(f_r) \mu_0(f)^{p_2-p_1} \left(\frac{f_r}{f}\right)^{\frac{1}{2}p_1 + \frac{3}{2}}, & \mu_0(f_r) \geq 1, \mu_0(f) < 1 \\ U(f_r) \frac{\mu_0(f)^{p_2-p_1}}{\mu_0(f_r)^{p_2-p_1}} \left(\frac{f_r}{f}\right)^{\frac{1}{2}p_1 + \frac{3}{2}}, & \mu_0(f_r) < 1, \mu_0(f) < 1 \end{cases} \quad (4-75)$$

where f_r is the reference frequency.

Equation (4-48) has implied that a statistically equivalent field realization can be generated by imposing the above desired SDF on white noise. With the field realization, the propagation

equations from the phase screen to the observation plane can be implemented in the simulation with normalized units as:

$$\bar{\Phi}_m = \sum_{l=0}^{M-1} \sqrt{P(l\Delta\mu)\Delta\mu/(2\pi)} \eta_n \exp\{-2\pi ilm/M\} \quad (4-76)$$

$$\tilde{\psi}(0; l\Delta\mu) = \sum_{m=0}^{M-1} \exp\{i\bar{\Phi}_m\} \exp\{-2\pi ilm/M\} \quad (4-77)$$

$$\psi(\rho_F; m\Delta y/\rho_F) = \frac{1}{M} \sum_{l=0}^{M-1} \tilde{\psi}(0; l\Delta\mu) \exp\{-i(l\Delta\mu)^2/2\} \exp\{2\pi ilm/M\} \quad (4-78)$$

To convert the complex field from the space domain to the time domain, the effective scan velocity v_{eff} discussed in Section 4.2.6 is used, such that $y = v_{eff}t$. The conversion from Doppler frequency f_D to normalized wavenumber is

$$\mu = 2\pi f_D(\rho_F/v_{eff}) \quad (4-79)$$

A sampled phase screen constructed with $P(\mu_n)2\pi\Delta f_D/\Delta\mu = P(\mu_n)\rho_F/v_{eff}$ where $\Delta f_D = 1/(N\Delta t)$ (Δt is the sample interval, and N is the total number of samples) generates a statistically equivalent realization in the time domain of the scintillation defined by the phase screen structure.

To summarize, in this data surrogate simulation method, a time-domain GNSS complex-field scintillation realization can be generated by specifying the structure parameters: U, p_1, p_2, μ_0 , the time scaling factor: ρ_F/v_{eff} , and the sampling parameters: $\Delta t, N$.

5. CHAPTER 5 – DETECTION METHODOLOGY FOR SCINTILLATION DETECTION

An efficient scintillation event detection system lays the foundation for scintillation research, as it extracts scintillation events of interest for study from collected raw GPS data. This PhD dissertation research proposes new scintillation detectors based on a machine learning algorithm to detect amplitude and phase scintillation events, which offers several advantages over the traditional NP detectors. This chapter introduces the fundamental detection theory, followed by a detailed mathematical derivation of the machine learning algorithm used in the proposed scintillation detectors.

5.1. Fundamental Detection Theory

Detection theory is fundamental to the design and application of modern electronic signal processing systems for decision making and information extraction. It has a wide application nowadays in many fields, such as radar, telecommunication, biomedicine, and psychology etc. The fundamental detection theory is developed upon the simple hypothesis testing problem in which the PDF for each assumed hypothesis is known. The primary approaches to solving this simple hypothesis testing problem are the classical approach based on the Neyman-Pearson (NP) theorem, and the Bayesian approach based on minimization of the Bayes risk [Kay, 1998]. This section introduces the fundamentals of a NP detector that is most frequently used in previous study of scintillation signal detection.

Assume the simple binary detection case, where two hypotheses are assigned: H_0 and H_1 . H_0 is referred to as the null hypothesis where the target is absent, and H_1 as the alternative hypothesis

where the target is present. An observation x is made from the data and is drawn from one of two possible PDFs, $p(x|H_0)$ and $p(x|H_1)$. A decision is made to determine the class of x . Denote D_0 if deciding $x \in H_0$, and D_1 if deciding $x \in H_1$. Comparing the decision with reality, four cases can happen: D_0 is made and $x \in H_0$; D_0 is made but $x \in H_1$; D_1 is made but $x \in H_0$; D_1 is made and $x \in H_1$. The probabilities of the four conditions are called true negative rate (TNR) or correct rejection rate, false negative rate (FNR) or miss rate, false positive rate (FPR) or false alarm rate, and true positive rate (TPR) or hit rate. Consider the following decision rule made regarding a threshold γ : make D_0 if $L(x) = \frac{p(x|H_1)}{p(x|H_0)} < \gamma$ and make D_1 if $L(x) = \frac{p(x|H_1)}{p(x|H_0)} > \gamma$.

Using the illustration shown in Figure 5-1, the calculations of the four rates are reached as follows:

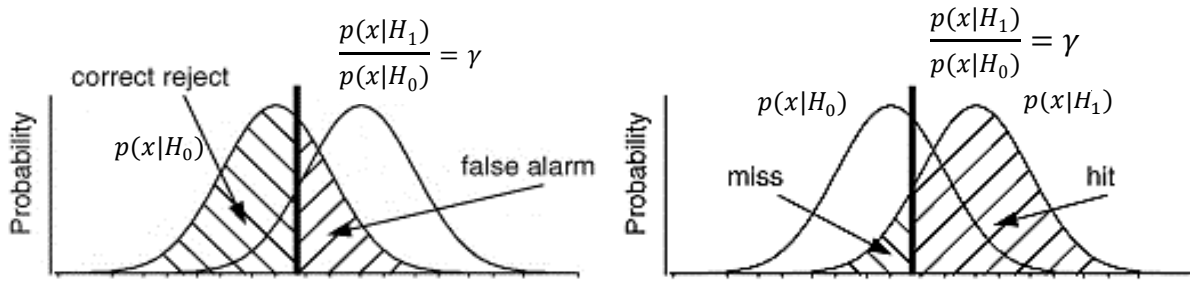


Figure 5-1. Illustration of TNR, FNR, FPR, and TPR.

$$\text{TNR} = P(D_0|H_0) = \int_{\{x:L(x)<\gamma\}} p(x|H_0)dx \quad (5-1)$$

$$\text{FNR} = P(D_0|H_1) = \int_{\{x:L(x)<\gamma\}} p(x|H_1)dx \quad (5-2)$$

$$\text{FPR} = P(D_1|H_0) = \int_{\{x:L(x)>\gamma\}} p(x|H_0)dx \quad (5-3)$$

$$\text{TPR} = P(D_1|H_1) = \int_{\{x:L(x)>\gamma\}} p(x|H_1)dx \quad (5-4)$$

A confusion matrix can be obtained using TNR, FNR, FPR, and TPR, which is a specific table layout that visualizes the performance of a classifier (also a detector in binary cases). As illustrated in Table 5-1, a confusion matrix contains information about the actual and predicted classes generated by a classification system, and the larger the total percentage of the matrix diagonal, the better the classifier performs in terms of correct classification.

Table 5-1. Illustration of the components of a confusion matrix
Predicted Class

		D_0	D_1
		TNR	FPR
True Class	H_0	TNR	FPR
	H_1	FNR	TPR

Another measure that visualizes the performance of a binary detector/classifier is the receiver operating characteristic (ROC) curve which plots the TPR against the FPR at various threshold values γ . A ROC curve is always concave, and the larger the area under the curve the better the performance of the system.

5.2. Mathematics of Support Vector Machines (SVMs)

Support vector machines are popular classification and regression techniques that have led to progress in state-of-the-art handwriting recognition, database search, and many other fields of classification and machine intelligence [Cortes and Vapnik, 1995]. SVM is an optimization technique based upon Structural Risk Minimization (SRM) [Vapnik and Chervonenkis, 1974]. SRM defines an upper bound on the generalization error rate by seeking the boundary with the greatest separation of observed training samples. Additionally, when implemented in kernel form,

the SVM is an optimum linear machine in kernel space. SVM can be configured as a back propagated neural network or a radial basis function machine, and it is also commonly used in nonlinear regression, formally known as Support Vector Regression [Haykin, 2009]. While SVM is typically used for two-class problems, such as in this dissertation, it can be configured in a number of ways for multi-class applications. In this section an overview is provided of the derivation for finding the optimal hyperplane described by the SVM and the extension of this model to a hyperplane in a much higher dimensional space by using the so called “kernel trick” [Haykin, 2009].

5.2.1. Optimal Hyperplane via Margin of Separation

Given a training data set $\{\mathbf{x}_p, d_p\}_{p=1}^P$ where $\mathbf{x}_p \in \mathbb{R}^N$ is the p^{th} input pattern, $d_p = \pm 1$ represents the desired label for two-classes. If classes are linearly separable in \mathbb{R}^N , then the discriminant functions $g(\mathbf{x}) = \mathbf{w}^T \mathbf{x} + b$ exist such that

$$\begin{aligned} \mathbf{x}_p \in C_1 &\rightarrow g(\mathbf{x}_p) \geq 0, & \text{then } d_p &= +1 \\ \mathbf{x}_p \in C_2 &\rightarrow g(\mathbf{x}_p) < 0, & \text{then } d_p &= -1 \end{aligned} \tag{5-5}$$

To find the optimal hyperplane that separates C_1 and C_2 samples, a SVM maximizes the separation or distance between the decision hyperplane and closest data samples in the training set. The distance is called the margin of separation and is represented by the variable ρ . The goal is to find the hyperplane that maximizes ρ . If \mathbf{w}_o and b_o are parameters of the optimum hyperplane, then $g(\mathbf{x}) = \mathbf{w}_o^T \mathbf{x} + b_o$ gives distance of \mathbf{x} to the hyperplane. This can be better illustrated through the following expression (Figure 5-2),

$$\mathbf{x} = \mathbf{x}_o + r \frac{\mathbf{w}_o}{\|\mathbf{w}_o\|} \quad (5-6)$$

where $\frac{\mathbf{w}_o}{\|\mathbf{w}_o\|}$ is a unit normal to the plane, r represents distance from the plane, and \mathbf{x}_o is the closest point on the optimal decision boundary to \mathbf{x} . Note that $r > 0$ indicates that \mathbf{x} is on the positive side of the plane and vice versa. Using this observation, $g(\mathbf{x})$ can be rewritten as the following,

$$\begin{aligned} g(\mathbf{x}) &= \mathbf{w}_o^T \mathbf{x} + b_o \\ &= \mathbf{w}_o^T \left(\mathbf{x}_o + r \frac{\mathbf{w}_o}{\|\mathbf{w}_o\|} \right) + b_o \\ &= (\mathbf{w}_o^T \mathbf{x}_o + b_o) + r \|\mathbf{w}_o\| \end{aligned} \quad (5-7)$$

Thus, $r = \frac{g(\mathbf{x})}{\|\mathbf{w}_o\|}$, since $g(\mathbf{x}_o) = \mathbf{w}_o^T \mathbf{x}_o + b_o = 0$. In particular, distance from origin $\mathbf{x} = \mathbf{0}$ is

$$r = \frac{b_o}{\|\mathbf{w}_o\|}.$$

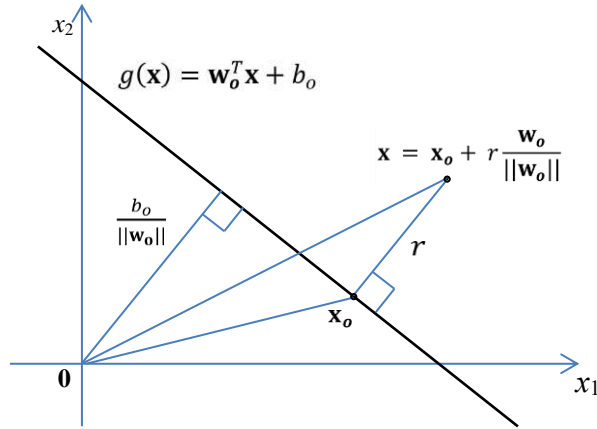


Figure 5-2. Illustration of optimal decision boundary in SVM.

For mathematical optimization, the objective of this classification problem is modified to determine \mathbf{w}_o and b_o for a given training set $\{\mathbf{x}_p, d_p\}_{p=1}^P$, such that if $d_p = 1$ (i.e. $\mathbf{x} \in C_1$) then $\mathbf{w}_o^T \mathbf{x} + b_o \geq 1$ and if $d_p = -1$ (i.e. $\mathbf{x} \in C_2$) then $\mathbf{w}_o^T \mathbf{x} + b_o \leq -1$ or combined

$(\mathbf{w}_o^T \mathbf{x} + b_o)d_p \geq 1$. Those samples satisfying the equal relationship: $\mathbf{w}_o^T \mathbf{x} + b_o = 1$ and $\mathbf{w}_o^T \mathbf{x} + b_o = -1$ form the support vectors (SV), hence the name SVM. These samples are the closest to the decision surface and are the most difficult (as far as training data is concerned) to classify, and thus, they define the optimal hyperplane. For SVs $\mathbf{x}(s) \in C_1$ and $\mathbf{x}(r) \in C_2$:

$$\begin{aligned} g(\mathbf{x}(s)) &= \mathbf{w}_o^T \mathbf{x}(s) + b_o = 1 \\ g(\mathbf{x}(r)) &= \mathbf{w}_o^T \mathbf{x}(r) + b_o = -1 \end{aligned} \quad (5-8)$$

Therefore, the margin of separation between two classes is

$$\rho = r_1 - r_2 = \frac{g(\mathbf{x}(s))}{\|\mathbf{w}_o\|} - \frac{g(\mathbf{x}(r))}{\|\mathbf{w}_o\|} = \frac{2}{\|\mathbf{w}_o\|} \quad (5-9)$$

With the optimal hyperplane lying directly between support vectors, the optimization problem reduces to finding the optimal hyperplane \mathbf{w}_o and b_o to maximize ρ :

$$\max_{\{\mathbf{w}_o, b_o\}} \rho \Leftrightarrow \min_{\{\mathbf{w}_o, b_o\}} \left\{ \frac{2}{\rho^2} = \frac{\|\mathbf{w}\|^2}{2} \right\} \quad (5-10)$$

subject to

$$(\mathbf{w}^T \mathbf{x}_p + b)d_p \geq 1, \quad \forall p \in [1, P]. \quad (5-11)$$

Lagrangian cost function can be constructed as

$$J(\mathbf{w}, b, \mathbf{x}) = \frac{1}{2} \mathbf{w}^T \mathbf{w} - \sum_{p=1}^P \alpha_p [(\mathbf{w}^T \mathbf{x}_p + b)d_p - 1] \quad (5-12)$$

where the first term is a convex function of \mathbf{w} and the decision related constraint is a linear function of \mathbf{w} , and $\alpha_p > 0$ are Lagrange parameters. Solutions are saddle points of the cost function $J(\mathbf{w}, b, \mathbf{x})$. The saddle points have to be minimized with respect to \mathbf{w} and b , but maximized with respect to α . Differentiating with respect to the hyperplane parameters yields

$$\frac{\partial J}{\partial \mathbf{w}} = 0 \Rightarrow \mathbf{w}_o = \sum_{p=1}^P \alpha_p d_p \mathbf{x}_p \quad (5-13)$$

$$\frac{\partial J}{\partial b} = 0 \Rightarrow \sum_{p=1}^P \alpha_p d_p = 0 \quad (5-14)$$

As can be seen, \mathbf{w}_o is expressed in terms of the training samples and coefficients α_p . This is a primal problem whose optimal solution can be found by jointly solving its dual problem. In order to define the dual problem, the original Lagrangian function is expanded as

$$J(\mathbf{w}, b, \mathbf{x}) = \frac{1}{2} \mathbf{w}^T \mathbf{w} - \sum_{p=1}^P \alpha_p d_p \mathbf{w}^T \mathbf{x}_p - b \sum_{p=1}^P \alpha_p d_p + \sum_{p=1}^P \alpha_p \quad (5-15)$$

From conditions (5-13) and (5-14), the objective function is obtained for the dual problem in terms of α 's, $J(\mathbf{w}, b, \mathbf{x}) = Q(\boldsymbol{\alpha})$ as

$$\begin{aligned} Q(\boldsymbol{\alpha}) &= \sum_{p=1}^P \alpha_p - \frac{1}{2} \sum_{p=1}^P \sum_{q=1}^P \alpha_p \alpha_q d_p d_q \mathbf{x}_p^T \mathbf{x}_q \\ &= \boldsymbol{\alpha}^T \mathbf{1} - \frac{1}{2} \boldsymbol{\alpha}^T \mathbf{D}^T \mathbf{K} \mathbf{D} \boldsymbol{\alpha} \end{aligned} \quad (5-16)$$

where $\boldsymbol{\alpha} = [\alpha_1 \dots \alpha_P]^T$, $\mathbf{1} = [1 \dots 1]^T$, $\mathbf{D} = \text{diag}[d_1 \dots d_P]$, and $\mathbf{K} = [K_{p,q}]_{p,q=1}^P = \mathbf{x}_p^T \mathbf{x}_q$.

Matrix $\mathbf{K} \in \mathbb{R}^{P \times P}$ is a Gram matrix of inner products, a positive semi-definite and symmetric matrix. Now, (5-16) is expressed in terms of α and \mathbf{x} rather than \mathbf{w} . To solve the primal

problem, we first optimize on the dual problem. Formally, given $\{\mathbf{x}_p, d_p\}_{p=1}^P$ (assumed to be

linearly separable), we desire to find $\{\alpha_p\}_{p=1}^P$ that maximizes $Q(\alpha)$ subject to

$$\sum_{p=1}^P \alpha_p d_p = \boldsymbol{\alpha}^T \mathbf{d} = 0 \quad (5-17)$$

$$\alpha_p \geq 0 \quad \forall p \in [1, P] \quad (5-18)$$

where \mathbf{d} is a vector of the P training labels. Once α_o optimal is found, it will be applied to (5-16) to find $\mathbf{w}_o = \sum_{p=1}^P \alpha_p d_p \mathbf{x}_p$. Recall that for support vectors $\mathbf{x}(s) \in C_1$, $\mathbf{w}_o^T \mathbf{x}(s) + b_o = 1$, and $\mathbf{x}(r) \in C_2$, $\mathbf{w}_o^T \mathbf{x}(r) + b_o = -1$. Thus, $b_o = -\frac{1}{2} \mathbf{w}_o^T [\mathbf{x}(s) + \mathbf{x}(r)]$. Note that the solution is sparse, i.e. for constraint (5-18) inequality happens only for SVs while for other samples α 's are zero.

Having constructed SVM, a decision about an unknown pattern $\mathbf{y} \in \mathbb{R}^N$ is made based on

$$o(y) = g(y) = \mathbf{w}_o^T \mathbf{y} + b_o \begin{cases} >_{\{y \in C_1\}} \\ = \\ <_{\{y \in C_2\}} \end{cases} 0 \quad (5-19)$$

5.2.2. Optimal Hyperplane with Soft Margin SVM

For the task of finding an optimal hyperplane for non-separable patterns, a new SVM goal is adopted to find an optimal hyperplane that minimizes probability of misclassification error over the training set. The margin of separation is said to be “soft” if a data point violates condition $(\mathbf{w}^T \mathbf{x}_p + b)d_p \geq 1$.

To remedy cases where a perfect separation cannot be accomplished, we modify the constraint on each sample by softening the margin with slack variables, $\xi_p > 0$, which give a measure of a sample's deviation from the ideal condition of separability, i.e. $(\mathbf{w}^T \mathbf{x}_p + b)d_p \geq 1 - \xi_p, \forall p \in [1, P]$. To minimize the misclassification error, we use the metric

$$\Psi(\xi_p) = \sum_{p=1}^P \xi_p \quad (5-20)$$

which takes higher values when there are more misclassifications. Now, the primal problem for the non-separable training case becomes: Given training set $\{\mathbf{x}_p, d_p\}_{p=1}^P$, find \mathbf{w}_o and b_o such that

$$\Psi(\mathbf{w}, \xi_p) = \frac{1}{2} \mathbf{w}^T \mathbf{w} + C \sum_{p=1}^P \xi_p \quad (5-21)$$

is minimized subject to

$$(\mathbf{w}^T \mathbf{x}_p + b) d_p \geq 1 - \xi_p, \quad (5-22)$$

$$\xi_p > 0, \forall p \in [1, P] \quad (5-23)$$

where C is a user-specified parameter that presents a trade-off between misclassification error and maximum margin. Thus, the modified Lagrangian function becomes:

$$\begin{aligned} J(\mathbf{w}, b, \alpha, \xi) = & \frac{1}{2} \mathbf{w}^T \mathbf{w} + C \sum_{p=1}^P \xi_p \\ & - \sum_{p=1}^P \alpha_p [(\mathbf{w}^T \mathbf{x}_p + b) d_p - 1 + \xi_p] - \sum_{p=1}^P \mu_p \xi_p \end{aligned} \quad (5-24)$$

where α_p and μ_p are Lagrangian multipliers. Solving this objective function is similar to solving (5-12), which requires solving the primal problem and the dual problem. However, it is interesting to note that slack variables do not appear in the dual problem cost function.

5.2.3. SVM Kernel Extension

To build a SVM for pattern classification, the input data (original features) space is first mapped to a higher dimensional feature space using nonlinear mapping function $\Phi(\mathbf{x}_p) =$

$[\Phi_1(\mathbf{x}_p) \dots \Phi_M(\mathbf{x}_p)]^T$, where $\dim(\Phi) = M \gg N$. This technique of utilizing a higher dimensional feature space is motivated by Cover's theorem which states that when a complex pattern-classification problem is cast to a high-dimensional space nonlinearly, it is more likely to be linearly separable than in a low-dimensional space, provided that the space is not densely populated [Cover, 1965]. However, a larger dimensional feature mapping typically requires very large (maybe even infinite for mapping associated with Gaussian kernel) dimensions of the feature space M . Therefore, the direct computation of operations in M space would be impossible.

This problem can be solved using the kernel trick to implicitly construct an optimal hyperplane in a higher dimensional feature space, as the objective functions depend only on inner products of the data and training samples. Given training data $\{\mathbf{x}_p, d_p\}_{p=1}^P$, a mapping $\Phi(\cdot): \mathbb{R}^N \rightarrow \mathbb{R}^M$, $M \gg N$ is applied to transform each data point to a higher-dimensional feature space, $\Phi(\mathbf{x}_p) = [\phi_1(\mathbf{x}_p) \dots \phi_M(\mathbf{x}_p)]^T$. A hyperplane (or discriminant function $g(\Phi(\mathbf{x})) = \mathbf{w}^T \Phi(\mathbf{x}) + b = 0$) is then constructed in this feature space. Assuming that the mapped features are linearly separable, the constraints become: $d_p(\mathbf{w}^T \Phi(\mathbf{x}_p) + b) \geq 1, \forall p \in [1, P]$. The problem of finding the optimal hyperplane can then be summarized as: minimize $\frac{1}{2} \mathbf{w}^T \mathbf{w}$, subject to $d_p(\mathbf{w}^T \Phi(\mathbf{x}_p) + b) \geq 1, \forall p \in [1, P]$. Following the same procedure as in the linear case, we have

$$\mathbf{w}_o = \sum_{p=1}^P \alpha_p d_p \Phi(\mathbf{x}_p) \quad (5-25)$$

$$b_o = -\frac{1}{2} \mathbf{w}_o^T (\Phi(\mathbf{x}(s)) + \Phi(\mathbf{x}(r))) \quad (5-26)$$

$$\sum_{p=1}^P \alpha_p d_p = \boldsymbol{\alpha}^T \mathbf{d} = 0 \quad (5-27)$$

where $\mathbf{x}(s)$ and $\mathbf{x}(r)$ are SVs for each class, and \mathbf{d} is a vector of the P training labels.

Substituting the equation for optimal hyperplane \mathbf{w}_o into the hyperplane equation gives,

$$\begin{aligned} g(\mathbf{x}) &= \mathbf{w}_o^T \Phi(\mathbf{x}) + b_o \\ &= \sum_{p=1}^P \alpha_p d_p \Phi^T(\mathbf{x}_p) \Phi(\mathbf{x}) + \frac{1}{2} \sum_{p=1}^P \alpha_p d_p \Phi^T(\mathbf{x}_p) (\Phi(\mathbf{x}(s)) + \Phi(\mathbf{x}(r))) \end{aligned} \quad (5-28)$$

Denote $k(\mathbf{x}, \mathbf{y}) = \Phi^T(\mathbf{x}) \Phi(\mathbf{y})$ as the inner product kernel in the high dimensional feature space.

Thus, the hyperplane equation becomes,

$$\begin{aligned} g(\mathbf{x}) &= \sum_{p=1}^P \alpha_p d_p k(\mathbf{x}_p, \mathbf{x}) + b_o \\ \text{where } b_o &= \frac{1}{2} \sum_{p=1}^P \alpha_p d_p (k(\mathbf{x}_p, \mathbf{x}(s)) + k(\mathbf{x}_p, \mathbf{x}(r))) \end{aligned} \quad (5-29)$$

As in the linear case, we first solve the dual problem, which in this case is maximizing the following:

$$Q(\boldsymbol{\alpha}) = \boldsymbol{\alpha}^T \mathbf{1} - \frac{1}{2} \boldsymbol{\alpha}^T \mathbf{D}^T \mathbf{K} \mathbf{D} \boldsymbol{\alpha} \quad \text{s.t. } \boldsymbol{\alpha}^T \mathbf{d} = 0 \quad \text{and } \alpha_p > 0 \quad (5-30)$$

where $\boldsymbol{\alpha} = [\alpha_1 \dots \alpha_p]^T$, $\mathbf{1} = [1 \dots 1]^T$, $\mathbf{D} = \text{diag}[d_1 \dots d_p]$, and $\mathbf{K} = [K_{\{p,q\}}]_{p,q=1}^P = [k(\mathbf{x}_p, \mathbf{x}_q)]_{p,q=1}^P$ is the Kernel matrix of mapped inner products. The kernel functions chosen must

satisfy the following two conditions [Mercer, 1909]:

- a) Kernel function $k(\mathbf{x}_p, \mathbf{x}) = k(\mathbf{x}, \mathbf{x}_p) = \sum_{m=1}^M \phi_m^T(\mathbf{x}_p) \phi_m(\mathbf{x})$ must be symmetrical about the center \mathbf{x}_p , and attain its maximum at $\mathbf{x} = \mathbf{x}_p$;
- b) Area under $k(\mathbf{x}_p, \mathbf{x})$ must be constant.

An example of kernel function is Gaussian Kernel: $k(\mathbf{x}, \mathbf{y}) = e^{-c|\mathbf{x}-\mathbf{y}|^2}$, where $c > 0, M = \infty$.

The dimension of the dual problem is still P , as in the linear case. That is, even though the hyperplane is constructed in the higher dimensional feature space, the estimation is carried out in the original input space. This is the essence behind the kernel trick. Furthermore, there is no need to explicitly compute \mathbf{w}_o as the decision-making is done using the discriminant function $g(\mathbf{x})$ as above in the kernel domain.

6. CHAPTER 6 – RESULTS ON SCINTILLATION SIGNAL CHARACTERIZATION

Analysis of the characteristics of ionospheric scintillation signals has been done using real scintillation data collected by CSU GPS Lab. Signal characterization is conducted in both the frequency and the time domains. This chapter provides scintillation characterization results based on real GPS data collected from Ascension Island, where IF samples are available for custom-designed SDRs. Further comparison of characteristics of simulated data with real data will be presented in Chapter 7.

6.1. Data Set for Scintillation Signal Characterization

The data analyzed in this chapter were collected on Ascension Island in March 2013 (Section 1.4). During the data collection period, severe signal attenuations and large carrier phase fluctuations resulted in frequent cycle slips and loss of lock of signals in the Septentrio ISM. Data statistics shows that the Septentrio ISM lost lock for 2.3% of the time for PRN 24, 25, 29, and 31 during the IF data collection periods with an elevation mask of 10° [Skone *et al.*, 2001; Jiao *et al.*, 2016a]. As a result, the data used in this chapter are post-processed using the FPF tracking algorithm to preserve the true behavior of the ionosphere and its impact on signal processing (see Section 1.4 for more details).

Among all the data collected, scintillation events observed on GPS PRN 24, 25, 29, and 31 are of special interest, as these satellites transmit L2C and/or L5 signals. Several segments of the data totaling 15.4 hours have been selected when scintillation was mostly intense and L2C and/or L5 signals were present for analysis with an elevation mask of 10° . Table 6-1 summarizes the durations

of the data segments used to generate the results in this chapter. Table 6-2 lists the ranges of elevation angles for the specific satellites in the data segments. Figure 6-1 shows the sky views of all the visible satellites during the IF data collection period on Ascension Island. The satellite tracks are also color-coded according to the values of the S_4 index on L1 to show the intensity of amplitude scintillation. The tracks enclosed by the black lines in the figure correspond to the satellite paths that generated the data segments used in this study listed in Table 6-2. From Table 6-2 and Figure 6-1, it can be seen that the average elevation angles for PRN 24 and PRN 25, the only visible satellites broadcasting L5 signals, are relatively low, which to some extent limits the accuracy of the corresponding results.

Table 6-1. Data segment length (hours) used in this chapter from visible satellites that broadcast L2C signals. The elevation mask is 10°

PRN \ Date	3/7/13	3/8/13	3/9/13	3/10/13	Sum
24	0	1.28	0	1.42	2.70
25	1.21	0	1.07	0.78	3.06
29	1.11	1.00	1.00	1.28	4.39
31	0.83	1.28	1.11	2.00	5.22
Sum	3.15	3.56	3.18	5.48	15.37

Table 6-2. The ranges of satellite elevation angles for the data segments used in this chapter with the elevation mask of 10°

PRN \ Date	3/7/13	3/8/13	3/9/13	3/10/13
24	/	19.8° - 27.1°	/	19.8° - 27.2°
25	23.4° - 10.0°	/	21.3° - 10.0°	10.0° - 13.0°
29	42.6° - 15.1°	38.3° - 14.2°	71.4° - 41.6°	51.2° - 17.9°
31	32.0° - 55.2°	23.7° - 58.7°	40.6° - 73.9°	23.8° - 81.1°

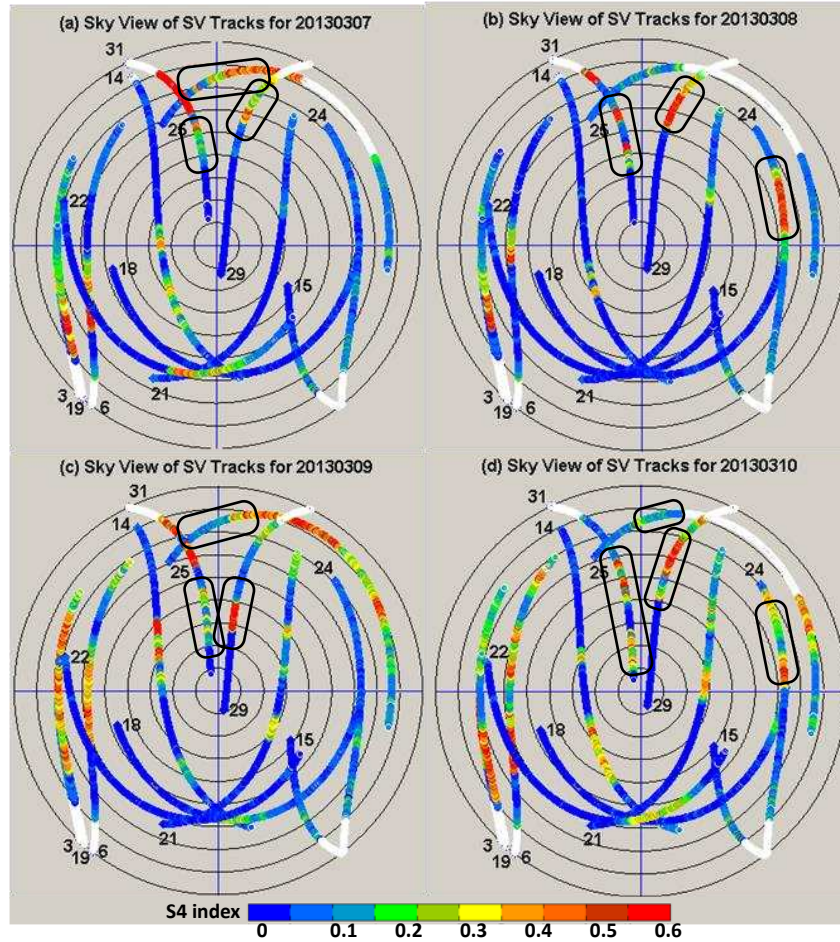


Figure 6-1. Sky view plots of all visible satellite (SV) tracks during local time 8 pm – 1 am on March 7-10 on Ascension Island. The tracks are color-coded by the values of the S_4 index on L1. White points in the plots are tracks without reliable S_4 observables below an elevation of 10° . The ends with PRN numbers represent the starting points of the tracks. The centers of the rings are elevation 90° , and the rings are equal-elevation contours with an increment of 10° . The tracks defined by the black lines are the approximate ranges of satellite elevation angles for the data segments used in this chapter listed in Table 6-1.

The results presented in this chapter are generated mainly from the signal intensity measurements of the data sets listed in Table 6-1. Figure 6-2 through Figure 6-4 show three examples of the raw and detrended signal intensity measurements in three example data sets. Note that the raw signal intensity on L5 is higher than on L1 and L2C due to the extra gain of the L5 signal at the antenna. The raw signal intensity measurements are detrended using a wavelet-based method, as it is more robust and effective than the traditional 6th order Butterworth filter [Niu *et al.*, 2012]. The trends

are shown as black lines in the top row in each plot. To better facilitate the data analysis, all the data sets are divided into 5-minute-long segments. The centers of the segments are shown as the black dots in the bottom row in each plot. The 5-minute segmentation length is selected as it is a good time interval for stationarity and for effectively capturing the major characteristics of the ionospheric irregularity contributions to the disturbances on the signal. From Figure 6-2 through Figure 6-4, it can be seen that these data sets include not only very strong amplitude scintillation but also quiet signals, which enables comparison analysis between the two conditions.

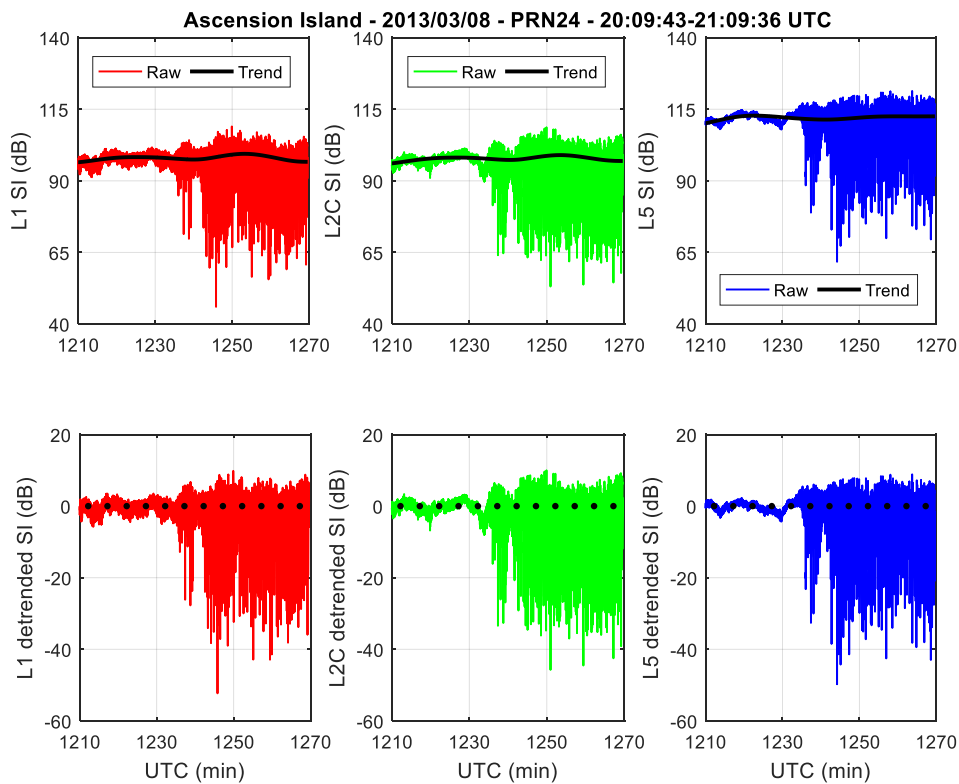


Figure 6-2. Signal intensity (SI) measurements collected from PRN 24 from 20:09:43 to 21:09:36 UTC on March 8, 2013 on Ascension Island. Subplots in the top row are raw signal intensity on different GPS frequencies with the black lines showing the trend using wavelet detrending. Bottom row subplots are detrended signal intensity. The data is divided into 5-minute segments for analysis, with the last one slightly shorter than 5 minutes. The centers of the segments are shown as the black dots in the bottom row.

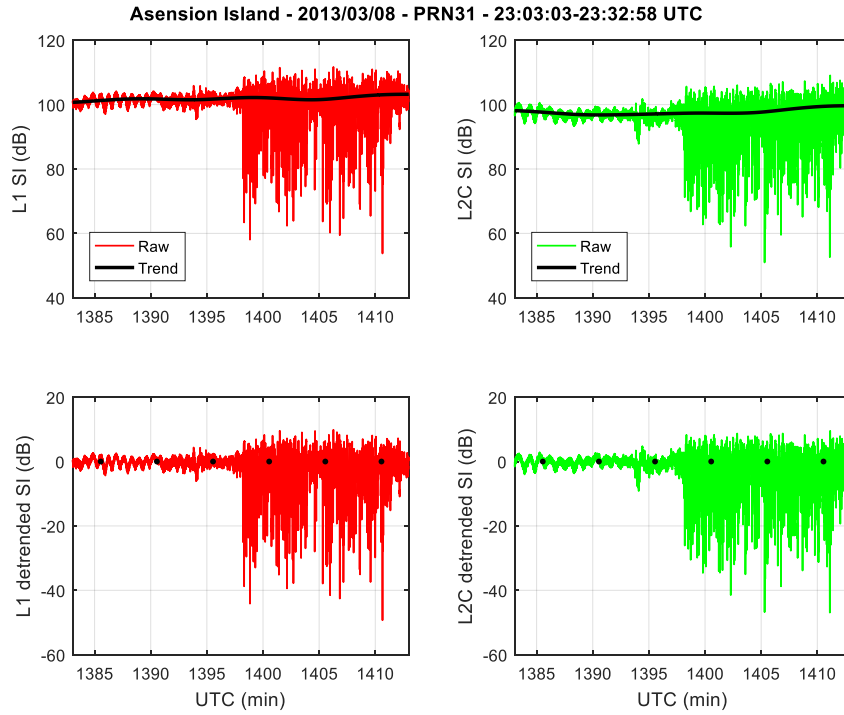


Figure 6-3. Same as Figure 6-2 but for PRN 31 from 23:03:03 to 23:32:58 UTC on March 8, 2013.

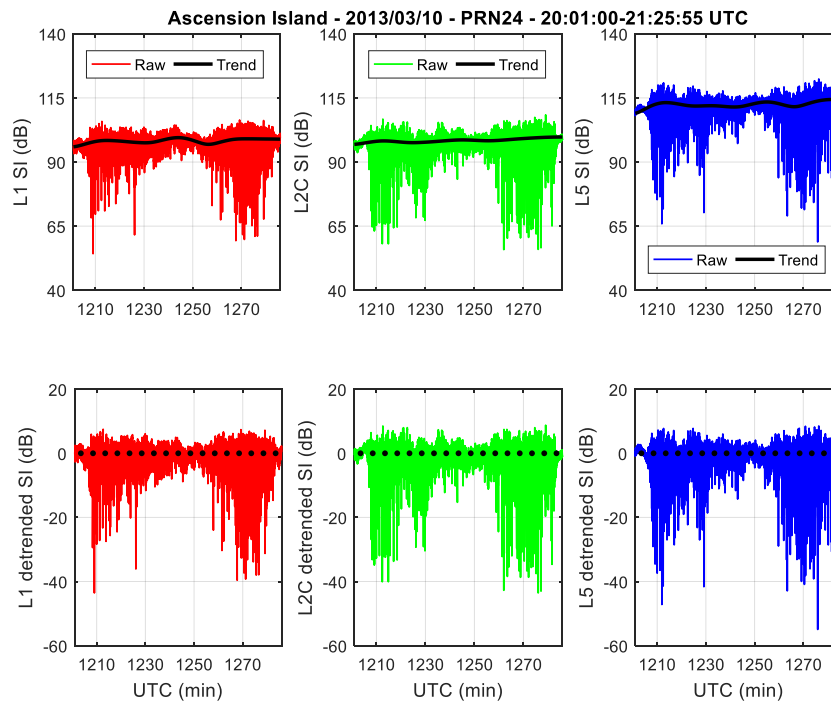


Figure 6-4. Same as Figure 6-2 but for PRN 24 from 20:01:00 to 21:55:55 UTC on March 10, 2013.

6.2. Spatial Spectrum Density Function

The spatial SDF of scintillation signals is of special interest in the study of ionosphere irregularity structures that cause scintillation [Bhattacharyya *et al.*, 1982]. According to the phase screen theory and the statistical theory of scintillation, the SDFs of scintillation signal phase and intensity follow an inverse power law form (Section 4.2)[Rino, 1979ab]. Therefore, the shape of the SDF of signal intensity reflects the values of the parameters of the phase screen, including the turbulent strength and the spectral index.

Figure 6-5 shows the spatial SDFs for the six segments in the data set collected from PRN 31 on March 8, 2013 first shown in Figure 6-3. The SDFs are computed assuming the eastward drift velocity of the ionospheric irregularity is 50 m/s. The top row for segments 1-3 corresponds to relatively quiet conditions. The bottom row for segments 4-6, on the other hand, corresponds to strong amplitude scintillation conditions (see Figure 6-3). The SDFs of the scintillation segments of the data in the bottom row in Figure 6-5 support strong-scatter phase screen predictions, particularly the enhancement at the lowest frequencies [Carrano and Rino, 2016]. A two-component power law form is also visible in the bottom row. Interestingly, the top row of Figure 6-5 shows an enhancement in the low frequency components (wavenumber between 10^{-4} and 10^{-3} m^{-1}), which corresponds to the periodicity of the intensity variation visible in the first half of Figure 6-3. The causes of this periodicity are most likely multipath or the effect of atmospheric acoustic gravity waves. In addition, Fresnel minima are also observed in segment 3, which can be used to derive some turbulence parameters including irregularity drift velocity and its height [Bhattacharyya *et al.*, 1982].

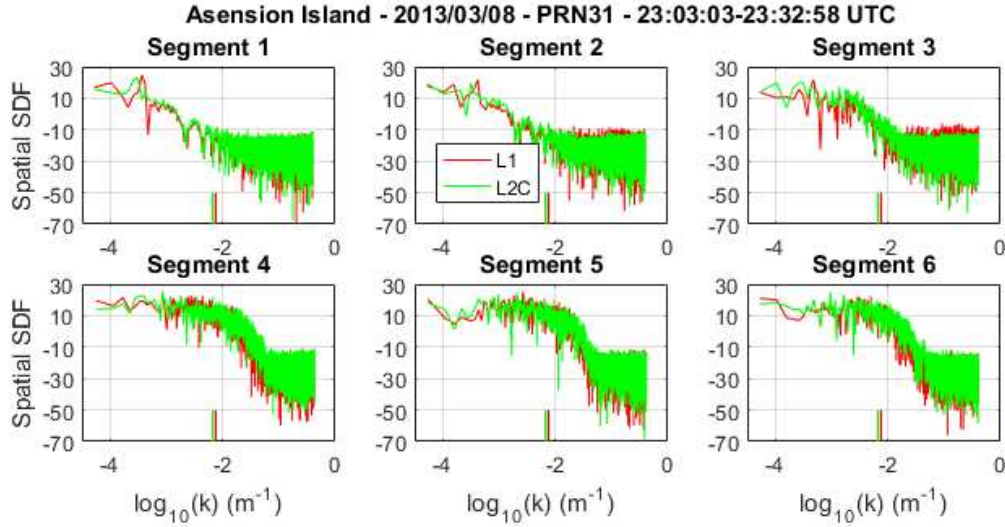


Figure 6-5. Spatial SDFs for the six segments of 5-min data from PRN 31 on March 8, 2013. The x-axes are the \log_{10} of the wavenumber. The vertical bars in the bottom center of each subplot are the Fresnel scales for L1 and L2 frequencies. The eastward drift velocity of the ionospheric irregularity is assumed to be 50 m/s.

To obtain spatial SDF from signal samples in the time domain, an effective scan velocity v_{eff} is needed [Rino, 2011]. The calculation of v_{eff} is described in Subsection 4.2.6, which requires knowledge of the nominal satellite scan velocity, the receiver velocity, the irregularity drift velocity, the anisotropy of the irregularity, and the altitude of the irregularity. The satellite scan velocity can be estimated based on known satellite orbit information. The receiver velocity is zero for a stationary receiver. The irregularity drift velocity is unknown, although it can be estimated if measurements from a closely spaced receiver array are available [Wang and Morton, 2017]. The anisotropy of the irregularity is set to 50:1 (north-south: east-west), and the height of IPP is set to 350 km in this study. In the low-latitude region, where Ascension Island is located, the irregularity drift velocity can be assumed to be purely one-dimensional in the east direction at the time the data was collected (on Ascension Island, the local time is the same as the UTC) [Basu et al., 2002].

To access the impact of the eastward drift velocity on the spatial SDF, several different eastward velocity magnitude values are used to compute the SDFs. Figure 6-6 shows the SDFs with varied eastward drift velocity for segments 2 and 5 in the data set shown in Figure 6-3 for quiet and scintillation conditions. To evaluate which drift velocity is closer to the predictions by theory, Fresnel scales for L1 and L2 frequencies are plotted as the vertical bars in the bottom center of each subplot in Figure 6-5 and Figure 6-6. The Fresnel scale is calculated using equations (4-68) and (4-69). It can be seen in Figure 6-6 that the SDFs shift left to smaller wavenumbers as the eastward drift velocity increases. For this set of data, an eastward drift velocity of around 25 m/s seems to be the most reasonable.

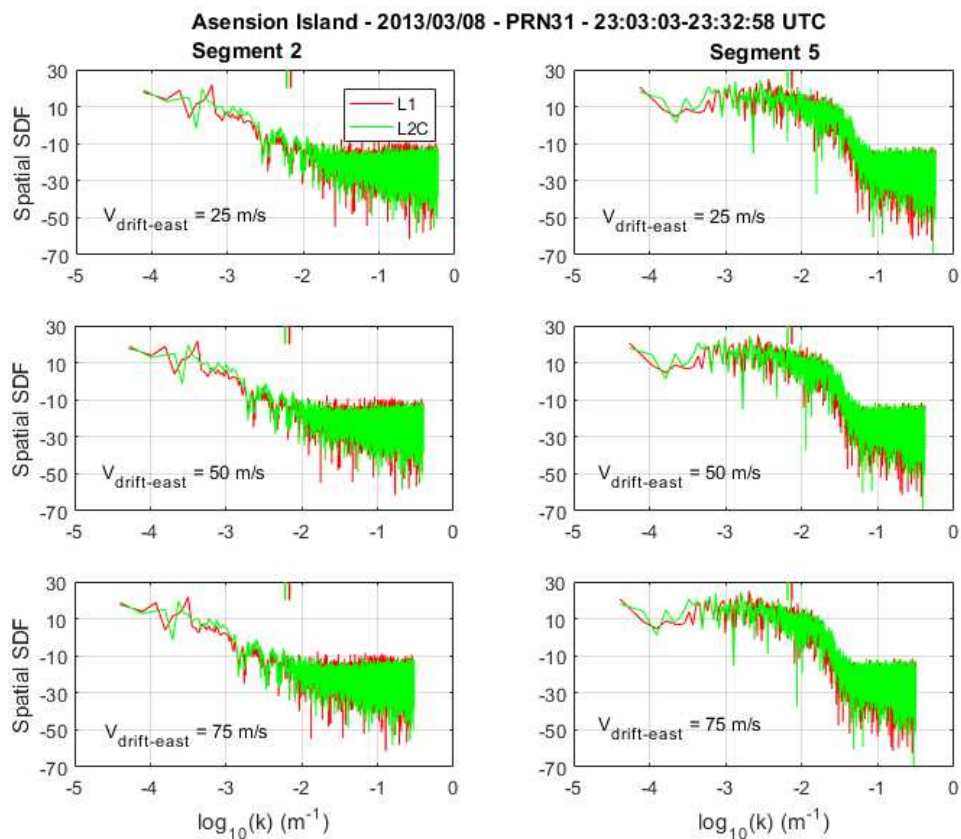


Figure 6-6. Spatial SDFs for segment 2 (quiet) and segment 5 (strong scintillation) in the data from PRN 31 on March 8, 2013. The eastward drift velocity of the ionospheric irregularity is altered to be 25 m/s, 50m/s or 75 m/s.

The other sets of data are also processed with similar resulting SDFs. For those data sets, the realistic eastward drift velocity ranges from 25 m/s to 75 m/s. Clearly, the drift velocity plays an important role in determining the SDF, and the resulting auto-correlation function (ACF) that will be discussed in the following subsection. Approaches have been developed to assess the drift velocity using GNSS measurements. Interested readers are referred to the work in [Carrano *et al.*, 2015, 2016; Wang and Morton, 2015; Wang and Morton, 2017].

6.3. Auto-correlation Function

The inverse Fourier transform of the spatial SDF is the ACF of the scintillation signal in the space, which further reveals the scale of the irregularity structure across the propagation path. Figure 6-7 shows some examples of the normalized ACFs for segments 1 and 4 in the Figure 6-3 data set corresponding to quiet and scintillation signals respectively. The circles in the plot are the $1/e$ de-correlation distances whose values are denoted in the legends.

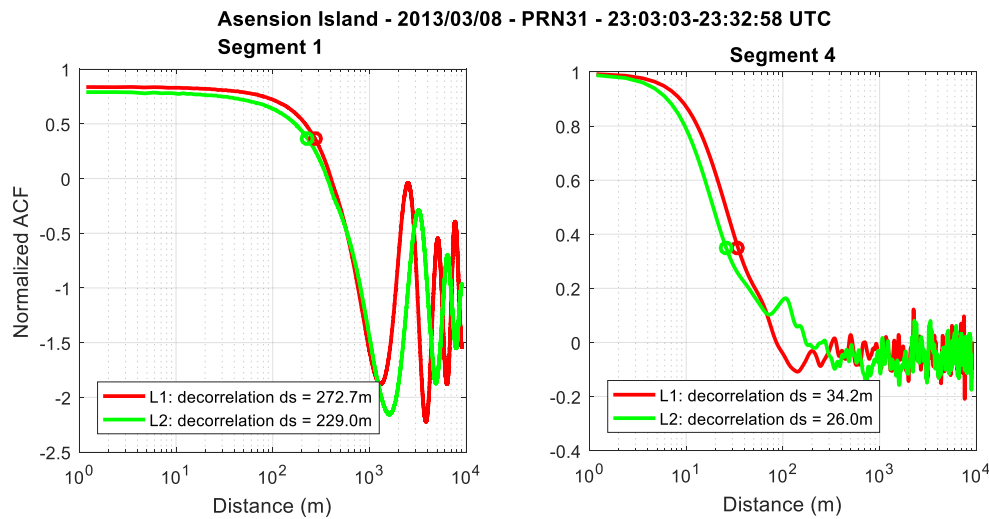


Figure 6-7. ACFs for segment 1 (quiet) and segment 4 (strong scintillation) in the data from PRN 31 on March 8, 2013. The circles and the legends in the plot denote the $1/e$ de-correlation distances.

The eastward drift velocity of the ionospheric irregularity is assumed to be 50 m/s.

To investigate the relationship between de-correlation distance and turbulence strength, Figure 6-8 through Figure 6-10 plot the S_4 index values and the $1/e$ de-correlation distances for all the frequency bands in the three example data sets. Note that a de-correlation data point is set as invalid if its value is bigger than 300 meters, which only happens under quiet conditions. These results partially confirm that in the weak scatter regime ($S_4 < 0.5$), the normalized ACF is independent of the turbulent strength reflected by the value of the S_4 index; in the strong scatter regime ($S_4 > 0.5$), the correlation length decreases with increasing turbulent strength (S_4 value) [Carrano and Rino, 2016]. It is also noteworthy that varying the eastward drift velocity of the irregularity inversely varies the resulting coherence length.

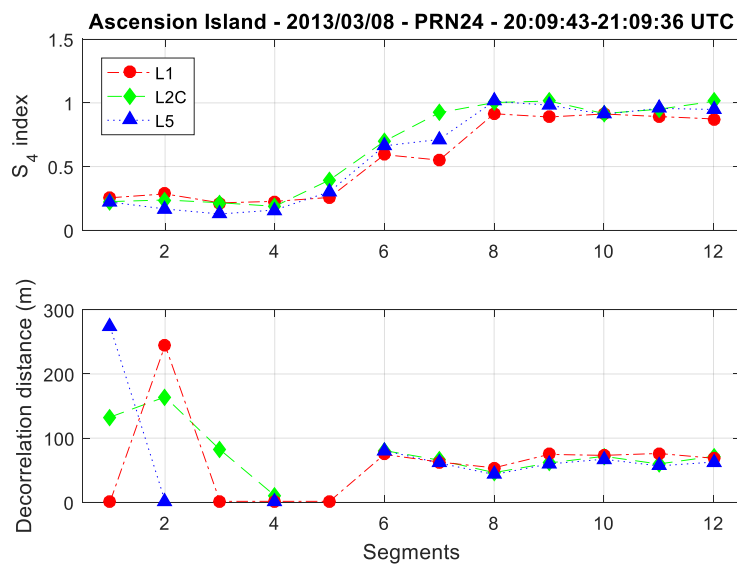


Figure 6-8. The S_4 index values and the $1/e$ de-correlation distances for all the data segments from PRN 24 on March 8, 2013. The eastward drift velocity of the irregularity is assumed to be 50 m/s. Any de-correlation value that is greater than 300 m is set as invalid.

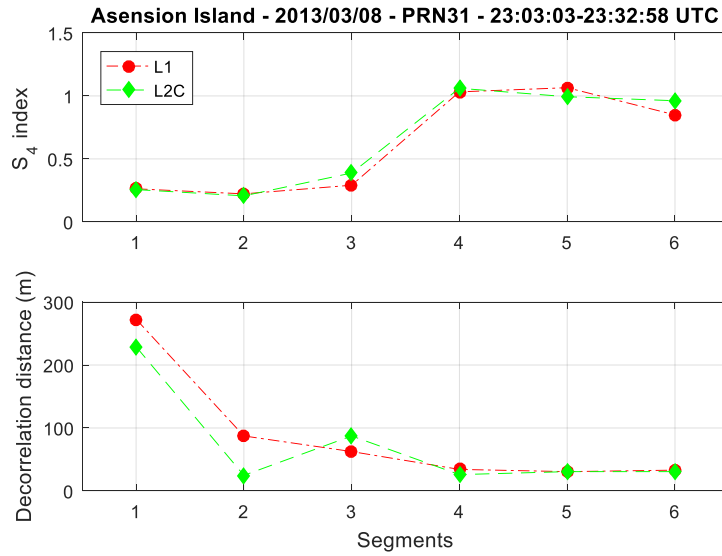


Figure 6-9. Same as Figure 6-8, but for PRN 31 on March 8, 2013.

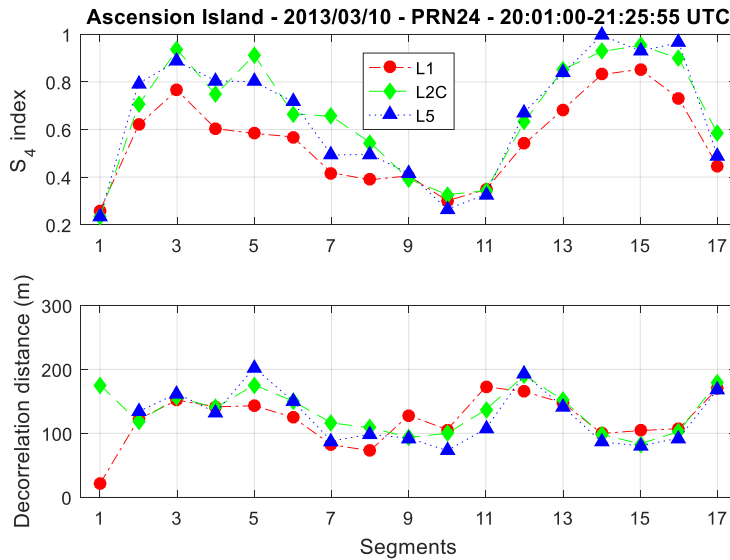


Figure 6-10. Same as Figure 6-8, but for PRN 24 on March 10, 2013.

6.4. Probability Distribution Function on Detrended Signal Intensity

A PDF in this research is acquired by differentiating the corresponding cumulative distribution function (CDF), which is the normalized histogram of the detrended signal intensity measurements, and then smoothing the result with a moving window filter. Figure 6-11 and Figure 6-12 show the

PDFs for all the data segments in Figure 6-2 and Figure 6-3 for PRN 24 and 31 on March 8, 2013. In some of the data segments in the first data set for PRN 24, such as segments 5 and 7, non-scintillation and scintillation signals are mixed causing distortions in the PDFs. Overall from the analysis of all the five data sets, for quiet signals, the detrended signal intensity is close to log-normal distributions for all three frequencies. For strong scintillation signals, different from previous study on the statistics of scintillation amplitude, the distribution of the \log_{10} of the detrended signal intensity appears to be near uniform within the range of ~ -25 to -5 dB, and exponential outside the range, although the shape varies with different scintillation levels. It can also be observed that L2C is most adversely affected by scintillation in our data with the highest probability of very deep fading below -20 dB.

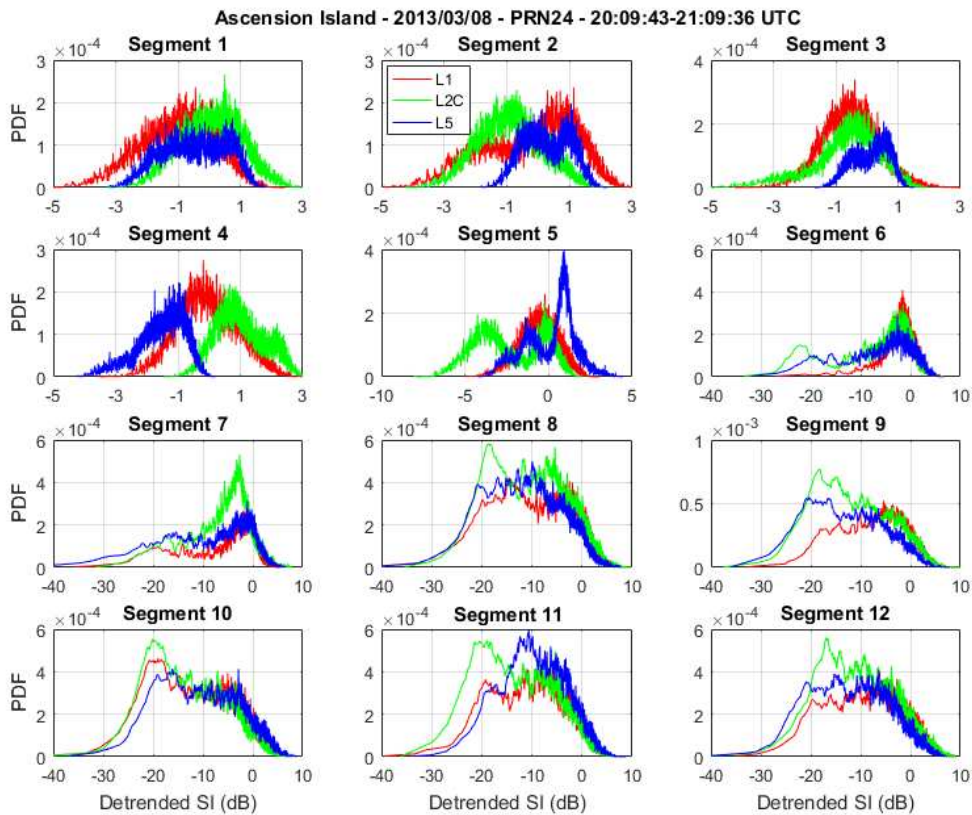


Figure 6-11. PDFs of the detrended signal intensity (SI) on L1, L2C, and L5 for all the data segments collected from PRN 24 on March 8, 2013 on Ascension Island.

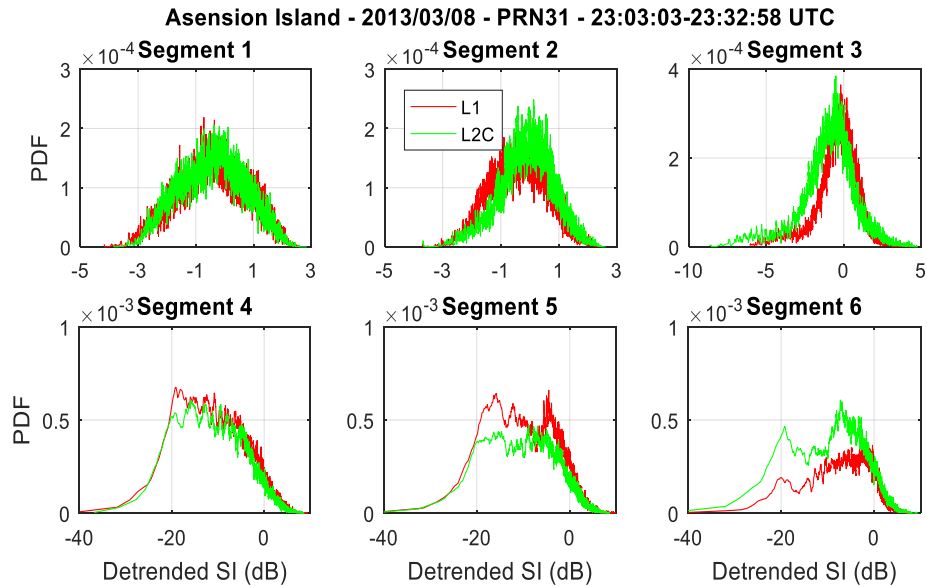


Figure 6-12. PDFs of the detrended signal intensity (SI) on L1 and L2C for all the data segments collected from PRN 31 on March 8, 2013 on Ascension Island.

6.5. Multi-band Fading Characteristics on Signal Intensity

The probability distributions of signal intensity measurements do not reflect the timing relationship of the signal fading on the three GPS bands as signals at different frequencies may fade at different times with different durations (Figure 6-13). In this research, the high-rate detrended signal intensity measurements are analyzed to infer timing-related signal fading characteristics. Different threshold values are used as references for analysis: -10 dB, -15 dB, -20 dB, and -25 dB. Table 6-3 lists the number of fades for each band corresponding to the thresholds. Based on these fading events, fading duration, time separation between fades, and fading overlap among bands will be analyzed.

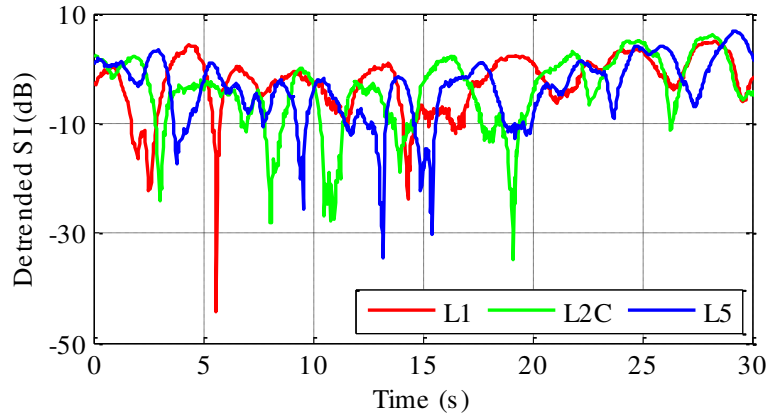


Figure 6-13. Detrended signal intensity (SI) fading example across three GPS bands on PRN 24 on March 10, 2013 on Ascension Island. During deep fading, the signals on different frequencies become less correlated both in time and in magnitude.

Table 6-3. Total number of observed deep signal intensity fades on GPS L1, L2C, and L5 under different thresholds

Fading Number	L1	L2C	L5
-10 dB	9,449	12,707	3,928
-15 dB	4,421	6,423	1,899
-20 dB	1,949	3,014	871
-25 dB	774	1,246	415

6.5.1. Fading Duration

The duration of signal fading is an important feature for receiver signal processing. It determines whether reacquisition is needed if the signal has lost lock and the accuracy of the positioning solutions if tracking is maintained. The duration of a fade is defined here as the difference between the times when the detrended signal intensity drops below a threshold and when it rises above the threshold, as illustrated in Figure 6-14. Note that we also need to take into consideration the quantization time interval. At a 50 Hz rate, the time duration is an integer multiple of 20 ms.

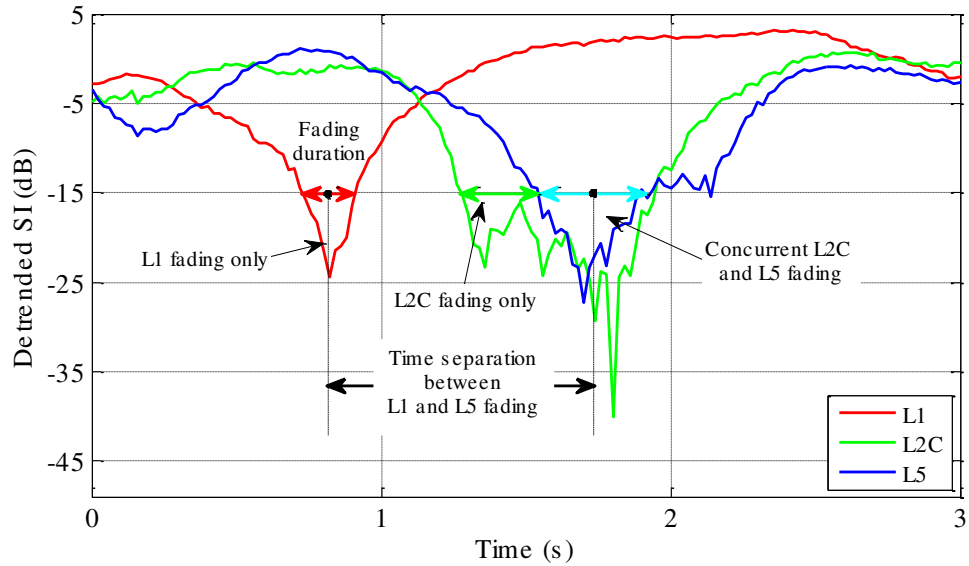


Figure 6-14. Illustration of fading duration, time separation between fades and fading overlaps on normalized signal intensity using the threshold of -15 dB.

Figure 6-15 shows the distributions of signal intensity fading duration on L1, L2C, and L5 under the four thresholds with mean durations labeled in the legends. Note that the distributions are discrete, while the connecting lines are depicted to show the trends. The results indicate that the predominant fading durations are very short, typically under 100 ms, although much longer durations of more than 300 ms do occur occasionally. On average, fades on L1 have the shortest duration, and those on L5 have the longest. This is consistent with the theory that lower frequency signals are more susceptible to scintillation.

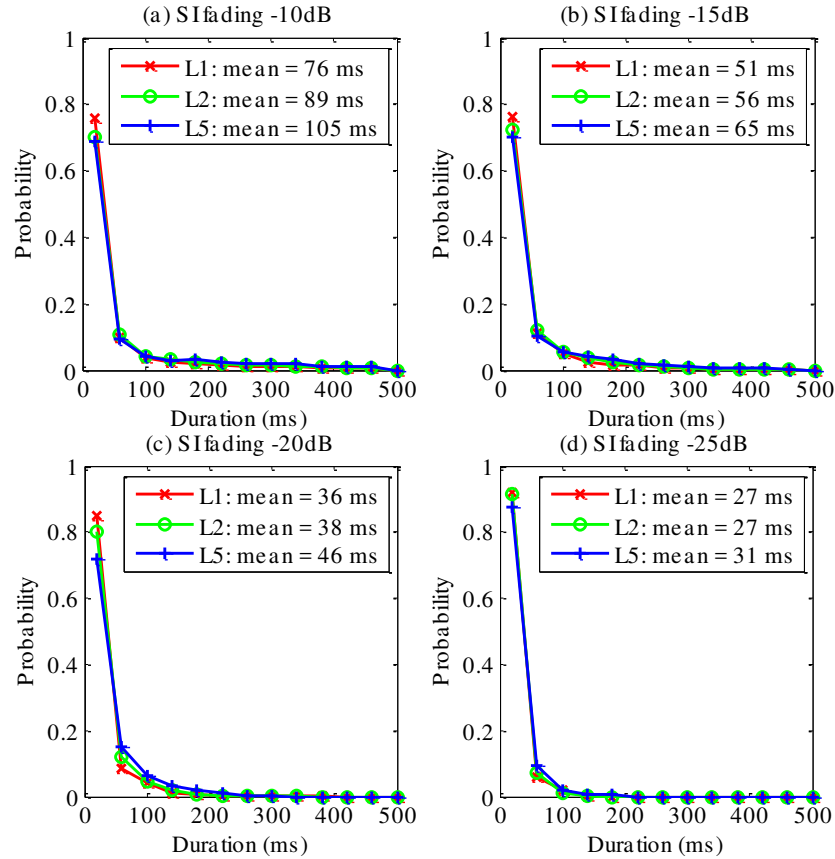


Figure 6-15. Distributions of GPS L1, L2C, and L5 fading duration on detrended signal intensity (SI) under the thresholds of (a) -10 dB, (b) -15 dB, (c) -20 dB, and (d) -25 dB. Mean durations are labeled in the legends.

6.5.2. Fading Time Separation

The time separation between deep fades is another important feature studied by previous researchers [Seo *et al.*, 2009, 2011]. It has an impact on signal reacquisition as well as the carrier smoothing process of code measurements for high accuracy applications. The time separation of fades on different bands also determines whether and how the diversity of signal frequencies can be utilized to minimize the effects of scintillation.

The fading time separation is defined as the time difference between the mid-points of two consecutive fades (Figure 6-14). The two fades can be on the same band, but can also be on two different bands.

Figure 6-16 and Figure 6-17 show the distributions of single-band and multi-band time separations for detrended signal intensity fading across the GPS bands for the four thresholds. The mean separations in the legends are averages of all separations less than 1 minute, as separations beyond that will not have significant impact on practical applications. Figure 6-16 shows that in single-band fading cases, the average time separation between L1 fades are similar to that between L2C fades, while fades on L5 are slightly more separated in general. In multi-band cases (Figure 6-17), the time separation of fades between L1 and L2C is similar to the separation of fades between L2C and L5 (excluding subplot d). However, fades on L1 are farther separated from those on L5, which is reasonable as their central frequencies are farther apart.

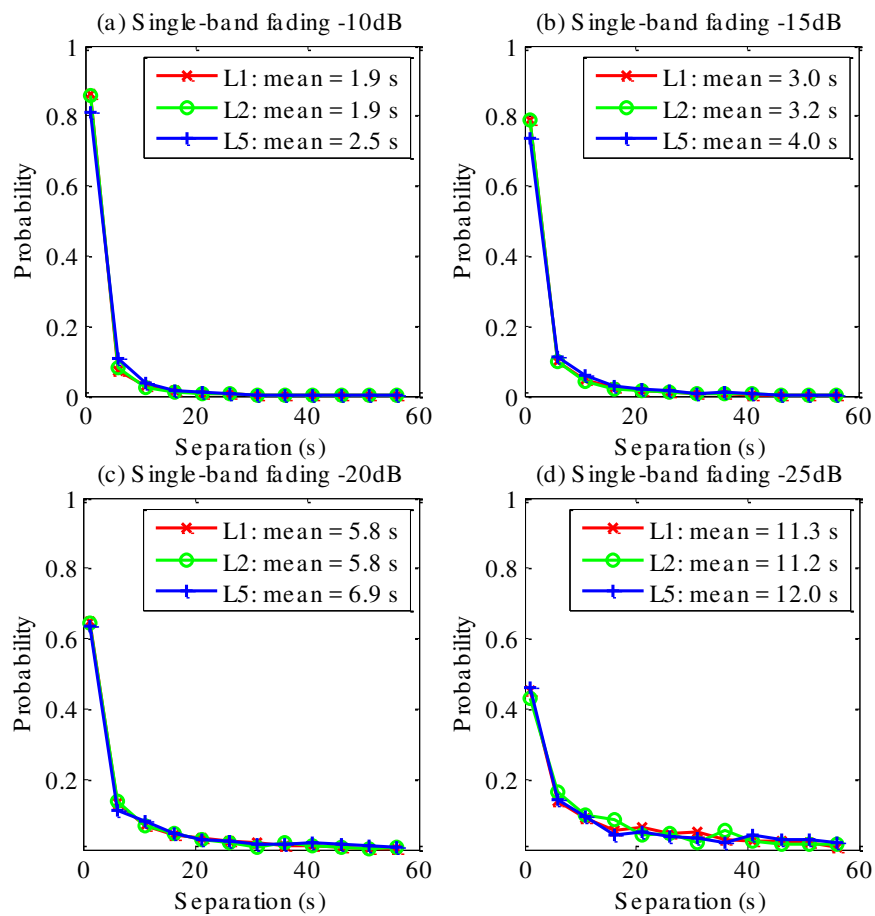


Figure 6-16. Distributions of single-band fading time separation for GPS L1, L2C, and L5 under the thresholds of (a) -10 dB, (b) -15 dB, (c) -20 dB, and (d) -25 dB. Mean time separations are labeled in the legends. The mean separations are averaged among separations under 60 seconds.

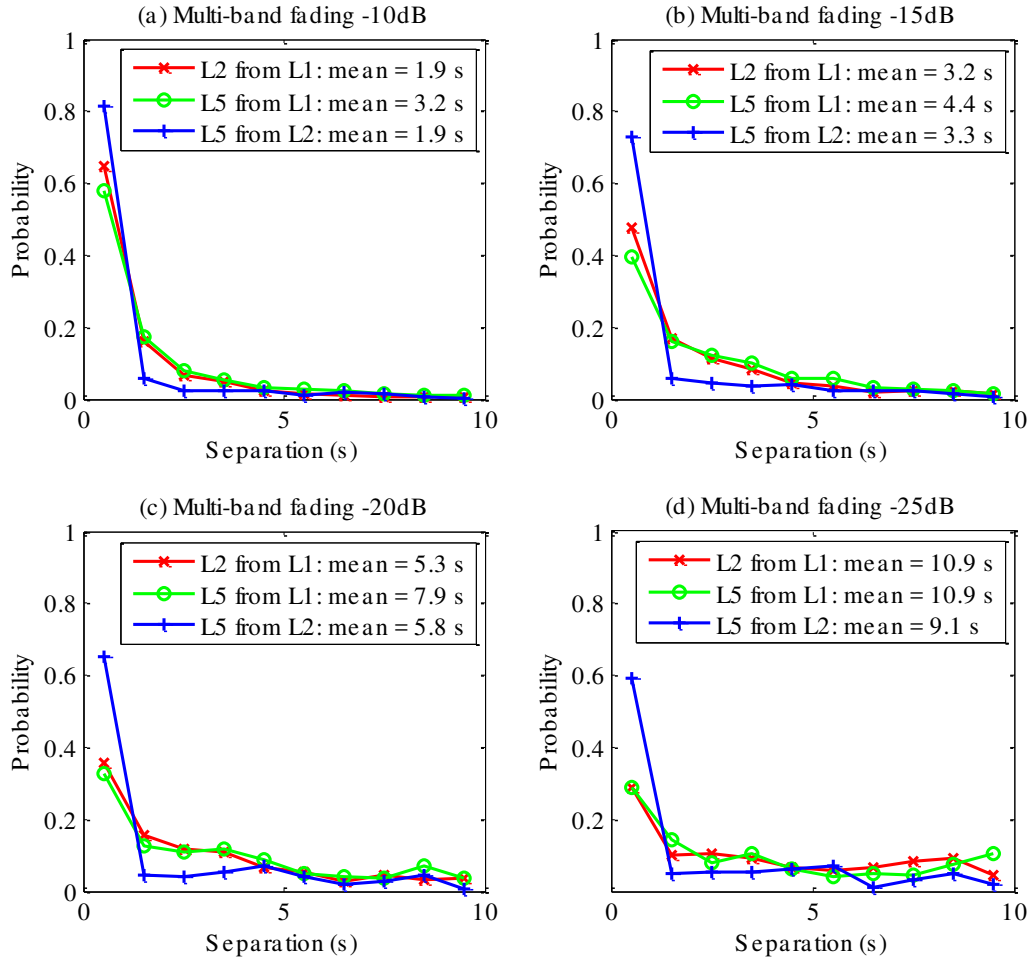


Figure 6-17. Distributions of multi-band fading time separation for L2C from L1, L5 from L1, and L5 from L2C under the thresholds of (a) -10 dB, (b) -15 dB, (c) -20 dB, and (d) -25 dB. Mean time separations are labeled in the legends. The mean separations are averaged among separations under 60 seconds.

6.5.3. Fading Characteristics vs. Scintillation Level

In order to establish a quantitative relation between amplitude scintillation and signal intensity fading levels, we investigated the mean fading number and the mean fading duration dependency on the values of S_4 index shown in Figure 6-18. The fading number in the left panel is obtained by counting the number of fades having their center times within an S_4 calculation interval. As the length of the S_4 index calculation interval is fixed, the number of fades computed is also inversely proportional to the average time separation between fades. The mean fading duration shown in the

right panel is then obtained by averaging the duration of these fades. Note that the S_4 values in the plot are calculated for individual frequency bands.

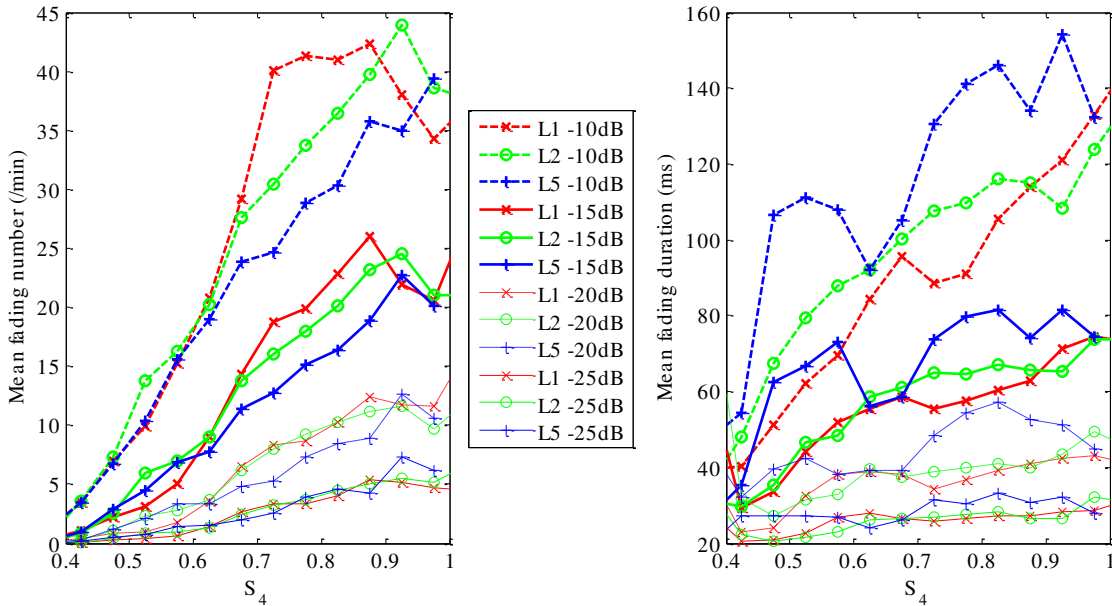


Figure 6-18. Mean fading numbers and fading durations as a function of S_4 index values on the three GPS bands under the thresholds of -10 dB, -15 dB, -20 dB, and -25 dB. The fading number in (a) is the number of fades observed with their mid-points within an S_4 calculation interval (60 s). It is reciprocally related to the mean time separation. The average duration of these fades is the mean fading duration shown in subplot (b).

The left panel in Figure 6-18 shows that the numbers of fades increases when amplitude scintillation becomes stronger (S_4 index becomes larger). The right panel shows that the mean duration of fades also increases as scintillation gets stronger, but not as dramatically, especially for deeper fading cases. The unevenness of trends when $S_4 > 0.9$ is due to a small number of cases in which S_4 is beyond 0.9. Also, the roughness for L5 statistics is caused by a much smaller number of samples for L5 fading (Table 6-3). Consistent with the results in Figure 6-15 and Figure 6-16, L5 tends to have a smaller number of fades, yet are of longer duration than those on L1 and L2C at a given S_4 level.

6.5.4. *Fading Overlap*

Signal fading that overlaps in time between different frequency bands is another important parameter, as sufficient time separations enable us to take advantage of frequency diversity during deep fading to apply inter-frequency aiding. As illustrated in Figure 6-14, we categorize fades on different bands as either stand-alone or concurrent. For example, the fades in the figure start with stand-alone L1 fading at 0.8 s, then stand-alone L2C fading at around 1.2 s, followed by concurrent L2C and L5 fading after 1.5 s.

In this study, time duration is used to compute fading overlap percentages. Table 6-4 and Table 6-5 list the percentage of each type of occurrence among all possible types of fades. Table 6-4 shows that for signals from satellites transmitting only L1 and L2C, over 85% are stand-alone fades. For signals transmitted from PRN 24 and 25 (with L5), the majority of fades are also observed on only one band. However, L2C and L5 are more likely to fade concurrently with a chance of around 40% under the threshold of -10 dB. It is also noteworthy that concurrent deep fading on all three bands is very unlikely, especially for deep fading under the thresholds of -20 dB and -25 dB (< 1%). These results again indicate that it is possible to utilize tracking results of other bands to assist the tracking of the deep fading band during scintillation.

Table 6-4. The percentage of detrended signal intensity fading overlaps on GPS L1 and L2C observed on PRN 29 and PRN 31 on March 7-10, 2013 on Ascension Island

Fading band	Threshold	L1 only	L2C only	Concurrent L1 and L2C
L1	-10 dB	85.8%	/	14.2%
	-15 dB	95.1%	/	4.9%
	-20 dB	98.7%	/	1.3%
	-25 dB	99.7%	/	0.3%
L2C	-10 dB	/	91.1%	8.9%
	-15 dB	/	96.9%	3.1%
	-20 dB	/	99.1%	0.9%
	-25 dB	/	99.8%	0.2%

Table 6-5. The percentage of detrended signal intensity fading overlaps on GPS L1, L2C, and L5 observed on PRN 24 and PRN 25 on March 7-10, 2013 on Ascension Island

Fading band	Threshold	L1 only	L2C only	L5 only	Concurrent L1, L2C	Concurrent L1, L5	Concurrent L2C, L5	Concurrent L1, L2C, L5
L1	-10 dB	78.4%	/	/	9.3%	3.8%	/	8.6%
	-15 dB	87.0%	/	/	4.5%	6.5%	/	2.0%
	-20 dB	96.3%	/	/	1.9%	1.1%	/	0.7%
	-25 dB	96.9%	/	/	1.3%	1.7%	/	0.2%
L2C	-10 dB	/	48.0%	/	6.4%	/	39.6%	6.0%
	-15 dB	/	70.4%	/	3.1%	/	25.1%	1.4%
	-20 dB	/	84.3%	/	1.1%	/	14.2%	0.4%
	-25 dB	/	92.6%	/	0.7%	/	6.6%	0.1%
L5	-10 dB	/	/	46.9%	/	2.9%	43.6%	6.6%
	-15 dB	/	/	65.0%	/	5.0%	28.5%	1.6%
	-20 dB	/	/	81.5%	/	0.8%	17.3%	0.5%
	-25 dB	/	/	91.7%	/	1.0%	7.2%	0.1%

6.6. Concluding Remarks on Scintillation Signal Characterization

This chapter presented results on scintillation signal characterization using real GPS scintillation data collected on Ascension Island. The high quality IF data processed using the custom-designed SDR algorithm enable the analysis of amplitude scintillation spectra and the characterization of deep fades observed on all three GPS bands. Below is a summary of the findings in this chapter.

The SDFs and ACFs of the quiet and scintillation signals partially confirm the prediction of phase screen theory and statistical theory on saturated scintillation signals. When comparing the characteristics revealed by real data to theoretical predictions, the selection of the value of the drift velocity is important for deducing the scale of the irregularity structures. Analysis of the statistics of the signal intensity measurements during strong scintillation shows that the CDFs and PDFs of the real data depart from previous statistical models on scintillation amplitudes. The PDFs of the detrended signal intensity in dB for strong amplitude scintillation are close to uniform within a certain range and exponentially decreasing to approaching zero outside the range.

This chapter also discussed the characteristics of signal intensity fading during scintillation on all L1, L2C, and L5 bands. Fades on the last two bands were seldom mentioned in previous literature as they are new signals and scintillation observations are relatively rare on these signals. In this dissertation research, fading duration, fading time separation and fading overlap are mainly addressed in characterizing fades observed in detrended signal intensity measurements. The quantitative statistics in fading duration and separation will help with the study of signal reacquisition and receiver development. Moreover, the fading overlap results confirm that deep fades usually occur on one band at a time, which further supports the exploitation of multi-frequency signals during strong scintillation.

In addition to the data from Ascension Island, the author also studied the fading characteristics of real scintillation signals collected from Singapore and Hong Kong. The extra results are presented in Appendix A.

7. CHAPTER 7 – RESULTS ON SCINTILLATION SIGNAL SIMULATION

This chapter presents results for scintillation signal simulation for stationary and dynamic receiver platforms. For scintillation simulation on stationary platforms, the traditional phase-screen wave propagation method is mainly used. The effectiveness of the simulator is demonstrated by comparing the characteristics of the real and the simulated scintillation signals. The effects of the receiver processing on signal characteristics is also revealed.

For scintillation simulation on dynamic receiver platforms, the time-domain data surrogate method is used. To assess and compare worst case and average signal scintillation effects for different platforms, various dynamic receiver platform trajectories are simulated to reflect receiver velocities along and across the geomagnetic field directions, together with the effect of the drift velocity of the ionospheric irregularities.

The simulators presented in this dissertation will provide viable tools for simulating GNSS scintillation signals on different receiver platforms, and the results can aid the design of robust GNSS receiver processing algorithms during strong ionospheric scintillation in the equatorial region.

7.1. Scintillation Simulation Scheme

The flow chart for the GPS scintillation signal simulation for both stationary and dynamic platforms is shown in Figure 7-1. The user inputs specify the stationary or starting receiver location (latitude, longitude, height), the receiver velocity (east, north, up), the satellite PRN, the

scintillation level (S_4 value), and other data parameters (e.g. UTC, carrier frequency, data duration etc.). The simulator then searches for a segment of real GPS scintillation data in a data bank that was collected by stationary receivers and best matches the specification. The segment of the real scintillation data serves as the initializer of the simulation process, from which the ionospheric structure is abstracted into a two-component power-law phase screen (Chapter 4). Also, using the initializer and the user input, the signal propagation geometry can be established (Chapters 3). A plane wave is then propagated through a realization of the phase screen, following the specified geometry, yielding a scintillation wave field at the receiver. The simulated scintillation amplitude and phase are then modulated onto nominal GPS IF samples to generate GPS scintillation signals for receiver processing (Chapter 2).

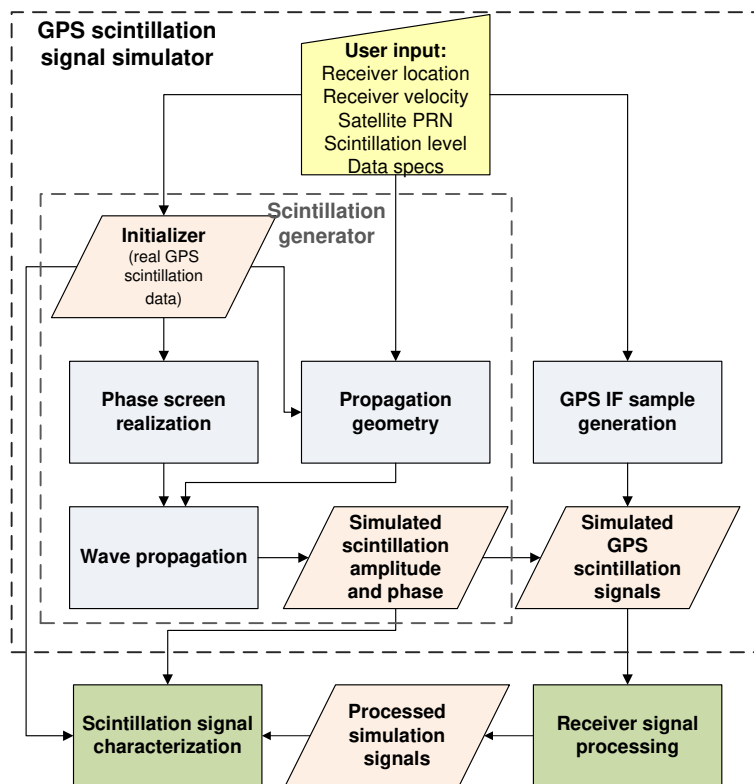


Figure 7-1. Flow chart of the static GPS scintillation signal simulation using phase screen theories, and its relationship with signal post-processing. The GPS scintillation signal simulator consists of user input, scintillation generator, and GPS IF sample generator. The output of the simulator can be used to test receiver signal processing algorithms and to characterize signal statistics.

7.2. Scintillation Simulation Initialization Data

The example initialization data used in this dissertation for both stationary and dynamic platform simulation was collected from Hong Kong using a Septentrio PolaRxS ISM receiver (Section 1.4). Figure 7-2 shows a segment of one-hour scintillation data from Hong Kong on October 5, 2013 observed on PRN 24. The lines represent detrended signal intensity measurements on the three GPS bands. It can be seen that scintillation on the signals is very strong with frequent deep fading of more than 20 dB from the nominal values, lasting for almost 40 minutes. The data is divided into small segments of five minutes each in length. The center of each segment is labeled with a star marker at the bottom in Figure 7-2. Segment 6 is selected in this example to demonstrate the simulation process. The reason for this selection is that Segment 6 contains very strong scintillation with good stationarity, as the signal fluctuations in this segment appear relatively consistent.

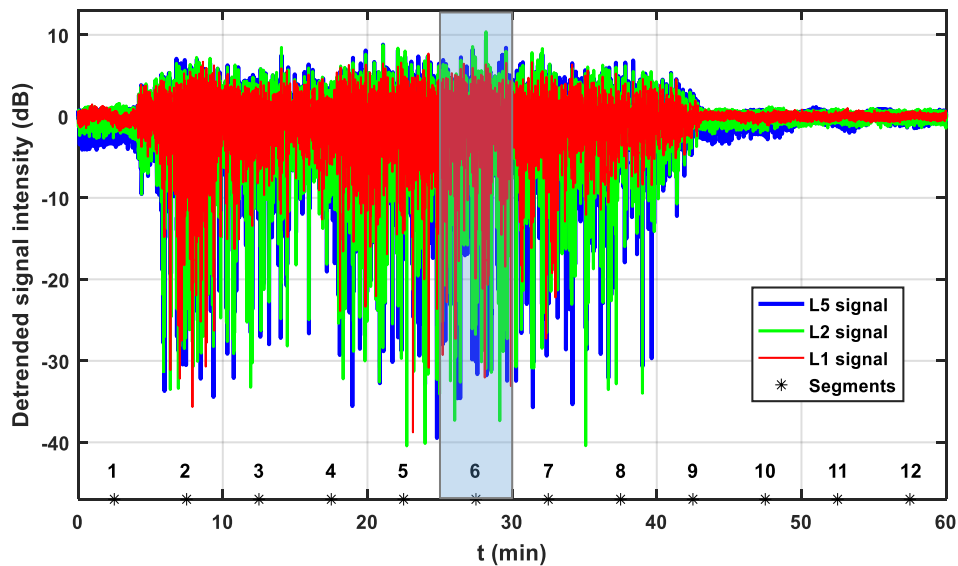


Figure 7-2. Detrended signal intensity measurements on GPS L1, L2, L5 on PRN 24 collected in Hong Kong from 12:00:00 to 12:59:59 UTC on October 5, 2013. The stars mark the centers of each 5-minute segment of data. The 6th segment is picked as the simulator initializer.

7.3. Scintillation Simulation for Stationary Receivers Using Wave Propagation Method

This section mainly discusses how the parameters are extracted from the initializer and used to generate simulation scintillation signals on a stationary platform using the phase-screen wave propagation method. To demonstrate the effectiveness of the simulator, the simulated scintillation signals are compared with the initialization data to validate their statistical similarities. Additionally, the simulator generated data are used as input to custom-designed SDR signal processing algorithms to assess the impact of receiver signal processing on scintillation signal structures, which is achieved by comparing characteristics of the SDR processed simulated data with the initializer.

7.3.1. Parameter Extraction and Data Interpretation

This subsection discusses the interpretation of the initialization data in order to extract parameter values for scintillation signal simulation. There are mainly two types of parameters extracted from the initialization data: propagation geometry parameters for forward wave propagation, and spectral parameters for structure realization. This subsection will provide an example of how these parameters are obtained from the initialization data.

7.3.1.1. Propagation Geometry

The phase-screen wave propagation geometry is illustrated in Figure 7-3 and calculated using the satellite-broadcasted ephemeris and the IGRF-11 model (Sections 3.2 and 3.3). With the ephemeris and the assumption that the height of IPP is 350 km, propagation geometry parameters including signal propagation range, propagation angles (θ and φ), and satellite scan velocity at IPP can be obtained. With the knowledge of the geomagnetic field at IPP, we can also calculate the anisotropy

factors (A , B , and C) assuming the principal and secondary elongation factors $a = 50$ and $b = 1$ [Rino, 2011], and the effective velocity (v_{eff}) which was discussed in Subsection 4.2.6.

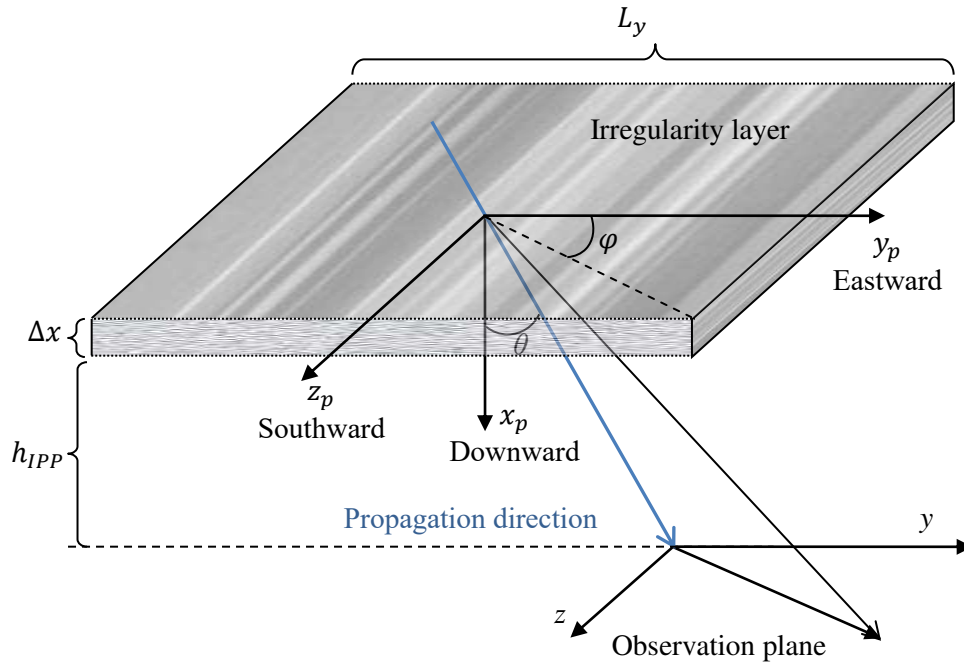


Figure 7-3. Scintillation signal propagation geometry in the reference coordinate system for oblique propagation in the single layer phase screen simulation. The coordinate system was introduced in Figure 4-1 with the origin at the IPP. The irregularity layer is a slab of Δx thickness above the IPP and perpendicular to the x -direction. The irregularity is assumed to be invariant along the z_p -direction.

Figure 7-4 shows several important time-varying geometry parameters of the initialization data (segment 6 of the Hong Kong data), represented in between the dashed vertical lines. The geometry parameters of the entire one-hour real data of Figure 7-2 are plotted to provide a broader picture. The geometry parameters shown in this figure are the satellite range between the satellite and the receiver, the IPP range between the IPP and the receiver, the propagation angles θ and φ , and the signal effective scan velocity v_{eff} .

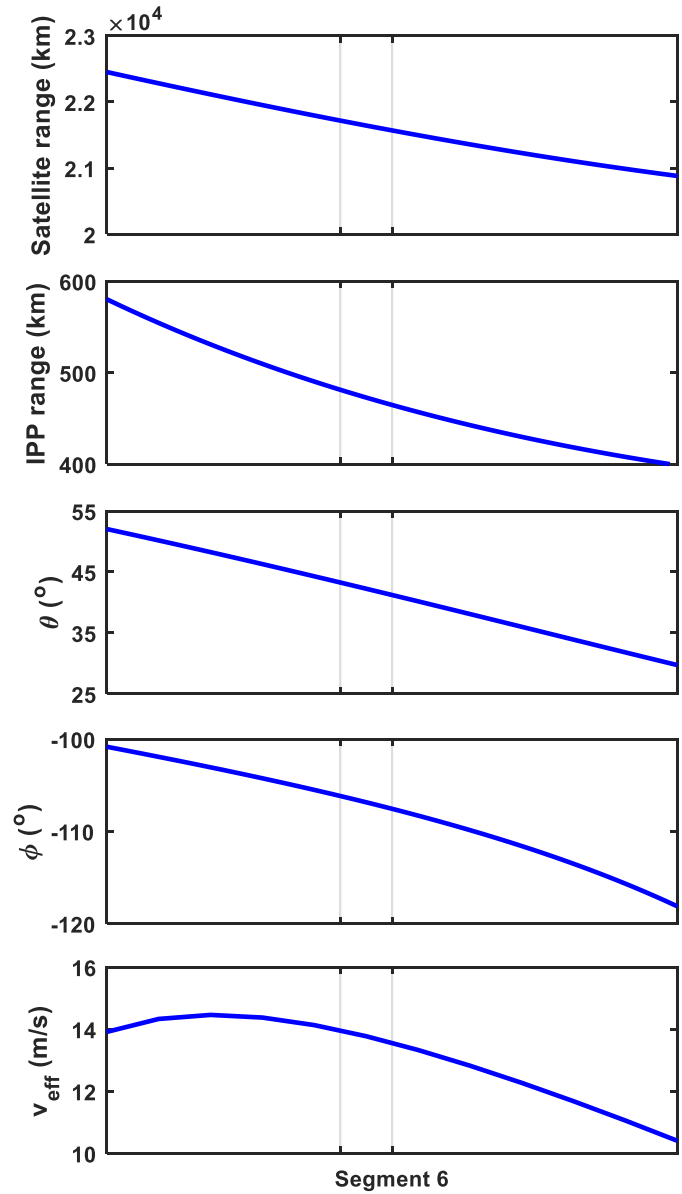


Figure 7-4. Propagation geometry of the one-hour Hong Kong data in Figure 7-2. The geometry for the selected initialization data (Segment 6) is shown between the vertical lines. The geometry parameters included in this figure are satellite range from the satellite to the receiver, IPP range from IPP to the receiver, propagation angles θ and ϕ , and effective velocity v_{eff} .

Using these values, the simulated signal is propagated through the phase screen. In this study, assuming the ionospheric irregularities are highly elongated along the north-south direction, we implement a two-dimensional single layer phase screen simulation with a two-component power-law structure realization. With a single layer phase screen approximation, the equations (4-36)

through (4-38) are only implemented once. The irregularity layer is set to be above the IPP with thickness $\Delta x = 50$ km. Below the irregularity layer, free-space propagation is applied until the signal reaches the observation plane. In the y_p -direction (east-west direction), $2^{13} - 1$ samples in the diffraction calculation with separation Δy_p approximately 5.0 meters extend from $y_p = -20.3$ km to $y_p = +20.3$ km ($L_y = 40.6$ km). This range in the y_p -direction is determined by the actual scan range in the east-west direction of the satellite in the initialization data. Additionally, in the spatial frequency domain, the wave number grid can be obtained using equation (4-40):

$$k_{y_p} = \left[-\frac{M}{2}, -\frac{M}{2} + 1, \dots, -1, 0, 1, \dots, \frac{M}{2} - 1 \right] \Delta k_{y_p}, \text{ where } M = 2^{13} \text{ and } \Delta k_{y_p} = \frac{2\pi}{M\Delta y_p}.$$

7.3.1.2. Spectral Parameters

The structure realization is directly obtained from the SDF of the initialization data. Figure 7-5 shows the SDFs of the detrended signal intensity measurements obtained from the initialization data for the three GPS bands. The figure shows that the SDF of the L1 signal is slightly lower than that of L2 and L5 signals. This indicates that L1 signal has lower turbulent strength (equation (4-54)). Otherwise, the three SDFs have very similar shapes and slope rates. As a result, the values of the spectral parameters on L1 are obtained first and they are then scaled to L2 and L5 frequencies (listed in Table 7-1). The technique used to obtain the parameters is the Iterative Parameter Estimation (IPE) technique developed in [Carrano *et al.*, 2012], which is applied to the wavenumber range in $10^{-3} < q < 10^{-1.5}$ (m^{-1}). It should be noted that the most commonly used method to obtain spectral parameters is the linear least squares algorithm [Deshpande *et al.*, 2014; Ghafoori and Skone, 2015]. Here we adopt the recent-developed IPE technique as it has been demonstrated to be more suitable for two-component power law form [Carrano *et al.*, 2012]. It is also noteworthy that in Figure 7-5, the L2 and L5 (but not L1) spectra show a few high

frequency interference structure for $q > 10^{-1}$. These interferences do not affect this study as they are beyond the wavenumber range under analysis and are not present on L1 frequency (also see Figure 7-8).

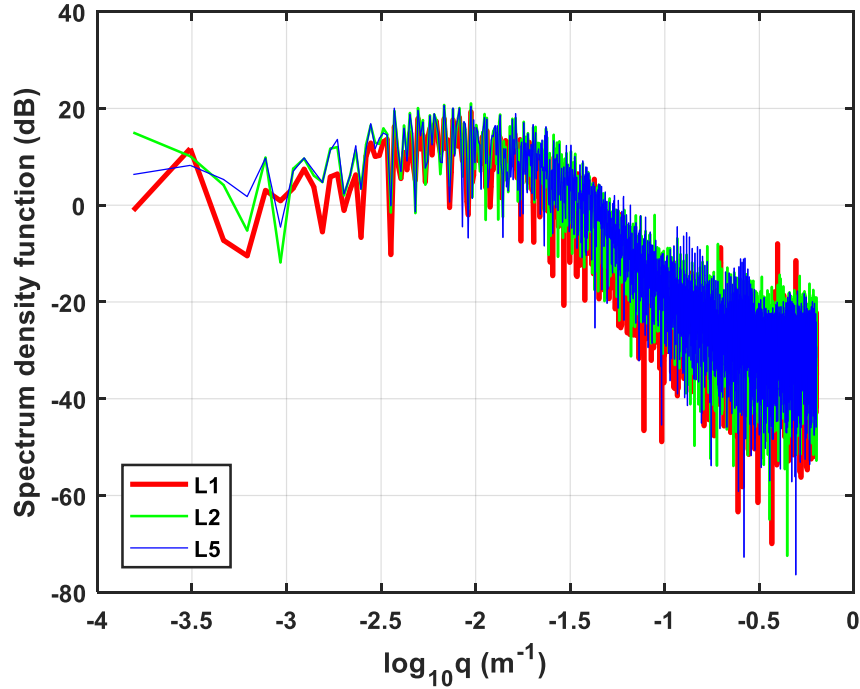


Figure 7-5. Spectrum density functions of the L1, L2, and L5 detrended signal intensity measurements in the initialization data from Hong Kong. In this study, wavenumber $q = |k_{yp}|$.

Table 7-1. Values of the spectral parameters obtained using the IPE technique for the two-component power-law structure model for scintillation signal simulation using the traditional wave propagation method

Spectral parameters \ Frequency band	L1	L2	L5
C_p	8.00×10^{-8}	1.32×10^{-7}	1.43×10^{-7}
p_1	2.00		
p_2	4.00		
q_0	6.28×10^{-3}		

7.3.1.3. Construction and Receiver Processing of Simulated GPS Scintillation Data

The procedures discussed above generate the wave field at the observation plane. More specifically, the signal intensity (I) and phase (φ) can be directly obtained from the complex field at the observation plane:

$$I = |\psi_{\mathbf{k}}|^2 = \psi_{\mathbf{k}}\psi_{\mathbf{k}}^* \quad (7-1)$$

$$\varphi = \text{unwrap}\{\text{atan2}[\text{imag}(\psi_{\mathbf{k}}), \text{real}(\psi_{\mathbf{k}})]\} \quad (7-2)$$

where the phase unwrapping procedure in (7-2) is necessary to correct discontinuity in phase measurements. The scintillation signal intensity and phase obtained from (7-1) and (7-2) do not include satellite-receiver range or Doppler frequency caused by the relative motion between the receiver and the satellite. To further construct the realistic GPS samples at the IF typically available at the output of a GNSS receiver front end, the wave field is modulated with appropriate ranging code, satellite-receiver range, and Doppler frequency. The ranging codes are generated according to the GPS ICDs (Chapter 2), and the satellite-receiver range and Doppler frequency are calculated based on the satellite orbit from the ephemeris and the receiver position (Section 3.3). More specifically, the ranging codes used here for the three GPS frequencies are L1 C/A, L2C, and L5Q, respectively. Also, the IF for these signals are set to 5 MHz, 5 MHz, and 20 MHz, respectively.

Since the initialization data is generated by the Septentrio ISM receiver, a fair comparison should be made by applying similar receiver signal processing algorithms to the simulated GPS data. In this study, conventional SDR algorithms similar to the ISM processing are used to track the simulated GPS signals. The algorithms use 10 ms integration time for the correlators and 0.3 chips for correlator spacing. The code tracking is accomplished using an early-minus-late envelope discriminator, followed by a 2nd order un-aided delay-lock-loop (DLL) with a 0.25 Hz bandwidth.

The carrier tracking is done through an arctangent Costas discriminator and a 3rd order phase-lock-loop (PLL) with a 10 Hz bandwidth [Kaplan and Hegarty, 2005]. Details in the implementation of the SDR can be found in [Xu and Morton, 2015]. In consistency with the ISM receiver, the output rates are 100 Hz for both signal intensity and phase measurements, and L1 C/A, L2 CL, and L5Q signals are tracked for the three GPS frequencies [Septentrio Satellite Navigation, 2016].

7.3.1.4. Measurement Detrending Methods

The measurements in the real initialization data are detrended before obtaining the spectral parameters and other statistical characteristics in order to remove low frequency variations associated with the satellite-receiver geometry range and background ionosphere and troposphere effects. In this section, the Symmlet order 6 wavelet is used to detrend the signal intensity, as it is more robust and effective in retaining scintillation signatures than the traditional sixth order Butterworth filter [Niu et al., 2012; Jiao et al., 2016a]. For phase measurements, the detrending process is more complicated and involves multiple steps. First, the satellite-receiver range is computed based on satellite orbit calculated using ephemeris and receiver position and the result is removed from the phase measurements. Second, other low frequency components such as ionospheric TEC, troposphere delay, and clock drift etc. are then removed using a fifth order polynomial filter. The Symmlet order 6 wavelet is finally applied to detrend the residual low frequency components.

For simulated wave, the signal intensity and phase in equations (7-1) and (7-2) are obtained directly from the wave field after wave propagation. They are free from satellite-receiver range and other background trend, thus are considered already ‘detrended’.

The simulated wave is then up-converted to GPS IF frequency to mimic receiver RF front end outputs. The signals are tracked by the conventional SDR algorithms described in Section 7.3.1.3. For the receiver processed data, signal intensity detrending is implemented using the Symmlet order 6 wavelet method, while phase detrending is performed by removing the satellite-receiver range which is the only background trend and is known beforehand.

7.3.2. *Comparison of Signal Characteristics of Simulated Data and Real Data*

This subsection presents results for stationary scintillation signal characterization using real and simulated data. A case study is first presented to demonstrate that the simulator can effectively generate statistically similar scintillation signals to the initialization data. Then a large amount of real and simulated data will be used to characterize scintillation signals and demonstrate the effectiveness of the simulator.

In this subsection, three different signals will be discussed:

- a) Real scintillation data collected at Hong Kong using an ISM receiver. Among the real data, one data segment of five minutes in length (Segment 6 in Figure 7-2) has been picked as the initializer for the simulator. We shall refer to this data segment as the “initialization data” or “initializer”. In the later statistical study, more real scintillation data from Hong Kong other than the initialization data will be used for characterization. These data as a whole will be referred to as the “real data”. These data are processed data from the ISM receiver, thus are comparable with the receiver-processed simulation data.
- b) Simulated scintillation data. This is the wave field that has been propagated through the phase screen and reached the receiver but has yet to be processed by the GPS receiver. The data are essentially the signal intensity and phase calculated from equations (7-1) and

(7-2). We will refer to these data as the “simulation data”.

- c) Receiver-processed simulation data. The simulator generated scintillation signal intensity and carrier phase are used to modulate GPS carrier and ranging code, then acquired and tracked by conventional SDR processing algorithms. New signal intensity and carrier phase of these processed data are then obtained, similar to the way the initialization data signal intensity and carrier phases are obtained. We shall refer to these data as the “processed data”.

The similarity between the initialization data and the receiver-processed simulation data will show the effectiveness of the simulator. The difference between the simulated scintillation data and the receiver-processed simulation data will highlight the artifacts produced by the receiver signal processing.

7.3.2.1. A Case Study of the Simulator Performance

Using the spectral and geometrical parameters extracted from the initialization data, simulated scintillation wave field can be obtained and further processed by conventional receiver processing algorithms. Different realizations of the random media can be produced with different random number generators (see equation (4-48)). The same realization can then be used to simulate signals at all three GPS frequencies. In this case study, one realization of simulation data of 5 minutes in length is selected to demonstrate the performance of the simulator.

Figure 7-6 compares the detrended signal intensity and phase in the initializer, the five-minute realization of simulation data, and its corresponding receiver processed simulation data for all three

GPS frequencies. For the processed data, the first 30-seconds data is discarded to eliminate the transient responses due to receiver tracking loop filtering and the detrending process. The figure shows that the simulation data and the initialization data have similar levels and frequencies of deep fades in signal intensity. The S_4 index values are also similar for each corresponding GPS frequency. Finally, the simulated phase varies within the same range as the initialization data.

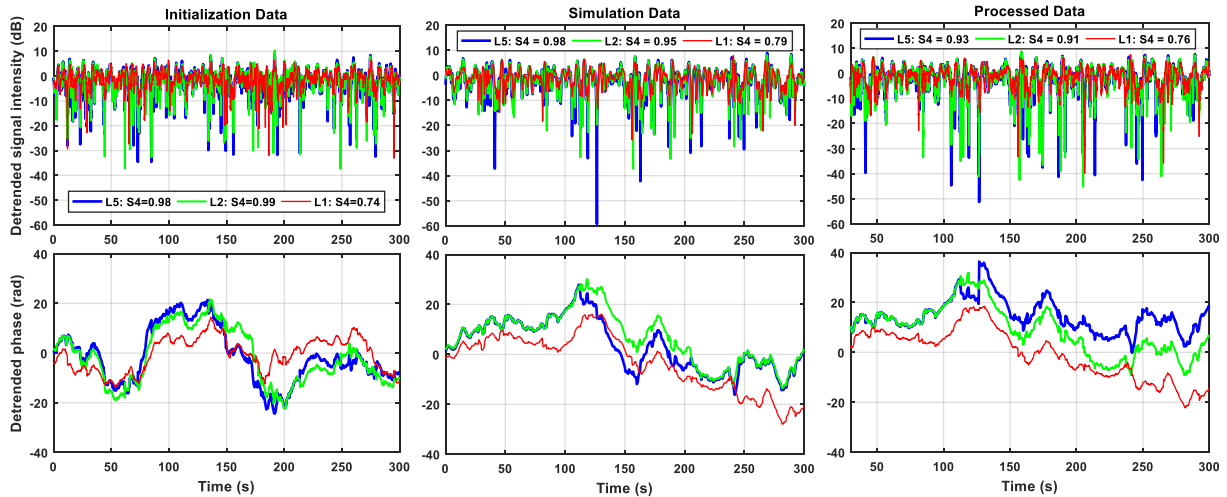


Figure 7-6. The detrended signal intensity and phase of the initialization data (left), the example segment of simulation data (middle), and its processed data (right) on the three GPS bands. The S_4 values of the signals are labeled in the legends.

Figure 7-7 highlights the simulation data with the receiver-processed data for different frequencies. Compared to the simulated data, the processed data appear to have deeper fades. However, the S_4 index values of the processed data are slightly lower than its corresponding simulation data. One possible reason for this is the shorter duration of the fades in the processed data which will be discussed later in Figure 7-11. In the phase data, tracking errors accumulate due to noise and cycle slips. The most obvious cycle slip is observed on L5 at around 125 second. Detailed analysis of tracking loop errors during scintillation using simulated data is the subject of an on-going project.

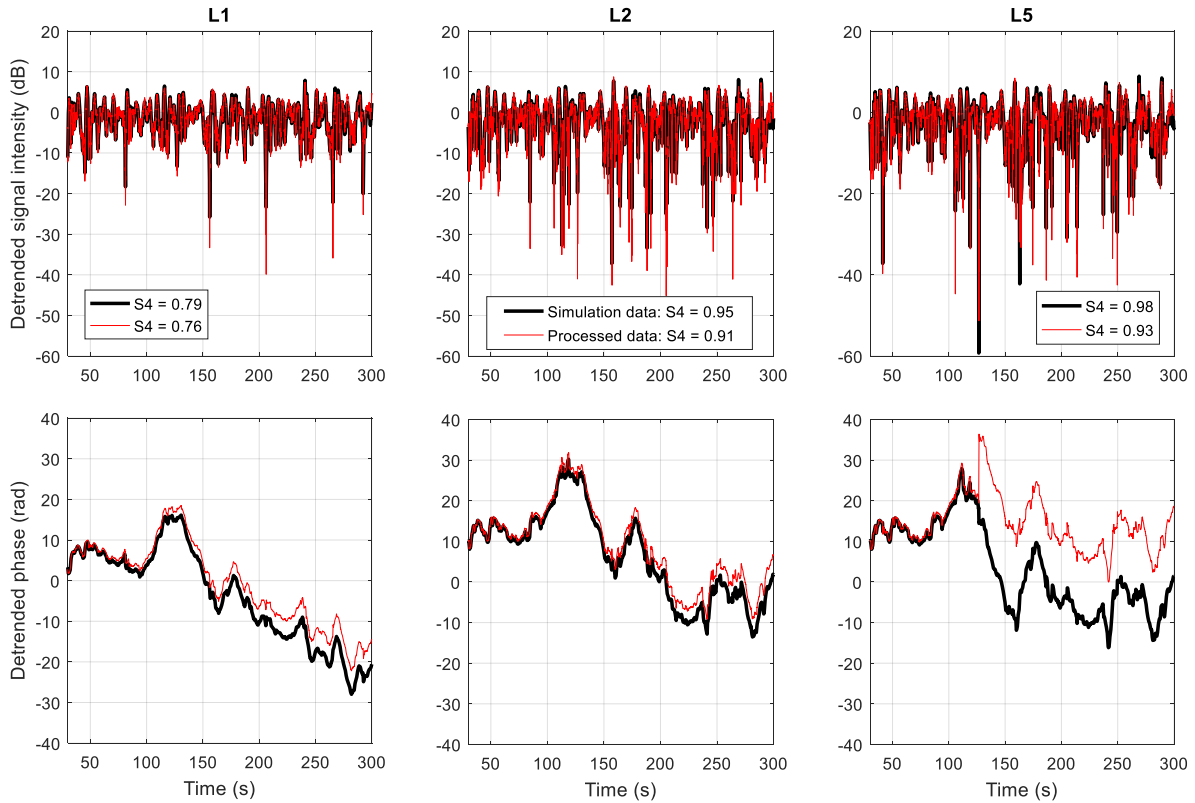


Figure 7-7. Comparison of the detrended signal intensity and phase of the simulation, and its processed data in Figure 7-6 on the three GPS bands. The S_4 values of the signals are labeled in the legends.

Parallel to the results in Sections 6.2 and 6.4, Figure 7-8 compares the spatial SDF and the PDF of the detrended signal intensity measurements in the initializer, the example realization of simulation data and the processed data (refer to Sections 6.2 and 6.4). Both the spatial SDFs and the PDFs for each GPS frequency are very similar between the initialization data and the simulation, showing the effectiveness of the simulator. Compared to the simulation data, the SDFs of the initialization data and the processed data both contain enhanced high-frequency components. This observation indicates that receiver signal processing introduces high-frequency noise in SDF.

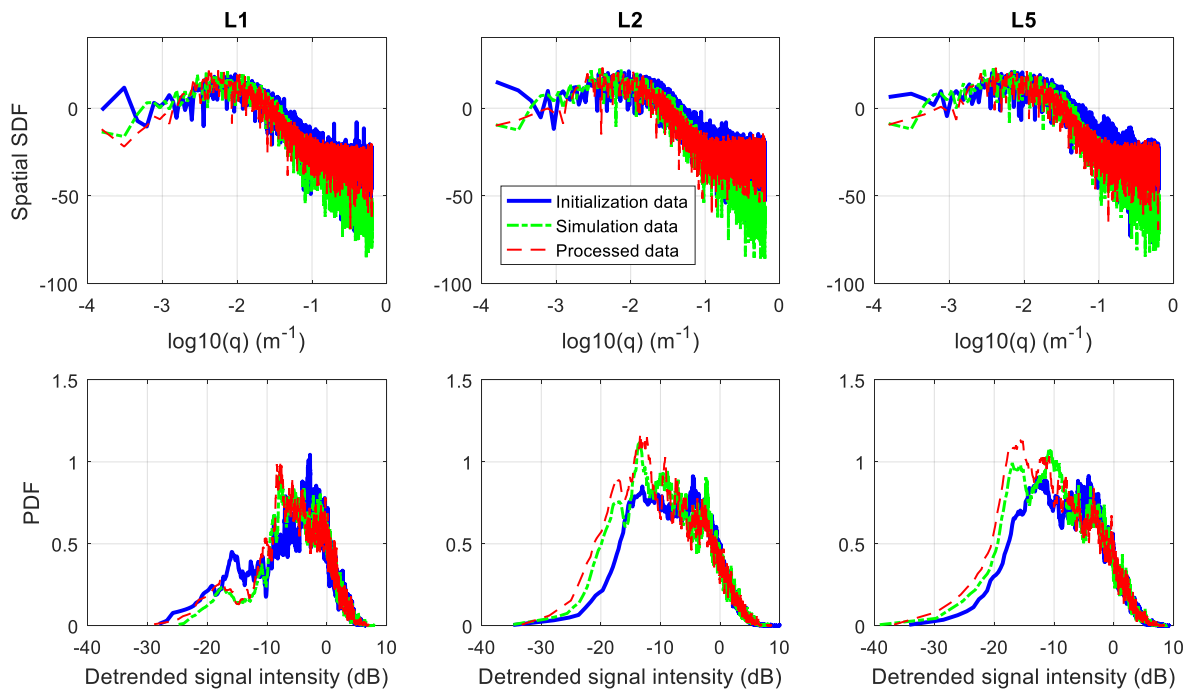


Figure 7-8. The spatial SDFs and the PDFs of the detrended signal intensity of the initializer (blue), the example segment of simulation data (green), and its processed data (red) on the three GPS bands. A raised noise floor at high frequencies can be observed on SDFs of the initializer and the processed data.

7.3.2.2. Statistics of Scintillating Amplitude and Phase on Simulated and Real Signals

The above case study shows that the simulator can effectively reproduce the scintillation structure and generate similar strong scintillation signals from the initialization data. Therefore, it would be interesting to study the statistical characteristics of the scintillation signals and the receiver's effects on them by comparing the simulation data with the processed data. In this subsection, we are specifically interested in the characteristics of the fading pattern on the signal intensity measurements and the variation patterns on the phase measurements.

To facilitate this statistical study, we generate twenty different realizations of simulated wave fields, each 5 minutes in length with the same initialization data used in the previous sections, and

processed the simulation data with the conventional receiver algorithms described earlier. In addition, several other segments of real scintillation data from Hong Kong are also used for analysis. The real data segments were collected from 12:00:00 to 15:59:59 UTC on Sept. 24, 2013, from 12:00:00 to 12:59:59 on Oct. 5, 2013 (including the initialization data), and from 12:00:00 to 13:59:59 on Oct. 6, 2013 all on PRN 24. It is noteworthy that although most scintillation events in the selected real data are fairly strong, the actual scintillation level still varies (e.g. with different spectral parameters). Therefore, it is important to keep in mind that the statistics obtained from these real data may not entirely reflect the signal characteristics of the initialization data, thus may not fully present a similarity to the characteristics of the processed simulation signals.

A -10 dB threshold is established for the signal intensity measurements to extract fading events. Table 7-2 lists the number of fading events on the three GPS bands extracted from the three segments of real data, the 20 realizations of simulation data, and their corresponding processed data. Using these events, several parameters are characterized which are illustrated in Figure 7-9. For the signal intensity, the parameters are fading duration, fading depth, and fading separation. For the carrier phase, the parameters are peak-to-peak phase change and max phase rate during signal intensity fading.

Table 7-2. Number of fades below the -10 dB threshold on the three GPS frequencies in the three segments of real data, 20 segments of simulation data, and their corresponding processed data

Number of fades below threshold	Real data	Simulation data	Processed data
L1	349	498	536
L2	1072	1031	1295
L5	1175	1129	1196

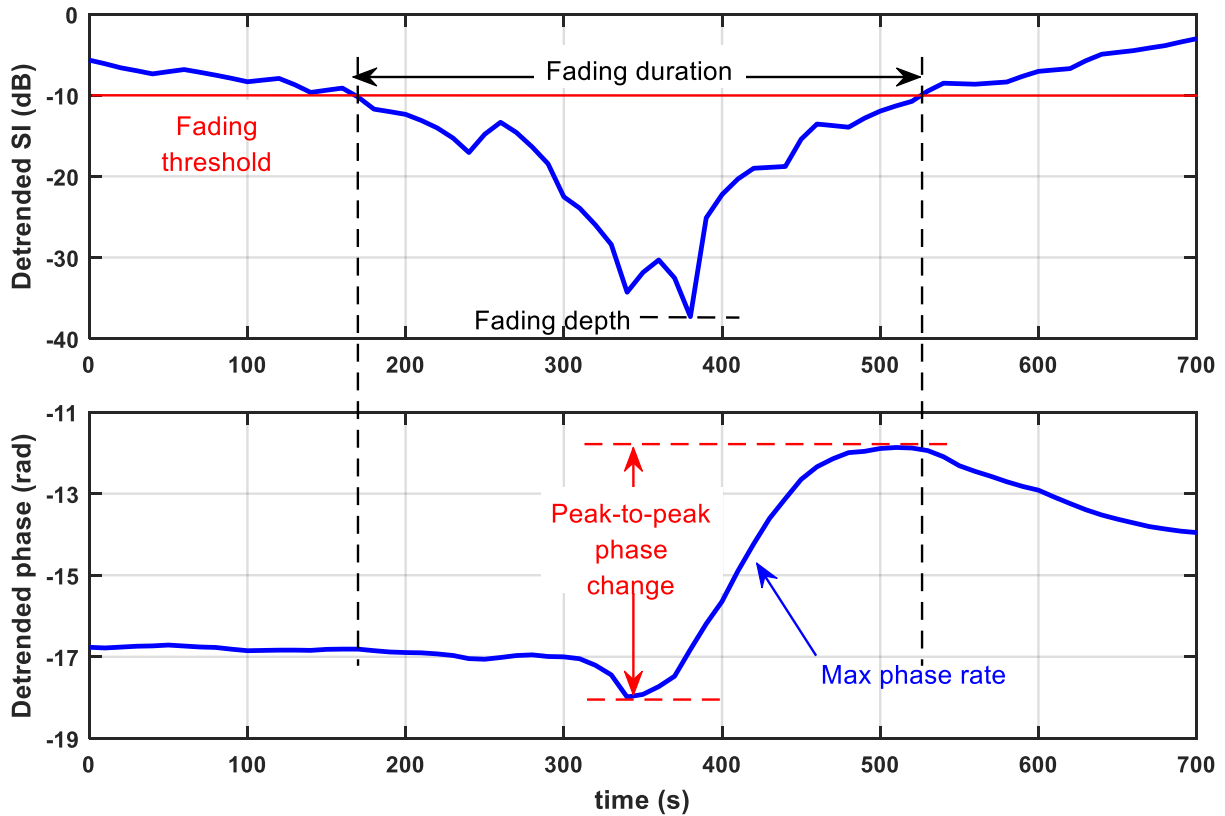


Figure 7-9. Illustration of the parameters characterized in the statistics in Subsection 7.3.2.2, which include fading duration and depth, peak-to-peak phase change, and max phase rate during fading.

Fading duration is defined as the time duration when the detrended signal intensity is below the threshold (-10 dB) (Subsection 6.5.1). Fading depth is defined as the difference between 0 dB and deepest fading level during a fading event. These two parameters are important features for receiver signal processing, as they affect the performance of the receiver and the accuracy of the positioning solution [Seo *et al.*, 2011]. Figure 7-10 and Figure 7-11 show the histograms of the fading duration and fading depth on all three GPS frequencies in the real data, the simulation data, and the processed data. Compared to the simulation, the real data contains generally shorter and shallower fading events. It can also be seen from subplots (b) and (c) that the receiver tends to make the fades deeper (which is consistent with the observation in Figure 7-7), but shorter. Figure 7-12 shows the relationships between fading depth and fading duration. The results for simulation

are consistent with those for the real data, which reveal that deeper fades may last longer on average but the correlation between fading depth and duration is relatively low.

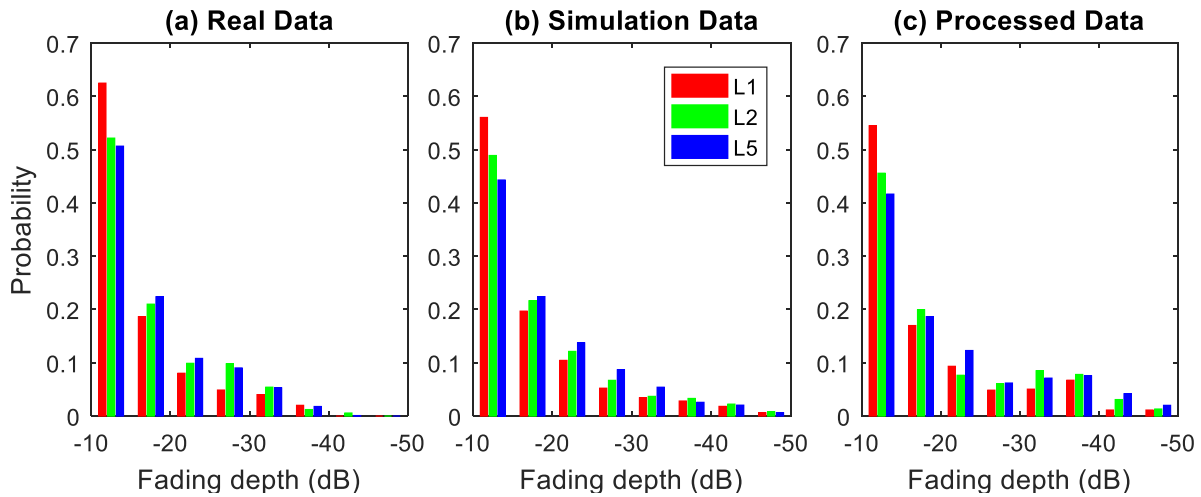


Figure 7-10. Histograms of the fading depth for fades below the -10 dB threshold on the three GPS frequencies in (a) the real data, (b) the simulation data, and (c) the processed data.

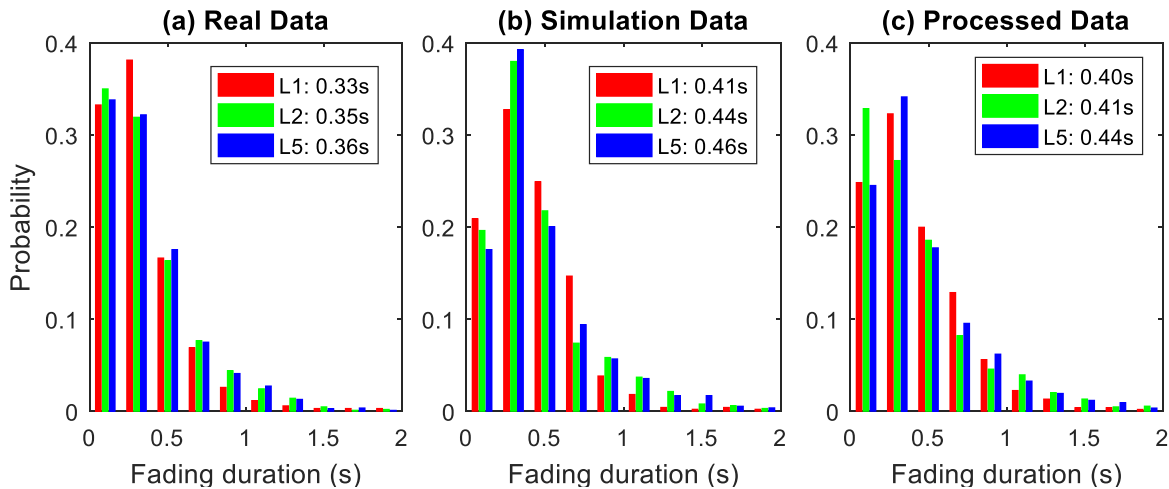


Figure 7-11. Histograms of the fading duration for fades below the -10 dB threshold on the three GPS frequencies in (a) the real data, (b) the simulation data, and (c) the processed data. The legends indicate the average fading duration.

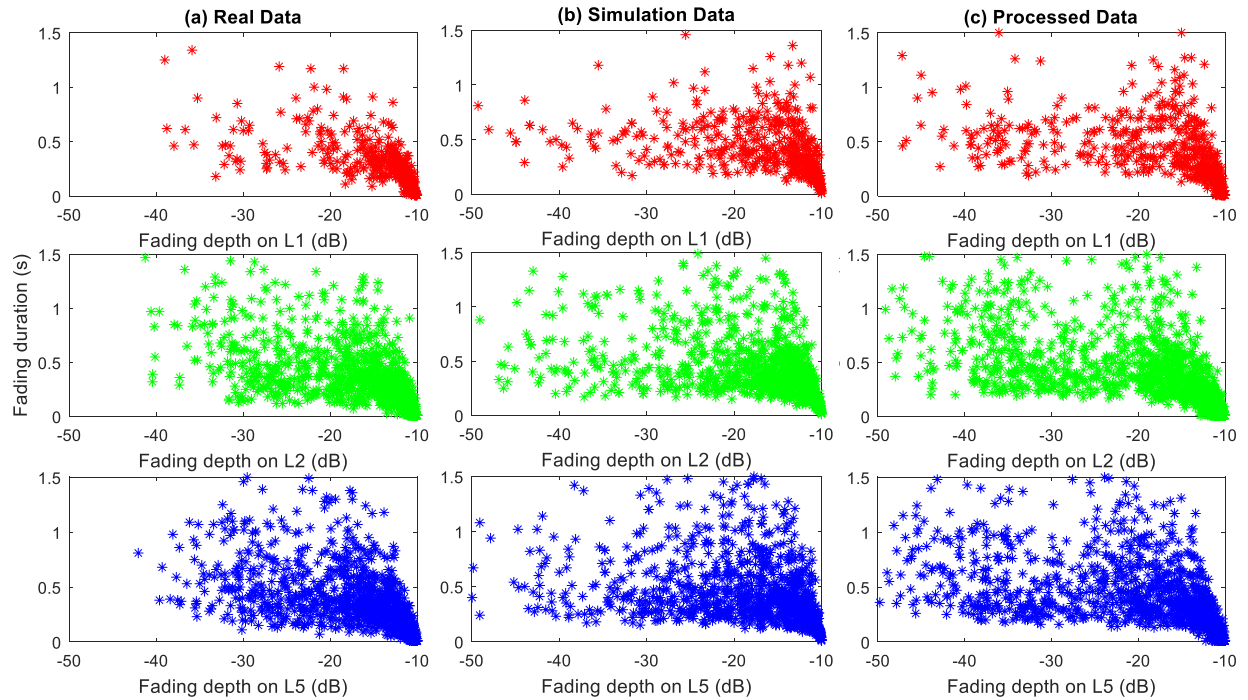


Figure 7-12. Relationships between fading duration and fading depth for fades below the -10 dB threshold on the three GPS frequencies in (a) the real data, (b) the simulation data, and (c) the processed data.

Fading separation here is defined the same way as in Subsection 6.5.2, and has been illustrated in Figure 6-14. The histograms of the single-band fading separation in real, simulation, and processed data are shown in Figure 7-13, with the mean separations denoted in the legends for separations below 60 seconds. Compared with the simulation data, the processed data have shorter average separation between fades, which is caused by the increased number of fades in the processed data (see Table 7-2). Figure 7-14 shows the histograms of multi-band fading separation, with the mean separations labeled in the legends. From Figure 7-14, it can be seen that the multi-band separations of real data and processed data are statistically similar with comparable means and histograms.

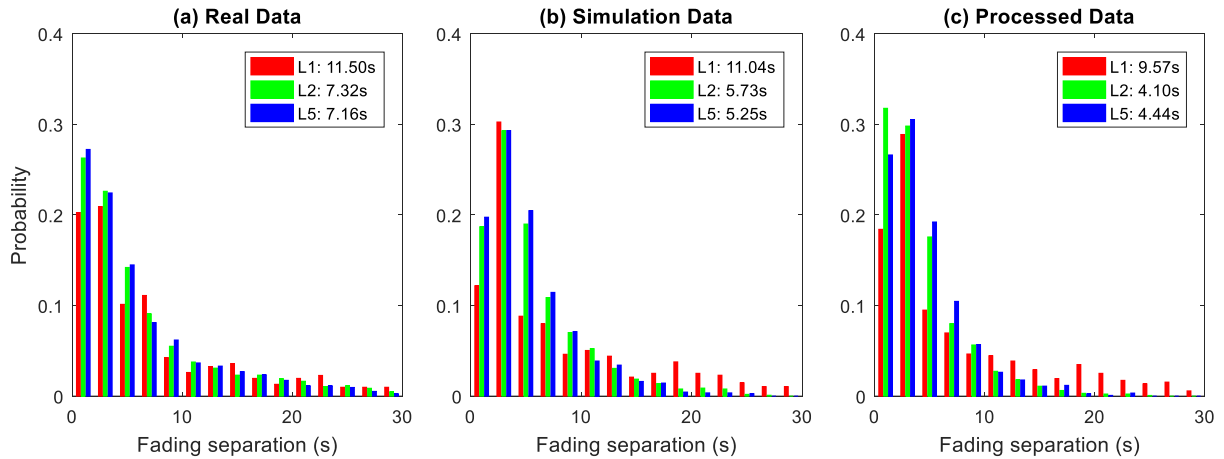


Figure 7-13. Histograms of the single-band fading separation for fades below the -10 dB threshold on the three GPS frequencies in (a) the real data, (b) the simulation data, and (c) the processed data. The legends indicate the average fading separation for the separations below 60 seconds.

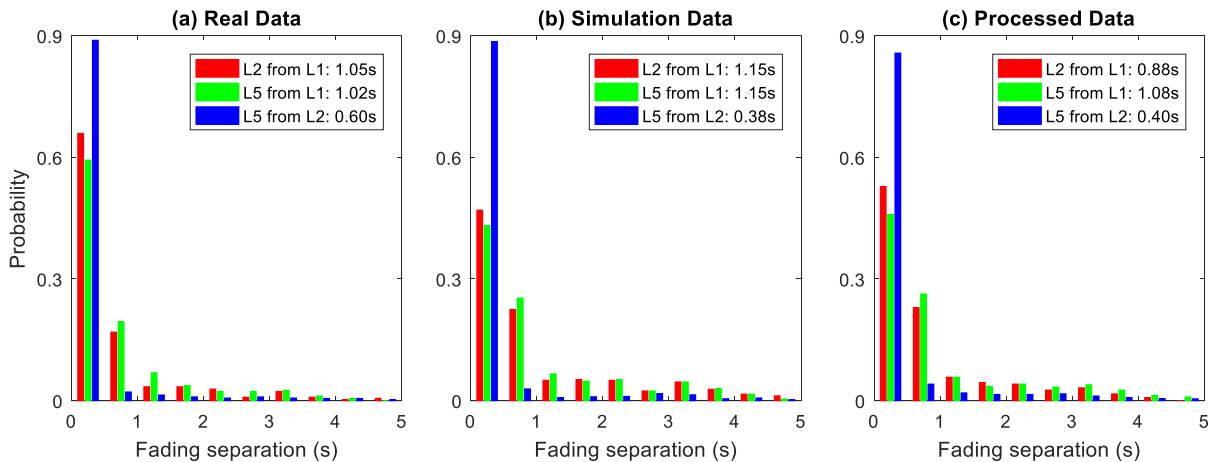


Figure 7-14. Histograms of the multi-band fading separation for fades below the -10 dB threshold on the three GPS frequencies in (a) the real data, (b) the simulation data, and (c) the processed data. The legends indicate the average fading separation for the separations below 60 seconds.

Phase scintillation, especially strong phase scintillation has not been studied extensively in previous research. This is because there is a limited amount of strong phase scintillation data available. Most ISMs lose lock of carrier tracking during strong scintillation and for those that manage to maintain lock during strong scintillation, their phase estimations are not reliable. In this

study, the simulator is capable of generating strong scintillation and therefore offers a unique opportunity to characterize phase scintillation.

To characterize the phase variations during strong scintillation, we define two quantities: peak-to-peak phase change and max phase rate (illustrated in the bottom panel in Figure 7-9). The peak-to-peak phase change is the phase difference between the second phase peak value (maximum/minimum) and first phase peak value (minimum/maximum) during a fading event. The max phase rate is the peak value (maximum/minimum) of the first derivative of the signal phase during a fading event. From the definitions, it can be seen that both parameters can be either positive or negative. These two parameters can directly affect the performance of the PLL in the receiver.

Figure 7-15 and Figure 7-16 are histograms of the peak-to-peak phase change and the max phase rate on the three GPS frequencies in the real data, the simulation data, and the processed data. The resolution in Figure 7-16 is set high to show details around zero phase rate. Figure 7-15 and Figure 7-16 show that both peak-to-peak phase change and max phase rate histograms are nearly symmetrical around zero, which indicates that during scintillation, signal phase can either increase or decrease with equal probabilities. Compared to the simulation data, the phase statistics for the processed data has larger variance and are more similar to the phase statistics for the real data. The larger variance may be caused by the receiver processing artifacts.

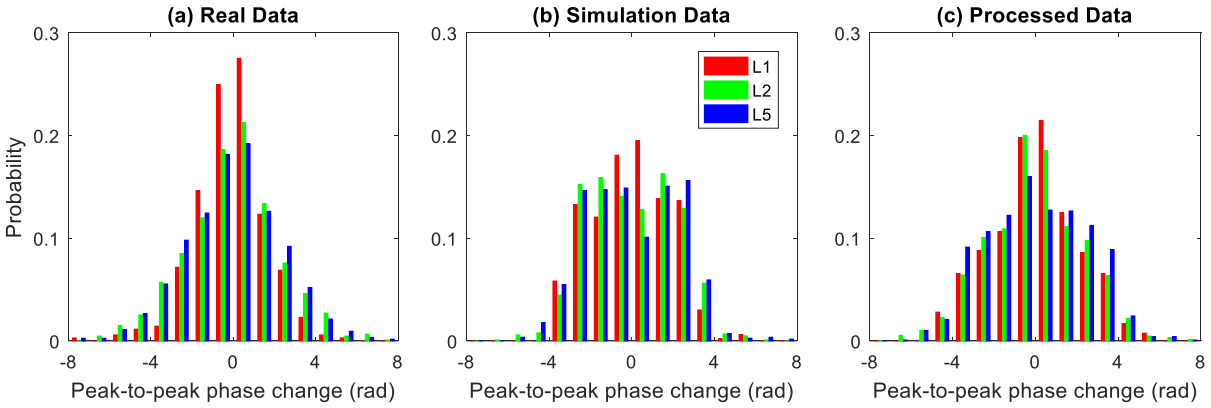


Figure 7-15. Histograms of the peak-to-peak phase change during fading below the -10 dB threshold on the three GPS frequencies in (a) the real data, (b) the simulation data, and (c) the processed data.

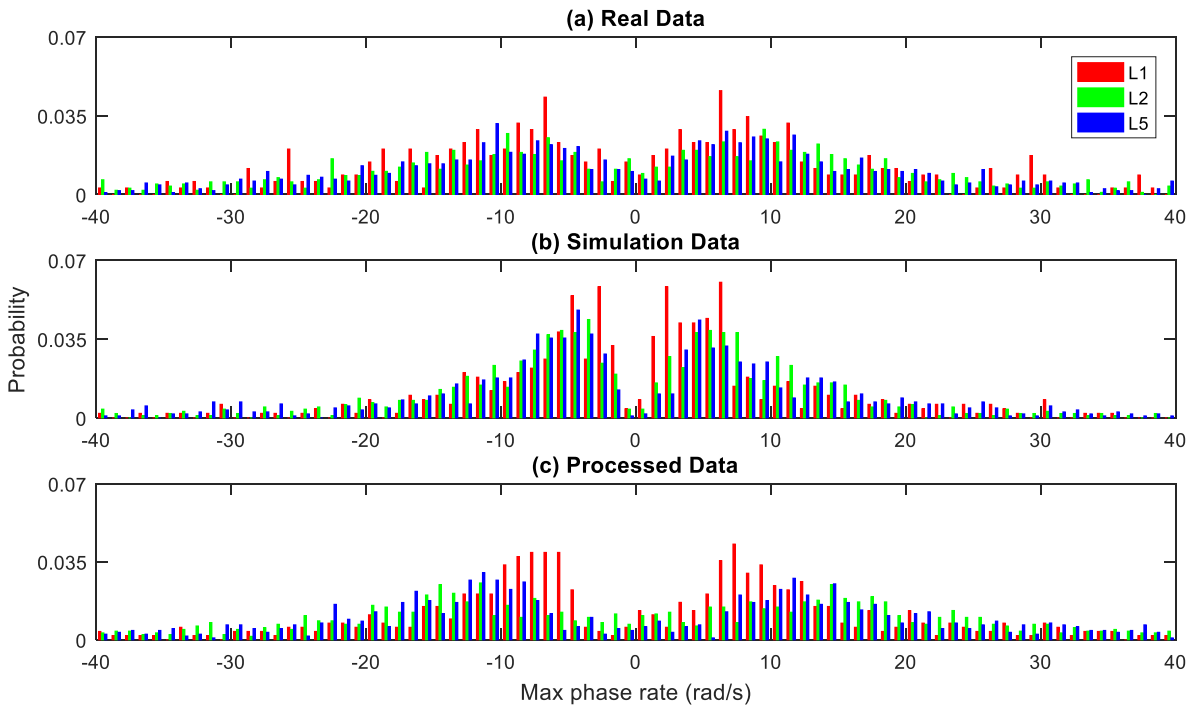


Figure 7-16. Histograms of the max phase rate during fading below the -10 dB threshold on the three GPS frequencies in (a) the real data, (b) the simulation data, and (c) the processed data.

In addition to the stand-alone statistics, we are also interested in the relationship between amplitude fading and phase variations. Figure 7-17 shows the relationship between the absolute value of the peak-to-peak phase change and the fading depth on the three GPS bands. It shows that deeper fades

are typically associated with larger peak-to-peak phase change. Although these two measures are well correlated, the relationship is not linear, especially in the simulation data.

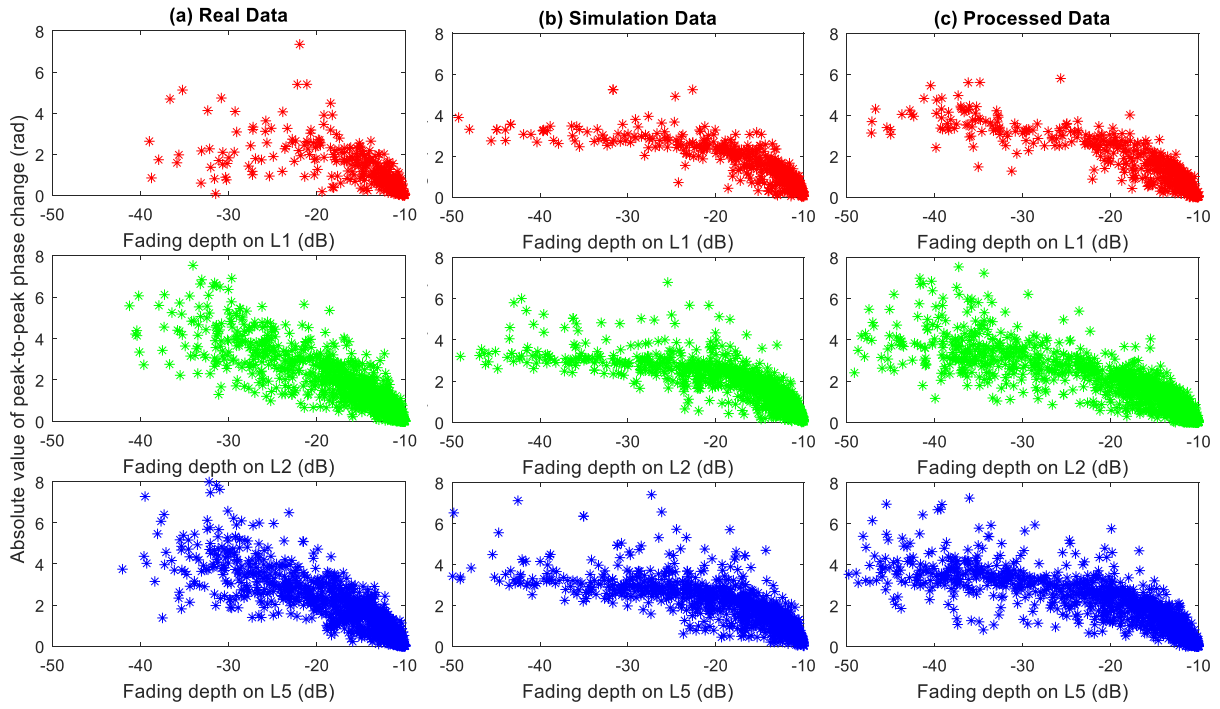


Figure 7-17. Relationships between the absolute value of the peak-to-peak phase change and the fading depth for fades below the -10 dB threshold on the three GPS frequencies in (a) the real data, (b) the simulation data, and (c) the processed data.

Figure 7-18 plots the \log_{10} of the absolute value of the max phase rate as a function of the fading depth, which reveals a well-correlated linear relationship. The correlation coefficients show medium to high linear correlation of the two measures, especially for the simulation and the processed data. Compared to the simulation data, the linear relationships in the processed data have more gradual slopes, yet higher y-interceptions. This shows that the absolute value of the max phase rate in the processed data does not change as dramatically as in the simulation data, which may be a manifestation of the smoothing effect of the receiver tracking loop filters. This linear relationship is an interesting finding which may assist the design of tracking algorithm during deep fading caused by ionospheric scintillation.

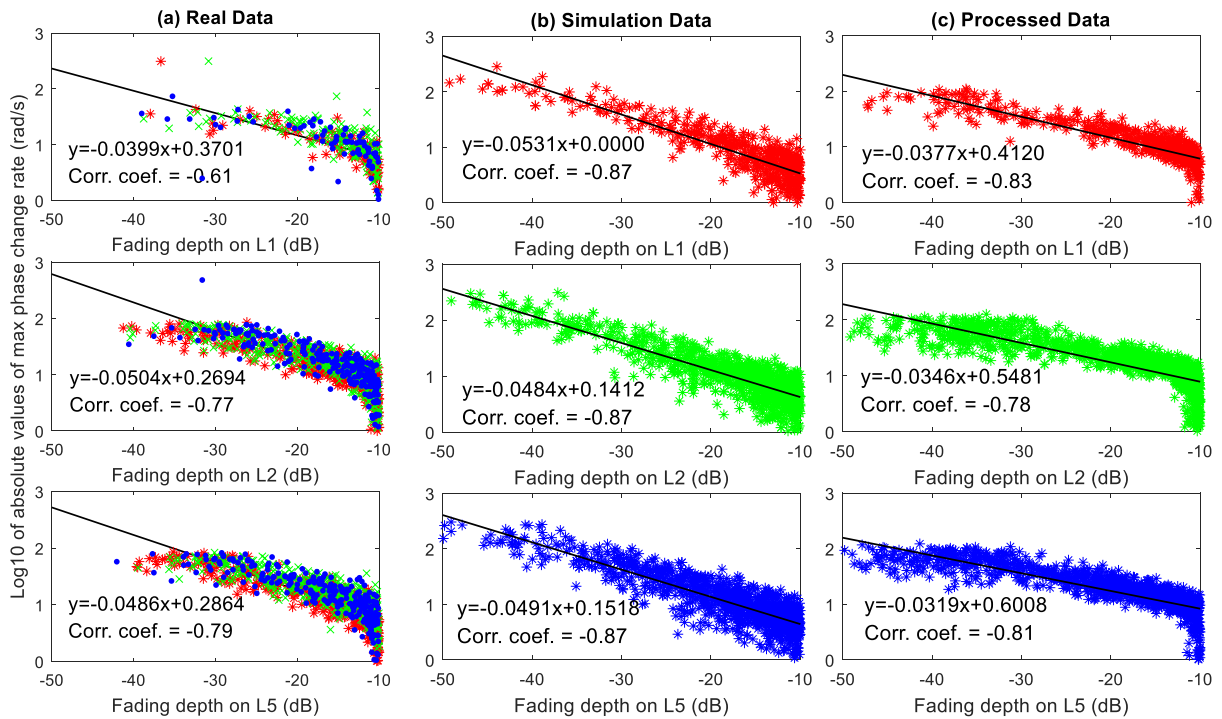


Figure 7-18. Relationships between the log10 of the absolute value of the max phase rate and the fading depth for fades below the -10 dB threshold on the three GPS frequencies in (a) the real data, (b) the simulation data, and (c) the processed data. The two show well-correlated linear relationships. The linear fits are given in black lines with corresponding equations shown below the lines together with the correlation coefficients. In subplot (a), red, green, and blue markers represent data collected on Sept. 24, Oct. 5, and Oct. 6 2013, respectively.

7.4. Scintillation Simulation for Dynamic Receivers Using Data Surrogate Method

This section presents scintillation signal simulation results with a focus on the effects of different dynamics of the receiver platform. The model used in the simulation is based on the time-domain data surrogate method discussed in Section 4.3. The dynamics of the receiver platform mainly affects the ρ_F/v_{eff} parameter, which yields varying time scales of the scintillation signal intensity fading and phase variation. In addition, the drift velocity of the ionospheric irregularities also plays a role in determining the characteristics of the simulation signals.

7.4.1. Propagation Geometry for Dynamic Platforms

As discussed in Section 4.3, the data surrogate model is completely defined by a set of parameters which include three subsets of parameters. The parameter subsets are the structure parameters: U, p_1, p_2, μ_0 , the time scaling factor: ρ_F/v_{eff} , and the sampling parameters: $\Delta t, N$. The structure parameters can be obtained from the SDF of the initializer, and they are not affected by the dynamics of the platform. The sampling parameters are specified by the user. Thus, the only parameter that is determined by the platform dynamics is the time scaling factor ρ_F/v_{eff} . While the calculation of ρ_F is straightforward (equations (4-68) and (4-69)), the calculation of v_{eff} requires the knowledge of the ionosphere anisotropy, the signal propagation direction with respect to the geomagnetic field, and the apparent velocity in the measurement plane (Subsection 4.2.6). To compute the apparent velocity, we need to obtain the IPP velocity v_{IPP} and the drift velocity of the ionosphere irregularities v_{drift} . The former is determined by the motion of the satellite and receiver platform. Figure 7-19 illustrates the relationship of the different velocities using a one-dimensional case. From Figure 7-19, it can be seen that the IPP velocity can be calculated from the user input and the satellite ephemeris. The drift velocity of the irregularities can be obtained from other co-located instruments, such as radar or an array of closely spaced GNSS receivers, or from empirical values (25-150 m/s in the equatorial region) [Wang and Morton, 2017].

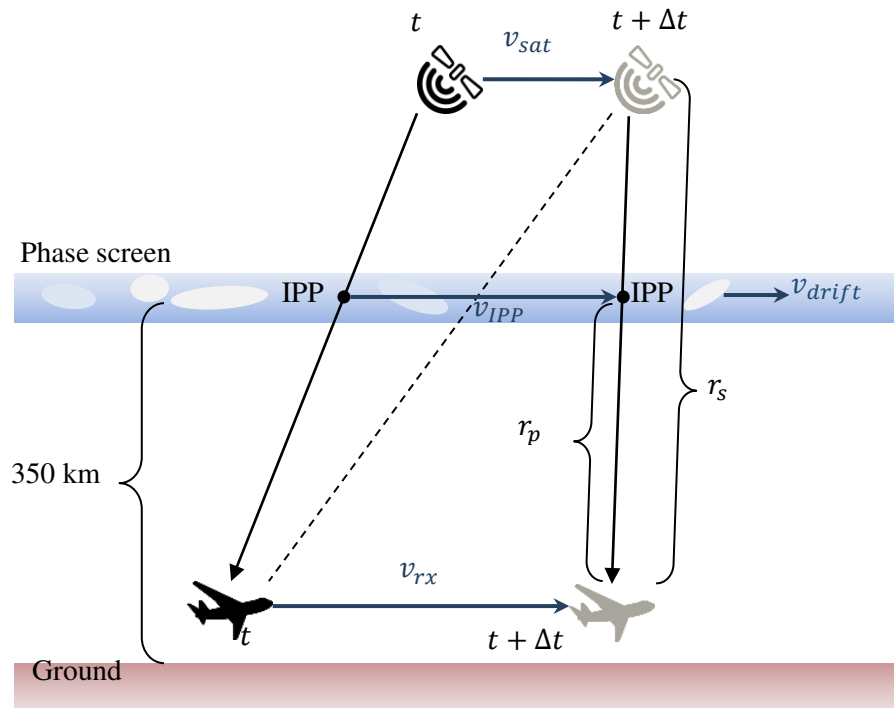


Figure 7-19. One-dimensional illustration of the IPP velocity v_{IPP} at the phase screen which includes contributions from the satellite velocity v_{sat} and the receiver velocity v_{rx} . The ionospheric irregularity drift velocity v_{drift} and v_{IPP} together determine the value of v_{eff} . The illustration is not to scale.

A larger ρ_F/v_{eff} corresponds to a smaller v_{eff} value. A smaller v_{eff} value is associated with larger time scale, namely longer decorrelation time of the scintillation signal. Conversely, a smaller ρ_F/v_{eff} corresponds to shorter signal decorrelation time.

7.4.2. Receiver Dynamics, Geomagnetic Field, and Irregularity Drift

In the equatorial region, the ionospheric irregularities are known to be highly elongated along the geomagnetic field lines [Kintner *et al.*, 2004]. Therefore, the phase screen model is reduced to two dimensions as explained in Section 4.3. This dimension reduction effectively neglects the irregularity variation along the geomagnetic north-south direction. As a result, the movement of the receiver with respect to the geomagnetic field lines is a factor that controls the time scale of

the scintillation signal. Intuitively, assuming the irregularity drift velocity is zero, when the receiver moves across the geomagnetic lines, the scintillation signal will have shorter decorrelation time (i.e. smaller ρ_F/v_{eff}) due to higher variability in the irregularities, compared to when the receiver moves along the geomagnetic lines.

To quantitatively demonstrate how the time scale is influenced by the receiver trajectories, we calculate the geomagnetic field at the IPP in the initialization data shown in Figure 7-2. Using the International Geomagnetic Reference Field (IGRF-11) (Subsection 3.2.2), the components of the geomagnetic field at the Hong Kong site are $X = 32791.2$ nT (northward), $Y = -1001.6$ nT (eastward), $Z = 14213.1$ nT (downward). Using these values, several trajectories of the receiver platform are simulated with corresponding velocity vectors as listed in Table 7-3 and illustrated in Figure 7-20. The magnitude of these velocity vectors is set to 100 m/s (except for stationary platform), which is approximately the speed of the currently fastest trains.

Table 7-3. Velocities for a receiver platform with respect to the geomagnetic field direction. The magnitude of the velocities is 100 m/s except for Velocity #0

Velocity #	Eastward velocity (m/s)	Northward velocity (m/s)	Upward velocity (m/s)
0	0	0	0
1	-1.825	97.00	-24.25
2	1.825	-97.00	24.25
3	99.98	1.881	0
4	-99.98	-1.881	0
5	-0.4560	24.24	97.02
6	0.4560	-24.24	-97.02

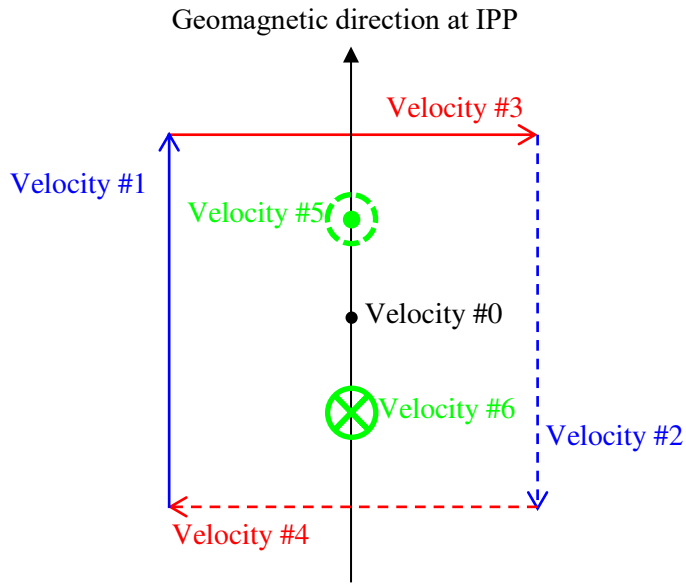


Figure 7-20. Illustration of the different velocity configurations of the receiver platform listed in Table 7-3 with respect to the geomagnetic field direction.

From Table 7-3 and Figure 7-20, it can be seen that Velocity #0 is for a stationary receiver platform, Velocities #1 and #2 are for receivers moving along and against the geomagnetic field lines, and Velocities #3-6 are across the geomagnetic field lines. In addition, Velocities #1,3,5 are mutually orthogonal.

Figure 7-21 shows the calculated ρ_F/v_{eff} values for the various velocity cases in Table 7-3. Consistent with the previous analysis, when the receiver moves along the geomagnetic field lines, the ρ_F/v_{eff} value is generally larger than when the receiver moves across the geomagnetic field.

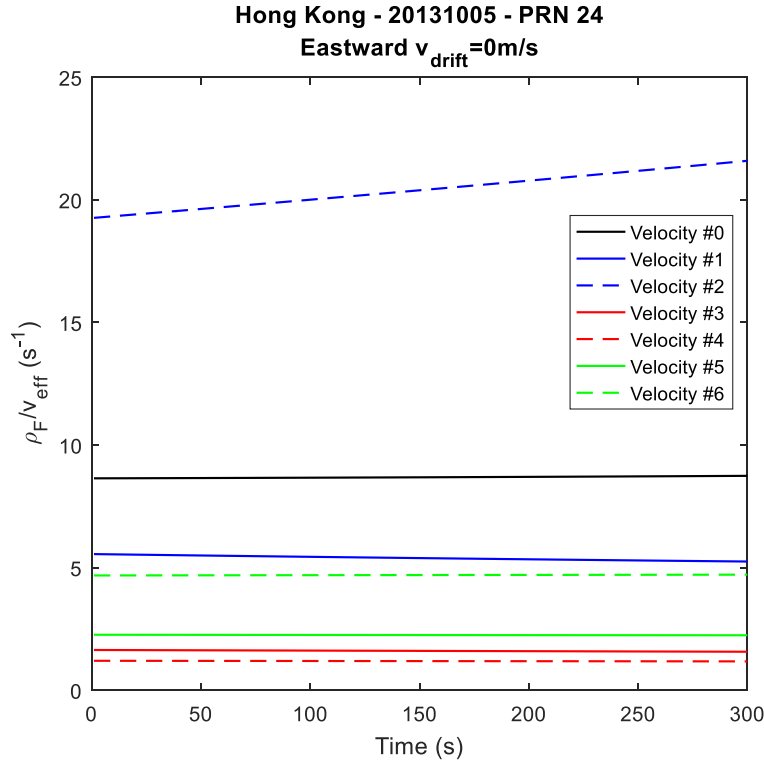


Figure 7-21. The values of the time scale factor ρ_F/v_{eff} for different velocity designs of the receiver platform with respect to the local geomagnetic field direction. The geometry used is extracted from the initializer shown in Figure 7-2.

We also conduct the same calculation on another set of initialization data with similar platform dynamics configurations designed using the corresponding geomagnetic direction at the IPP in this initialization data. This set of initialization data was collected on PRN 24 from 14:30:00 to 14:34:59 UTC on September 24, 2013 at Hong Kong. The calculated values of ρ_F/v_{eff} using the geometry in this initializer are shown in Figure 7-22. Figure 7-22 also demonstrates that when the receiver moves along the geomagnetic field lines, the ρ_F/v_{eff} value is generally larger than when the receiver moves across the geomagnetic field. However, comparing Figure 7-21 and Figure 7-22, the absolute values of ρ_F/v_{eff} are very different, especially for Velocities #0-2. This shows that the absolute value of ρ_F/v_{eff} can be significantly influenced by the actual propagation geometry in the initialization data.

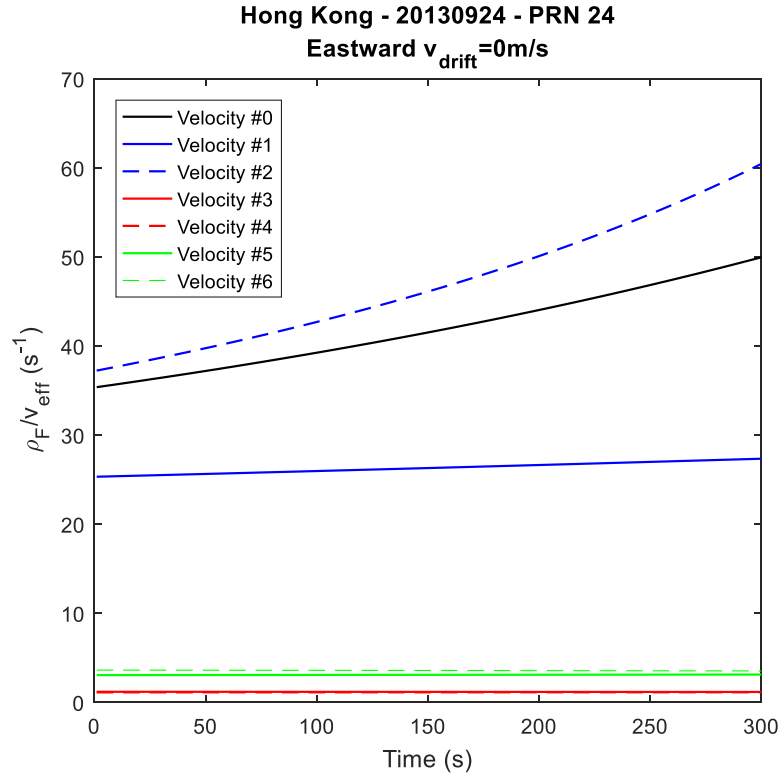


Figure 7-22. Same as Figure 7-21 but for the geometry in the data collected on PRN 24 from 14:30:00 to 14:34:59 UTC on September 24, 2013 at Hong Kong. The velocity configurations are designed the similar way to those listed in Table 7-3 according to the geomagnetic direction at the IPP.

In Figure 7-21 and Figure 7-22, the drift velocity of the ionospheric irregularities is set to 0. Whereas in reality, the irregularities in the equatorial region carry a dominantly eastward drift velocity, which is typically between 50 and 150 m/s during the post-sunset period when scintillation is most frequent and strong [Basu *et al.*, 2002]. If we assume a 100 m/s eastward drift velocity of the irregularities for the initializer in Figure 7-2, the values of ρ_F/v_{eff} are recalculated as shown in Figure 7-23.

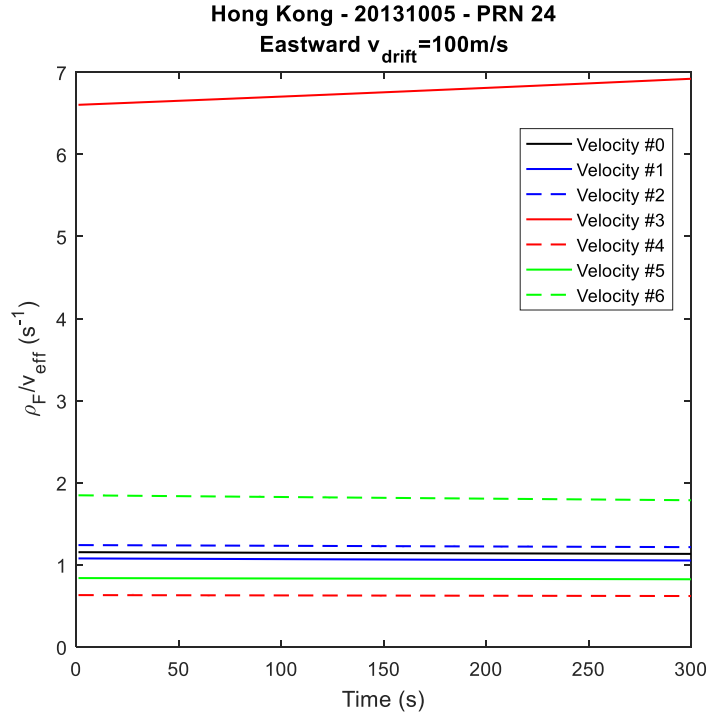


Figure 7-23. Same as Figure 7-21 but an eastward irregularity drift velocity of 100 m/s is added.

In Figure 7-23, ρ_F/v_{eff} for Velocity #3 becomes the largest, as Velocity #3 contains an eastward velocity of 99.98 m/s. This means the receiver moves almost at the same speed as the ionospheric irregularities in the eastward direction, which significantly increases the decorrelation time of the scintillation signal. On the other hand, ρ_F/v_{eff} for Velocity #4 is the smallest as the receiver has the largest relative velocity in the eastward direction with respect to the drifting irregularities. These two scenarios can be considered the slowest and the fastest scenarios for this initializer with a platform velocity magnitude of 100 m/s.

7.4.3. Scintillation Simulation Parameters for Dynamic Receiver Platforms

Based on the analysis in the previous text, scintillation signal segments are simulated with specified parameters for different dynamics of the receiver platform. Each signal segment is five minutes in length. The eastward drift velocity of the irregularities is set to 100 m/s. Judging from

Figure 7-23, ρ_F/v_{eff} does not change significantly within 5 minutes for each scenario, thus will be considered constant (the mean value is used) in the simulation for each velocity configuration in this dissertation. In addition, the spectral parameters U, p_1, p_2, μ_0 are obtained from the SDF of the detrended signal intensity in the initialization data in Figure 7-2. Here we also used the IPE method developed in [Carrano *et al.*, 2012] to derive the spectral parameters. Table 7-4 lists the values of all necessary parameters for the scintillation simulation. These include the spectral parameters at GPS L1, L2, and L5, time scale factor corresponding to the platform dynamics configurations, and the sampling interval and number of samples. It should be noted that only the spectral parameters for L1 are obtained using the IPE method. The values of U, μ_0 , and ρ_F/v_{eff} for L2 and L5 are scaled from L1 using equations (4-73) through (4-75).

Table 7-4. Values of the parameters used in the scintillation signal simulation for dynamic receiver platforms

Parameter symbol	Parameter definition	Value for GPS L1, L2, L5
U	Universal scattering strength	1.30, 2.92, 3.36
p_1	Spectral index 1	2.5
p_2	Spectral index 2	3.5
μ_0	Normalized break wavenumber	0.50, 0.57, 0.58
ρ_F/v_{eff_0}	Time scale factor for Velocity #0	1.14, 1.29, 1.32 s ⁻¹
ρ_F/v_{eff_1}	Time scale factor for Velocity #1	1.06, 1.21, 1.23 s ⁻¹
ρ_F/v_{eff_2}	Time scale factor for Velocity #2	1.23, 1.39, 1.42 s ⁻¹
ρ_F/v_{eff_3}	Time scale factor for Velocity #3	6.76, 7.66, 7.82 s ⁻¹
ρ_F/v_{eff_4}	Time scale factor for Velocity #4	0.63, 0.71, 0.72 s ⁻¹
ρ_F/v_{eff_5}	Time scale factor for Velocity #5	0.83, 0.94, 0.96 s ⁻¹
ρ_F/v_{eff_6}	Time scale factor for Velocity #6	1.82, 2.06, 2.10 s ⁻¹
v_{drift}	Irregularity drift velocity	100 m/s
Δt	Sample time interval	0.01 s
N	Number of samples in time domain	30000

7.4.4. Evaluation of Dynamic Scintillation Signal Simulation

To evaluate the scintillation simulation results, we first compare the initialization data with its corresponding simulation signal for Velocity #0, as shown in Figure 7-24. The detrending methods used for the initialization data and the simulation data are the same as described in Subsection 7.3.1.4.

It can be seen from Figure 7-24 that the simulation data and the real data show similar characteristics in a statistical sense for both signal intensity and carrier phase. For both sets of data, the range of their S_4 index values for each GPS band is also similar. It should be noted that in scintillation simulation, the random number sequence (η_n in equation (4-76)) is the same for the three GPS carrier frequencies, in order to generate correlated simulation signals across the frequency bands originated from the same ionospheric irregularities.

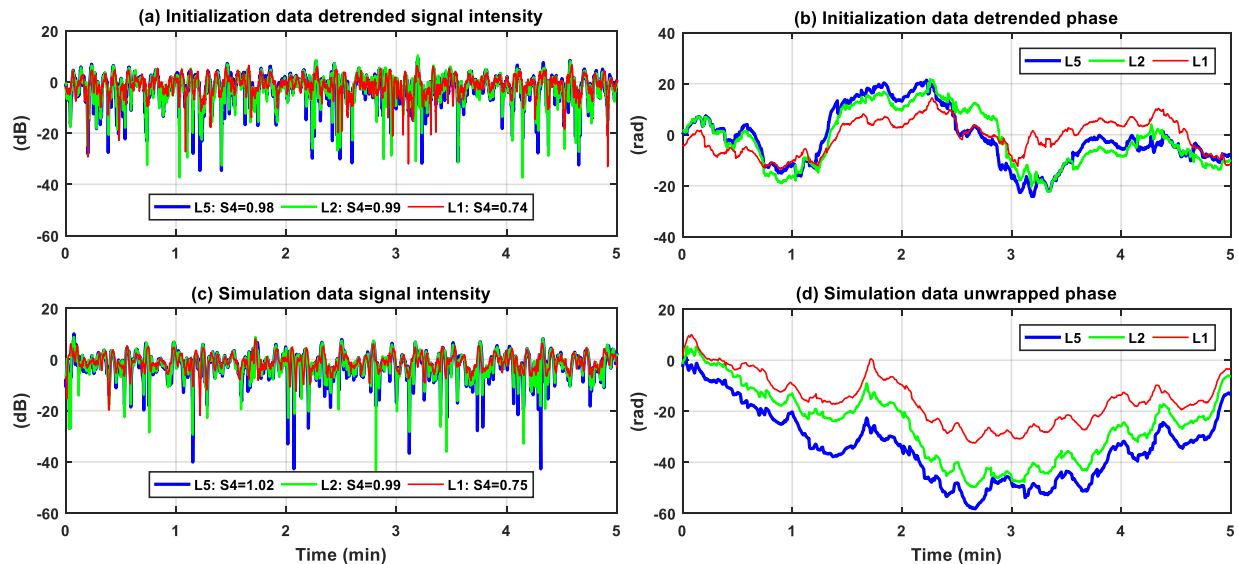


Figure 7-24. Comparison of the signal intensity and phase in the initialization data and the simulation data for Velocity #0.

Next, we compare simulation signals for different receiver platform velocity configurations. Figure 7-25 compares Velocity #3 (the largest ρ_F/v_{eff}) and Velocity #4 (the smallest ρ_F/v_{eff}) with Velocities #0 (the stationary receiver scenario). Figure 7-26 is a zoom-in plot of Figure 7-25 between Minute 1 and 2. It can be observed that the simulation signal for Velocity #3 contains the mildest signal fading and phase variation, while the simulation signal for Velocity #4 has the fastest variation in both the signal intensity and phase measurements, which represents the most serious threat to the receiver processing of the scintillation signal.

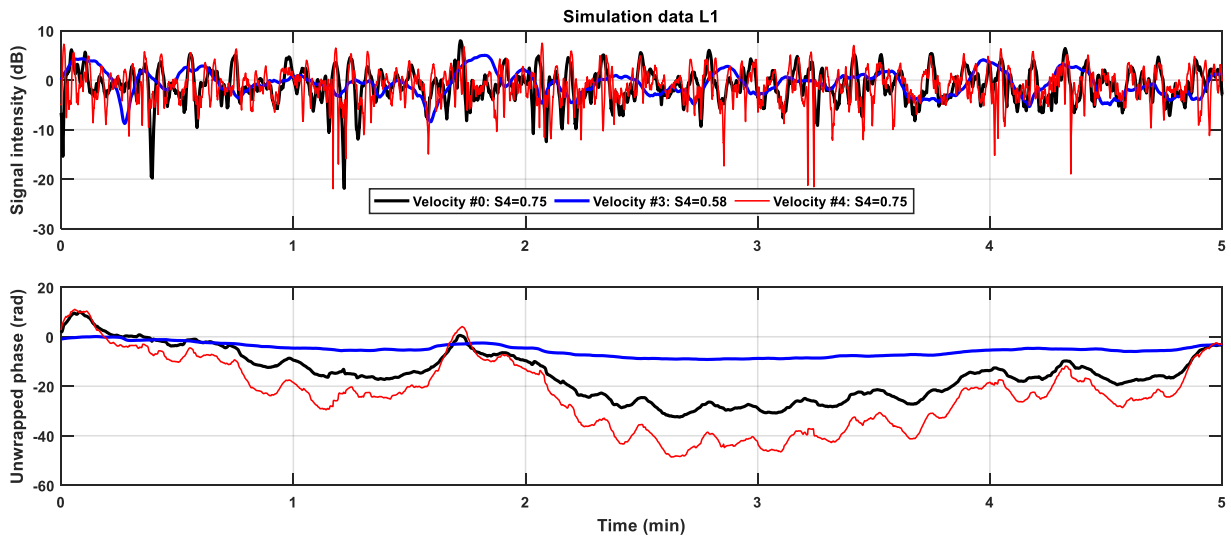


Figure 7-25. Simulation signal intensity and phase on GPS L1 band for Velocities #0, 3, and 4. Velocities #3 and 4 are the slowest and the fastest scenarios in Figure 7-23. The S_4 index values are denoted in the legend in the upper subplot. The random number sequence η_n used in the three scenarios is the same.

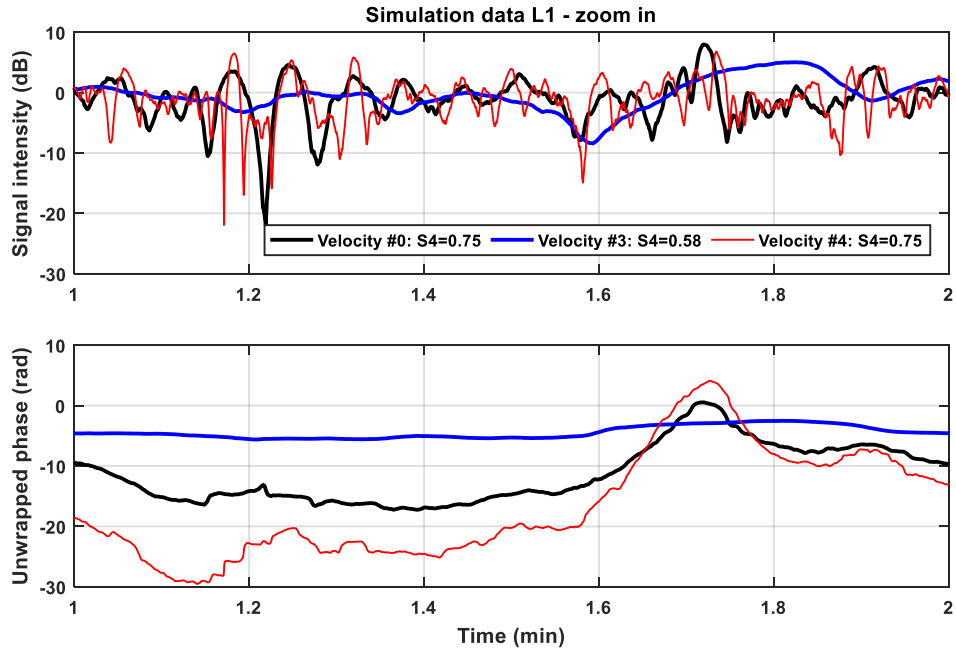


Figure 7-26. A zoom-in plot of Figure 7-25 between the 1st and 2nd minute. The difference in the decorrelation time of the signal intensity and phase for different velocity designs is obvious.

The simulation signals shown in Figure 7-27 and Figure 7-28 for GPS L2 and L5 bands are very similar to that on L1, except that the scintillation levels on these bands are higher due to their lower carrier frequencies.

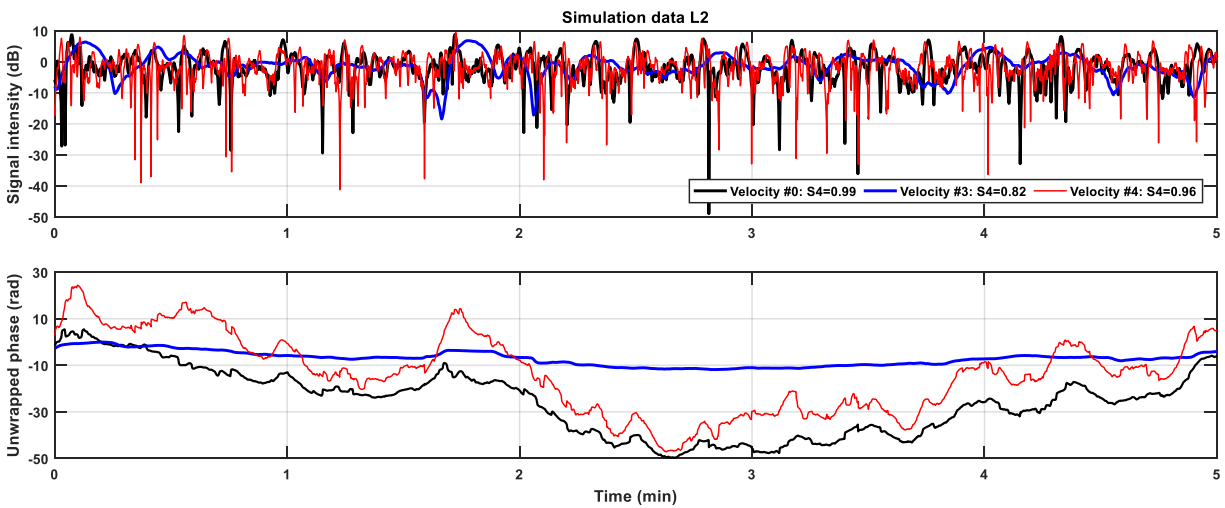


Figure 7-27. Same as Figure 7-25 but for GPS L2 band.

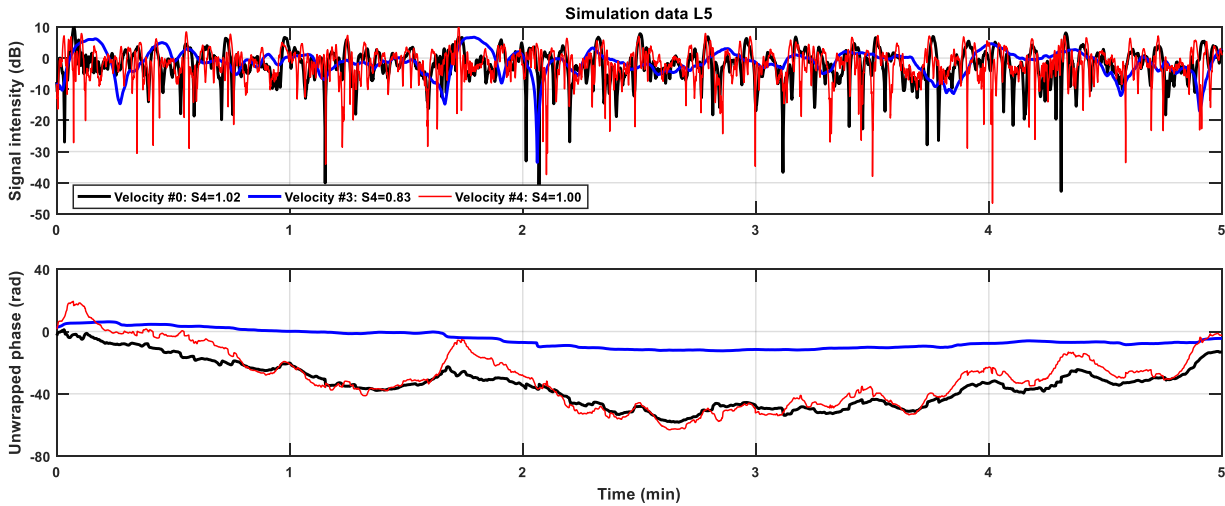


Figure 7-28. Same as Figure 7-25 but for GPS L5 band.

7.5. Concluding Remarks on Scintillation Signal Simulation

In this chapter, two scintillation simulators have been implemented based on the two-dimensional two-component power-law phase screen theory. The first simulator uses the traditional phase-screen wave propagation method to mainly simulate scintillation signals on a stationary receiver platform. The second simulator utilizes the time-domain data surrogate method to generate scintillation signals with various dynamics of the receiver platform. In both scintillation simulators, a segment of real initialization data is used to facilitate the extraction of ionosphere irregularity structural and geometrical parameters, which enables the construction of the signal propagation model and the medium structure model. The similar characteristics of the real data and the simulation data for stationary receivers demonstrate that the two simulators can effectively reproduce the scintillation medium structure and produce similar strong scintillation signals to the initialization data

For stationary scintillation simulation, the simulated complex field at the observation plane is further modulated to generate GPS IF samples, which are then processed by conventional receiver signal tracking algorithms. Comparisons between the simulation data and the receiver-processed data further reveal the effects of receiver processing on signal characteristics.

For dynamic scintillation simulation, the time scaling factor ρ_F/v_{eff} plays an important role in determining the temporal structure of the output simulation signal, which can be affected by the propagation geometry, the irregularity drift velocity, and the receiver dynamics.

A summary of the results in this chapter is provided as follows:

- The simulated signals share numerous statistical similarities with the initialization data, including the signal intensity SDF and PDF, and general signal intensity and phase characteristics. This demonstrates the effectiveness of the models used in the simulation.
- Compared to the simulation data, the processed data have more frequent cycle slips, enhanced high-frequency noise in the signal intensity SDF, more deep fading events, and lower S_4 values. For the phase statistics, the processed signals are closer to the real data than to the simulation data, which further shows the effects of receiver processing. The smoothing effects of the receiver tracking loops are obvious in the statistics of phase change magnitude and phase change rate.
- A deeper fade is more likely to be associated with a more rapid phase change. The \log_{10} of the absolute value of the max phase rate and the fading depth appear to be linearly correlated. This quantitative relationship may provide a guidance for the receiver design to mitigate strong scintillation.

- When the drift velocity of the ionosphere is zero, the simulation signal decorrelation time becomes longer when the receiver moves along the geomagnetic field than when the receiver moves across the field. When the eastward drift velocity is not zero, the signal decorrelation time typically becomes longer when the receiver moves eastward along with the irregularities, and becomes shorter when the receiver carries a westward velocity.

There are several points that are worthy of remark in the end of this chapter. First of all, the phase screen and propagation model used in this simulator has been simplified to two dimensions which assumes infinite axial ratio of the ionosphere anisotropy. As a result, when the angle between the propagation direction and the geomagnetic field is small (e.g. below 3 degrees), the resulting simulation signal is no longer valid. Also, this model is not suitable for high-latitude scintillation simulation due to the increased complexity of the propagation geometry and ionospheric plasma dynamics. A full three-dimensional simulator for high-latitude scintillation simulation will be a subject in the future work.

Second, the first simulator based on the traditional phase-screen wave propagation method is only suitable for scintillation signal simulation on a stationary receiver platform, due to the limited scale of the propagation space and the large amount of computation. For signal simulation on dynamic platforms, the use of the newly developed data surrogate method is necessary. Conversely, the data surrogate method can be used for stationary scintillation simulation. Because of its simplicity and flexibility, the simulator based on the data surrogate method will be mainly used in future work.

In addition, for the current scintillation simulation on dynamic platforms, the value of ρ_F/v_{eff} used for each velocity scenario is set to a constant due to its small variance within a 5-minute interval when the receiver velocity is constant. When an acceleration is added, ρ_F/v_{eff} may change significantly during a 5-minute interval (or longer simulation time). Simulation of such signals require dividing the time into smaller segments and stitching segments together, assuming the signal in each segment is stationary.

8. CHAPTER 8 – RESULTS ON SCINTILLATION SIGNAL DETECTION

The SVM machine learning algorithm is proposed in this dissertation research to build new automatic scintillation signal detectors. Different from previous NP detectors, the SVM detectors do not rely on prior knowledge of the PDFs of different classes. Instead, they try to separate the classes with the maximum margin in the frequency domain. This chapter presents detailed training procedures and performance evaluations of the SVM-based amplitude and phase scintillation detectors. Additionally, the performance of the SVM detectors on simulated scintillation signals is also presented to verify the effectiveness of the detectors and the scintillation simulator.

8.1. Amplitude Scintillation Signal Detection

Jiao et al. [2016c, 2017b] first introduced the SVM-based amplitude scintillation detector, and discussed its detailed methodology and performance evaluation. This detector works on raw signal intensity measurements, so that no artifacts introduced by post-processing are included. This section summarizes the training, validation and testing procedures in this SVM amplitude scintillation detector.

8.1.1. Training Data and Observation Matrix

To train the SVM, empirical class labels are assigned to the training data based on visual inspection. 30 segments of data from Ascension Island, Hong Kong, and Jicamarca Peru are selected for training, in which scintillation signals are clearly distinguishable from the background via visual inspection. Only two class labels are assigned in this work: 0 for non-scintillation data and 1 for scintillation data.

Non-scintillation signals typically include background noise, multipath, and interference. Multipath usually affects signals with low-elevation angles, thus a 30° elevation mask is applied to the data to reduce the effect of multipath [Jiao *et al.*, 2013c; Jiao and Morton, 2015]. Also, some multipath can be distinguished with its daily repetitive nature for stationary receivers due to the repetition of GPS satellite orbits [Axelrad *et al.*, 2005]. Examples of repetitive multipath events can be found in Figure 7 in [Taylor *et al.*, 2012] and Figure 2.5 in [Jiao, 2013]. In addition, multipath has special frequency domain features caused by the gradually varying reflection angles, an example of which can be found in Figure 13 in [Xu and Morton, 2016].

Interference usually features spikes or persistent raise in the scintillation indices or the C/N_0 measurements. It is usually observed simultaneously on the signals from all visible satellites and is dependent on the signal frequency. This means interference is often observed on one or two GNSS bands but not on the other bands. Examples of interference events can be found in Figure 2.6 in [Jiao, 2013] and Figure 8 in [Jiao *et al.*, 2015].

With the knowledge of the distinguishable features of scintillation and non-scintillation signals, visual inspection is applied to all the training data to label the classes. A detailed list of the training data segments is provided in Table 8-1. Examples of the training data segments from the three locations are illustrated in Figure 8-1. The training data is divided into two groups: strong scintillation training data, which consists of 15 segments of data in 46 hours from Ascension Island and Hong Kong [Morton *et al.*, 2015b]; moderate scintillation training data, which consists of 15 segments of data in 67 hours from Peru. Total length of all the training data is approximately 113.5 hours. The ratio of scintillation over non-scintillation signals in the training data is around 1:2.4.

Table 8-1. Data used for training and validation. The data are divided into strong scintillation data from Ascension Island and Hong Kong, and moderate scintillation data from Jicamarca, Peru. The elevation mask for all the data is 30°

Location	PRN	Date	Start and End UTC	Duration
Ascension Island	14	03/07/2013	20:58:18 – 23:59:59	3h 01m 41s
	31	03/07/2013	23:22:24 – 23:59:59	0h 37m 35s
	14	03/08/2013	20:54:18 – 23:59:59	3h 05m 41s
	21	03/09/2013	20:17:39 – 23:59:59	3h 42m 20s
	31	03/10/2013	23:09:48 – 23:59:59	0h 50m 11s
Hong Kong	24	09/24/2013	12:38:57 – 16:26:53	3h 47m 56s
	24	10/05/2013	11:53:51 – 15:41:41	3h 47m 50s
	27	02/27/2014	11:00:00 – 14:30:29	3h 30m 29s
	27	03/01/2014	11:00:00 – 14:22:17	3h 22m 17s
	27	03/02/2014	11:00:00 – 14:18:11	3h 18m 11s
	01	03/05/2014	13:55:57 – 16:59:58	3h 04m 01s
	24	09/14/2014	12:25:21 – 16:14:56	3h 49m 35s
	24	09/15/2014	12:21:15 – 16:10:53	3h 49m 38s
	25	11/05/2015	12:09:03 – 15:20:59	3h 11m 56s
25	11/17/2015	11:20:39 – 14:33:17	3h 12m 38s	
Strong scintillation data subtotal				46h 11m 59s
Jicamarca, Peru	06	02/07/2013	00:00:01 – 02:48:17	2h 48m 16s
	01	02/13/2013	02:14:42 – 06:30:17	4h 15m 35s
	01	02/20/2013	01:46:21 – 06:01:53	4h 15m 32s
	20	02/21/2013	00:31:33 – 06:56:14	6h 24m 41s
	20	02/22/2013	00:27:39 – 06:52:23	6h 24m 44s
	20	03/06/2013	00:00:01 – 06:05:50	6h 05m 49s
	13	03/07/2013	01:32:57 – 05:44:35	4h 11m 38s
	20	03/07/2013	00:00:01 – 06:01:56	6h 01m 55s
	13	03/09/2013	01:25:03 – 05:36:41	4h 11m 38s
	20	03/11/2013	00:00:01 – 05:46:20	5h 46m 19s
	20	03/27/2013	00:00:01 – 04:43:53	4h 43m 52s
	04	03/07/2014	03:49:21 – 07:07:44	3h 18m 23s
	13	03/07/2014	00:51:03 – 05:04:11	4h 13m 08s
	19	03/12/2014	00:00:03 – 01:17:08	1h 17m 05s
	04	03/19/2014	03:00:42 – 06:18:50	3h 18m 08s
Moderate scintillation data subtotal				67h 16m 43s
Total				113h 28m 42s

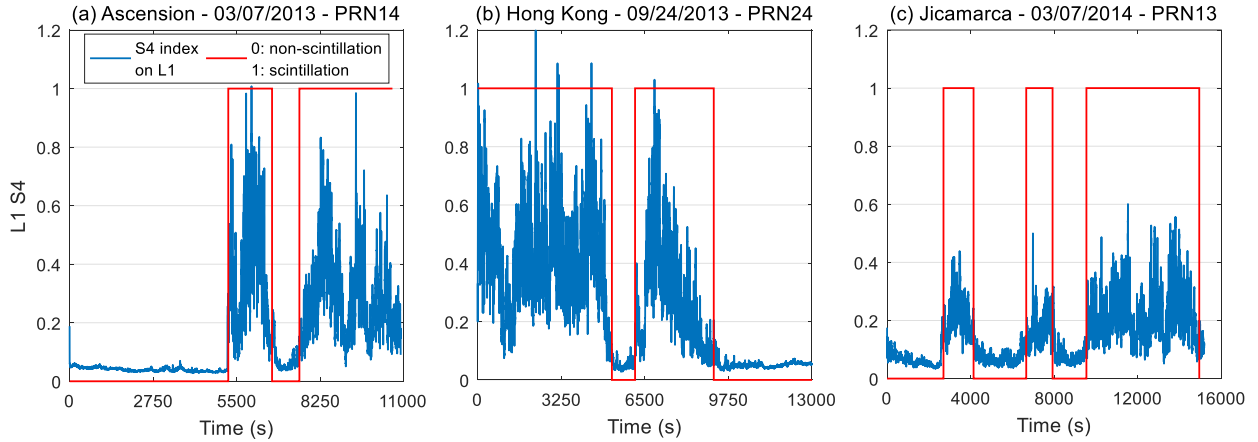


Figure 8-1. Examples of S_4 index values on GPS L1C/A in the training data from (a) Ascension Island, (b) Hong Kong, and (c) Jicamarca, Peru. Scintillation observed in Ascension Island and Hong Kong is generally stronger than that observed in Jicamarca, Peru. The stair lines in the plot are class labels, assigned manually.

To extract the column training vectors $\{d_p; \mathbf{x}_p\}_{p=1}^P$ discussed in Section 5.2, all training data is partitioned into 3-minute blocks without overlap. The 3-minute length is selected so that the decision resolution is neither too coarse nor too fine. The first entry of each column vector is the class label assigned manually (0 or 1) with expert decisions that were made via visual inspection of S_4 index values. The second and third entries are the maximum and the average S_4 index values within the block. The S_4 index is calculated with a sliding window of 10-second long, which shifts 1 second at a time [Jiao and Morton, 2015]. Thus, the sampling rate for S_4 is 1 Hz. The second and third entries are optional in the training in order to test their importance in determining the decision boundary.

A short-time Fourier Transform (STFT) is then performed on the training data to obtain the spectrogram with a non-overlap window of 3 minutes. The number of fast Fourier Transform (FFT) points is limited to 2048 to avoid the frequency resolution being too fine. A power spectrum density (PSD) function for each block of data can be acquired from the spectrogram, which is entered as

the rest of the entries in the training vector. To reduce the impact of the direct current component, the first value in the PSD is discarded. Also, PSD for frequency components above 2 Hz is also discarded to reduce the impact of high frequency noise, which is unlikely to be contributed by scintillation. These column training vectors when combined constitute a training observation matrix that can be used as an input to the SVM to train the system. The structure of a training vector is summarized in Table 8-2.

Table 8-2. Content of a column training vector used in the SVM amplitude scintillation detector

Row #	Content	Note
1 st row:	Class label	0: non-scintillation 1: scintillation
2 nd row	Maximum S_4	Selective in training
3 rd row	Mean S_4	
4 th row	PSD in dB from STFT	First value in PSD is discarded; Only components below 2 Hz are included
:		
End row		

The author would like to emphasize that from the perspective of scintillation physics, the 3-minute window length is also a reasonable choice. This is because S_4 and σ_ϕ indices are conventionally calculated every minute, which is the minimum window size for PSD calculation. Scintillation observed within several minutes on the same satellite signal is caused by the same ionospheric irregularity structure due to the relatively slow satellite scan velocity compared to the scale of irregularities causing scintillation [Kintner *et al.*, 2004; Jiao *et al.*, 2016a]. The 3-minute length is a good balance between satisfying the stationary signal assumption (which requires a relatively short time window) and maintaining sufficient PSD resolution (which requires a sufficiently long window length).

8.1.2. Validation Performance

A 25% hold-out validation is configured to evaluate the performance of the training. This means 75% of the training data listed in Table 8-1 is selected randomly to train the machine, while the rest is reserved to validate the trained system. The validation procedure is similar to testing, but the ground truth of the correct classes is known. To evaluate the impact of different factors on the performance, the following combinations (a total of 12) are applied in the training:

- Training data (including validation): strong scintillation only, moderate scintillation only, and all the data in Table 8-1 are used respectively.
- Observation matrix: all the entries in the training vectors described in subsection 8.1.1 are considered; the second and the third entries regarding the S_4 index values are excluded.
- Learning algorithm: linear SVM; medium Gaussian kernel SVM with a kernel scale (i.e. variance) of 9.1.

The performance is evaluated in terms of ROC curves and confusion matrices (Section 5.1). Figure 8-2 through Figure 8-4 show the performance analysis for the 12 combinations described in the previous paragraph. The confusion matrix under each scenario is obtained from classifying the 25% validation data using the trained model. This operating point is also marked as the circle on the corresponding ROC curve, with its corresponding TPR and FPR values listed in Table 8-3. The numbers in each confusion matrix are the validation sample numbers, and the percentages sum up to 100% for all four elements. It is noteworthy that the performance varies with every run of the program, because the 75% training data is selected randomly from the entire dataset. Also, the operating point is not necessarily the best operating point for the trained model, due to potential bias introduced by the training data and the variation in the validation data.

From Figure 8-2, it can be seen that the classifiers provide almost perfect ROC curves using only strong scintillation data in the training and validation. The overall accuracy is above 98% for all cases. This is not surprising, as strong scintillation signals contain significantly different features from those of non-scintillation signals. It is also interesting to note that, excluding S_4 features does not degrade the performance in any way. This means the PSD of the raw signal intensity already contains all the information needed to separate the two classes. Moreover, linear SVM and medium Gaussian SVM show similar accuracy, indicating that the two classes are linearly separable in the frequency domain alone.

Figure 8-3 shows the classification performance when only using moderate scintillation data in the training and validation. Not surprisingly, the general performance is around 90% accuracy. While this outcome is still good, it is not as impressive as using only strong scintillation data. Including S_4 features does help to improve the results. This is because the distinguishing signature in the frequency domain is relatively weak in this case, and the empirical class labels were assigned partially based on visual inspection of S_4 index values.

When using both strong and moderate scintillation data for training and validation, the performance of the classifiers is between those in Figure 8-2 and Figure 8-3. Figure 8-4 shows a good performance of an overall accuracy above 95%. Again, the two SVMs perform similarly, and excluding S_4 features in the training does not significantly affect validation accuracy.

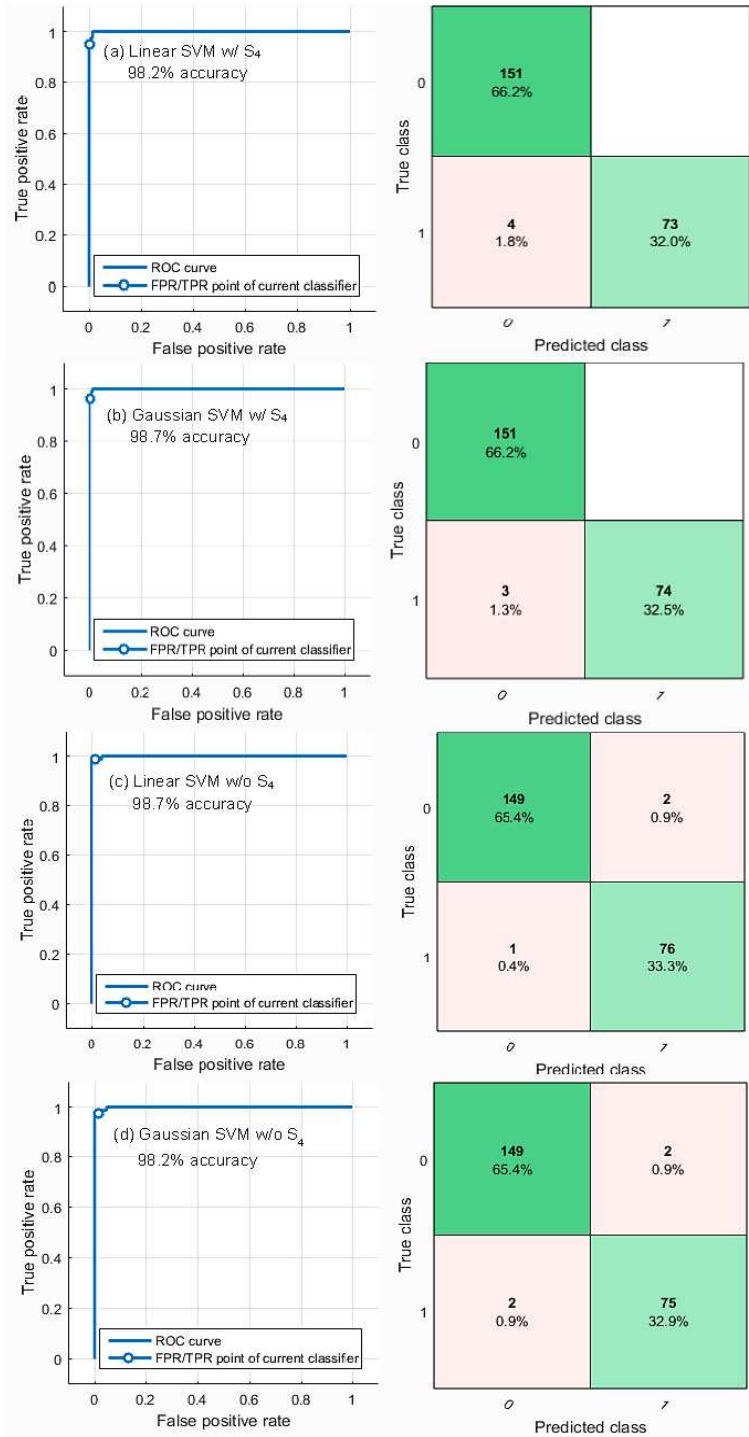


Figure 8-2. Validation performance on (a)(c) linear SVM and (b)(d) medium Gaussian SVM. Only strong scintillation data from Ascension Island and Hong Kong are used here for training and validation. S_4 features (2nd and 3rd entries in training vectors) are included in training in (a) and (b), but excluded in (c) and (d). The circle markers on the ROC curves on the left are the operating points for the confusion matrices on the right. The total accuracies of the classifiers are denoted in the labels on the left.

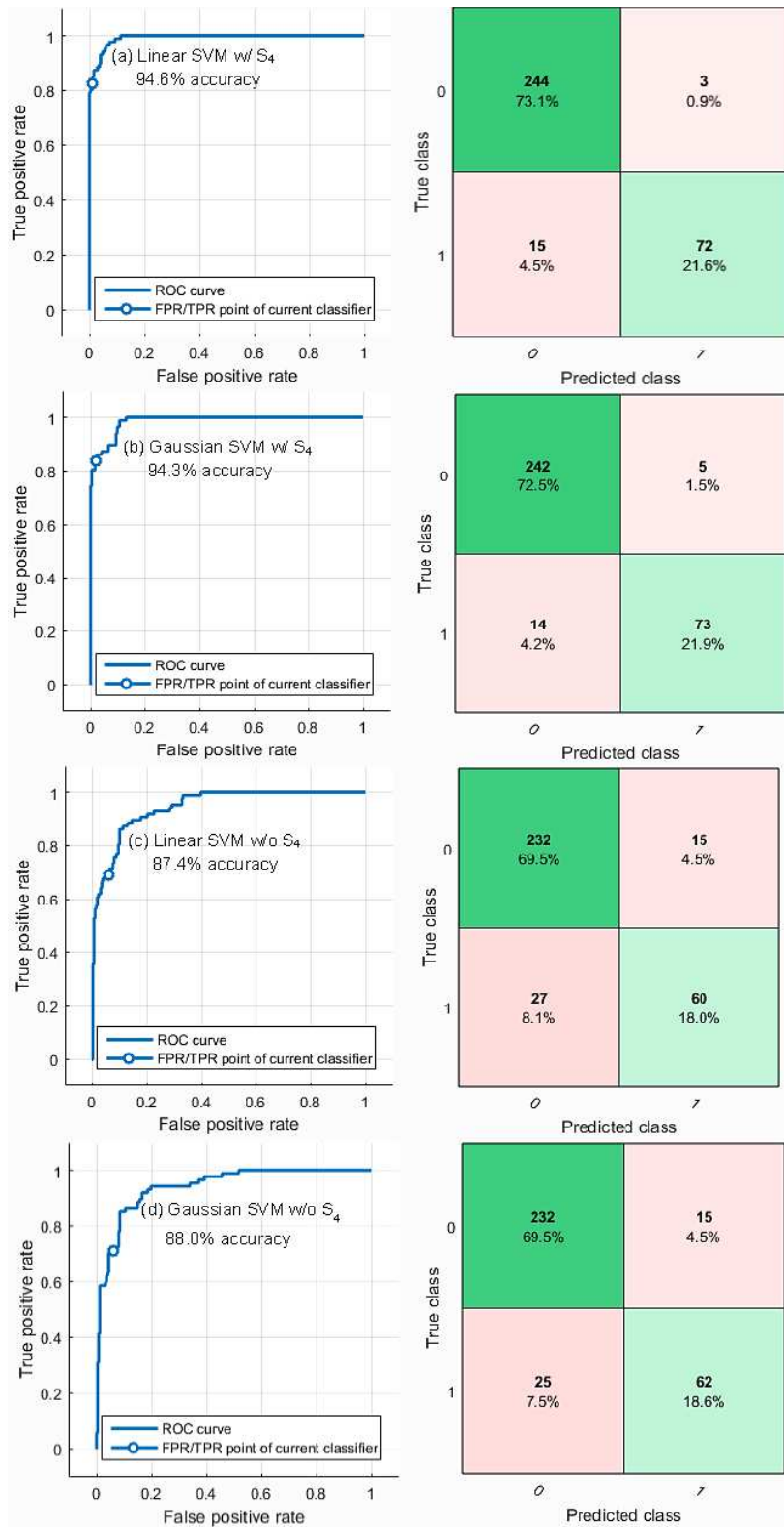


Figure 8-3. Same as Figure 8-2, but only moderate scintillation data from Jicamarca, Peru is used here for training and validation.

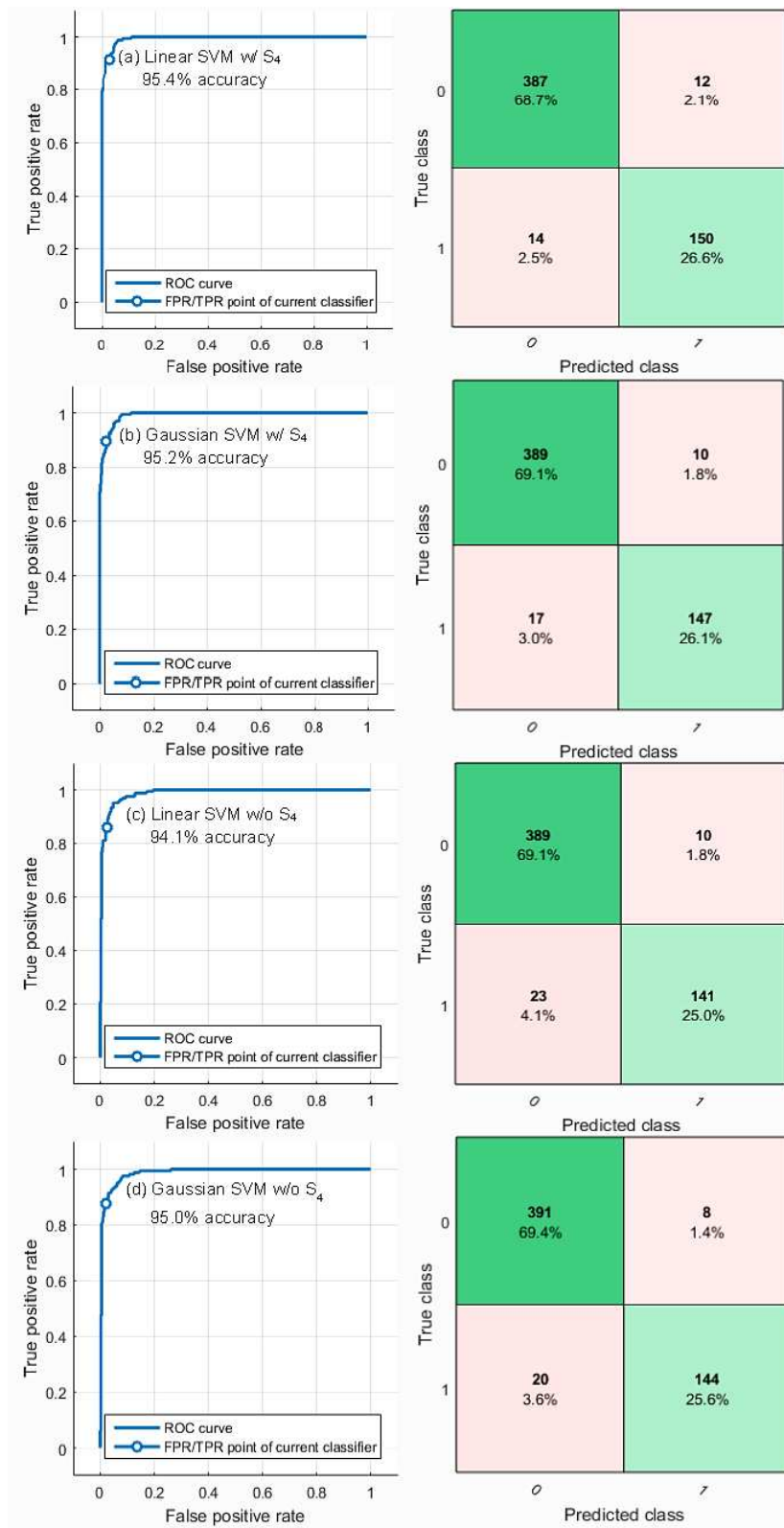


Figure 8-4. Same as Figure 8-2, but all the data listed in Table 8-1 is used here for training and validation.

Table 8-3. The TPR and FPR at the operating points in the validation for the 12 combinations shown in Figure 8-2, Figure 8-3, and Figure 8-4

Training Data Set	SVM Algorithm	TPR	FPR
Strong scintillation only	Linear w/ S ₄	0.95	0
	Gaussian w/ S ₄	0.96	0
	Linear w/o S ₄	0.99	0.01
	Gaussian w/o S ₄	0.97	0.01
Moderate scintillation only	Linear w/ S ₄	0.83	0.01
	Gaussian w/ S ₄	0.84	0.02
	Linear w/o S ₄	0.69	0.06
	Gaussian w/o S ₄	0.71	0.06
All the data in Table 8-1	Linear w/ S ₄	0.91	0.03
	Gaussian w/ S ₄	0.90	0.03
	Linear w/o S ₄	0.86	0.03
	Gaussian w/o S ₄	0.88	0.02

8.1.3. Test on Novel Data

This section presents some test results on novel data using the trained SVMs. To demonstrate the effectiveness of the trained models, a segment of scintillation data from a fourth location in Singapore is firstly used. Data from Singapore is not involved in the training. In general, scintillation observed there falls into the moderate scintillation category [Jiao *et al.*, 2015; Jiao and Morton, 2015; Morton *et al.*, 2015b].

Considering that there are no truth references for the classes in the novel data, scintillation event trigger results obtained from the hard threshold-based trigger system discussed in subsection 1.5.3 are used for comparison. To familiarize readers with this trigger system, a brief summary of the criteria in the system is provided here (see [Jiao *et al.*, 2013c; Jiao and Morton, 2015] for more detailed criteria):

- The elevation mask is 30° ;
- The threshold for S_4 is 0.2 for equatorial data;
- To exclude certain interference cases, the S_4 value needs to remain above the threshold for at least 30 seconds;
- An event detected within 3 minutes from the end of another event is combined with the previous event.

The last criterion is slightly different from that in previous literature (it was 5 minutes), as the selection of this number is relatively arbitrary. The implementation of this criterion is based on the rationale that scintillation observed within several minutes should be caused by the same ionospheric irregularity [Kintner *et al.*, 2004]. We use 3 minutes here to comply with the 3-minute block size used in this detection study. Alternatively, to accommodate this last criterion in the trigger system, two events detected by the SVMs that are only 3 minutes apart will also be combined.

Figure 8-5 shows the test results on a segment of novel data collected on GPS L1C/A PRN01 from 13:19:55 to 17:12:39 UTC on March 26, 2012 in Singapore. Similar to Figure 8-1, each subplot shows the S_4 index values and the prediction of classes for all blocks. Subplots Figure 8-5 (a) through (l) correspond to the 12 combinations mentioned in subsection 8.1.2, in which different SVMs, training data sets and observation matrices are implemented. Overall, by visual inspection all the trained models in the 12 scenarios are able to capture the major scintillation events in the novel data. Models trained by only strong scintillation data are also able to make correct classification for major events as shown in subplots Figure 8-5 (a) through (d), although the

intensity of most events in this test data is moderate. Moreover, these results again demonstrate that S_4 features are not necessarily needed in the observation matrix during training. Compared with the detection result from the hard threshold-based trigger system shown in subplot (m), the SVM detectors not only detect major events, but also capture some weak scintillation events with S_4 below 0.2. In spite of the fact that these weak events are not likely to cause problems in commercial receivers, they are useful for scientific study of ionosphere structures and scintillation mechanisms.

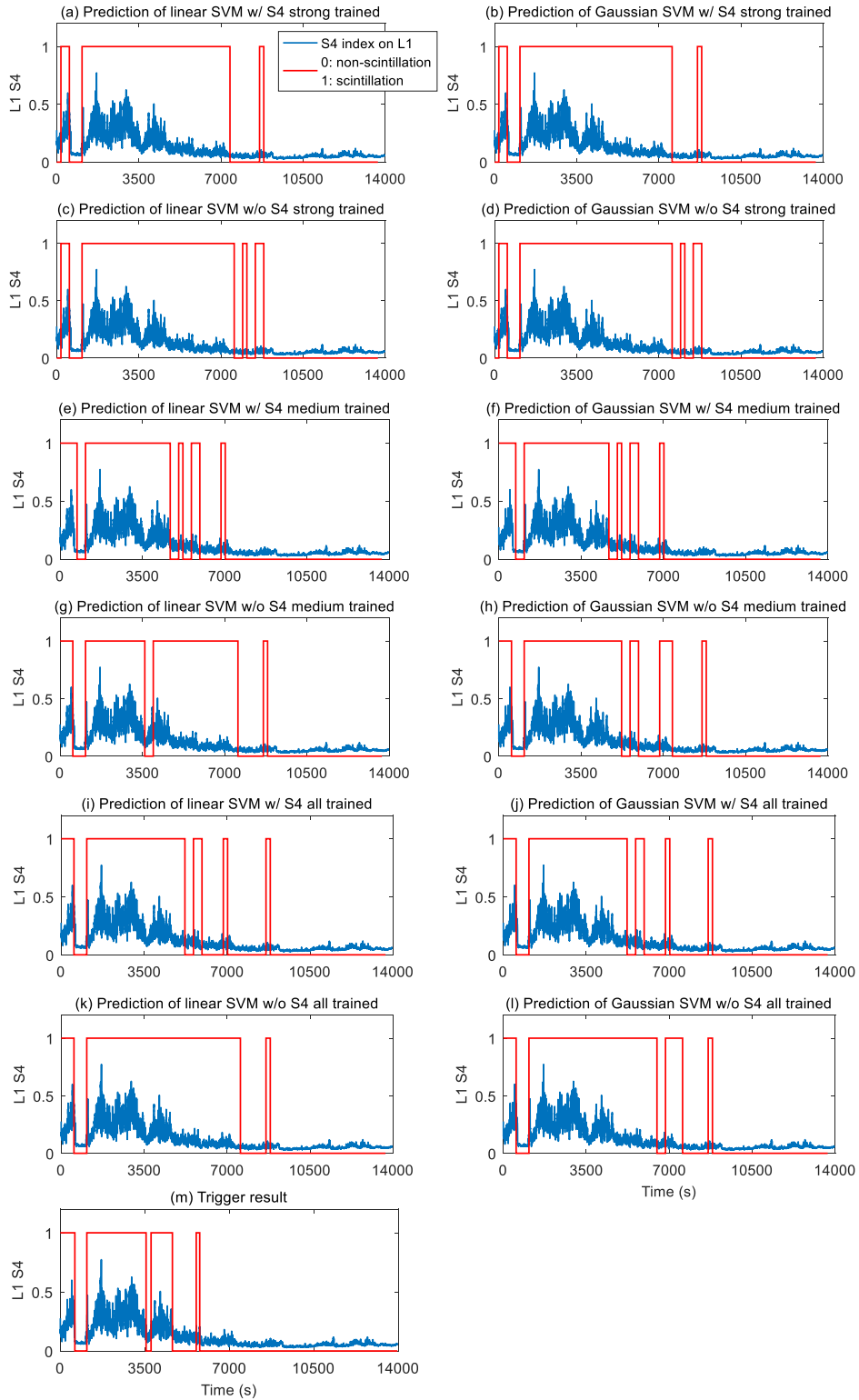


Figure 8-5. Test results on the novel data from Singapore. The data was collected on GPS L1C/A PRN01 from 13:19:55 to 17:12:39 UTC on March 26, 2012. Subplots (a) through (l) correspond to the test results using the 12 SVM variations. Last subplot (m) shows the trigger result.

Additional tests on the trained models have been conducted with a large amount of novel data from all four receiver sites. Incorrect classification was observed in strong scintillation test data classified by SVMs trained by only moderate scintillation data. Figure 8-6 shows some examples of incorrect classification results using a segment of data from Ascension Island. This segment of data contains two major events: a strong one in the first third and a moderate to strong one in the last third. Most classifiers have trouble making a right prediction on the first event. This may be because the moderate scintillation data used in the training does not contain enough distinguishable signatures of scintillation signals from non-scintillation signals, and some of the more insignificant signatures learned by the machine can be misleading. On the other hand, with models trained by only strong scintillation data, no misclassification was observed during testing (see Figure 8-7). Models trained by all the data listed in Table 8-1 also make no obvious misclassification most of the time (occasionally on strong scintillation but rarely). In short, SVMs trained by only strong scintillation are preferred in the test.

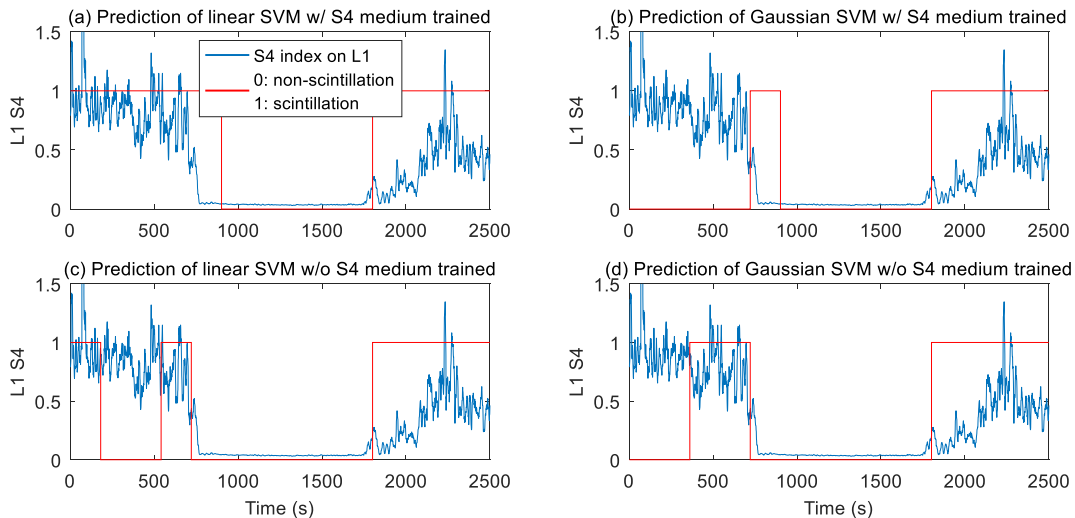


Figure 8-6. Incorrect classification results on a segment of novel data containing strong scintillation signals. The data was collected on GPS L1C/A PRN31 from 23:14:00 to 23:59:59 UTC on March 9, 2013 on Ascension Island.

Figure 8-7 through Figure 8-9 show some more test results on segments of novel data collected from Ascension Island, Hong Kong, and Peru, using the SVM detectors trained by only strong scintillation data. Detection results from the hard threshold-based trigger system are also shown in subplots (e). In Figure 8-9, compared with the trigger results, the SVM detectors not only detect major events, but also capture some weak scintillation events and combine them with adjacent bigger events. This again shows that SVM detectors make decisions based on the nature of scintillation instead of solely on the S_4 index values.

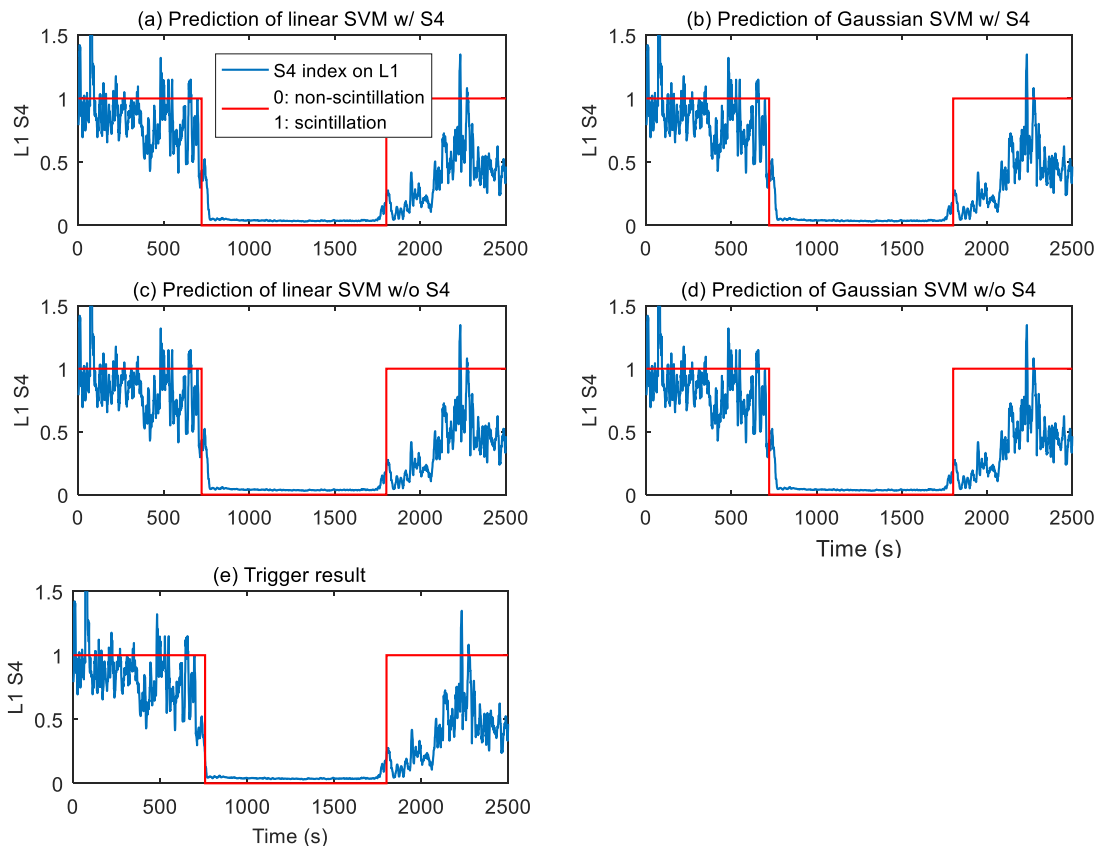


Figure 8-7. Test results on the novel data from Ascension Island. The data was collected on PRN 31 from 23:14:00 to 23:55:39 UTC on March 9, 2013. Subplots (a) through (d) correspond to the results using the four training combinations. Subplot (e) shows the result using the trigger criteria.

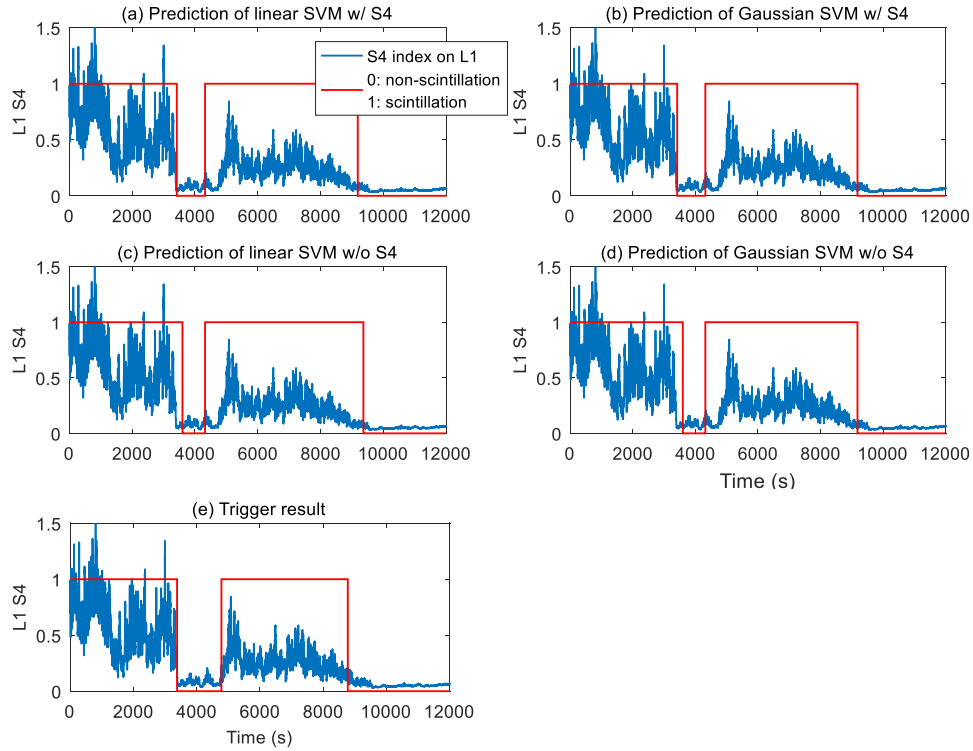


Figure 8-8. Same as Figure 8-7, but for test data from Hong Kong which was collected on PRN 24 from 12:18:27 to 15:38:26 UTC on September 29, 2013.

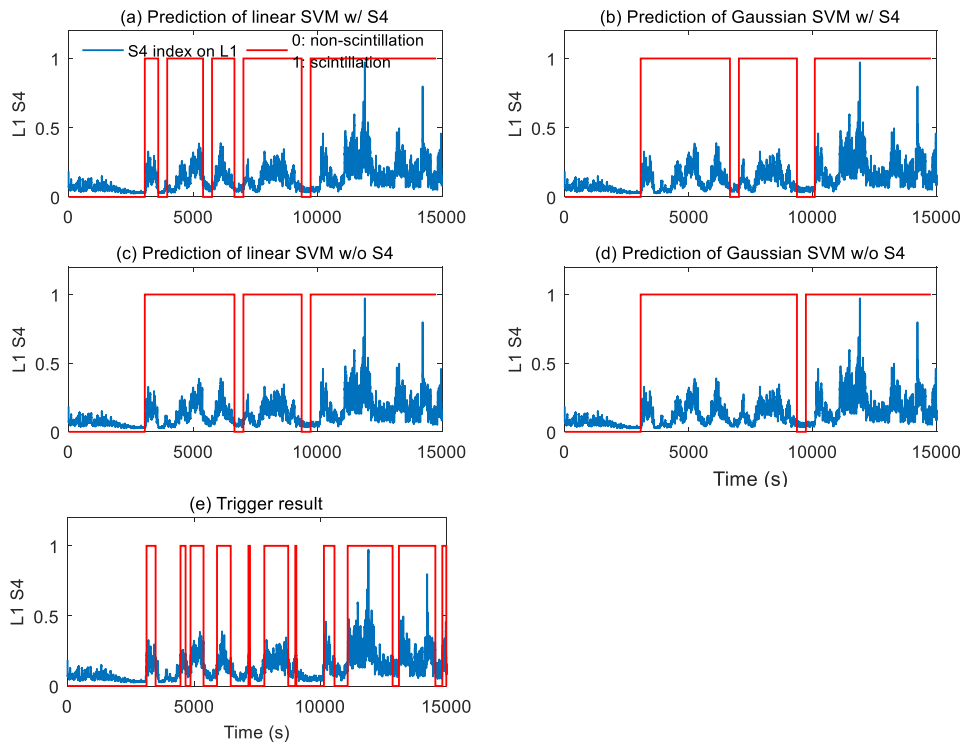


Figure 8-9. Same as Figure 8-7, but for test data from Jicamarca, Peru which was collected on PRN 23 from 00:22:06 to 04:32:05 UTC on March 11, 2013.

8.2. Phase Scintillation Signal Detection

As a follow-up study of the work of *Jiao et al.* [2016c, 2017b], *Jiao et al.* [2017a, 2017c] extended the SVM-based detection technique to detect phase scintillation events observed in both high-latitude and low-latitude regions. The detector shows good generalization capability with data from a vast range of locations. This section summarizes the training, validation, and testing procedures in this phase scintillation detector.

8.2.1. Training and Validation Performance

The training procedure of the phase scintillation detector is very similar to that for amplitude scintillation detection as described in Section 8.1.1. A total of 28 hours of data consisting of 30 segments from Gakona, AK are selected for training. The training data are partitioned into 3-minute blocks without overlap. Empirical class labels are assigned to the training data based on visual inspection of the values of σ_ϕ index within each block (an example shown in Figure 8-10a). Same as in the amplitude scintillation detector, only two class labels are assigned: 0 for non-scintillation data, and 1 for scintillation data. With the empirical class assignment, the number of non-scintillation blocks versus the number of scintillation blocks in the training data is around 1:1.33. Detailed information of the training data set is listed in Table 8-4.

Table 8-4. Training data set from Gakona, AK

Date	PRN	Start UTC	End UTC	Duration
10/01/2012	06	00:42:42	02:55:47	2:13:05
	18	01:46:44	03:28:04	1:41:20
	21	00:13:51	01:09:34	0:55:43
10/08/2012	13	08:43:38	10:16:26	1:32:48
	23	08:19:56	09:34:04	1:14:08
	26	13:23:23	14:45:53	1:22:30
10/09/2012	10	10:48:42	11:25:22	0:36:40
	13	09:40:50	10:16:43	0:35:53
	14	04:06:54	04:58:08	0:51:14
	18	01:53:36	02:25:58	0:32:22
	20	06:44:23	07:22:05	0:37:42
	31	06:43:43	07:18:01	0:34:18
10/13/2012	05	11:19:26	12:24:09	1:04:43
	07	11:38:32	12:29:06	0:50:34
	08	11:38:51	12:43:17	1:04:26
10/14/2012	05	11:16:39	12:19:37	1:02:58
	07	10:49:10	11:54:27	1:05:17
	08	12:02:45	12:43:21	0:40:36
	26	12:33:56	13:58:42	1:24:46
11/01/2012	28	13:15:45	13:47:56	0:32:11
11/14/2012	07	08:43:37	09:17:53	0:34:16
	10	08:02:38	08:28:59	0:26:21
	13	08:51:20	09:12:34	0:21:14
	20	04:23:04	05:27:24	1:04:20
	32	03:19:14	04:03:20	0:44:06
03/17/2013	06	15:16:18	15:53:15	0:36:57
	16	12:49:54	13:44:46	0:54:52
	18	13:48:03	15:04:57	1:16:54
	22	15:14:52	15:51:35	0:36:43
	32	19:06:56	19:53:45	0:46:49
Total				27:55:46

The content of a training vector for a 3-minute data block is listed in Table 8-5, which is a slight variation of Table 8-2 in Section 8.1.1. The first entry in a column training vector is the class label assigned manually. The second and third entries are the maximum and the average σ_ϕ index values

within the block. As with the S_4 index calculation, the σ_ϕ index is calculated with a 10-second sliding window that shifts 1 second at a time, making the sampling rate for both indices 1 Hz [Jiao and Morton, 2015]. To test the impact of the σ_ϕ index values on the performance of the SVM detector, the second and third entries are selective in the training. The rest of the entries in the training vector are PSD for different frequencies using STFT on detrended phase measurements. A visualization of the PSD functions (i.e. spectrogram) for an example of training data is shown in Figure 8-10b.

Table 8-5 Content of a column training vector used in the SVM phase scintillation detector. Each training vector corresponds to a training data block of 3 minutes in length

Row #	Content	Note
1 st row:	Class label	0: non-scintillation 1: scintillation
2 nd row	Maximum σ_ϕ	Selective in training
3 rd row	Mean σ_ϕ	
4 th row	PSD in dB from STFT of the detrended phase measurements	Only components below 2 Hz are included
⋮		
End row		

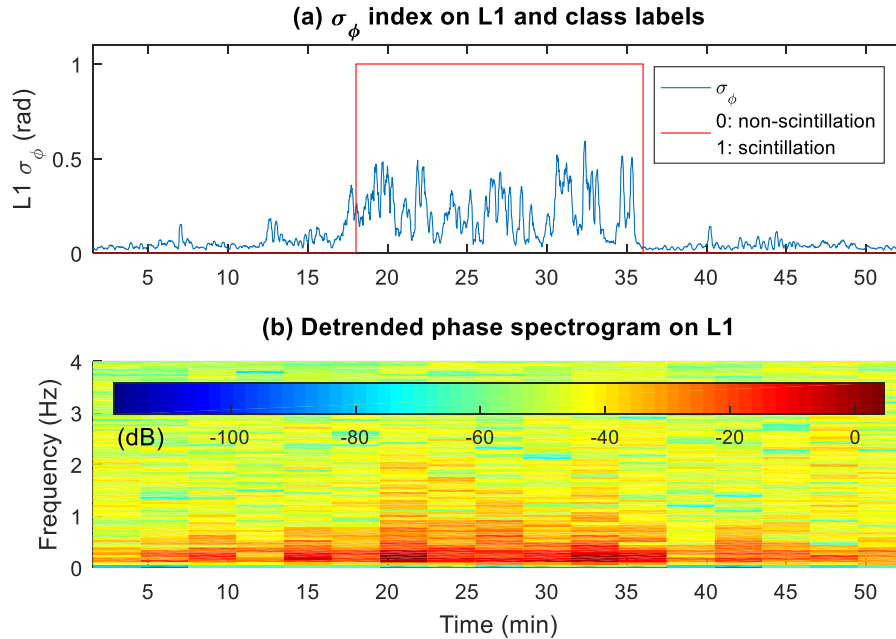


Figure 8-10. An example of training data from Gakona, AK. The data was collected on PRN 16 from 12:49:54 to 13:44:46 UTC on March 17, 2013. Subplot (a) shows σ_ϕ index values and class labels assigned manually. Subplot (b) shows the spectrogram on the detrended phase measurements with 3-minute non-overlapping windows.

A notable difference between the phase scintillation detection and the amplitude scintillation detection is that the measurements used here to calculate PSD functions are detrended phase measurements, whereas the measurements used in amplitude scintillation detection are raw signal intensity without detrending. The detrending procedure is necessary for phase scintillation detection in order to filter out low-frequency components in the phase measurements. These low-frequency components include Doppler and clock drift etc., which may drastically affect the PSD for different satellite orbits and different time periods. The detrending method used here is the conventional 6th order Butterworth high-pass filter with a cutoff frequency at 0.1 Hz [Van Dierendonck et al., 1993]. Although this detrending method is under debate [Forte and Radicella, 2002; Beach, 2006], the selection of the detrending method should not affect the SVM design approach.

The validation method used for phase scintillation detection is the so-called 5-fold cross-validation due to limitations in the amount of available training data. In this method, the training data is randomly partitioned into 5 subsets of equal sizes. One subset is retained as the validation data to test the model that is trained by the remaining 4 subsets. This cross-validation process is then repeated 5 times, so that each of the subset is used exactly once as the validation data set. The final validation performance is the average of the 5 validation results [Haykin, 2009].

The validation performance of the phase scintillation detector using SVM algorithms is presented in the form of ROC curves and confusion matrices (Figure 8-11). There are four variations of the detector implementation: the σ_ϕ features (2nd and 3rd entries) are either included (Figure 8-11ab) or excluded (Figure 8-11cd) in the training vectors; and the SVM algorithm is either linear SVM (Figure 8-11ac) or medium Gaussian kernel SVM with a kernel scale of 9.1 (Figure 8-11bd).

The ROC curves shown on the left panels in Figure 8-11 demonstrate relatively good validation performance of the trained phase scintillation detector, although the general performance of the amplitude scintillation detector seems to be slightly better as presented in Section 8.1.2. The four variations of the phase scintillation detector show comparable performance with an average accuracy of around 92%. The red solid dot on each ROC curve is the operating point of the current detector, which corresponds to the confusion matrix on the right. The TPR and FPR at the operating point are also denoted which can be calculated directly from the sample numbers in the confusion matrix. It should be noted that the validation performance varies somewhat with different selection of training subsets, but the results shown in Figure 8-11 are representative.

The results in Figure 8-11 demonstrate the capability of the SVM detector to successfully detect ionospheric phase scintillation. The results also indicate that non-scintillation and scintillation events are almost linearly separable in the high-dimensional space. Furthermore, excluding σ_ϕ features from the training vectors does not appear to influence the validation performance of the phase scintillation detector.

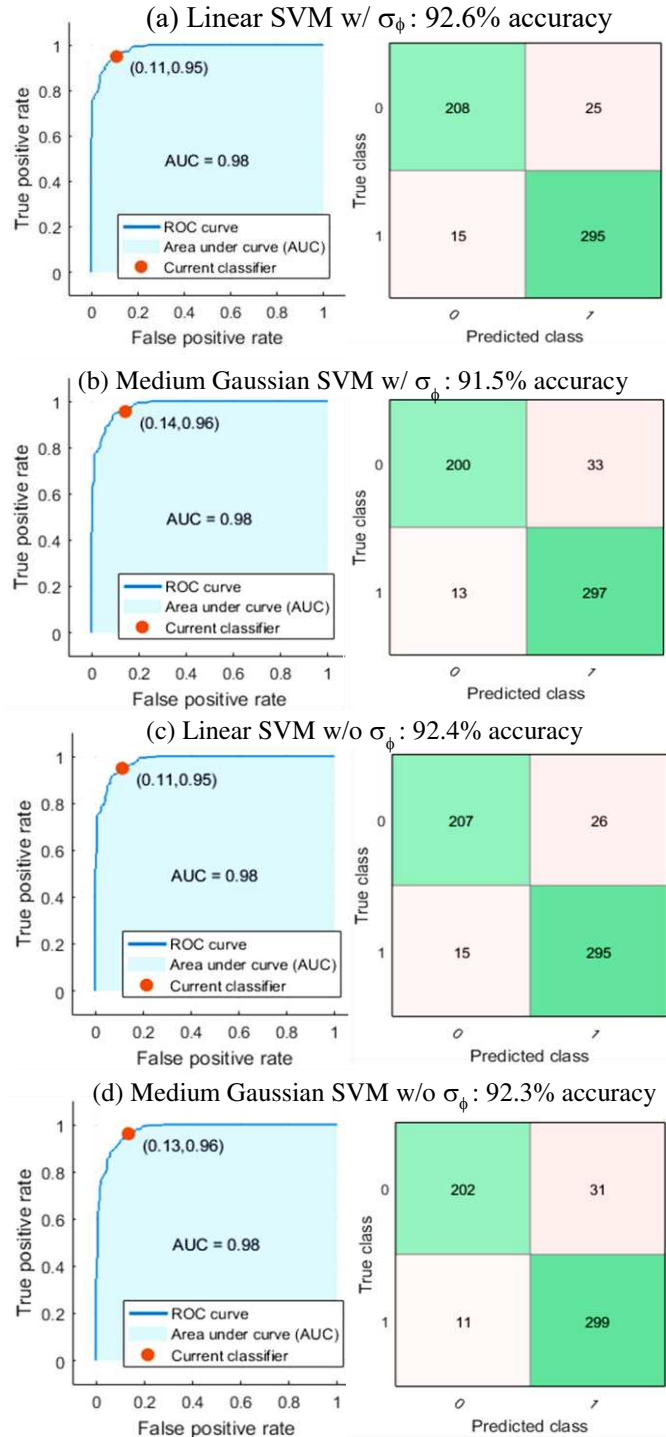


Figure 8-11. Validation performance on (a)(c) linear SVM and (b)(d) medium Gaussian SVM. σ_ϕ features (2nd and 3rd entries in training vectors) are included in (a) and (b) in the training, but excluded in (c) and (d). The red dots on the ROC curves on the left are the operating points for the confusion matrices on the right, with the corresponding TPR and FPR denoted. The total accuracies of the classifiers are given in the subplot titles.

8.2.2. Test Performance on Novel Data

To test the generalization capability of the SVM phase scintillation detector that is trained on data solely from Gakona, AK, several segments of novel data from Gakona and from four other stations are used. Since the truth references for the classes in the novel data are unknown, the detection results obtained from the hard threshold-based trigger system developed in [Taylor et al., 2012] are also presented to provide visual comparisons. The criteria in the threshold-based trigger system for phase scintillation is similar to those for amplitude scintillation, except that the threshold here is set for the σ_ϕ index. A brief summary of the trigger criteria is given as follows: a) The threshold for σ_ϕ index is 15° (0.26 rad); b) the σ_ϕ index needs to remain above the threshold for at least 30 seconds; c) An event detected within 3 minutes from the end of another event is combined with the previous event. To comply with the last criterion, in the SVM detector two detected events that are only three minutes apart will also be combined.

Figure 8-12 and Figure 8-13 are test results on two segments of novel data from Gakona and Poker Flat. Subplots (a) through (d) correspond to the test results using the four variations of the phase scintillation SVM detector, and subplots (e) represent results obtained by the trigger system. Results in Figure 8-12 and Figure 8-13 show that all four variations of the SVM detector are able to capture strong scintillation events. However, the SVM detector trained *with* σ_ϕ features show obvious miss-detection of moderate to weak scintillation events (e.g. between 70-120 min in Figure 8-13b). On the contrary, the SVM detector trained *without* σ_ϕ features seem to have no problem in detecting weak to strong scintillation, and it has a tendency to combine events compared to trigger results. Overall, the results generated by the SVM detector trained without σ_ϕ appear to be able to capture the events as a whole, instead of small segments with moderate and

weak scintillations, while the SVM detector trained with σ_ϕ appears to be effective in identifying strong scintillation events.

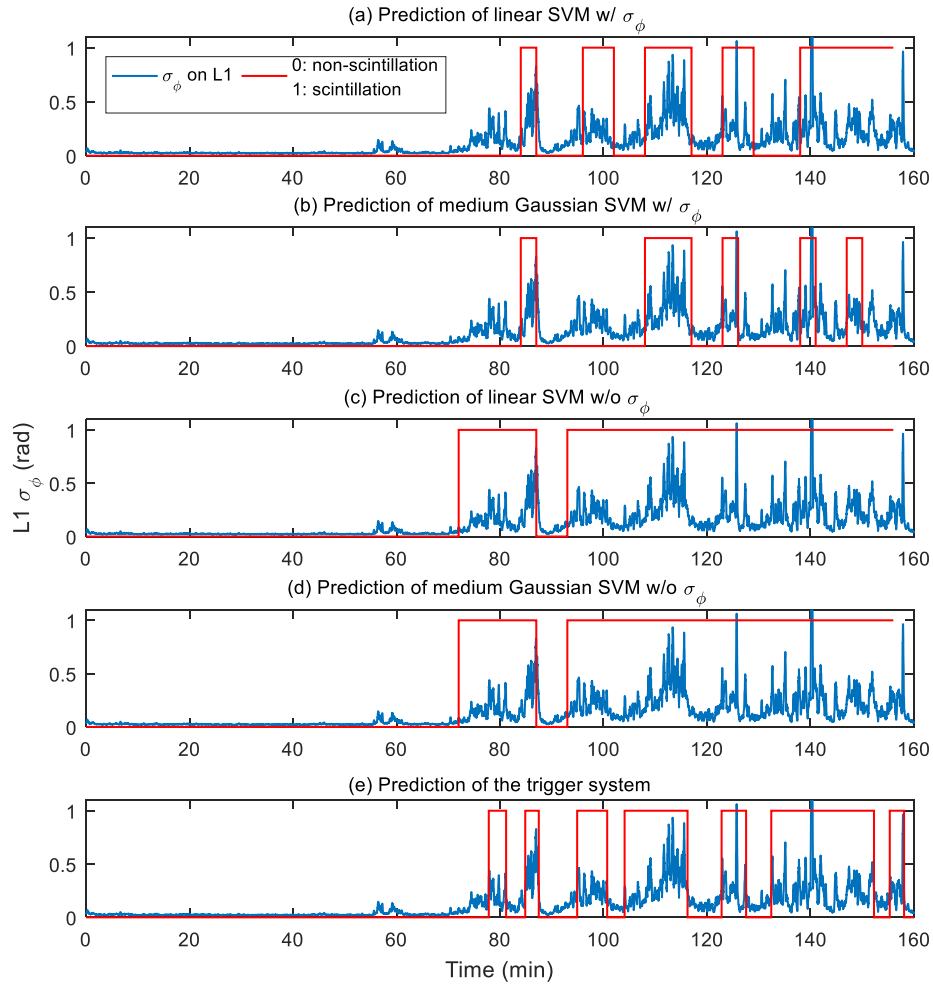


Figure 8-12. Classification prediction results on novel data collected on GPS L1C/A PRN01 from 01:43:18 to 04:23:18 UTC on November 14, 2012 at Gakona, AK. Subplots (a) through (d) are test results using different SVM algorithms with (w/) and without (w/o) σ_ϕ features. Last subplot (e) shows the trigger result using the four trigger criteria.

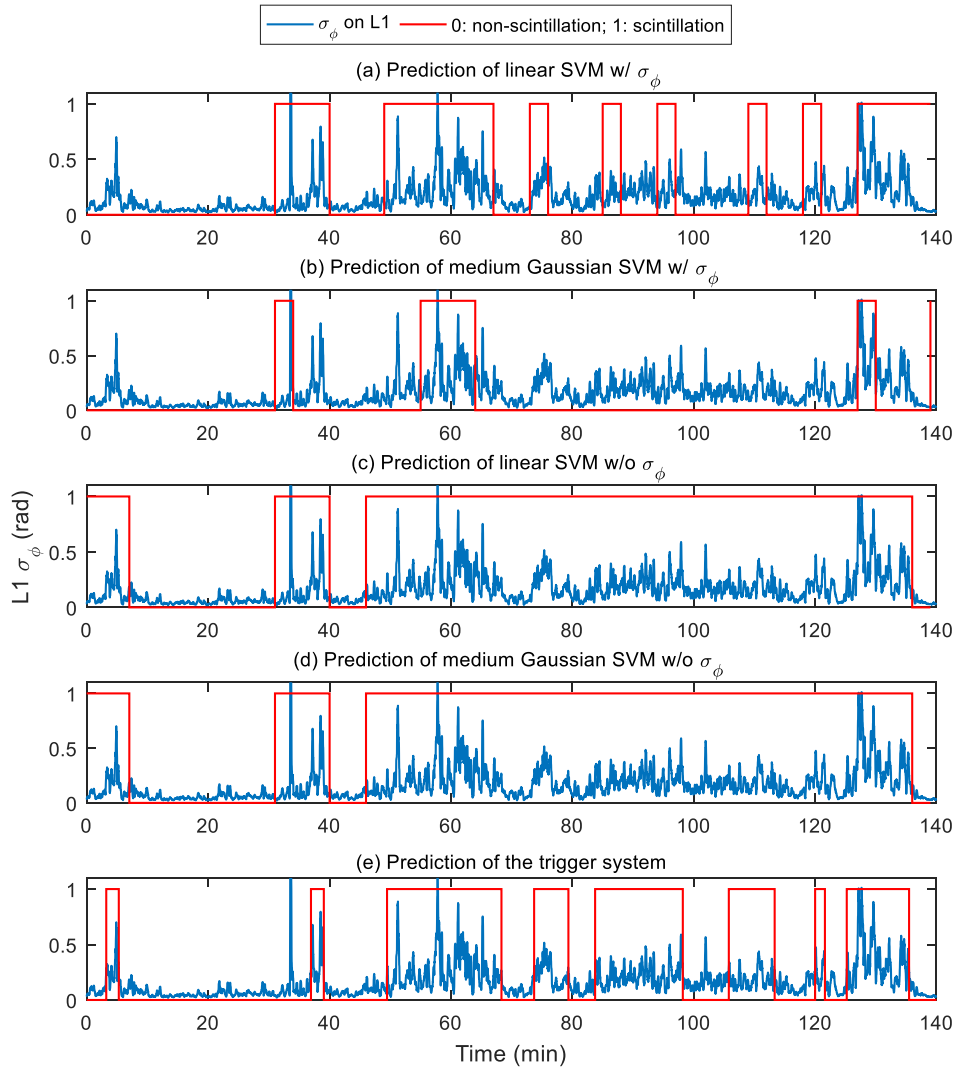


Figure 8-13. Classification prediction results on novel data from Poker Flat, AK. The data was collected on GPS L1C/A PRN25 from 11:27:33 to 13:47:33 UTC on December 20, 2015.

The apparent miss-detection of the SVM detectors trained with phase scintillation index features is not observed in the amplitude scintillation detector. One possible explanation for this phenomenon is that σ_ϕ index is far more complicated than S_4 index in the training data, which may have confused the SVM during training process. This phenomenon again shows that the absolute values of S_4 and σ_ϕ indices alone are not reliable indicators of scintillation activity. For phase scintillation, high dimension features such as the spectral contents may offer a more reliable means

to distinguish scintillation from other activities that impact phase measurements. This is the main reason why a machine learning-based approach that exploits the high dimension features can outperform traditional Neyman-Pearson detectors which are solely based on assumed models of scintillation indices [Fu et al., 1999; Ratnam et al., 2015].

Figure 8-12 and Figure 8-13 also show that the linear SVM and medium Gaussian kernel SVM have similar test performance, which is expected from the validation performance. This indicates that scintillation and non-scintillation events are almost linearly separable in the high-dimensional space of the original feature domain. Because of its relatively lower computational complexity, the linear SVM is preferred over the kernel SVM. Furthermore, Figure 8-13 demonstrates that the trained SVM detector is effective on novel data taken at a different location from the training data site at high latitudes.

8.3. Concurrent Amplitude and Phase Scintillation Signal Detection

In addition to the stand-alone amplitude or phase scintillation detection, we are also interested in investigating the relationships in SVM detector performances for both amplitude and phase scintillation on the same data set from low latitudes. Unlike high-latitude scintillation, which is dominated by phase scintillation, scintillation observed in the low-latitude area often features concurrent amplitude fading and rapid phase fluctuations [Basu et al., 2002; Kintner et al., 2007; Jiao et al., 2013c; Jiao and Morton, 2015]. Using the data from low-latitude stations, we are able to investigate this feature of low-latitude scintillation from the perspective of detection performance.

To ensure that we make a reasonable comparison, the linear SVM detector trained without σ_ϕ features is used for phase scintillation detection. For amplitude scintillation, the linear SVM detector trained without S_4 features using only strong amplitude scintillation data (i.e. data from Hong Kong and Ascension Island) is selected (Table 8-1).

Figure 8-14 through Figure 8-16 subplots (a) and (c) show results for concurrent phase and amplitude scintillation detection using SVM on novel data from Jicamarca, Singapore, and Hong Kong. For the purpose of comparison, hard threshold-based trigger results are also plotted in subplots (b) and (d) in all three figures, with thresholds for σ_ϕ and S_4 indices being set to 15° and 0.2 respectively. The results show that the SVM phase scintillation detector trained with data from Gakona, AK can effectively operate on data from the low-latitude area. Compared to trigger detection results which may have scintillation events in short time segments close to each other, the SVM detectors (for both phase and amplitude scintillation) contain more weak scintillation events which are combined with adjacent stronger events.

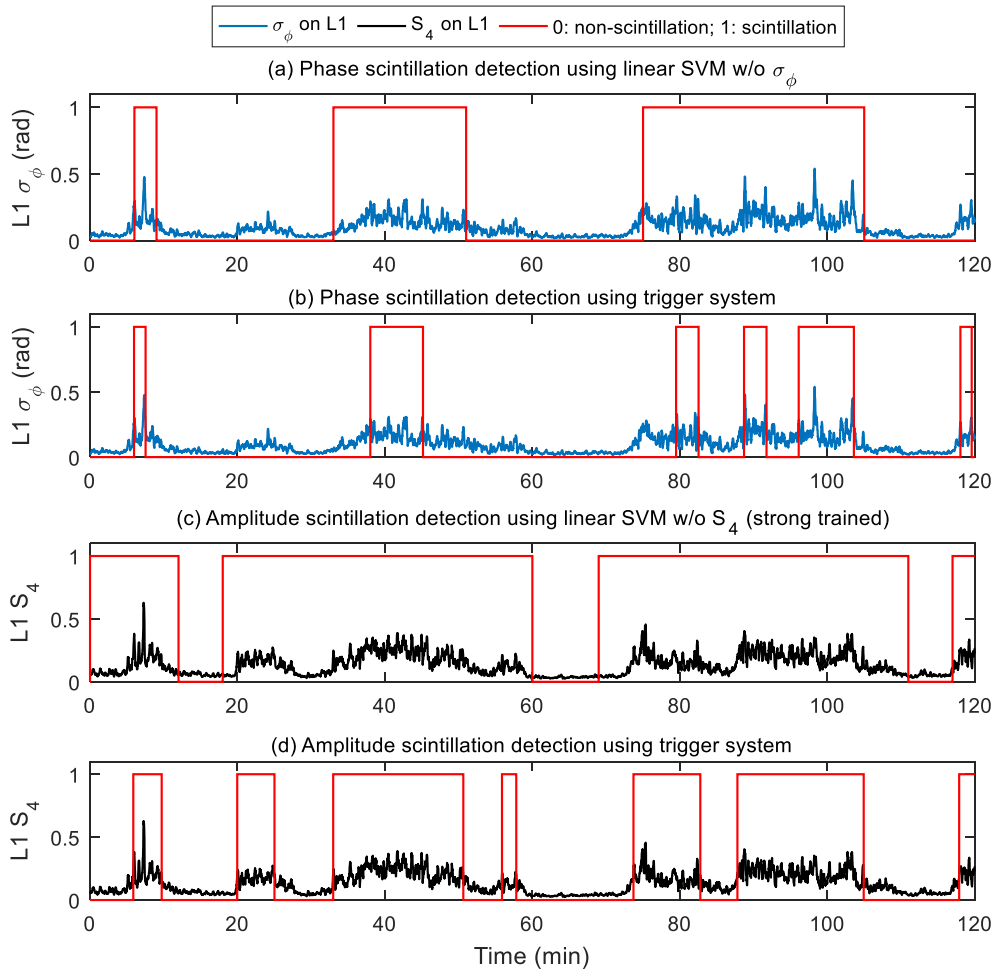


Figure 8-14. Concurrent phase and amplitude scintillation detection on novel data from Jicamarca, Peru. The data was collected on GPS L1C/A PRN13 from 01:40:00 to 03:40:00 UTC on March 11, 2013. Subplots (a) and (c) are detection results using linear SVM without σ_ϕ/S_4 features. Subplots (b) and (d) are detection results using the hard threshold-based trigger systems. The detector used in subplot (c) is trained only by strong scintillation data listed in Table 1 in [14].

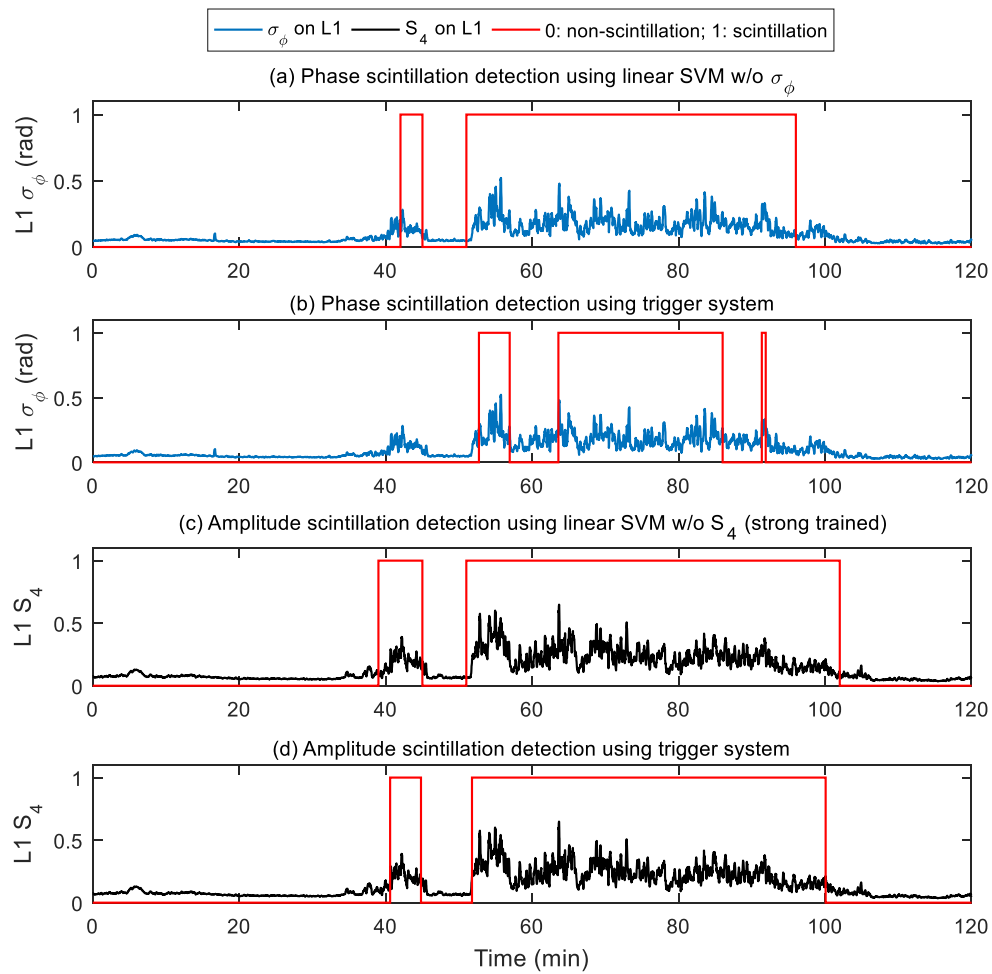


Figure 8-15. Concurrent phase and amplitude scintillation detection on novel data from Singapore. The data was collected on GPS L1C/A PRN01 from 12:22:28 to 14:22:28 UTC on April 09, 2012.

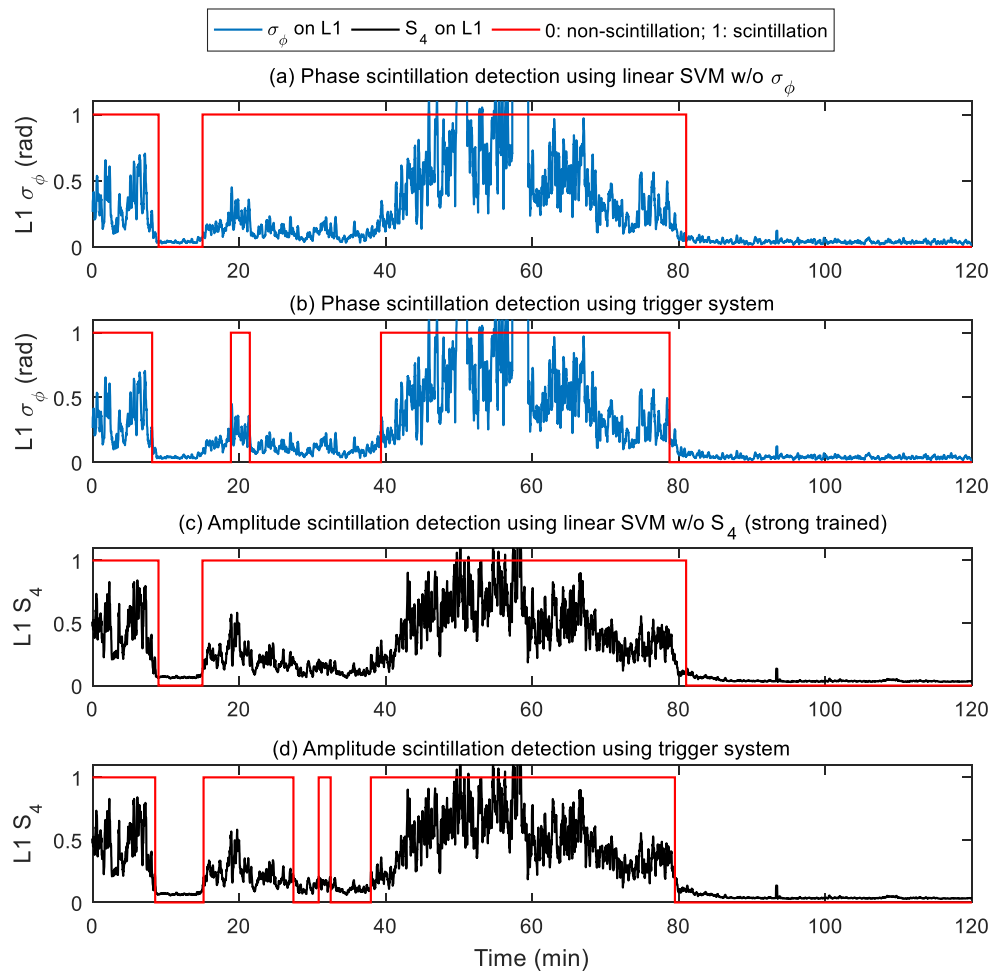


Figure 8-16. Concurrent phase and amplitude scintillation detection on novel data from Hong Kong. The data was collected on GPS L1C/A PRN24 from 12:41:36 to 14:41:36 UTC on September 10, 2014.

Based on visual inspection of the values of σ_ϕ and S_4 indices in Figure 8-14 through Figure 8-16, the two indices are highly correlated at low latitudes. Figure 8-17 shows the quantitative relationship between observed σ_ϕ and S_4 index values when amplitude scintillation events are detected using the SVM detector. There are a total of 15 segments of novel data used in this plot from Jicamarca, Singapore, and Hong Kong, with a total length of approximately 53 hours. The correlation coefficient between the two indices is greater than 0.8 with a linear ratio of around 0.7 for σ_ϕ (in radians) versus S_4 , for all data points satisfying $\sigma_\phi < 1$ and $S_4 < 1$.

Despite this high correlation relationship, phase scintillation and amplitude scintillation detections are not concurrent. Subplots (a) and (c) in Figure 8-14 through Figure 8-16 show that amplitude scintillation appears to be detected more often than phase scintillation. This can be partly explained using Figure 8-17. For example, when the average S_4 is 0.2, the corresponding average σ_ϕ is only around 0.14 rad ($\sim 8^\circ$) which is usually considered insignificant in phase scintillation [Jiao *et al.*, 2013c; Jiao and Morton, 2015].

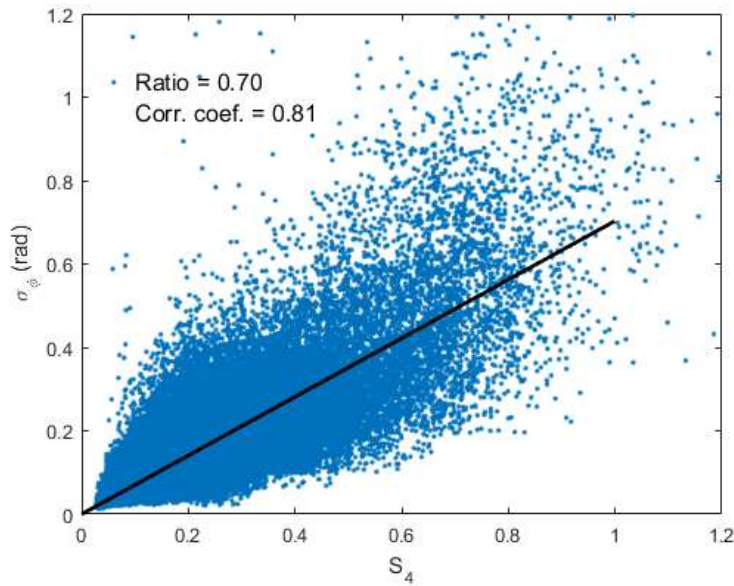


Figure 8-17. Relationship between σ_ϕ and S_4 index values with detected amplitude scintillation in the 15 segments of test data from Jicamarca, Singapore, and Hong Kong. The detectors are linear SVM detectors trained without σ_ϕ/S_4 features. The linear fit shown as the black line in the plot is zero-intercept using data points satisfying $\sigma_\phi < 1$ and $S_4 < 1$.

To further quantify the relationship between concurrent phase and amplitude scintillation detection, Figure 8-18a plots the percentage of positive phase scintillation detection during positive amplitude scintillation, with respect to different amplitude scintillation levels represented by the mean S_4 values within its 3-minute block. The data used is the same 15 segments of test data from low latitudes. Figure 8-18a shows that the percentage of phase scintillation detection increases as

the amplitude scintillation level becomes stronger. When the average S_4 index within a block exceeds 0.3, a concurrent phase scintillation event will definitely be detected if an amplitude scintillation event is detected. A reverse study of Figure 8-18a has also been conducted and the results are shown in Figure 8-18b where a positive phase scintillation detection is nearly always accompanied by a positive amplitude scintillation detection.

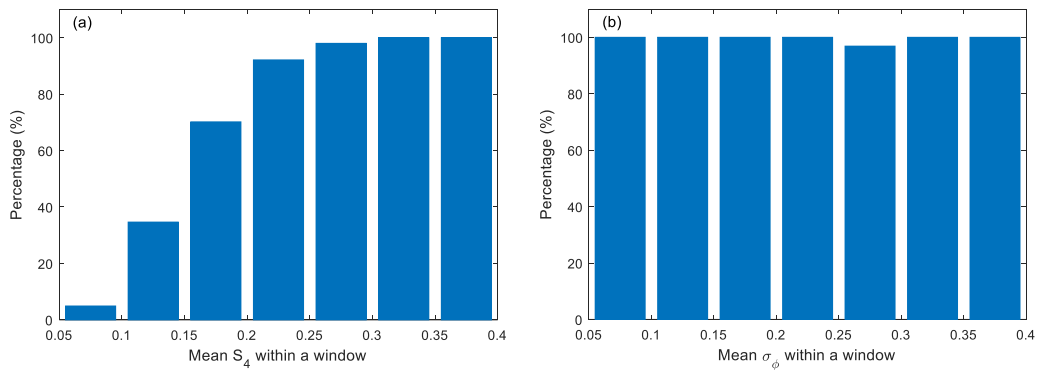


Figure 8-18. (a) The percentage of phase scintillation detection when amplitude scintillation is detected within a block, and (b) the percentage of amplitude scintillation detection when phase scintillation is detected within a block. The percentage is evaluated with respect to the scintillation level (mean S_4/σ_ϕ) within that block. The detectors are linear SVM detectors trained without σ_ϕ/S_4 features.

The above relationships indicate that at low latitudes, an amplitude scintillation detector alone is sufficient to detect scintillation activities. Low level amplitude scintillation may not be accompanied by noticeable phase scintillation. However, all phase scintillations are associated with amplitude scintillations. This observation is important for low-latitude scintillation monitoring because signal intensity measurements are more reliable than phase measurements at low latitudes. For high latitudes, phase scintillation detector is needed because of the more dominant nature of phase scintillation [Jiao et al, 2013c; Jiao and Morton, 2015].

8.4. Scintillation Detection on Simulated Scintillation Signals

The trained SVM detectors are also tested with simulated scintillation signals to verify the effectiveness of the detectors and the simulator. The amplitude and phase scintillation detectors used here are the same as those in Section 8.3. The simulator used here is based on the traditional wave propagation method with the same initialization data as in Chapter 7. Figure 8-19 shows the simulated raw signal intensity and detrended phase (using Butterworth filter) with their corresponding detection results. In the simulation, the first two minutes of the data is set to scintillation-free, while the last three minutes of the data is scintillating. The detection results shown as the red stair lines in Figure 8-19 demonstrate that the SVM-based scintillation detectors can correctly detect scintillation events on simulated scintillation amplitude and phase.

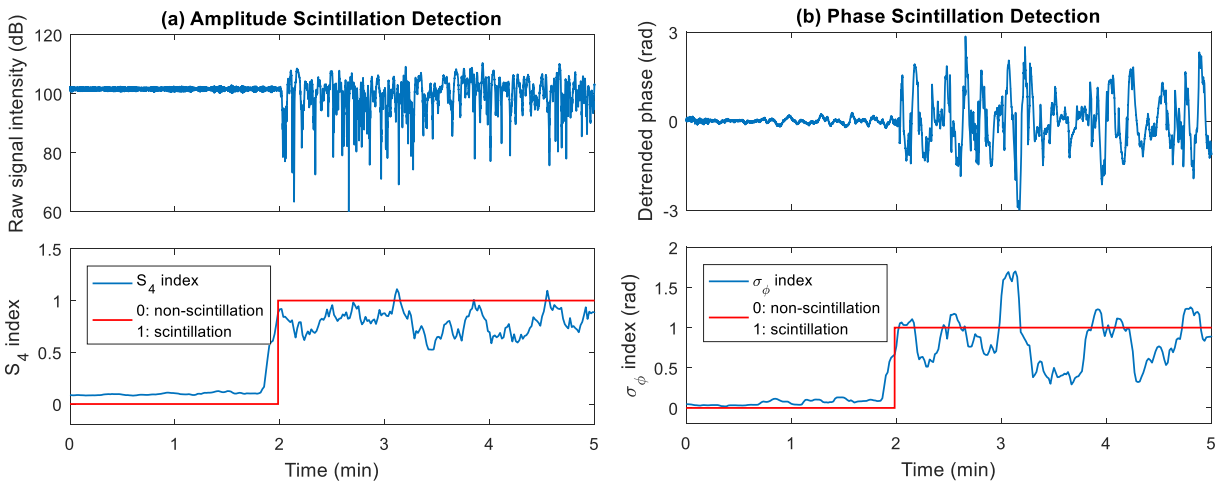


Figure 8-19. Detection results on simulated scintillation signals using SVM techniques for (a) amplitude scintillation and (b) phase scintillation. The detector outputs shown as the red lines in the lower panels demonstrate that the detectors can work correctly on simulated signals.

8.5. Concluding Remarks on Scintillation Signal Detection Using SVM

From the results in this chapter, it can be seen that the SVM detectors show good capabilities in detecting amplitude and phase scintillation events. The average accuracies in the data validation

are around 95% and 92% for amplitude scintillation detection and phase scintillation detection, respectively. Tests on novel data also confirm their superior performance to the hard threshold-based trigger system previously used at CSU GPS Lab. A summary of the results and conclusions obtained in this chapter is reviewed as follows:

- For amplitude scintillation detection, raw signal intensity measurements can be used directly as the input to the SVM detector. Distinguishing features of scintillation are already sufficiently represented in the PSD of the raw signal intensity.
- For amplitude scintillation detection, including S_4 index values in the training vector does not necessarily improve the performance of the SVM detector. For phase scintillation detection, including σ_ϕ index values in the training vector can even lead to miss-detection of weak to moderate phase scintillation events. These results show that scintillation index values may not be good indications of the scintillation activities. Future development of the detectors can be based solely on frequency domain features of the raw signal intensity or the detrended signal phase measurements.
- For both amplitude and phase scintillation detections, linear SVM and medium Gaussian SVM generate similar performances. Considering the relative simplicity in implementation, a linear SVM is adequate in future implementations.
- For amplitude scintillation, the SVM detector trained by only strong scintillation data works best for novel test data regardless of the intensity of the scintillation. The use of the SVM detector trained by only moderate scintillation data should be avoided due to its possible miss-detection of strong scintillation events.

- Both the amplitude and phase SVM detectors can be expanded to work for data from other antenna sites not involved in training. In short, the detectors appear to be location-independent.
- Although the values of σ_ϕ and S_4 features are highly-correlated at low latitudes, the detections of phase and amplitude scintillation may not be simultaneous with similarly implemented SVM detection techniques. At low latitudes, whenever phase scintillation is detected, it is almost certain that amplitude scintillation will be detected at the same time. On the other hand, when amplitude scintillation is detected, phase scintillation may not be simultaneously detected but the likelihood increases as scintillation intensifies. These results suggest that at low latitudes, an amplitude detector alone is sufficient to capture scintillation in general, while at high latitudes, a phase scintillation detector is necessary to capture the dominating phase scintillation events.
- Both SVM amplitude and phase scintillation detectors are able to work properly with simulated scintillation signals. This demonstrates the effectiveness of the scintillation simulator and the SVM scintillation detectors.

9. CHAPTER 9 – CONCLUSIONS AND FUTURE WORK

This PhD dissertation research studied low-latitude ionospheric scintillation characterization, simulation, and detection on GPS signals comprehensively, using a large volume of real and simulated GPS scintillation data. The results in this research fulfilled the dissertation outline depicted in Figure 1-6, and will provide guidance for future scintillation mechanism studies and the development of robust receiver algorithms during scintillation.

There are three major topics in this dissertation research: scintillation signal characterization, scintillation signal simulation, and scintillation signal detection. Regarding scintillation signal characterization, this research characterized a large amount of real scintillation data collected at low latitudes, and compared the characteristics with those of simulated data. The characterization was conducted in both the spatial frequency and time domains. The future work of this topic involves processing more real and simulated data from different low-latitude stations, and building a more complete tomography of scintillation at different locations.

For scintillation signal simulation, this dissertation established two data-driven multi-frequency scintillation signal simulators based on the two-dimensional two-component power-law phase screen theory. The simulators can simulate low-latitude scintillation signals on both stationary and dynamic receiver platforms. The simulated signals have been shown to have similar characteristics with the initialization data, and can be detected by the SVM-based scintillation detectors. The future work regarding the scintillation simulators is to generate more simulated signals with different initialization data and dynamic settings, in order to test the robustness of receiver processing algorithms and investigate the effects of receiver processing on signal characteristics.

For scintillation signal detection, new amplitude and phase scintillation detectors have been developed based on the SVM techniques, which can effectively and efficiently detect scintillation events in both high-latitude and low-latitude regions. Future work following the development of these detectors is to implement the detectors on the raw data collected by CSU GPS Lab at different locations to extract scintillation events for further analysis and save storage space for more incoming data. In addition, capability of classifying multipath and interference events can also be explored in the future, for the study of their specific features and the development of corresponding mitigation algorithms.

REFERENCES

- Aarons, J. (1982), Global morphology of ionospheric scintillation, *Proc. IEEE*, 70, 360-378, doi: 10.1109/PROC.1982.12314.
- Aarons, J., and S. Basu (1994), Ionospheric amplitude and phase fluctuations at the GPS frequencies, Proceedings of the 7th International Technical Meeting of the Satellite Division of The Institute of Navigation (ION GPS 1994), 1569-1578, Salt Lake City, UT.
- Akala, A. O., P. H. Doherty, C. S. Carrano, C. E. Valladares, and K. M. Groves (2012), Impact of ionospheric scintillations on GPS receivers intended for equatorial aviation applications, *Radio Sci.*, 47, doi: 10.1029/2012RS004995.
- Akala, A. O., L. L. N. Amaeshi, E. O. Somoye, R. O. Idolor, E. Okoro, P. H. Doherty, K. M. Groves, C. S. Carrano, C. T. Bridgwood, P. Baki, F. M. D'ujanga, and G. K. Seemala (2015), Climatology of GPS amplitude scintillations over equatorial Africa during the minimum and ascending phases of solar cycle 24, *Astrophys. Space Sci.*, 357(17), doi: 10.1007/s10509-015-2292-9.
- Alfonsi, L., L. Spogli, G. De Franceschi, V. Romano, et al (2011), Bipolar climatology of GPS ionospheric scintillation at solar minimum, *Radio Sci.*, 46, doi:10.1029/2010RS004571.
- Aquino, M., T. Moore, A. Dodson, S. Waugh, J. Souter and F. S. Rodrigues (2005), Implications of ionospheric scintillation for GNSS users in northern Europe, *Journal of Navigation*, 58(2), 241-256, doi: 10.1017/S0373463305003218.
- Axelrad, P., K. Larson, and B. Jones (2005), Use of the correct satellite repeat period to characterize and reduce site-specific multipath errors, Proc. ION ITM, Long Beach, CA.
- Azeem, I., G. Crowley, A. Reynolds, J. Santana, and D. Hampton (2013), First results of phase scintillation from a longitudinal chain of ASTRA's SM-211 GPS TEC and scintillation receivers in Alaska, Proc. ION PNT, 735-742, Honolulu, HI.
- Basu, S., K. Grovesa, Su. Basu, and P. Sultana (2002), Specification and forecasting of scintillations in communication and navigation links: current status and future plans, *J. Atmo. Solar-Terr. Phys.*, 64, 1745-1754, doi: 10.1016/S1364-6826(02)00124-4.
- Beach, T. L. (2006), Perils of the GPS phase scintillation index (Sigma Phi), *Radio Sci.*, 41, doi: 10.1029/2005RS003356.
- Beniguel, Y., V. Romano, L. Alfonsi, M. Aquino, et al (2009), Ionospheric scintillation monitoring and modelling, *Annals of Geophysics*, 52, 391-416, doi: 10.4401/ag-4595.

Bhattacharyya, A., K. C. Yeh, and S. J. Franke (1982), Deducing turbulence parameters from transionospheric scintillation measurements, *Space Science Reviews*, 61, 335-386.

Booker, H., J. Ratcliffe, and D. Shinn (1950), Diffraction from an irregular screen with applications to ionospheric problems, *Philos. Trans. Roy. Soc. London. Ser. A.*, 242, 579-607.

Borre, K., D. M. Akos, N. Bertelsen, P. Rinder, and S. H. Jensen (2007), A software-defined GPS and Galileo receiver: a single-frequency approach, Springer Science & Business Media, Birkhäuser, Boston.

Briggs, B. H., and I. A. Parkin (1963), On the variation of radio star and satellite scintillations with zenith angle, *J. Atmos. Terr. Phys.*, 25, 339-365.

Buchau, J., E. J. Weber, D. N. Anderson, H. C. Carlson Jr., J. G. Moore, B. W. Reinisch, and R. C. Livingston (1984), Ionospheric structures in the polar cap: Their origin and relation to 25-MHz scintillation, *Radio Sci.*, 20(3), 325-338, doi:10.1029/RS020i003p00325.

Budden, K. G. (1988), *The propagation of radio waves: the theory of radio waves of low power in the ionosphere and magnetosphere*, Cambridge University Press, New York, NY.

Campbell, W. H. (2003), *Introduction to geomagnetic fields*, 2nd ed., Cambridge University Press.

Carrano, C. S., C. E. Valladares, K. M. Groves (2012), Latitudinal and local time variation of ionospheric turbulence parameters during the conjugate point equatorial experiment in Brazil, *International Journal of Geophysics*, 2012, doi:10.1155/2012/103963.

Carrano, C. S., K. M. Groves, S. H. Delay, and P. H. Doherty (2015), A novel approach for monitoring zonal irregularity drift using a stand-alone GNSS scintillation monitor, Proc. ION ITM, Dana Point, CA.

Carrano, C. S., and C. L. Rino (2016), A theory of scintillation for two-component power law irregularity spectra: I. overview and numerical results, *Radio Sci.*, 51, doi:10.1002/2015RS005903.

Carrano, C. S., K. M. Groves, C. M. Rino, and P. H. Doherty (2016), A technique for inferring zonal irregularity drift from single-station GNSS measurements of intensity (S_4) and phase (σ_ϕ) scintillations, *Radio Sci.*, doi:10.1002/2015RS005864.

Carroll, M., Y. Morton, and E. Vinande (2014), Triple frequency GPS signal tracking during strong ionospheric scintillations over Ascension Island, Proc. IEEE/ION, 43-49, doi: 10.1109/PLANS.2014.6851356.

- Chartier, A., B. Forte, K. Deshpande, G. Bust and C. Mitchell (2016), Three-dimensional modeling of high-latitude scintillation observations, *Radio Sci.*, *51*, 1022-1029, doi: 10.1002/2015RS005889.
- Cherniak, I., and I. Zakharenkova (2016), High-latitude ionospheric irregularities differences between ground- and space-based GPS measurements during the 2015 St. Patrick's Day storm, Earth, *Planets and Space*, *68*, doi: 10.1186/s40623-016-0506-1.
- Chytil, B. (1967), The distribution of amplitude scintillation and the conversation of scintillation indices, *J. Atmos. Terr. Phys.* *29*, 1175-1177.
- Cortes, C., and V. Vapnik (1995), Support-vector networks, in *Machine Learning*, pp. 273-297, Kluwer Academic Publishers, Boston, MA.
- Cover, T. M. (1965), Geometrical and Statistical properties of systems of linear inequalities with applications in pattern recognition, *IEEE Transactions on Electronic Computers EC-14*, 326–334. doi:10.1109/pgec.1965.264137.
- Dagg, M. (1957), The correlation of radio-star-scintillation phenomena with geomagnetic disturbances and the mechanism of motion of the ionospheric irregularities in the F region, *J. Atmos. Terr. Phys.*, *10*, 194-203, doi: 10.1016/0021-9169(57)90086-7.
- Dana, P. H. (2015), Geodetic datum overview, http://www.colorado.edu/geography/gcraft/notes/datum/datum_f.html.
- Das Gupta, A., A. Maitra, and S. K. Das (1985), Post-midnight scintillation activity in relation to geomagnetic disturbances, *J. Atmos. Terr. Phys.*, *47*, 911–916, doi: 10.1016/0021-9169(85)90067-4.
- De Franceschi, G., L. Alfonsi, and V. Romano (2006), Isacco: an Italian project to monitor the high latitude ionosphere by means of GPS receivers, *GPS Solut.*, *10*, 263-267, doi: 10.1007/s10291-006-0036-6.
- Deshpande, K. B., G. S. Bust, C. R. Clauer, C. L. Rino and C. S. Carrano (2014), Satellite-beacon Ionospheric-scintillation Global Model of the uppder Atmosphere (SIGMA) I: High-latitude sensitivity study of the model parameters, *J. Geophys. Res. Space Physics*, *119*, 4026-4043, doi: 10.1002/2013JA019699.
- Deshpande, K. B., G. S. Bust, C. R. Clauer, W. A. Scales, N. A. Frissell, J. M. Ruohoniemi, L. Spogli, C. Mitchell and A. T. Weatherwax (2016), Satellite-beacon Ionospheric-scintillation Global Model of the upper Atmosphere (SIGMA) II: Inverse modelling with high-latitude observations to deduce irregularity physics, *J. Geophys. Res. Space Physics*, *121*, 9188–9203, doi: 10.1002/2016JA022943.

Forte, B., and S. M. Radicella (2002), Problems in data treatment for ionospheric scintillation measurements, *Radio Sci.*, 37(6), doi: 10.1029/2001RS002508.

Forte, B., C. Coleman, S. Skone I. Häggström, C. Mitchell, F. Da Dalt, T. Paniciari, J. Kinrade, and G. Bust. (2016), Identification of scintillation signatures on GPS signals originating from plasma structures detected with EISCAT incoherent scatter radar along the same line of sight, *J. Geophys. Res. Space Physcis*, 122, doi: 10.1002/2016JA023271.

Fortes, L. P. S., T. Lin, and G. Lachapelle (2014), Effects of the 2012–2013 solar maximum on GNSS signals in Brazil, *GPS Solutions*, 19(2), 309-319, doi: 10.1007/s10291-014-0389-1.

Fremouw, E. J., R. C. Livingston, and D. A. Miller (1980), On the statistics of scintillating signals, *J. Atmos. Terr. Phys.*, 42, 717-731.

Fu, W., S. Han, C. Rizos, M. Knight, and A. Finn (1999), Real-time ionospheric scintillation monitoring, Proc ION GPS, Nashville, TN.

Ghafoori, F., and S. Skone (2015), Impact of equatorial ionospheric irregularities on GNSS receivers using real and synthetic scintillation signals, *Radio Sci.*, 50, 294-317, doi: 10.1002/2014RS005513.

Ghoddousi-Fard, R., L. Nikitina, D. Danskin, P. Prikryl, and F. Lahaye (2015), Analysis of GPS phase rate variations in response to geomagnetic field perturbations over the Canadian auroral region, *Advances in Space Research*, 55, 1372-1381, doi: 10.1016/j.asr.2014.12.021.

Goldston, R. J., and P. H. Rutherford (1995), *Introduction to plasma physics*, CRC Press.

Hamilton, B., V. A. Ridley, C. D. Beggan, and S. Macmillan (2015), The BGS magnetic field candidate models for the 12th generation IGRF, *Earth, Planets and Space*, doi:10.1186/s40623-015-0227-x.

Hasbi, A. M., M. A. M. Ali, and N. Misran (2007), Ionospheric TEC and scintillation during the 15-16 May 2005 major storm over equatorial anomaly region at ARAU, 2007 Asia-Pacific Conference on Applied Electromagnetics Proceedings, 1-5, Melaka, Malaysia.

Haykin, S. (2009), *Neural networks and learning machines*, 3rd ed., Pearson Education Inc., Upper Saddle River, New Jersey.

Hewish, A. (1951), The diffraction of radio waves in passing through a phase-changing ionosphere, *Proc. Roy. Soc. London. Ser. A*, 209, 81-96.

Humphreys, T. E., M. L. Psiaki, J. C. Hinks, and P. M. Kintner (2009), Simulating ionosphere-induced scintillation for testing GPS receiver phase tracking loops, *IEEE J. Sel. Top. Signal Process.*, 3, 707–715. doi:10.1109/JSTSP.2009.2024130.

Humphreys, T. E., M. L. Psiaki, B. M. Ledvina, A. P. Cerruti, and P. M. Kintner (2010a), Data-driven testbed for evaluating GPS carrier tracking loops in ionospheric scintillation, *IEEE Trans. Aero. & Elec. Sys.*, 46(4), 1609-1623.

Humphreys, T. E., M. L. Psiaki, P. M. Kintner (2010b), Modeling the effects of ionospheric scintillation on GPS carrier phase tracking, *IEEE Trans. Aero. & Elec. Sys.*, 46(4), 1624-1637

Hysell, D. L., M. C. Kelley, W. E. Swartz, and R. F. Woodman (1990), Seeding and layering of equatorial spread F by gravity waves, *J. Geophys. Res.*, 95(A10), 17253–17260, doi:10.1029/JA095iA10p17253.

Hysell, D. L., and E. Kudeki (2004), Collisional shear instability in the equatorial F region ionosphere, *J. Geophys. Res.*, 109, A11301, doi:10.1029/2004JA010636.

IS-GPS-200 Revision H Navstar Global Positioning System (2013), Interface Specification: Navstar GPS Space Segment/Navigation User Interface, Navstar GPS Joint Program Office.

IS-GPS-705 Revision D Navstar Global Positioning System (2013), Interface Specification: Navstar GPS Space Segment/User Segment L5 Interfaces, Navstar GPS Joint Program Office.

IS-GPS-800 Revision D Navstar Global Positioning System (2013), Interface Specification: Navstar GPS Space Segment/User Segment L1C Interface, Navstar GPS Joint Program Office.

Jiao, Y. (2013), High latitude ionosphere scintillation characterization, M.S. thesis, Dept. of Electrical and Computer Engineering, Miami University, Oxford, Ohio, USA.

Jiao, Y., Y. Morton, S. Taylor, and W. Pelgrum (2013a), High latitude ionosphere scintillation characterization, Proc. ION ITM, 579-584, San Diego, CA.

Jiao, Y., Y. Morton, S. Taylor, and W. Pelgrum (2013b), On the correlation between ionospheric scintillation and geomagnetic field activities, Proc. ION GNSS+, 77-83, Nashville, TN.

Jiao, Y., Y. Morton, S. Taylor, and W. Pelgrum (2013c), Characterization of high-latitude ionospheric scintillation of GPS signals, *Radio Sci.*, 48(6), 698-708, doi: 10.1002/2013RS005259.

Jiao, Y., Y. Morton, and S. Taylor (2014a), Comparative studies of high-latitude and equatorial ionospheric scintillation characteristics of GPS signals, Proc. IEEE/ION PLANS, 37-42, doi: 10.1109/PLANS.2014.6851355.

Jiao, Y., Y. Morton, S. Taylor, and M. Carroll (2014b), Characteristics of low-latitude signal fading across the GPS frequency bands, Proc. ION GNSS+, 1203-1212, Tampa, FL.

Jiao, Y., Y. Morton, D. Akos, and T. Walter (2015), A comparative study of triple frequency GPS scintillation signal amplitude fading characteristics at low latitudes, Proc. ION GNSS+, 3819-3825, Tampa, FL.

Jiao, Y., and Y. Morton (2015), Comparison of the effect of high-latitude and equatorial ionospheric scintillation on GPS signals during the maximum of solar cycle 24, *Radio Sci.*, 50(9), 886-903, doi: 10.1002/2015RS005719.

Jiao, Y., D. Xu, Y. Morton, and C. Rino (2016a), Equatorial scintillation amplitude fading characteristics across the GPS frequency bands, *Navigation*, 63(3), 267-281, doi: 10.1002/navi.146.

Jiao, Y., D. Xu, Y. Morton, and C. Rino (2016b), Equatorial amplitude scintillation spectrum analysis and fading characteristics on GPS signals, Proc. ION GNSS+, 1680-1687, Portland, OR.

Jiao, Y., J. Hall, and Y. Morton (2016c), Performance evaluation of an equatorial GPS amplitude scintillation detector using a machine learning algorithm, Proc. ION GNSS+, 195-199, Portland, OR.

Jiao, Y., J. Hall, and Y. Morton (2017a), Automatic GPS phase scintillation detector using a machine learning algorithm, Proc. ION ITM/PTTI, 1160-1172, Monterey, CA.

Jiao, Y., J. Hall, and Y. Morton (2017b), Automatic equatorial GPS amplitude scintillation detection using a machine learning algorithm, *IEEE Trans. Aerosp. Electron. Syst.*, 53(1), 405-418, doi: 10.1109/TAES.2017.2650758.

Jiao, Y., J. Hall, and Y. Morton (2017c), Performance evaluation of an automatic GPS ionospheric phase scintillation detector using a machine learning algorithm, *NAVIGATION*, accepted.

Jiao, Y., C. Rino, and Y. Morton (2017d), Scintillation simulation on equatorial GPS signals for dynamic platforms, Proc. ION GNSS+, Portland, OR.

Jin, Y., J. I. Moen and W. J. Miloch (2014), GPS scintillation effects associated with polar cap patches and substorm auroral activity: direct comparison, *J. Space Weather Space Clim.*, 4(2014).

Jin, Y., J. I. Moen and W. J. Miloch (2015), On the collocation of the cusp aurora and the GPS phase scintillation: A statistical study, *J. Geophys. Res. Space Physics*, 120, doi:10.1002/2015JA021449.

Jin, Y., J. I. Moen, W. J. Miloch, L. B. N. Clausen, and K. Oksavik (2016), Statistical study of the GNSS phase scintillation associated with two types of auroral blobs, *J. Geophys. Res. Space Physics*, 121, 4679–4697, doi:10.1002/2016JA022613.

Kaplan, E. D., and C. Hegarty (2005), *Understanding GPS: Principles and Applications*, 2nd ed., Artech House.

Kay, S. M. (1998), *Fundamentals of statistical signal processing, Vol. II: Detection theory*, Signal Processing, Upper Saddle River, NJ: Prentice Hall.

Kelley, M. C., M. F. Larsen, C. LaHoz, and J. P. McClure (1981), Gravity wave initiation of equatorial spread F: A case study, *J. Geophys. Res.*, 86(A11), 9087–9100, doi:10.1029/JA086iA11p09087.

Kelley, M. C., J. J. Makela, B. M. Ledvina, and P. M. Kintner (2002), Observations of equatorial spread F from Haleakala, Hawaii, *Geophys. Res. Lett.*, 29(20), doi:10.1029/2002GL015509.

Kersley, L., S. Pryse, and N. Wheadon (1988), Amplitude and phase scintillation at high latitudes over northern Europe, *Radio Sci.*, 23(3), 320–330.

Kersley, L., C. Russell, and D. Rice (1995), Phase scintillation and irregularities in the northern polar ionosphere, *Radio Sci.*, 30(3), 619–629.

Kintner, P. M., B. M. Ledvina, E. R. de Paula, and I. J. Kantor (2004), Size, shape, orientation, speed, and duration of GPS equatorial anomaly scintillations, *Radio Sci.*, 39, doi:10.1029/2003RS002878.

Kintner, P. M., B. M. Ledvina, and E. R. de Paula (2007), GPS and ionospheric scintillations, *Space Weather*, 5, doi: 10.1029/2006SW000260.

Klobuchar, J. (2002), Ionospheric research issues for SBAS – a white paper, SBAS Ionospheric Working Group, Ver 225.

Knight, M. F., A. Finn, M. Cervera (1997), Ionospheric effects on Global Positioning System receivers, DSTO-RR-0121 Report, Electronics and Surveillance Research Laboratory, Defence Science and Technology Organisation, Australia.

Knight, M. and A. Finn (1998), The effects of ionospheric scintillation on GPS/satellite-based augmentation system availability, Proc. ION GPS-98, 673-686, Nashville, TN.

Ledvina, B. M., J. J. Makela, and P. M. Kintner (2002), First observations of intense GPS L1 amplitude scintillations at midlatitude, *Geophys. Res. Lett.*, 29(14), 1659, doi:10.1029/2002GL014770.

Leick, A. L. Rapoport, and D. Tatarnikov (2015), *GPS satellite surveying*, 4th ed., John Wiley & Sons Inc., Hoboken, NJ.

Li, G., B. Ning, Bi. Zhao, L. Liu, J. Y. Liu, and K. Yumoto (2008), Effects of geomagnetic storm on GPS ionospheric scintillations at Sanya, *J. Atmos. Sol.-Terr. Phys.*, 70(7), 1034-1045, doi: 10.1016/j.jastp.2008.01.003.

Li, G., B. Ning, Z. Ren, and L. Hu (2010), Statistics of GPS ionospheric scintillation and irregularities over polar regions at solar minimum, *GPS Solut.*, 14, 331-341, doi: 10.1007/s10291-009-0156-x.

Liu, Z., R. Xu, Y. Morton, J. Xu, W. Pelgrum, W. Chen, and X. Ding (2013), A comparison of GNSS-based ionospheric scintillation observation in north and south Hong Kong, Proc. ION PNT, 694-705, Honolulu, HI.

Mao, X., and Y. T. Morton (2013), GNSS receiver carrier tracking loop impact on ionosphere scintillation signal C/N0 and carrier phase estimation, Proc. ION GNSS+, Nashville, TN.

Matteo, N. A., and Y. T. Morton (2011), Ionosphere geomagnetic field Comparison of IGRF model prediction and satellite measurements 1991–2010, *Radio Sci.*, 46, doi:10.1029/2010RS004529.

Mercer, J. (1909), Functions of positive and negative type, and their connection with the theory of integral equations, *Philosophical Transactions of the Royal Society of London A: Mathematical, Physical and Engineering Sciences*, 209, 415-446.

Miriyala, S., P. Koppireddi, and S. Chanamallu (2015), Robust detection of ionospheric scintillations using MF-DFA technique, *Earth, Planets and Space*. 67(98), 1-5.

Misra, P, and P. Enge (2011), *Global Positioning System: signals, measurements, and performance*, revised 2nd ed., Ganga-Jamuna Press, Lincoln, MA.

Moore, T. M., M. Aquino, A. Dodson and S. Waugh (2002), Impact of ionospheric scintillation on EGNOS and DGPS users in northern Europe, Proceeding of GNSS 2002, Copenhagen, Denmark.

Moraes, A. O., E. R. de Paula, W. J. Perrella, and F. Rodrigues (2013), On the distribution of GPS signal amplitudes during low-latitude ionospheric scintillation, *GPS Solut.*, 17, 499-510, doi: 10.1007/s10271-012-0295-3.

Moraes, A. O., E. Costa, E. R. de Paula, W. J. Perrella, and J. F. G. Monico (2014), Extended ionospheric amplitude scintillation model for GPS receivers, *Radio Sci.*, 49, doi:10.1002/2013RS005307

Morton, Y., H. Bourne, M. Carroll, Y. Jiao, N. Kassabian, S. Taylor, J. Wang, D. Xu, and H. Yin (2014), Multi-constellation GNSS observations of equatorial ionospheric scintillation, Proc. URSI General Assembly & Sci. Sym., Beijing, China.

Morton, Y. (2014-16), Lectures for ECE 511 Introduction to GNSS, Colorado State University, Fort Collins, CO, USA.

Morton, Y., Y. Jiao and S. Taylor (2015a), High-latitude and equatorial ionospheric scintillation based on an event-driven multi-GNSS data collection system, Proc. Ionospheric Effects Sym., Alexandria, VA.

Morton, Y., Y. Jiao, F. Graas, E. Vinande, and N. Pujara (2015b), Analysis of receiver multi-frequency response to ionospheric scintillation in Ascension Island, Hong Kong, and Singapore, Proc. ION PNT, 10-16, Honolulu, HI.

Mushini, S., P. Jayachandran, R. Langley, J. MacDougall, D. Pokhotelov (2011), Improved amplitude- and phase-scintillation indices derived from wavelet detrended high-latitude GPS data, *GPS Solutions*, doi: 10.1007/s1029-011-0238-4.

Myer, G. (2017), Ionospheric scintillation effects on GPS measurements and algorithms to improve positioning solution accuracy, M.S. thesis, Dept. of Electrical and Computer Engineering, Colorado State University, Fort Collins, Colorado, USA

Nakagami, M. (1960), Statistical methods, in *Radio Wave Propagation*, pp. 3-36, Pergamon, Elmsford, New York.

Niu, F., Morton, Y., Wang, J., Pelgrum, W. (2012), GPS carrier phase detrending methods and performances for ionosphere scintillation studies, Proc. ION ITM, Newport Beach, CA.

Niu, F. (2012), Performances of GPS signal observables detrending methods for ionosphere scintillation studies, M.S. thesis, Dept. of Electrical and Computer Engineering, Miami University, Oxford, Ohio, USA.

Oliveira, K., A. Moraes, E. Costa, M. Muella, E. de Paula, and W. Perrella (2014), Validation of the alpha-mu model of the power spectral density of GPS ionospheric amplitude scintillation, *International Journal of Antennas and Propagation*, 2014, doi: 10.1155/2014/573615.

Pelgrum, W., Y. Morton, F. van Graas, P. Vikram, S. Peng (2011), Multi-domain analysis of the impact on natural and man-made ionosphere scintillations on GNSS signal propagation, Proc. ION GNSS, 617-625, Portland, OR.

Pi, X., A. J. Mannucci, U. J. Lindqwister, and C. M. Ho (1997), Monitoring of global ionospheric irregularities using the Worldwide GPS Network, *Geophys. Res. Lett.*, 24(18), 2283–2286, doi:10.1029/97GL02273.

Prikryl, P., P. T. Jayachandran, S. C. Mushini, D. Pokhotelov, J. W. MacDougall, E. Donovan, E. Spanswick, and J.-P. St.-Maurice (2010), *Ann. Geophys.*, 28, 1307-1316, doi: 10.5194/angeo-28-1307-2010.

- Prikryl, P., P. T. Jayachandran, S. C. Mushini, and R. Chadwick (2011), Climatology of GPS phase scintillation and HF radar backscatter for the high-latitude ionosphere under solar minimum conditions, *Ann. Geophys.*, 29, 377-392, doi: 10.5194/angeo-29-377-2011.
- Priyadarshi, S. (2015), A review of ionospheric scintillation models, *Surv. Geophys.*, 36(2), 295-324, doi: 10.1007/s10712-015-9319-1.
- Psiaki, M. L., T. E. Humphreys, A. P. Cerruti, S. P. Powell, and P. M. Kintner (2007), Tracking L1 C/A and L2C signals through ionospheric scintillations, Proc. ION GNSS, Fort Worth, TX.
- Ratnam, D. V., G. Sivavaraprasad, and J. Lee (2015), Automatic ionospheric scintillation detector for global navigation satellite system receivers, *IET Radar, Sonar & Navigation*, 702-711.
- Redmon, R. J., D. Anderson, R. Caton, and T. Bullett (2010), A Forecasting Ionospheric Real-time Scintillation Tool (FIRST), *Space Weather*, 8, S12003, doi:10.1029/2010SW000582.
- Reggiani, N., O. C. Branquinho, T. A. Xastre, T. C. Nascimento, et al. (2005), Influence of the geomagnetic activity on the GPS signal, *IEEE*, 125-128, doi: 10.1109/IMOC.2005.1580097.
- Remodi, B. M. (2004), GPS Tool Box: Computing satellite velocities using the broadcast ephemeris, *GPS Solut.*, 8(3), 181-183, doi: 10.1007/s10291-004-0094-6.
- Rino, C. L., and E. J. Fremouw (1977), The angle dependence of singly scattered wavefields, *J. of Atmos. Terr. Phys.*, 39, 859-868.
- Rino, C. L. (1979a), A power law phase screen model for ionospheric scintillation: 1. Weak scatter, *Radio Science*, 14, 1135-1145.
- Rino, C. L. (1979b), A power law phase screen model for ionospheric scintillation: 2. Strong scatter, *Radio Science*, 14, 1147-1155.
- Rino, C. L. (1980), Transionospheric radiowave propagation and signal statistics, Agard. Conf. Proc. No. 284, Propagation Effects in Space/Earth Paths, London, UK.
- Rino, C. L. (1982), On the application of phase screen models to the interpretation of ionospheric scintillation data, *Radio Sci.*, 17(4), 855-867, doi: 10.1029/RS017i004p00855.
- Rino, C. L., R. C. Livingston, R. T. Tsunoda, R.M. Robinson, J. F. Vickrey, et al (1983), Recent studies of the structure and morphology of auroral zone F region irregularities, *Radio Sci.*, 18, 1167-1180.
- Rino, C. L., and V. R. Kruger (2001), A comparison of forward-boundary-integral and parabolic-wave-equation propagation models, *IEEE Proc. Antennas Propagate.*, 49(4), 574-582.

Rino, C. L. (2011), *The theory of scintillation with applications in remote sensing*, John Wiley & Sons, Inc., Hoboken, New Jersey.

Rino, C. L., and C. S. Carrano (2013), A compact strong-scatter scintillation model, Proceedings of the International Beacon Satellite Symposium, Bath, UK.

Rino, C. L., C. S. Carrano, and P. Roddy (2014), Wavelet-based analysis and power law classification of C/NOFS high-resolution electron density data, *Radio Sci.*, *49*, 680-688, doi: 10.1002/2013RS005272.

Rino, C. L., C. S. Carrano, K. M. Groves, and P. A. Roddy (2016), A characterization of intermediate-scale spread F structure from four years of high-resolution C/NOFS satellite data, *Radio Sci.*, *51*, doi: 10.1002/2015RS005841.

Rino, C. L., C. S. Carrano, B. Breitsch, Y. Jiao and Y. Morton (2017), A new GNSS scintillation model, Proc. ION GNSS+, Portland, OR.

Rodrigues, F. S., M. Aquino, A. Dodson, T. Moore, S. Waugh (2004), Statistical analysis of GPS ionospheric scintillation and short-time TEC variations over Northern Europe, *Journal of ION*, *51*(1), 59-75.

Rufenach, C. L. (1974), Wavelength dependence of radio scintillation: ionosphere and interplanetary irregularities, *J. Geophys. Res.*, *79*, 1562-1566, doi: 10.1029/JA079i010p01562.

Seo, J., T. Walter, E. Marks, T. Y. Chiou, and P. Enge (2007), Ionospheric scintillation effects on GPS receiver during solar minimum and maximum, Proceedings of International Beacon Satellite Symposium 2007, Boston, MA.

Seo, J., T. Walter, T. Y. Chiou and P. Enge (2009), Characteristics of deep GPS signal fading due to ionospheric scintillation for aviation receiver design, *Radio Science*, *44*, doi: 10.1029/2008RS004077.

Seo, J., T. Walter and P. Enge (2011), Correlation of GPS signal fades due to ionospheric scintillation for aviation applications, *Advances in Space Research*, *47*(10), 1777-1788, doi: 10.1016/j.asr.2010.07.014.

Septentrio Satellite Navigation (2016), PolaRxS Reference Guide for version 2.9.6 of the GNSS Firmware, Leuven, Belgium.

Shang, S. P., J. K. Shi, P. M. Kintner, W. M. Zhen, X. G. Luo, S. Z. Wu, and G. J. Wang (2008), Response of Hainan GPS ionospheric scintillations to the different strong magnetic storm conditions, *Advances in Space Research*, *41*(4), 579-586, doi: 10.1016/j.asr.2007.05.020.

- Shishov, I. (1974), Dependence of the form of the scintillation spectrum on the form of the spectrum of refractive index inhomogeneities, I. phase screen, *Radiophysics and Quantum Electronics*, 17, 1287-1292.
- Shkarofsky, I. P. (1968), Generalized turbulence space-correlation and wave-number spectrum-function pairs, *Can. J. Phys.*, 46(19), 2133-2153, doi: 10.1139/p68-562.
- Singleton, D. G. (1970), Saturation and focusing effects in radio-star and satellite scintillations, *J. Atmos. and Terr. Phys.*, 32, 187-208, doi:10.1016/0021-9169(70)90191-1.
- Skone, S., and K. Knudsen (2000), Impact of ionospheric scintillations on SBAS performance, Proc. ION GPS 2000, Salt Lake City, UT.
- Skone, S. H. (2001), The impact of magnetic storms on GPS receiver performance, *J. Geodesy*, 75, 457-468, doi: 10.1007/s001900100198.
- Skone, S., K. Knudsen and M. de Jong (2001), Limitations in GPS receiver tracking performance under ionospheric scintillation conditions, *Phys. Chem. Earth (A)*, 26(6-8), 613-621.
- Skone, S., F. Man, F. Ghafoori, and R. Tiwari (2008), Investigation of scintillation characteristics for high latitude phenomena, Proc. ION GNSS, 2425-2434, Savannah, GA.
- Smith, A. M., C. N. Mitchell, R. J. Watson, R. W. Meggs, P. M. Kintner, K. Kauristie, and F. Honary (2008), GPS scintillation in the high arctic associated with an auroral arc, *Space Weather*, 6, doi:10.1029/2007SW000349.
- Snay, R.A., and T. Soler (2000), Modern terrestrial reference systems part 3: WGS 84 and ITRS, *Professional Surveyor*, 20(3).
- Sojka, J. J., D. Rice, V. Eccles, T. Berkey, P. Kintner, and W. Denig (2004), Understanding midlatitude space weather: Storm impacts observed at Bear Lake Observatory on 31 March 2001, *Space Weather*, 2, doi:10.1029/2004SW000086.
- Spilker, J., and A. J. Van Dierendonck (2001), Proposed new L5 civil GPS codes, *Journal of the Institute of Navigation*, 48(3), 135-144.
- Sreeja, V. (2016), Impact and mitigation of space weather effects on GNSS receiver performance, *Geosci. Lett.*, 2016(3:24), doi: 10.1186/s40562-016-0057-0.
- Strohbehn, J. W., and T. I. Wang (1972), Simplified equation for amplitude scintillations in a turbulent atmosphere, *J. Opt. Soc. Amer.*, 62, 1061-1068.

Taylor S., Y. T. Morton, Y. Jiao, J. Triplett, and W. Pelgrum (2012), An improved ionosphere scintillation event detection and automatic trigger for GNSS data collection systems, Proc. ION ITM, Newport Beach, CA.

Thébault, E, C. C. Finlay, C. D. Beggan, P. Alken, J. Aubert, O. Barrois, F. Bertrand, T. Bondar, et al. (2015), International Geomagnetic Reference Field: the 12th generation, *Earth, Planets and Space*, 67(1), 1-19, doi:10.1186/s40623-015-0228-9.

Tatarskii, V. I. (1967), *Wave propagation in a turbulent medium*, translated by R. A. Silverman, Dover, New York.

Tsunoda, R. T. (1985), Control of the seasonal and longitudinal occurrence of equatorial scintillations by the longitudinal gradient in integrated E region Pedersen conductivity, *J. Geophys. Res.*, 90(A1), 447-456, doi:10.1029/JA090iA01p00447.

Tsunoda, R. T. (1988), High-latitude F-region irregularities, a review and synthesis, *Rev. Geophys.*, 26(4), 719-760, doi: 10.1029/RG026i004p00719.

Vadakke Veetil, S., H. Haralambous, and M. Aquino (2017), Observations of quiet-time moderate midlatitude L-band scintillation in association with plasma bubbles, *GPS Solu.*, 2017, 1-12, doi: 10.1007/s10291-016-0598-x.

Valladares, C. E., R. Sheehan, M. P. Hagan, and E. MacKenzie (2002), Studies of ionospheric structures and their effects on systems, Air Force Research Laboratory Report, AFRL-VS-TR-2002-1668.

van der Meeren, C., K. Oksavik, D. A. Lorentzen, L. J. Paxton, and L. B. N. Clausen (2016), Scintillation and irregularities from the nightside part of a Sun-aligned polar cap arc, *J. Geophys. Res. Space Physics*, 121, 5723-5736, doi: 10.1002/2016JA022708.

Van Dierendonck, A. J., J. A., Klobuchar, Q. Hua (1993), Ionospheric scintillation monitoring using commercial single frequency C/A code receivers, Proc. ION ITM, Salt Lake City, UT.

Vapnik, V., and A. Chervonenkis (1974), *Theory of Pattern Recognition* [in Russian], Nauka, Moscow, Russia.

Veselov, A. P. (1995), Huygens' principle and integrable systems, *Physica D: Nonlinear Phenomena*, 87(1), 9-13.

Vikram, P. (2011), Event driven GPS data collection system for studying ionospheric scintillation, M.S. thesis, Dept. of Electrical and Computer Engineering, Miami University, Oxford, Ohio, USA.

- Wang, J., and Y. Morton (2015), High-latitude ionospheric irregularity drift velocity estimation using spaced GPS receiver carrier phase time-frequency analysis, *IEEE Transactions on Geoscience and Remote Sensing*, 53, 6099-6113, doi: 10.1109/TGRS.2015.2432014.
- Wang, J., and Y. Morton (2017), A comparative study of ionospheric irregularity drift velocity derived from a GNSS receiver array and PFISR measurements during high latitude ionospheric scintillation, *J. Geophys. Res.-Space*, accepted.
- Wang, T. I., and J. W. Strohbehn (1974), Perturbed log-normal distribution of irradiance fluctuations, *J. Opt. Soc. Amer.*, 64, 994-999.
- Wautelet, G, and R. Warnant (2014), Climatological study of ionospheric irregularities over the European midlatitude sector with GPS, *J. Geod.*, 88, 223–240, doi:10.1007/s00190-013-0678-4.
- Whitney, H. E., J. Aarons, R. S. Allen, and D. R. Seemann (1972), Estimation of cumulative amplitude probability distribution function of ionospheric scintillation, *Radio Sci.*, 7, 1095-1104.
- Wiener, N. (1964), *Time Series*, M.I.T. Press, Cambridge, MA.
- Xu, R., Z. Liu, M. Li, Y. Morton, and W. Chen (2012), An analysis of low-latitude ionospheric scintillation and its effects on precise point positioning, *J. Global Positioning Sys.*, 11(1), 22-32, doi:10.5081/jgps.11.1.22.
- Xu, D., and Y. Morton (2015), GPS signal fading and carrier phase variations during strong equatorial ionospheric scintillation, Proc. ION ITM, Dana Point, CA.
- Xu, D., Y. Morton, D. Akos, and T. Walter (2015), GPS multi-Frequency carrier phase characterization during strong equatorial ionospheric scintillation, Proc. ION GNSS+, Tampa, FL.
- Xu., D., and Y. Morton (2016), Semi-open loop tracking results of strong scattered GNSS signals, poster at the annual meeting of Consortium of Ohio Universities on Navigation and Timekeeping (COUNT), Columbus, OH.
- Yacoub, M. D. (2002), The α - μ distribution: a general fading distribution, Proceedings of 13th international symposium on personal, indoor and mobile radio communications PIMRC, Lisboa, Portugal.
- Yacoub, M. D. (2007) The α - μ distribution: a physical fading model for the stacy distribution, *IEEE Trans. Veh. Technol.*, 56, 24–27. doi: 10.1109/TVT.2006.883753.
- Yeh, C. K., C. H. Liu (1982), Radio wave scintillations in the ionosphere, *Proc. IEEE*, 70(4), 324-360.

Yin, H., Y. T. Morton, M. Carroll, and E. Vinande (2015), Performance analysis of L2 and L5 CNAV broadcast ephemeris for orbit calculation, *Navigation*, 62(2), 121-130.

APPENDIX

A. Fading Characteristics of Scintillation Data from Singapore and Hong Kong

Section 6.5 analyzed fading statistics using data from Ascension Island. This section of the appendix presents some additional analysis on results using real GPS data from Singapore and Hong Kong.

Table A- 1 summarizes the PRN, dates, starting and ending times, and durations of the Hong Kong and Singapore data used in this section. All the data were collected using Septentrio PolaRxS ISM receivers. An elevation mask of 30° has been applied to reduce the effects of multipath. The normalized signal intensity is obtained using a 6th order Butterworth low-pass filter with a cut-off frequency at 0.1 Hz [*Van Dierendonck et al*, 1993].

Table A- 1. Strong scintillation events for the analysis of fading characteristics from Singapore and Hong Kong

	PRN	Date	Start UTC	End UTC	Duration
Singapore	1	2012/03/22	13:38:05	13:51:42	13m 37s
	1	2012/03/24	13:29:46	13:59:54	30m 08s
	1	2012/03/26	14:00:15	14:18:20	18m 05s
	1	2012/03/29	13:16:50	13:59:51	43m 01s
	1	2012/03/30	13:06:21	13:59:37	53m 16s
	1	2012/03/31	13:00:11	13:33:52	33m 51s
	1	2012/04/04	12:43:03	12:59:54	16m 51s
	1	2012/04/09	13:17:13	13:59:44	42m 31s
Hong Kong	24	2013/09/24	13:02:02	13:59:41	57m 39s
	24	2013/09/25	12:35:10	13:22:56	47m 46s
	24	2013/09/29	12:18:27	13:14:43	56m 16s
	24	2013/10/05	12:04:05	12:41:41	37m 36s
	24	2013/10/06	12:04:30	12:44:44	40m 14s

	24	2013/10/08	11:41:50	12:04:41	22m 51s
	27	2014/02/27	12:50:24	13:54:25	64m 01s
	27	2014/03/01	12:14:52	12:46:40	31m 48s
	27	2014/03/02	12:45:01	13:52:20	67m 19s
	1	2014/03/05	13:56:12	14:48:03	51m 51s
	24	2014/09/10	13:27:13	13:52:46	25m 33s
	24	2014/09/14	13:38:41	13:59:45	21m 04s
	24	2014/09/15	12:24:16	12:59:45	35m 29s
	25	2014/10/03	14:45:54	14:59:41	13m 47s
	25	2014/11/05	12:22:18	12:50:14	27m 56s
	25	2014/11/10	13:37:43	13:59:00	21m 17s
	25	2014/11/10	12:10:05	12:41:35	31m 30s

Two thresholds, -10 dB and -15 dB, have been defined to extract fading events from the Hong Kong and Singapore data sets. Table A- 2 summarizes the number of signal intensity fading events on the three GPS frequencies using the two thresholds. The results presented in this section are based on these events. Fading duration, time separation between fades, and temporal overlap of fades are mainly discussed and compared among the frequencies and the receiver sites. It should be noted that the definitions of the characterized measures are the same as in Section 6.5, which were illustrated in Figure 6-14.

Table A- 2. Numbers of signal intensity fading events extracted on the three GPS frequency bands from the data collected at Singapore and Hong Kong under the thresholds of -10 dB and -15 dB

Fading Number	L1		L2C		L5	
	-10dB	-15dB	-10dB	-15dB	-10dB	-15dB
Singapore	479	99	1,730	701	1,758	746
Hong Kong	5,404	2,664	12,429	6,626	11,358	6,072

Figure A- 1 shows the distributions of signal fading duration for L1, L2C and L5 in Singapore and Hong Kong with mean durations labeled in the legends. The distributions are discrete, while the connecting lines are depicted to show the trends. The unevenness in subplot (a) is due to the limited

numbers of fading events obtained in Singapore. The results indicate that the predominant fading durations are very short, typically under 100 ms, although much longer durations of more than 300 ms do occur occasionally. On average, fades observed in the Hong Kong data have longer durations than at Singapore.

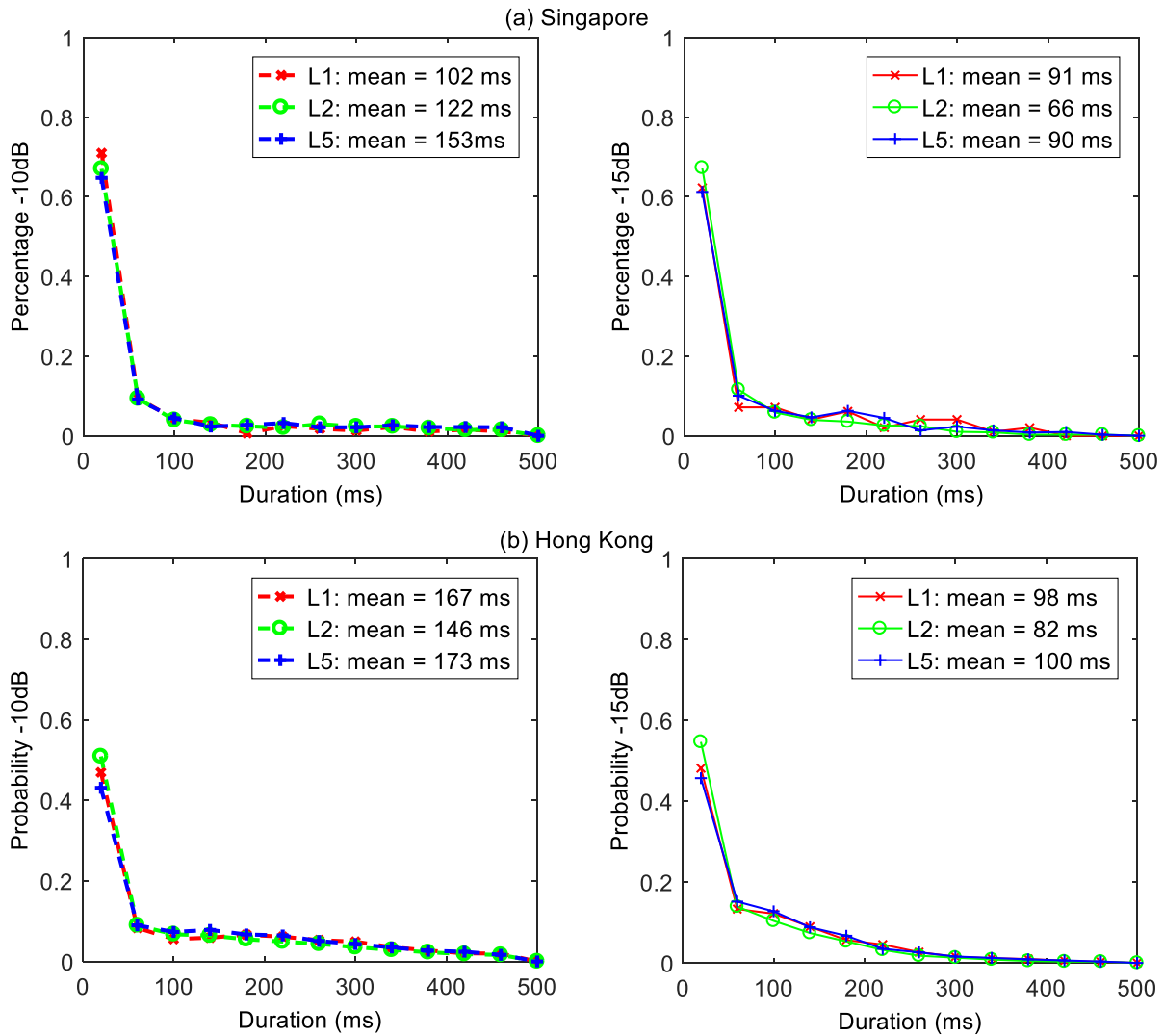


Figure A- 1. Distributions of GPS L1, L2C and L5 signal intensity fading duration in (a) Singapore and (b) Hong Kong under the thresholds of -10 dB and -15 dB. Mean durations are labeled in the legends.

Figure A- 2 and Figure A- 3 shows the distributions of single-band and multi-band time separation across the GPS frequency bands at Singapore and Hong Kong with mean separations shown in the legends. The mean separations in the plots are averages of all separations less than 1 minute as the maximum separation is infinite. The results in Figure A- 2 and Figure A- 3 show that the time separations observed in Hong Kong are generally shorter. Band-wise, in single-band cases, consecutive L2C fading appears to occur closer than that on L1 and L5. In multi-band cases, consecutive L2C and L5 fades are very close to each other, clearly due to the vicinity of their carrier frequencies.

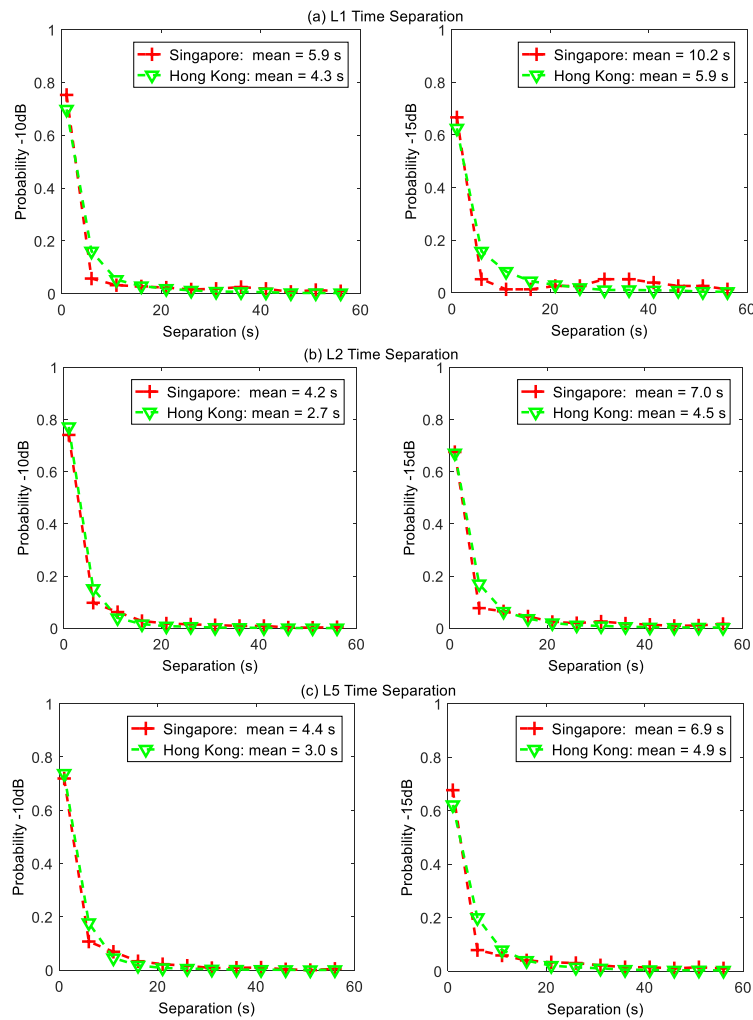


Figure A- 2. Distributions of single-band time separation for (a) L1, (b) L2C, and (c) L5 at Singapore and Hong Kong under the thresholds of -10 dB and -15 dB. The mean separations in the legends are averaged among separations under 60 seconds.

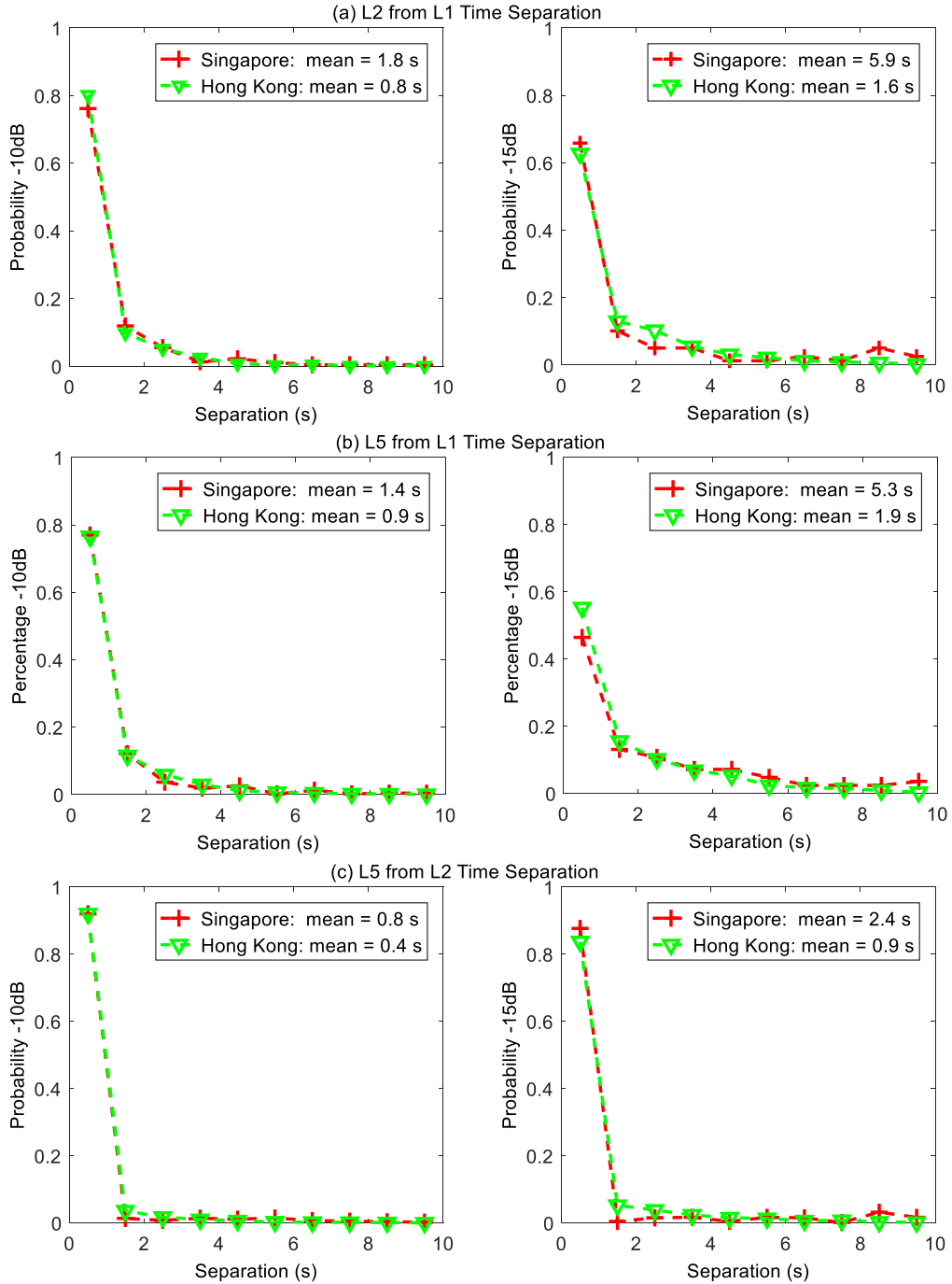


Figure A- 3. Distributions of multi-band time separation for (a) L2 from L1, (b) L5 from L1, and (c) L5 from L2 at Singapore and Hong Kong under the thresholds of -10 dB and -15 dB. The mean separations in the legends are averaged among separations under 60 seconds.

Figure A- 4 shows the quantitative relation between the intensity of amplitude scintillation (in terms of S_4 index values) and signal intensity fading. The left panels in Figure A- 4 show nicely increasing numbers of fades when amplitude scintillation becomes stronger (S_4 index becomes larger). Consistent with the previous discussion on fading duration and fading time separation (Figure A- 1 through Figure A- 3), L2C fading tends to have a larger number and shorter duration than fading on L1 and L5 at a given S_4 level, especially in Hong Kong where a larger number of events are observed. The unevenness in the right panels when $S_4 < 0.6$ is mainly due to the small number of fades (shown in the left panels) when scintillation level is low. When $S_4 > 0.6$, the mean fading duration generally keeps constant regardless of the level of scintillation at both locations.

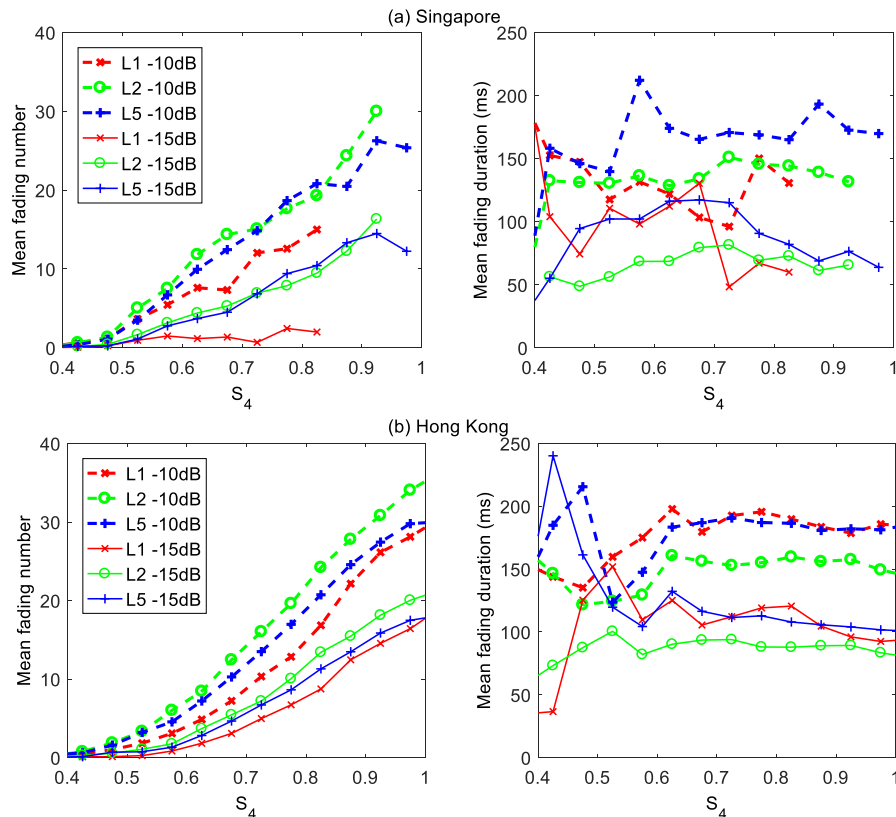


Figure A- 4. Mean fading numbers and fading durations for certain levels of S_4 index values on the three GPS bands under the thresholds of -10 dB and -15 dB in (a) Singapore and (b) Hong Kong. The fading number is the number of fades observed with their middle points within an S_4 calculation interval (60 s). It is reciprocally related to the mean time separation. The average duration of these fades is the mean fading duration shown in the right panel.

The last part of the results discusses the overlap on multi-frequency signal intensity which further demonstrates the feasibility of utilizing frequency diversity during deep fading. The fading overlap is defined the same as in Subsection 6.5.4. Table A- 3 lists the percentage of each type of occurrence among all possible types of fades in Singapore and Hong Kong. The percentages are computed only for those satellites that broadcast all three GPS signals. It can be seen in Table 6-5 and Table A- 3 that the percentages vary largely for different geographic locations. However, when the fading is relatively severe (-15 dB), the percentages of concurrent L1, L2C and L5 fading are very small in all cases, which indicates that it is possible to utilize tracking results of other bands to assist the tracking of the deep fading band during scintillation.

Table A- 3. The percentage of multi-frequency signal intensity fading overlaps on GPS L1, L2C and L5 in Singapore (first lines) and Hong Kong (second lines), for satellites that broadcast all three GPS signals only

Fading band	Threshold	L1 only	L2C only	L5 only	Concurrent L1, L2C	Concurrent L1, L5	Concurrent L2C, L5	Concurrent L1, L2C, L5
L1	-10 dB	67.0% 71.5%	/	/	7.3% 5.9%	5.2% 4.5%	/	20.5% 15.1%
	-15 dB	91.5% 87.6%	/	/	3.3% 5.4%	4.4% 3.3%	/	0.9% 3.8%
L2C	-10 dB	/	29.7% 31.0%	/	1.8% 4.4%	/	63.7% 57.1%	4.9% 7.5%
	-15 dB	/	53.4% 54.0%	/	0.6% 2.5%	/	45.8% 41.8%	0.2% 1.8%
L5	-10 dB	/	/	43.7% 37.2%	/	1.0% 2.1%	51.4% 53.7%	3.9% 7.1%
	-15 dB	/	/	65.5% 58.1%	/	0.6% 1.4%	33.8% 38.9%	0.1% 1.6%

LIST OF ABBREVIATIONS

ACF	Auto-Correlation Function
BPSK	Bi-Phase Shift Key
C/A	Coarse/Acquisition
CDCS	Continuously Displaced Coordinate System
CDF	Cumulative Distribution Function
CDMA	Code Division Multiple Access
C/N_0	Carrier-to-Noise ratio
CNAV	Civil NAVigation
CRC	Cyclic Redundancy Check
DFT	Discrete Fourier Transform
DGPS	Differential Global Positioning System
DLL	Delay Lock Loop
ECEF	Earth-Centered Earth-Fixed
FEC	Forward Error Correction
FFT	Fast Fourier Transform
FNR	False Negative Rate
FPE	Forward Propagation Equation
FPF	Fixed Position Feedback
FPR	False Positive Rate
GLONASS	GLObal Navigation Satellite System (Russia)
GNSS	Global Navigation Satellite System
GPS	Global Positioning System
IAGA	International Association of Geomagnetism and Aeronomy
ICD	Interface Control Document
IF	Intermediate Frequency
IGRF	International Geomagnetic Reference Field
IPE	Iterative Parameter Estimation
IPP	Ionosphere Penetration Point
IS	Interface Specification
ISM	Ionospheric Scintillation Monitoring
LNAV	Legacy NAVigation
MBOC	Multiplexed Binary Offset Carrier
MEO	Medium Earth Orbit
NH	Neuman-Hofman
NP	Neyman-Pearson
PDF	Probability Distribution Function
PLL	Phase Lock Loop
PRN	Pseudo-Range Noise
PSD	Power Spectrum Density
PWE	Parabolic Wave Equation
RF	Radio Frequency
ROC	Receiver Operating Characteristic

SBAS	Satellite Based Augmentation System
SDF	Spectral Density Function
SDR	Software-Defined Receiver
SNR	Signal-to-Noise Ratio
SOL	Semi-Open Loop
SRM	Structural Risk Minimization
STEC	Slant Total Electron Content
STFT	Short-Time Fourier Transform
SV	Support Vector
SVM	Support Vector Machine
TEC	Total Electron Content
TNR	True Negative Rate
TPR	True Positive Rate
UTC	Coordinated Universal Time
VHF	Very High Frequency
VTEC	Vertical Total Electron Content
WGS	World Geodetic System
WMM	World Magnetic Model